Interplay between microtubule organization and cell adhesions during epithelial morphogenesis

Mithila Burute

Communauté
UNIVERSITÉ Grenoble Alpes

THÈSE

Pour obtenir le grade de

DOCTEUR DE L'UNIVERSITE DE GRENOBLE ALPES

Spécialité : **Physique pour les sciences du vivant**

Arrêté ministériel : le 6 janvier 2005 - 7 août 2006

Présentée par

Mithila BURUTE

Thèse dirigée par **Manuel THERY**

préparée au sein de l'équipe Physique du cytosquelette et morphogénèse dans le laboratoire Physiologie Cellulaire et Végétale dans l'école doctoral de physique

Régulation de l'organisation des microtubules par les adhérences cellulaires au cours de la morphogénèse épithéliale

Thèse soutenue publiquement le 18 Mai 2016
devant le jury composé de :

Mme. Corinne ALBIGES-RIZO
CNRS, Institut Albert Bonnoit (Président)

Mme. Sandrine ETIENNE-MANNEVILLE
Institut Pasteur, France (Rapporteur)

Mme. Marina GLUKHOVA
Institut Curie, France (Rapporteur)

M. Cayetano GONZALEZ
Institute for Research in Biomedicin, Spain (Membre)

Mme. Joanne YOUNG
CYTOO, France (Membre)

M. Manuel THERY
CEA, Physique du Cytosquelette et Morphogénèse (Membre)

Mithila Burute

Interplay between Microtubule Organization and Cell-Cell Adhesions during Epithelial Morphogenesis

Thesis Dissertation

University Grenoble Alpes

Physics for Life sciences

Supervised by

Manuel Théry

Laboratory of physics of cytoskeleton and morphogenesis, within the graduate school of Physics

2016

Communauté
UNIVERSITÉ Grenoble Alpes

THESIS

For the degree of

DOCTOR OF PHILOSOPHY at the University of Grenoble

Speciality : **Physics for life sciences**

Arrêté ministériel : le 6 janvier 2005 - 7 août 2006

Presented by

Mithila BURUTE

Supervised by **Manuel THERY**

Prepared in the laboratory of physics of cytoskeleton and morphogenesis, PCV
within the graduate school of physics

Interplay between microtubule organization and cell-cell adhesions during epithelial morphogenesis

Thesis defense on 18th May, 2016

In front of the committee :

Mme. Corinne ALBIGES-RIZO
CNRS, Institue Albert Bonnoit (President)

Mme. Sandrine ETIENNE-MANNEVILLE
Institute Pasteur, France (Referee)

Mme. Marina GLUKHOVA
Institute Curie, France (Referee)

M. Cayetano GONZALEZ
Institute for Research in Biomedicine, Spain (Member)

Mme. Joanne YOUNG
CYTOO, France (Member)

M. Manuel THERY
CEA, Physics of Cytoskeleton and Morphogenesis lab (Member)

Acknowledgements

This work is a result of great inspirations and help from my supervisors, teachers, colleagues, friends and family.

I would first like to thank my thesis supervisor and mentor Manuel Théry, who has been a constant source of motivation. His extra-ordinary enthusiasm and interactive nature have always kept the scientific discussions very vibrant. One can get the gist of his working style through what he wrote in an award essay, *"It is not simply about pushing the boundaries between the real and imaginary, it is about rewiring the real"*. Talking to him even about any failed hypothesis has only brought better understanding of the scientific problem. He provided me absolute freedom to develop interest and adapt strategies to approach different projects and this made my thesis work really interesting and enjoyable. I owe him sincere gratitude for giving me amazing opportunity to learn and explore scientific problems to best of my capacities.

I would like to thank Laurent Blanchoin, the head of the lab, for his support throughout my stay in this lab. His critical approach for defining the scientific problems has always helped me to set rational goals for the project. Most importantly, he has been a caretaker for all kinds of administrative work, which reduced most of the hassles. His rigorous discipline for the lab-presentations has prompted me to be organized and well aware of the scientific literature. Furthermore, I would to thank Joanne Young, my thesis co-supervisor. She supervised the part of the work that was done in collaboration with CYTOO. She regularly followed my work, provided useful feedbacks and was always available for discussions.

I thank the Jury members of the thesis, Marina Glukhova, Sandrine Etienne-Manneville, Corinne Albiges-Rizo and Cayetano González who agreed to review my work and provide their invaluable feedback.

Odile Cochet is the 'EMT expert' in the team and I learnt a lot about the EMT pathways and 3D cultures from her. Discussions with her were very conducive to understand in vivo relevance of the experiments. Magali Prioux worked extensively on the EMT project and she performed all

the 3-D acini experiments. She was a great co-worker and her dedicated nature made it possible to extend breadth of the project to various cell line models and to reveal underlying mechanisms of the polarity reversal.

I would like to thank my lab-mate and a good friend, Gaëlle Letort. She helped me for image and statistical analysis. She is a superb programmer and has been extremely generous for any kind of help that I needed. I would also like to thank my dear PhD batch-mates Hajer and Laura who provided great company in the lab and the time I spent in this lab was really rocking because of them. I find myself fortunate to have them in my life, professionally and personally. I am grateful to Timothée Vignaud for training me for all the experimental work in the beginning of my PhD. He was very patient and helpful to teach and troubleshoot any kind of experimental issues. I would like to thank Qingzong Tseng who began the work on polarity reversal in EMT. He developed image analysis programs for force measurements and nucleus-centrosome position analysis, which provided me a good head start on this project.

I would like to thank Jerome Larghero and Valerie Vanneaux for integrating our cell biology team into their stem cell therapy group in the hospital Saint Louis. It is a great experience to work closely with medical doctors who are specialized for human stem cell therapy. I feel very fortunate to have had the opportunity to work with Susana Godinho and David Pellman on pioneering study of role of centrosome amplification in cancer. I learnt important aspects of centrosome and microtubules through work of this project. This project was very innovative and had brilliant experimental approach and thus working on this project was really exciting. I truly appreciate help of Sandrine Truchet who had very enthusiastic initiative to help us with the mouse mammary gland tissue studies. She was very generous in welcoming me in her lab to teach the tissue processing. Her expertise in mouse development helped us to look for events of polarity changes at the morphogenetic stages of mouse. I would also like to thank Guillaume Blin for his contribution to the project for precisely capturing polarity changes at the gastrulation stage in whole mouse embryo. I thank Lisa Gallegos and Joan Brugee who helped us to test siRNA library using the "EMT kit" assay. I thank Mathieu Piel who provided us compounds for dynamic micropatterning. I athank Marina Glukhova for giving us important advice on choice of epithelial cell lines and I also thank Priscilla Soulie for kindly providing the EpH4 cell line.

I would like to immensely thank Ana Jimenez who is a wonderful colleague and a very loving person. I turned to her in case of any trouble; whether it was inside or outside the lab and she has been extremely patient and generous in helping me. I truly adored Lucineh for her cheerful presence and positive vibe, which has always kept the lab environment very lively. I felt really motivated by the working style of James Sillibourne, who was really meticulous and had perfection at his work. I looked up to him for those qualities and feel thankful for all the needed help he has generously offered. I owe great thanks to Benoit Vianay for his timely help on the experimental, microscopy and analytical part of the work. He is the organizer of the lab and his immense efforts for setting up the lab infrastructure has helped everybody to work smoothly. Stéphane Brunet is the cheerful 'Microtubule guy' in the team to whom I could turn whenever microtubules showed intriguing behavior. He was always willing to engage in open discussions and provided helpful suggestions for the experiments as well as feedback on the thesis. I really enjoyed the company of Stéphane Biedzinski who is really genuine and a jolly person. Thomas Bessy is the head of the lab-gatherings and has always kept the lab environment cohesive and cheerful. He worked on the 'EMT kit' project and optimized the micropattern geometries to detect cell separation. Discussions with Jérémie Laurent are always amusing because of his great depth of knowledge and innovative ideas. I would like to thank Isabelle Cacciapuoti, Lionel Faivre, Alexandre Parouchev, Dimitri Ayollo, Camille Cordier, Clement Turpain, Laëtitia Pinte, Camille Portal, Thomas Domet, Gael Mbeleouengue, Mathilde Koch, and Helene Boucher for being truly awesome colleagues. They were always around in case of any help. Lunch-hours and celebrations in the lab with all of them have been really delightful.

I would like to thank my good friend Andreas Christ who built a stress-releasing wall in the lab. I would also like to thank Christophe Guerin, Amandine Pitaval, Alphée Michelot, Laëtitia Kurzawa, Lauréne Gressin, Emilie Barou, Karin John, Aleksandra Icheva, Tobias Klar, Illaria Scarfone, Virginie Mellet, Sebastien Degot, Jean-Louis Martiel, Aldo Leal, Daisuke, Charlotte Aumeier and Rajaa Paterski who provided assistance with different aspects of the lab work.

I would like to especially thank Jérémie Gaillard, Danielle Adelaide, Fabrice Senger, Sophie Mistri and Audrey Galmiche for their tremendous assistance with the lab purchase orders, microscopy and administration procedures. They really are the heroes who work behind the screen and let the lab run smoothly. I also wish to thank Sandrine Ferrari and Eglantine Zala who

helped me for administration procedure required at the doctoral school.

This goes without saying that I owe sincere thanks to all the people in the team who have been very kind to speak with me in English and have never let me feel the language barrier whenever I was in need.

I sincerely want to thank Litcheun Filhol and Bruno Filhol who welcomed me in their home during my initial stay in Paris. Litcheun has been warm and caring person all this time. I would like to express special thanks to Marriane Pierot who was my cheerful tandem french speaking partner when I arrived in France. I really appreciate her timely help with the visa procedure. I am grateful to have good friends Nupoor, Kamal and Surayya whose caring nature always made me feel at home. I would like to thank Srikanth Kesavan, Shriharsha, Lahiri and Agnieszka Kawska who are great friends and their company has always been a delight. I thank Snigdhadeep, Achal, Meenu, Kabila, Mani for their kind help.

I am truly grateful to Mithila Agnihotri, Kaustubh Gokhale and Sushrut Shirole for their priceless companionship.

I am sincerely grateful to my loving mother Pushpa, who has always supported and encouraged me to pursue what I liked. I am also grateful to my grandmother Radha for her unconditional love.

This thesis work has been a continuous enjoyable journey of learning and I am thankful to all who have been part of it.

Mithila Burute

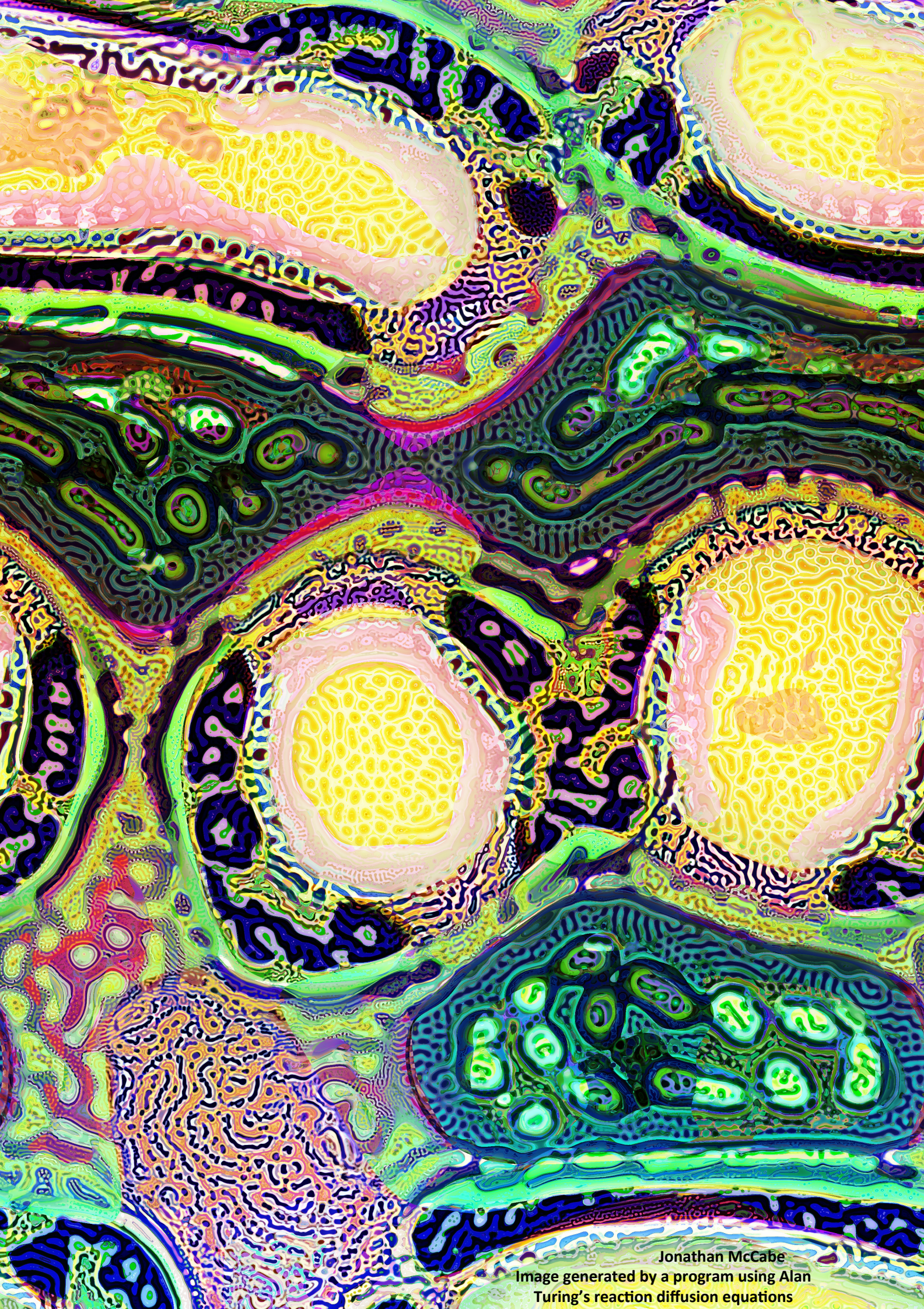

Jonathan McCabe
Image generated by a program using Alan Turing's reaction diffusion equations

This thesis is dedicated to the unfathomable biological forms that seem to emerge so effortlessly over and over again that the urge to understand them is almost unstoppable.

"It is not birth, marriage, or death, but gastrulation, which is truly the most important time in your life"

Lewis Wolpert (1986)

TABLE OF CONTENTS

Preface

While explaining how the form and function of the tissue reciprocate to guide the tissue organization at a TED talk by Mina Bissell, the hero of tissue-microenvironment and cancer studies, she said,

"I would like submit to you that we have sequenced the human genome, we know everything about the sequence of the gene, the language of the gene, the alphabet of the gene, but we know nothing but nothing about the language and the alphabet of form"

You may think that she referred it 20 years ago or so, but she mentioned it recently in 2012, eleven years after the first draft of human genome sequence was published. One of the reasons why we still do not completely understand function of the genome is because of lack of understanding of how DNA is regulated by not only genetic elements but also the environment.

This thesis work is performed in an attempt to understand tissue architecture and plasticity through regulation of sub-cellular cytoskeleton and cell-adhesion components. However, I would like readers, whether they are from scientific or non-scientific background, to appreciate the approach undertaken to study complex behavior of organs in a human body. With trillions of cells residing in our body, any model that is at a scale of ten or hundreds of cells may sound irrelevant straightaway. But if we look across the planet, the recurrence of pattern formation is evident in biological and non-biological forms. For example, fractal features seen at different scales in tree branching, river networks, blood vessel networks suggest common physical laws binding the final form in various systems. Moreover, branching network seen in mammary gland, lung and salivary gland support the notion that patterns emerge when subjected to proper boundary conditions. And thus, it is probably not so absurd to start thinking of human body as a manifestation of small modules generated with fewer cell number. To reiterate Lewis Wolpert,

It has been a great surprise and of considerable importance to find that most embryonic fields seem to involve distances of less than 100 cells, and often less than 50.

Today the biology is hugely dominated by organism level studies such as whole genome screens, the Human brain project etc. The importance of these approaches is undoubtedly crucial for medical treatments. However, in my opinion without the thorough understanding of the basic functioning unit of tissue we cannot completely comprehend how the organs and ultimately the human body work.

An inspiring and comprehensive description, "Building the cell: design principles of cellular architecture' by Susanne Rafelski and Wallace Marshall certainly provokes the question, do we harbor enough knowledge to build the cell? Cell is complex at the molecular scale, yet simpler at the form and it acts like a fundamental functional block of the organ. During the course of this thesis we observed amazing recapitulation of the tissue phenotype within mere 2-cell unit, which we call a minimal tissue model. Two cells with physical boundary condition and proper environmental cues exhibited phenotype that was comparable to tissue phenotype. Again, I would like to insist that recapitulation of phenotype with minimal tissue model does not implicate replica of the tissue at a smaller scale, but it means that the minimal model is a derivative of the final tissue form and function. With this in mind, I hope that the readers would appreciate the power of minimal-tissue models, which are extensively used throughout the work of this thesis to study tissue plasticity during embryogenesis and cancer progression. Within upcoming years, if we aspire to build a tissue or an organ, which will have countless applications in medical and fundamental research, I think starting with building a minimal tissue is the first step towards it…

Mithila Burute

Summary of the thesis (English version)

Development from a single cell embryo to the multicellular adult form of organism involves tremendous morphogenesis. The well defined and highly controlled morphonogenetic processes are crucial at every stage of the development including gastrulation, organogensis, wound healing and tissue maintenance. The necessary harmony between the cells for these processes is achieved by integration of internal and external polarity cues. This thesis work is focused on understanding how cells integrate polarity cues to drive morphogenetic events such as of Epithelial to mesecnhymal transition (EMT) and cancer metastasis. We used centrosome position as an indicator of internal cell polarity due to its active role in organization of microtubules and orientation of internal traffic of endocytosed and secreted proteins; while cortical polarity was inferred by polarized distribution of cell-cell adhesions (CCA) and cell-matrix adhesions (CMA). In the first part, we studied effect of centrosome amplification, which is very common in human cancer; on CCA. Inducible centrosome amplification in mammary gland cells led to destabilization of CCA alongwith generation of invasive cell protrusions. Using a minimal model of tissue; confined on micropatterns, we demonstrated that cells with amplified centrosome correctly oriented their internal polarity axis like normal cells although increased centrosomal protein and peri-centriolar material emanated higher centrosomal microtubules. Use of in vitro models of cell lines and controlled culture conditions revealed that mere amplification of centrosome was sufficient to drive cell fate for cancer-like events in the absence of any additional external growth signals capable of affecting cortical polarity. This study revealed that internal polarity cues interact with the cortical polarity signals and the crosstalk between the two governs the physiological state of the cell during transformation events like cancer metastasis. The second part of the study focused on exploring how internal polarity during EMT is modulated to drive precise spatial movements during development. Cell adhesion remodelling being central to EMT, we hypothesized that it was coupled to internal polarity changes. We monitored centrosome position in epithelial and in cells induced for EMT by TGF-β1 and we found that nucleus-centrosome axis was reversed after the EMT induction. This phenomenon of polarity reversal strongly suggested that internal polarity cues and positioning of organelles is coupled to signals that polarize CCA and CMA distribution. A shift in the force balance between CCA and CMA was observed upon EMT and suggested that CMA forces dominated in mesenchymal cells. Release of cells from the confinement clearly revealed that the ability of cell separation was dependent upon their internal polarity. These results demonstrated that cell-scattering events observed during mesoderm formation during gastrulation or metastasis events in cancer ; involve active and well controlled reversal of

internal polarity axis that is coupled to the cortical polarity of cells. From the understanding of the above two projects involving cancer-like scattering phenomenon, we developed a product to allow robust screening of anti-cancer drugs. We once again used the simplified two-cell model on micropattern geometries to develope an assay to detect scattering ability of cells after events like EMT. The assay was validated by EMT transformation of 4 different epithelial cells lines. The detection of their scattering ability was performed using single time point picture assay. We used internuclear distance between the cell-pair as the main parameter for scoring the scattering index of cells with a possibility of automated image processing. The final product was manufactured in 96-well plate format by our industrial collaborator CYTOO for high content screening. Preliminary validation performed using drugs against EMT constituted proof of concept of the product.

Summary of the thesis (French version)

Au cours de son développement depuis la cellule unique jusqu'à la forme adulte, l'embryon passe par de nombreuses étapes de morphogenèse. Les processus morphogénétiques, bien définis et très contrôlés, sont essentiels à chaque étape du développement. L'harmonie entre les cellules au cours de ces processus est assurée par l'intégration spatiale des signaux externes qui assurent la cohérence des polarités internes et externes des cellules. Ce travail de thèse se concentre sur la façon dont les cellules intègrent les informations spatiales dans la définition de leur polarité au cours de grandes transformations morphologiques comme la transition épithélium-mésenchyme et la dissémination des cellules tumorales. Nous avons utilisé la position du centrosome comme un indicateur de la polarité cellulaire interne en raison de son rôle actif dans l'organisation des microtubules et donc dans l'orientation du transport intra-cellulaire. La polarité corticale a été inférée à partir de la répartition spatiale des adhérences cellule-cellule (ACC) et cellule-matrice (ACM).

Dans la première partie, nous avons étudié l'effet de l'amplification du nombre de centrosomes, une caractéristique fréquente dans les cellules tumorales, sur l'adhérence inter-cellulaire. L'amplification des centrosomes dans les cellules de la glande mammaire a conduit à la rupture des adhérences inter-cellulaires ainsi qu'à la genèse de protubérances cellulaire invasive. A l'aide d'un modèle minimal de tissu, confiné sur micropatterns, nous avons démontré que les cellules comportant un nombre excessif de centrosomes étaient capables d'orienter correctement leur axe de polarité interne. Cependant le matériel centrosomal étant plus développé, de nombreux microtubules supplémentaires émanait de ces clusters de centrosomes surnuméraires. En conséquence Rac1 était suractivé ce qui avait pour effet d'induire des protrusions membranaires importantes. L'utilisation de modèles cellulaires in vitro

et de conditions de culture contrôlées ont révélé que la simple amplification des centrosomes est suffisante pour moduler le destin de cellules transformées et les rendre invasives. Cette étude a révélé que les mécanismes régissant l'orientation la polarité interne des cellules sont liés à l'arrangement spatial de la polarité corticale et qu'une rupture de conjugation les deux perturbrai la physiologie du tissu au point d'induire la formation de métastases tumorales.

La deuxième partie de l'étude a porté sur l'exploration de la transition épithélium-mésenchyme (EMT). Nous avons étudié le rôle potentiel des mécanismes de régulation de la polarité pour diriger la précision des mouvements cellulaire au cours de l'EMT. Le remodelage des adhérences inter-cellulaires jouant un rôle central au cours de l'EMT, nous avons supposé qu'il était couplé à des changements de polarité interne. Nous avons suivi le positionnement du centrosome dans les cellules épithéliales et dans les cellules dans lesquelles l'EMT était induite par stimulation au TGF-β. Nous avons constaté que l'orientation des cellules traitées au TGFb était complètement inversée. Ce phénomène d'inversion de polarité suggérait fortement que l'orientation de la polarité interne et le positionnement des organites étaient couplées à l'organisation polarisée des ACM et des ACC. Nous avons en outre constaté que Par3, un marqueur des jonctions apicales était responsable du repositionnement du centrosome pendant l'EMT. Un changement dans l'équilibre des forces en faveur des ACM par rapport aux ACJ nous a amené à penser que ces forces jouaient un rôle important dans les cellules mésenchymateuses et ce notamment pour leur capacité de migration. En effet la libération des cellules mésenchymateuses de leur confinement nous a montré que la séparation des cellules après l'EMT était dépendante de l'inversion de polarité interne dans ces cellules. Ces résultats suggèrent que la dispersion des cellules observée pendant la formation du mésoderme au cours de la gastrulation impliquent un renversement actif et finement contrôlé du couplage entre l'axe de polarité interne et l'asymétrie des deux types d'adhérences cellulaires.

Suite à l'étude de ces deux projets impliquant des dispersions cellulaires, nous avons développé un dispositif pour permettre le criblage de médicaments contre les dérèglements cellulaires impliqués dans la formation des métastases. Nous avons à nouveau utilisé un modèle simplifié de paires de cellules sur des micropatterns pour détecter la capacité de dispersion des cellules suite à des stimulations externes comme celle induisant l'EMT. Le test, qui permet de mesurer le degré de séparation des cellules à l'aide d'une seule image, a été validé sur quatre lignées de cellules épithéliales différentes. La distance internucléaire entre les deux cellules a été utilisée comme une mesure automatisable des capacités de dispersion des cellules. Le dispositif final a été adapté à un format de plaque 96 puits en collaboration avec l'entreprise Cytoo afin de permettre des criblages à haut contenu. Ce kit a ensuite été validé en testant des médicaments connus contre l'EMT. Enfin, une analyse de 20 gènes candidats a été faite à l'aide de siRNA ciblant les adhérences intercellulaires. Elle a abouti à la validation des gènes classiquement impliqués dans l'EMT ainsi qu'à la mise en évidence de nouveaux

candidats potentiels.

Short summary for the general public (English version)

The epithelial cells line up along the periphery of the organs that have an interface with the external environment such as the renal tubules or the mammary glands. This topology is severly perturbed during epithelial to mesechmal transition (EMT) that occurs during normal development and tumor progression. In this work, we induced this transition by addition of TGF-β to the cell culture of human mammary glands. We monitored the centrosome position, which is an important marker of cell polarity. We found changes in centrosome position during EMT and it's relocation predisposed mesenchymal cells to separate and migrate to the tissues, as they do during metastases. With this observation, we developed a commercial product to detect such errors and to test the potential role of new drugs which can interfere with this transformation.

Short summary for the general public (French version)

Les cellules épithéliales longent la périphérie des organes qui ont un interface avec le milieu extérieur tels que les tubules rénaux ou les glandes mammaires. Cette topologie des organes est sévèrement remodelé au cours du développement normal et de progression du cancer r par processus nommé transition épithélium-mésenchyme (EMT). Nous avons induit cette transition dans des cellules de glandes mammaires humaines en culture en les traitant au TGF-β. Nous nous sommes intéressés au positionnement du centrosome, qui est un marqueur important de la polarité cellulaire. Nous avons constaté qu'il changeait de position au cours de l'EMT et que cette relocalisation prédisposait les cellules mésenchymateuses à se séparer et à migrer vers l'intérieur des tissus, comme elles le font au cours de la formation des métastases. Forts de cette observation, nous avons développé un produit commercial permettant de tester le rôle éventuel de nouveaux médicaments capables d'interférer avec cette transformation.

0.0 General introduction to the thesis

Emergence of the epithelium

Primitive life existed in unicellular form. Multi-cellular metazoans life forms evolved from single cell prokaryotes over more than 3 billion years. Multi-cellularity required development of intercellular adhesions, synthesis and secretion of intercellular adhesion material, development of systems of attachment to extracellular medium and development of intercellular communication system. The structural integrity of multicellular organisms depends upon the establishment and maintenance of the stable cellular connections. The phyla of metazoans provide models of progressive evolution of specialized epithelial structures from primordial epithelia. The lower metazoan possess a basic body plan with a single central cavity enclosed by epithelia-like monolayers which lack the typical belt-form junctions of epithelial (eg Adherene or tight junction proteins) and hence are not capable of isolating any compartments; they are not considered to be true epithelial. The multicellular body form of phyla, Porifera (eg. Sponges) are considered non-epithelium because of lack of true cell-cell junction and basal lamina (Figure 0.1A). Their epithelia-like layer lacks typical belt-form of junction and thus do not isolate any compartments. The progressive grades of epithelial organization are observed in higher phyla of Cnidaria (eg. Hydra, Sea anemone) with formation of true epithelia (Figure 0.1A), which segregates internal cavity from exterior (Tyler, 2003). The salient features of true epithelium are, formation of the stable intercellular junctions with specialized functions such as prevention of passage of molecules across epithelium (Tight junctions), bringing adjacent cells together (adherene junctions), resisting mechanical stress (desmosomal junctions), allowing passage of small molecules between adjacent cells (gap junctions) and anchoring epithelium to basal lamina (focal adhesion) (Figure 0.1 B) (Abedin and King, 2010). The complexity of metazoan body plan arises from their capacity to develop organ systems. Formation of gut, kidney, liver, and secretary glands are the modules that are constructed by forming independent cavities within the organism. The capacity to develop these organs has emerged from differentiation of two main cell forms, epithelial and mesenchymal cell. (Figure0.1C).

Abbreviations: **APC**: adenomatous polyposis coli, **CA**: Centrosome amplification, **CCA**: Cell-Cell Adhesion, **CDK**: Cyclin dependent kinase, **MAPs**; CMA: Cell-Matrix adhesion, Microtubule associated proteins, **MTOC**: Microtubule organizing center, **PCM**: Pericentriolar Material, **SPD-2**: Spindle defective-2/CEP192 Centrosome associated pericentrin, **+TIPs**: plus-end tracking proteins, **TGN**: Tran-golgi network, **NC axis**: Vector passing through center of centrosome and nucleus

Figure 0.1

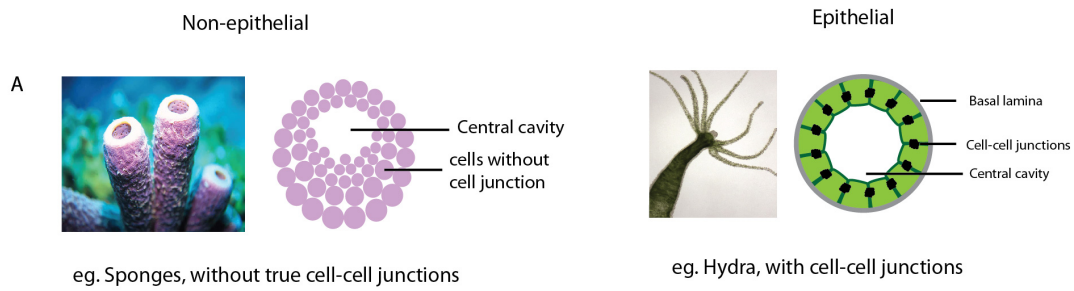

B

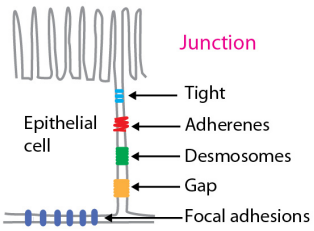

Junction	Structural Proteins	Function
Tight	Claudin, Occludins	Prevent passage of molecules across epithelium
Adherenes	Cadherins	Tether adjacent cells together
Desmosomes	Desmocollin, Desmoglein	Resist mechanical stress
Gap	Connexin, Pannexin	Allow passage of small molecues between adjacent cells
Focal adhesions	Integrin family	Anchor epithelium to basal lamina

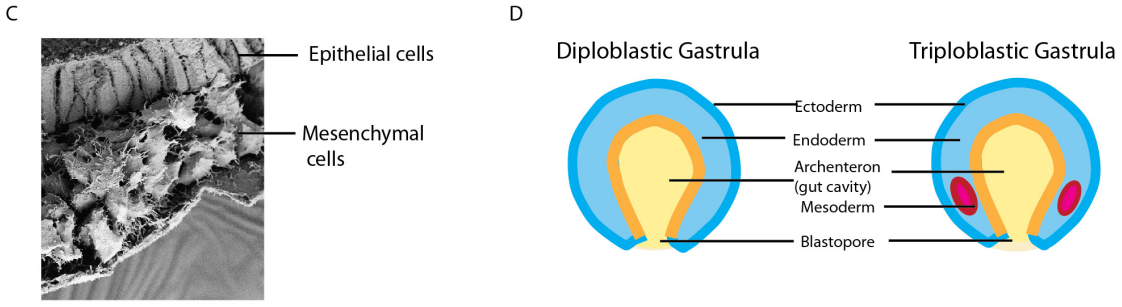

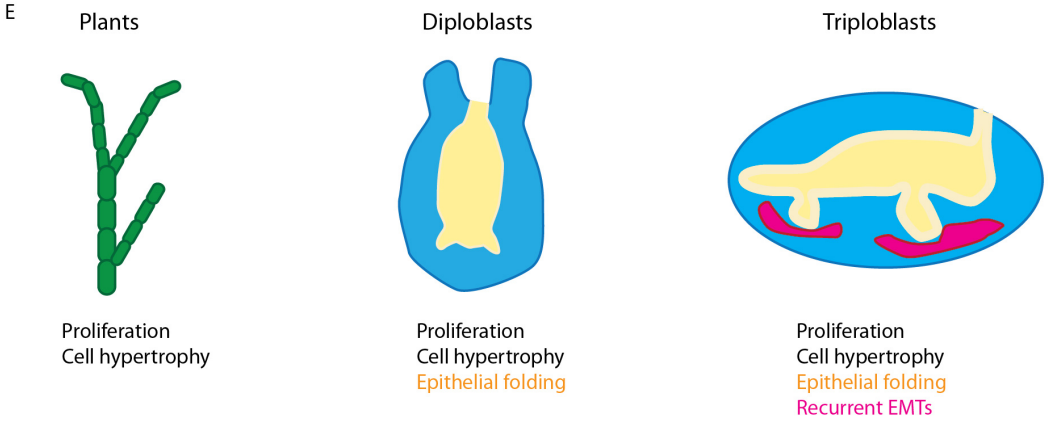

(A) Difference of epithelial and non-epithelial organization in sponges and hydra (B) Types of cell-cell junction proteins and thier functions (C) Comparison between diplobastic and triploblastic animals' germ layers after gastrulation (D) Electro-micrograph of gastrulation showing epithelial and mesenchymal cells. (E) Comparison between different cell behaviour in plants, diploblasts and triploblast animals for generating their respective tissue architecture

Emergence of Epithelial-to-mesenchymal transition

Over 500 million years ago evolution of the key event wherein epithelial cells could transform into migratory mesenchymal cells allowed the possibility of crossing cell sheets to the interior and redifferentiating to form epithelial organ structures. The basic difference between diploblastic (two germ layers) and triploblastic (three germ layers) metazoans can be visualized by their ability to form internal closed structures, which are derived from mesoderm (Figure 0.1D). The triploblastic body structures have advantage of compartmentalization owing to underlying epithelial structures, which enclose coelom (true body cavity) that is separated from the gut lumen (Figure 0.1D). The advantages of coelom is that it protects organ from external body pressure allows more extensive growth of organs including the digestive tract, it permits the formation of an efficient circulatory system and the fluid can transport materials faster than by diffusion.

The epithelium and mesenchyme thus the basic types that constitute metazoan embryo. The two types of cells possess different intercellular organization and different capacity to interact with the extracellular matrix. The epithelial cells are polarized with segregation of trans-membrane proteins into apical, baso-lateral and basal region, which are the fundamental polarity cues necessarily for polarized tissue formation. On the other hand, mesenchymal cells are thought to have emerged as derivative of epithelial cells during evolution (Shook and Keller, 2003; Tyler, 2003). In the context of development, Epithelial-Mesenchymal transition gives rise to mesenchyme-like cells with weaker cell-cell junction, migratory abilities and they can dedifferentiate into epithelial structures such as kidney by process of Mesenchyme-Epithelial transition (MET). The EMT process is the basis of organ formation consisting coelom in higher metazoans. In plants and fungi the body form arises from cell proliferation and cell growth (hypertrophy) while in addition to that, diploblastic animals posses ability of epithelial sheet folding to form a body cavity. The triploblastic animals can form organs which are separated from gastrointestinal cavity by ability of EMT (Tyler, 2003) (Figure 0.1E). The reproducible body forms seen across metazoan phyla with involvement of EMT reflect reproducible and tightly controlled processes that drive cellular movement in the correct sequence and direction. And hence it seems very plausible that execution of epithelial morphogenesis program would involve cellular-molecular compasses, which impart ability to cells to recognize their micro-environment and undergo coordinated local movements within the embryo without disturbing the overall body form. Here what I call cellular-molecular compass is the ability of cells to sense internal and external directional cues to organize and migrate in polarized manner. It has the same notion of what is often referred as 'positional information' of cells. Segregation of cellular components, formation of gradients, activation of signaling cascades, morphological asymmetry of cell as response to directional cues can be considered as part of cellular-molecular compass.

Figure 0.2

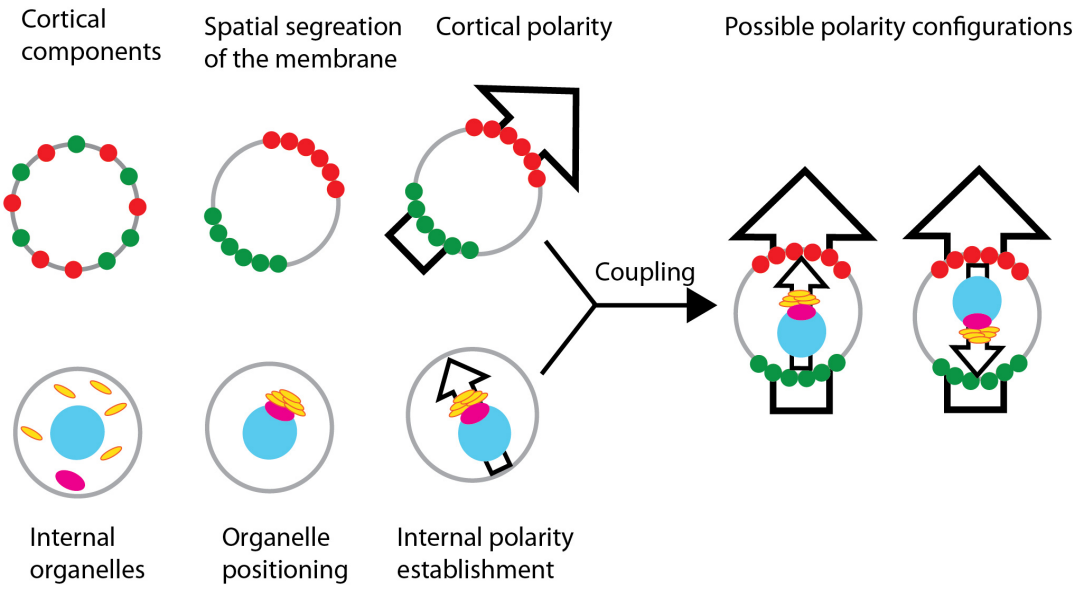

How do components of internal and cortical polarity interact with each other?

1. Effect of Centrosome and Microtubule network on cell-cell adhesion — Chapter I
2. Effect of cell-cell adhesion on centrosome position — Chapter II

Development of industrial product called the "EMT kit" from understanding of above two projects for anti-cancer drug screening — Chapter III

Main questions of the thesis

The two major components of the cellular-molecular compass can be defined,

1. **Cortical polarity** - Polarized distribution of cell membrane associated proteins such as Cell-cell adhesion, cell-matrix adhesion. It also involves asymmetric distribution of membrane lipids, small GTPases Rac, Rho, Cdc42 (Figure 0.2).
2. **Internal polarity**- Asymmetric distribution of organelles within the cell such as Nucleus-centrosome-golgi orientation. It also involves position of Cilium, movement of Rab proteins, recycling/sorting endosomes, mRNA and protein gradients (Figure 0.2).

Within the framework of this thesis I would like to discuss how these two polarity cues interact with each other and integrate the signals to give rise to the final polarity that is necessary for tissue establishment as well as tissue morphogenesis. The main questions addressed in this work are,

1. How do components of internal and cortical polarity interact with each other to establish tissue polarity?
2. How cortical and internal cell polarity is controlled and altered for the execution of morphogenetic events?

In a crowded cytoplasm inside a cell, cytoskeletal networks allow rapid and directed transport of organelles by motor proteins and their specific subcellular localization through regulation of cytoskeletal distribution and dynamics. Thus chemical and mechanical environmental cues can be transmitted to the cell interior by the cytoskeleton engaged at the cell cortex complexes. Actin, microtubules and intermediate filaments form distinct cytoskeletal networks within cells and perform function of organelle positioning, intracellular trafficking and regulate cytoskeletal distribution and dynamics. Microtubules are involved in majority of above function, as they are capable of extending over the whole length of cell and thus can transmit signals from the farthest part of the cell. Microtubule network generates polarized trafficking of molecules within cells, which is required for maintaining cortical polarity components at distinct locations. The position of microtubule array can in turn also affect the position of organelles (Rafelski and Marshall, 2008). Hence microtubules act as the main link that maintains the crosstalk between the internal organelles and cell cortex necessary for establishment of cell polarity. In this thesis we studied how cell polarity is modulated during different epithelial morphogenetic processes. We focused on understanding the cell-cell adhesions and microtubule network affect each other during tissue morphogenesis.

Over the 4 years of thesis work with help from collaboration work I explored mechanisms of cancer invasion and epithelial-to-mesenchymal transition (EMT), which involve dramatic tissue remodeling that mediated by microtubule network. In this thesis asymmetry of microtubule array is mainly inferred by centrosome position within the cell as microtubule network in animal cells is majorly organized at the centrosome.

I will begin the thesis introduction by describing cortical and internal polarity components. I will introduce fundamental processes of epithelial organization and mechanisms involved in spatial segregation of cell adhesion complexes and also describe typical organelle asymmetries generated within the epithelial cell.

The thesis is structured into three chapters for addressing specific aspects as shown in (Figure 0.2). Each chapter contains an introduction to describe the phenomenon under study and focused review of literature to describe synthesis of hypotheses. Chapter I and II include manuscripts of the articles. At the end of each chapter, I have taken liberty to discuss the implications of the results, possible mechanisms and newer hypotheses that I realized from this work.

In chapter I, I will describe the study undertaken to investigate, how cell-cell adhesions are modulated by microtubule network in cells having amplified centrosomes, which is a hallmark of human cancers. The altered microtubule network in these cells effectively damages the tissue integrity and triggers malignant phenotype.

In chapter II, I will focus mainly on how internal polarity within epithelial cells is altered during the course of EMT and how this change affects the final step of mesenchymal separation. The work mainly involves understanding of orientation of internal polarity guided by centrosome-MT network coordinated with remodeling of cell-cell adhesion on the onset of EMT.

This thesis work is also inspired from industrial point of view to develop the "EMT kit" to facilitate detection of EMT. I worked as a link between academia and industry to explore basic mechanisms of EMT in the lab of Manuel Thery and using this knowledge I developed the 'EMT kit" for pharmaceutical screen of cancer drugs, with the help from CYTOO. Hence in the final chapter I will summarize the progress of the "EMT kit" development using the knowledge gained from work in first two chapters regarding cell separation.

In each chapter, I have included a section of short questions and answers called 'short Q&A'. This section is added mainly to discuss technical points about the experiments, which were not discussed at length in the results section. I feel these short Q&A would help the reader to understand experimental set up more clearly. I have included the cumulative understanding of the work described in three chapters into the General Discussion section. The General Discussion also includes description of processes that were not studied in this thesis but which require consideration to paint the global picture of polarity and epithelial morphogenesis.

0.1 Introduction to cortical polarity of the cell

Epithelial polarity is defined by the demarcation of cell membrane into distinct domains, which are decorated by different molecular complexes. In an organism, the first event of epithelialization occurs very early during embryo development, just after three or four cleavages during compaction of embryo (Figure 0.3 A). At this stage 8-16 blastomeres adhere to one another to form circumferential junctions and begin physiological separation of internal environment from outside resulting into blastocoel cavity (Shook and Keller, 2003). During the later stages of embryogenesis and organ development distinct epithelial structures are formed such as simple squamous epithelium in lungs and blood vessels for gas diffusion, stratified epithelium in skin and the ciliated epithelium in respiratory tract. The polarized epithelial tissue decorated by polarity complexes at the cell membrane subdivides cell the cortex into apical, lateral, baso-lateral and basal domains (Figure 0.3 B). The protein and lipid composition of these domains differ and have specific functions.

Components of the cortical polarity

The exact molecular players of polarity complexes vary across species such as *C elegans*, *D melanogaster* and mammals although there are several common components, which are essential for the compartmentalization. Genetic analysis of polarity complexes revealed evolutionarily conserved proteins that are necessary for the cell polarization. The main polarity complexes are Par6/Par3/aPKC complex, Crib/Pals/Patj complex and Scrib/Dlg/Lgl complex which have common conserved members in all the three model organisms suggesting their crucial role. Par complex proteins are required for the asymmetric cell division and establishment of the apical domain (Assémat et al., 2008; St Johnston and Ahringer, 2010). The mutations in these genes lead to defects in partitioning during asymmetric divisions in *C. elegans* zygote (hence the name PAR). Par proteins are therefore essential for the partitioning of early determinations and development of the polarity. Crumbs (Crb) were discovered in *D. melanogaster* by mutations characterized by severe disruption of the cuticle (hence the name crumbs). In epithelial cells Crumbs is found extensively in apical membrane and at the borders between cells (St Johnston and Ahringer, 2010). The Scribble (Scrib) complex is restricted to lateral membranes and the main function of the Scrib in epithelial polarity consists exclusion of apical proteins from the baso-lateral membrane. Phoshoinositides (lipids) serve as lipid messengers and act as docking sites for signaling molecules. Their spatial localization is regulated by kinases and phoshatase and it is essential for fine-tuning the composition of membrane-cytosol interphase. Phosphatidylinositol-3,4,5-triphospahtes (ptdIns(3,4,5)P3) is located at basolateral membrane while PtdIns(4,5)P_2 (PIP_2) give apical membrane identity wherein

Figure 0.3

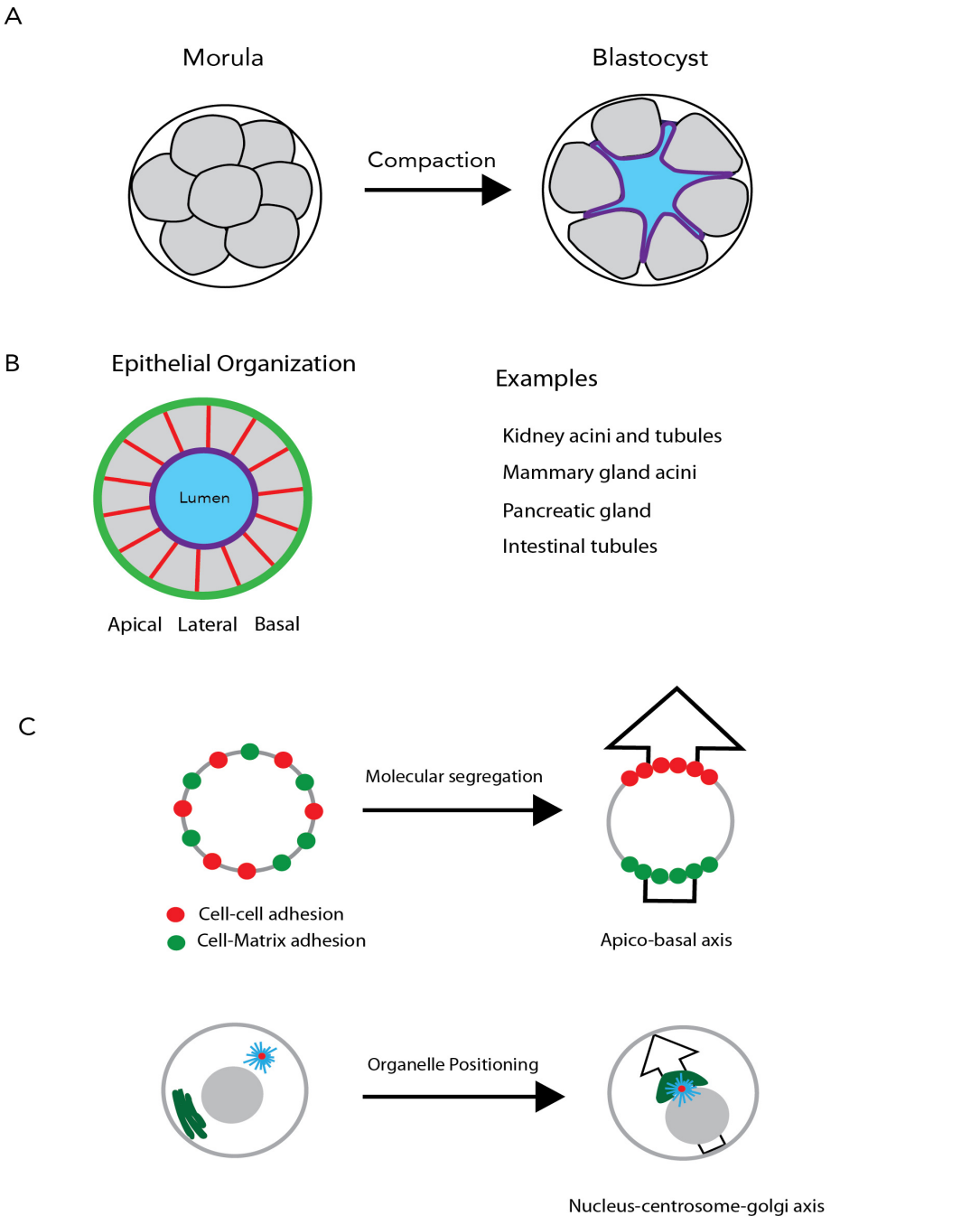

(A) Epithelialization by compaction of mammalian embryo from morula to blastocyst
(B) Typical membrane organization of lumen containing polarized tissues
(C) Molecular segreagation of cell adhesions establishes apico-basal axis and nucleus-centrosome axis

PtdIn-3 kinase (PIK3K) and PTEN; a lipid phosphotase have antagonizing action for conversion of PIP_3 to PIP_2. PIP2 acts as the central determinant of apical identity by recruiting series of molecules and activating Par complex at the apical side and subsequent lumen formation (Roignot et al., 2013). Another important member of epithelial polarity is RHO family GTPases. Over more than 20 member family including CDC42, RAC1, RHOA act as molecular switches that cycle between active (GTP-bound) and inactive (GDP-bound) conformations. Their localization within the cells is controlled by guanine nucleotide exchange factors (GEFs) and GTPase-activating proteins (GAPs). CDC42, Rac, Rho are involved in tight junction and adherene junction assembly. Rho GTPases control acto-myosin contractility modulate mechanical cues responsible for guiding polarization (Etienne-Manneville and Hall, 2002; Macara, 2004; Rodriguez-Boulan and Macara, 2014). The interplay between different polarity determinants also leads to mutual exclusions of molecules. The local molecular and mechanical feedbacks result into spatial segregation of CMA and CCA, which define the cortical polarity of a cell. In the following review we have summarized the key mechanisms that are responsible for modulating cortical polarity in an epithelium.

Available online at www.sciencedirect.com

SciVerse ScienceDirect

Current Opinion in Cell Biology

Spatial segregation between cell–cell and cell–matrix adhesions

Mithila Burute and Manuel Thery

Cell–cell adhesion (CCA) and cell–matrix adhesion (CMA) play determinant roles in the architecture and function of epithelial cells. CCA and CMA are supported by transmembrane molecular complexes that dynamically interact with the extracellular environment and the cell cytoskeleton. Although those complexes have distinct functions, they are involved in a continuous crosstalk. In epithelia, CCA and CMA segregate in distinct regions of the cell surface and thereby take part in cell polarity. Recent results have shown that the two adhesion systems exert negative feedback on each other and appear to regulate actin network dynamics and mechanical force production in different ways. In light of this, we argue that the interplay between these regulatory mechanisms plays an important role in the spatial separation of cell–cell and cell–matrix adhesions components in distinct regions of the cell surface.

Address
Laboratoire de Physiologie Cellulaire et Végétale, Institut de Recherche en Technologies et Sciences pour le Vivant, CNRS/UJF/INRA/CEA, 17 rue des martyrs, 38054, Grenoble, France

Corresponding author: Thery, Manuel (manuel.thery@cea.fr)

Current Opinion in Cell Biology 2012, **24**:628–636

This review comes from a themed issue on **Cell-to-cell contact and extracellular matrix**

Edited by **Carl-Phillip Heisenberg** and **Reinhard Fässler**

For a complete overview see the Issue and the Editorial

Available online 9th August 2012

http://dx.doi.org/10.1016/j.ceb.2012.07.003

Introduction

The microenvironment of a cell is made of extra-cellular matrix (ECM) and neighboring cells. Cells adhere to the ECM and their neighbors through spatially distinct regions of their surface, which contain molecular complexes interacting with extracellular ligands on one side and regulating and interacting with the cytoskeleton on the other side. The best characterized CMA complexes comprise transmembrane proteins integrins, directly binding to ECM proteins such as fibronectin, laminin and collagen and recruiting actin binding and regulatory proteins (such as talin, paxilin and focal adhesion kinase (FAK)) [1]. The most studied CCA complex comprise the transmembrane cadherins, which form homophilic bonds between neighbor cells and recruit actin binding and regulatory proteins of the catenin family [2]. This review focuses on integrin-based and cadherin-based cell adhesion, though other types of adhesion complexes also exist. These two types of adhesion complexes are remarkably similar. They have in common several structural components, they can bind actin filaments, they can utilize some of the same signaling pathways and act as mechanical sensors [3]. Despite this, they contribute differently to cell and tissue architecture. In addition to its well-known role of structural support, ECM regulates the intra-cellular level of contraction [4,5], transmits mechanical forces over long distances [6•], and acts as a basement and signaling platform for epithelia [7]. For example, CMA signaling regulates lamellipodial activity at the front of migrating cells [1] and the 3D organization of CMA regulates the confined migration processes of individual cells [8,9] and cell groups [10]. CMA signaling also regulates the orientation of epithelial cell polarity [11,12] as well as branching morphogenesis of several organs [13]. CCA regulates epithelia shape and remodeling [2] and propagate polarity signals [14]. CMA and CCA both act as cues for cell apico-basal polarity orientation [15] and the expression level of their components regulates the degree of polarization during epithelial morphogenesis [16].

These two adhesion systems appear not to act independently. Rather, their functions are connected by a permanent crosstalk [17]. CCA and CMA can upregulate and downregulate one another depending on the context [18,19•]. Spatial segregation of CMA and CCA seems to act as and/or result from a major morphogenetic force shaping cells and tissues. Although this segregation has been observed in many conditions, very few studies have been directly dedicated to find the underlying mechanism. Here we review recent examples in which CMA and CCA segregation has been observed *in vivo* and then describe the negative local feedbacks they exert on each other and finally propose a mechanism for their spatial segregation based on their mechanical interaction.

Spatial segregation in tissues

It has been appreciated for a long time that the expression of CCA and CMA components is increased during the epithelial morphogenesis and that they segregate in opposed locations [15]. Recently the list of organs displaying such a spatial segregation has been extended, which further confirmed the universal nature of this feature in multicellular organisms.

In mice, liver bile duct formation proceeds with the formation of new tubes along the portal vein. During lumen formation, cadherin localization on the portal side precedes the localization of laminin on the opposite basal pole [20,21•]. During pancreatic tubulogenesis, CMA and

CCA also appeared separated in the cells forming the early luminal structures [22] (Figure 1).

The direct effect of one adhesion system on the expression and location of the other has been reported during various morphogenetic events. During mouse lung and salivary gland morphogenesis, local engagement of cell–ECM adhesions reduce the expression of E-cadherin, which contributes to CCA disassembly and induces cleft formation [23,13]. During arteriolar morphogenesis in mice, the beta1 integrin deletion mutants exhibit upregulation of cadherins, extended cell–cell contacts and a lack of lumen [24], which suggests that assembly of CCA along short lateral contacts depends on the engagement of CMA along endothelial cell basal surface. Similarly, during bone formation, cell adhesion to collagen on basal surface seems to contribute to proper CCA formation on the cell's lateral surfaces [25]. During chick embryo somitogenesis, basal fibronectin assembly induces the restricted localization of cadherins at the apical surface [26•,27]. Conversely, tissue tension that requires cadherin adhesion on lateral surfaces of blastocoel cell roof cells mediates fibronectin assembly on upper surface during xenopus gastrulation [28,29] (Figure 1).

Cell–matrix adhesions locally weaken cell–cell adhesions

In the next two paragraphs we review recent works in which some results suggest that the two adhesion systems can negatively affect each other by various means and in many different and unrelated conditions. According to this view, the spatial segregation of the two adhesion systems may rely on their mutual exclusion by a process of local negative feedback (Figure 2A).

The local negative regulation of CCA by CMA has been directly shown in various contexts by several distinct approaches. Covering the apical poles of a monolayer of epithelial cells with ECM induced the formation of apical membrane protrusions leading to the disruption of CCA localized close to these apical poles and to the reassembly of CCA in ECM free regions at the opposite cell side [30]. Similarly, the formation of CMA in cancer cells prevents the proximal formation of E-cadherin

Figure 1

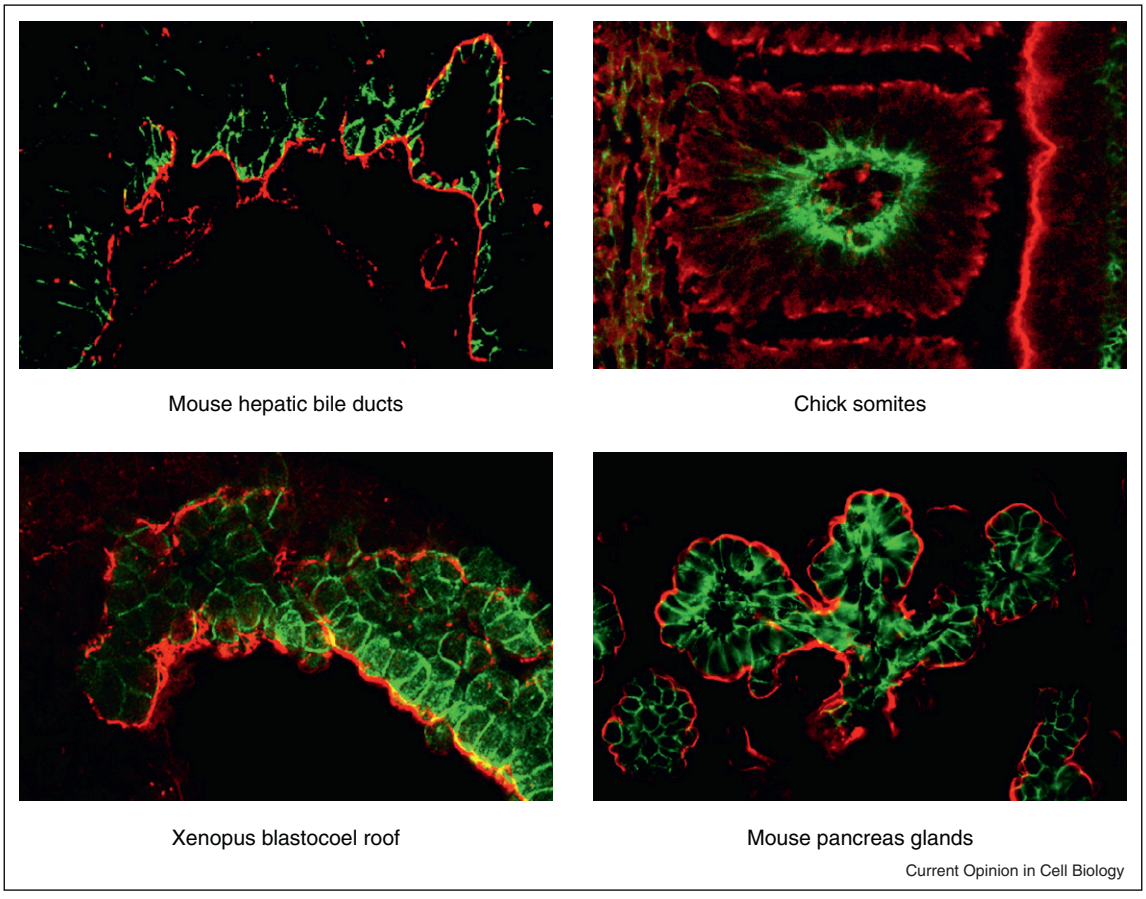

Several examples of the spatial segregation of CCJ (green) and CMA (red) in mouse hepatic bile duct (E-cadherin in green and laminin in red) [21•], in chick somites (N-cadherin in green and laminin in red) [26•], in *Xenopus* blastocoel roof (N-cadherin in green and fibronectin in red) [29] and in mouse pancreas (E-cadherin in green and laminin in red) [22].

Figure 2

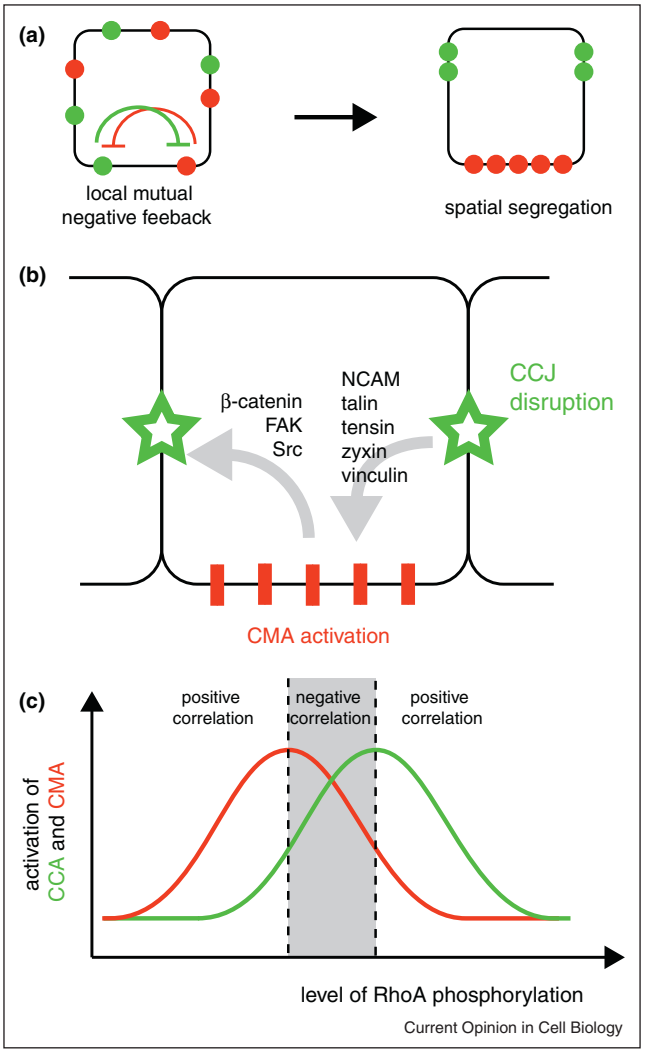

(A) The negative feedback CCA (green) and CMA (red) exert locally on each other can account for their spatial segregation. **(B)** Description of the players involved in CCA disruption upon CMA activation and vice versa. **(C)** Schematic illustration of the possibility for RhoA, or other RhoGTPases, to exert opposite effects on CCA and CMA despite similar activation curves. Positive correlation means that both CCA and CMA are activated, or inactivated, by an increase of RhoA. Negative correlation means that one gets activated while the other is inactivated.

complexes when cells are cultured on micropatterned substrate coated with ligands for both types of adhesions [31]. With an increase of cell spreading area on ECM, the rigidity modulus of a cadherin-mediated contact is reduced [19•].

CMA can activate Src, which in turn phosphorylates FAK. FAK relocalization to CCA results in the phosphorylation of β-catenin and the disruption of β-catenin association with the cadherin complex [32,33] (Figure 2B). The same Src pathway is involved in VEGF-induced vascular permeability [34]. In colon cancer cells, integrin associated Src activity is enhanced and perturbs E-cadherin localization [35]. *In vivo*, in squamous cell carcinoma, CMA activate FAK, which in turn activates E-cadherin internalization, CCA weakening and tumor cell dispersal [36].

RhoGTPase, RhoA and Rac1 have similar contributions CMA and CCA formation [3]. Rac1 is involved in initial formation and RhoA contributes to maturation, lengthening and strengthening of the adhesions [37,38•,39]. Excessive activation of RhoA or Rac1 induces junction disruption [3]. But how Rho GTPases are involved in the crosstalk between CCA and CMA is not clearly established. At first glance, they seem to have the same effect on both adhesions. For example, increase in the level of RhoA phosphorylation first activate and then disrupt the two types of cell adhesions, giving a 'bell shape' to CCA and CMA activation curves (Figure 2c). But if these similar curves are slightly shifted, a given variation of Rho concentration in the intermediate regime, between the two activation maxima, would have opposite effect on CCA and CMA and thereby mediate a negative correlation between the two types of adhesion (Figure 2C).

Abl kinases are also involved in both CCA and CMA formation and maintenance. Abl kinases support stabilization of CCA [40] and inhibition of β1-integrin mediated laminin assembly at the same time [11] and thus could also be key regulators of their crosstalk.

Noteworthy, the CMA-CCA crosstalk can be either dominated or dampened by CMA maturation in response to ECM rigidity [41,42,31,43•].

Cell–cell adhesions locally impair cell–ECM adhesions

Several examples directly showed that CCA locally impairs CMA formation and downstream signaling. In epithelial cells plated on micropatterned surfaces of cadherins and ECM, cadherin engagement prevents the formation of CMA at the same location, and reduces downstream signaling responsible for membrane protrusion formation in close-by CMA [44•]. The formation of CCA between two individual myocytes leads to the disassembly of the CMA that were present close to the contact region [43•]. When vascular smooth muscle cell density is increased, the formation of CCA is increased while the expressions of talin and vinculin required for CMA maturation and production of traction forces are reduced [41].

Downregulation of CMA by CCA is also indirectly revealed by the CMA formation in response to CCA disruption. Downregulation of CCA components, such as E-cadherin or a-catenin, correlates with increased cell migration on ECM [45,46]. The role of CCA weakening is particularly critical to epithelium to mesenchyme transition (EMT) during which CMA is activated. E-cadherin downregulation is required to potentiate the effect of TGF-β and promote metastatic growth [42]. Upon

E-cadherin loss of function, NCAM is overexpressed and translocated into lipid rafts where it activates FAK resulting into CMA assembly [47]. *NCAM-dependent activation of CMA formation is modulated by polysialic acid* [48]. Noteworthy, during EMT, E-cadherins are replaced by N-cadherins. During Xenopus gastrulation, tension on N-cadherins stimulate CMA displacement away from CCA [28,29]. In mouse astrocytes, N-cadherins maintain cell polarity by preventing the formation of CMA adjacent to cell–cell contact [49]. In some neuronal tumors, N-cadherin level is reduced resulting into enhanced CMA activity and increased cell migration [49].

In various physiological contexts, CCA disruption and CMA formation might be coupled through the regulated distribution of common structural components. Tensin relocalization from CCA to CMA in response cell attachment with fibronectin reduces the strength of CCA [50]. Zyxin, vinculin and talin are well characterized CMA components. However they are also localized to CCA where they regulate the strength of the CCA [51,52•,53]. This suggests that in the case of CCA disruption zyxin, vinculin and talin may be released from CCA and relocalize to CMA that would be subsequently reinforced (Figure 2B).

Interestingly, Plakoglobin, a CCA component, has been shown to stimulate ECM expression and therefore CMA formation [54]. When Plakoglobin is locally recruited on CCA subjected to external tension, it reorients the intermediate filament network and promotes the formation of membrane protrusions at the opposite cell pole [55•]. Although in this case, local CMA disruption is not involved, the possibility for cells to secrete and adhere to ECM seems to be limited to the diametrically opposed cell side.

The above examples show that in many conditions associated to epithelium remodeling (tubulogenesis, EMT, cancer, . . .) one adhesion system can dismantle or repulse the other. The signaling pathways involved in these regulations could, at lower activation levels, contribute to a local negative regulation and result into spatial segregation between CMA and CCA (Figure 2). Yet the mechanism supporting this segregation still has to be elucidated. In parallel to the cross signaling, several examples suggest that structural mechanisms participate in the spatial organization of cell adhesions. Notably, the two types of adhesions differently regulate the actin network. Hence, we argue that the coupling of these different actin-regulating processes could participate in CMA and CCA spatial segregation.

Actin network dynamics and force transmission to cell–matrix adhesion sites

CMA assembly, growth and maturation processes are associated with distinct mechanisms controlling actin dynamics [1]. Recent studies have shown that upon

Figure 3

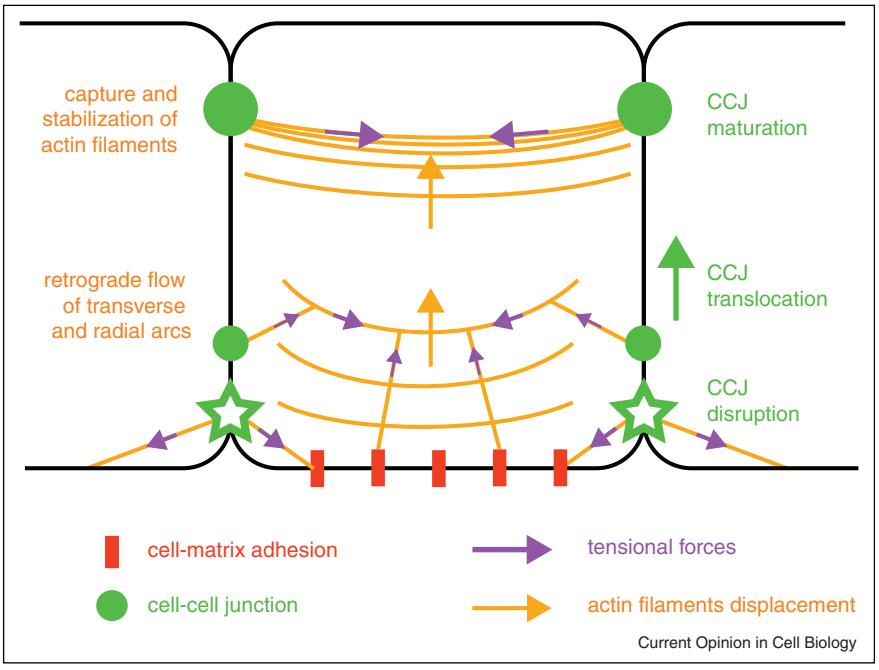

Speculative description of a mechanism supporting CCA displacement away from CMA. Force production on trans-cellular stress fibers lead to CCA disruption close to the basal surface. Retrograde flow of actin transverse arcs formed on CMA is coupled to CCA through radial fibers. Transmission of acto-myosin contractile forces through these fibers pulls CCA away from CMA. The accumulation of actin filaments at the apical pole and the production of acto-myosin forces along these cortical bundles induce CCA strengthening and maturation respectively.

engagement with the extra-cellular matrix, integrins induce actin filament growth. Lateral interactions and translocation of integrins promote their clustering and early adhesion formation [56]. Nascent CMA are then associated with Rac activation and the formation of membrane protrusions (lamellipodia, filopodia) based on actin polymerization and formation of a dendritic network [57,58]. At a later stage, CMA maturation and the increase of acto-myosin contraction are inter-dependent [56,57,59–61].

In migrating cultured cells, the subcellular localization of mature CMA determines the spatial transition between the dendritic network of actin filaments next to plasma membrane and the network of actin bundles in the cell interior [62]. The compression of this dendritic network nucleated at the plasma membrane leads to filament alignment and formation of transverse arcs [63•,64]. Acto-myosin contraction drives the retrograde movement of these arcs toward cell interior. As these arcs move inward, they bundle with CMA-associated actin filaments and induce the formation of radial fibers through which they transmit contractile forces to the extra-cellular matrix [65,66,63•] (Figure 3).

Actin network dynamics and force transmission at cell–cell contacts

The formation of a cell–cell contact triggers actin cytoskeleton assembly [67]. Extension and retraction of lamellipodia over adjacent cells leads to the formation of interconnecting actin filaments whose remodeling by fascin and myosin eventually lead to the assembly of CCA [68]. Arp2/3 [69], N-WASP [70] and α-actinin [71] nucleate, recruit and stabilize actin filaments along CCA. Rac-induced actin-network polymerization promotes cell–cell contact area growth and Rho activation promotes further CCA maturation [37,38•]. Furthermore, CCA are reinforced upon application of external or internal stress [72,73•,38•]. The application of tension can lead to the recruitment of vinculin [52•] and additional actin filaments through VASP and EPLIN [74•,75,76], which strengthen cell–cell adhesion [77]. However, excess forces can result in junction disassembly [78,79]. Abl kinase [40] and Cdc42 are involved in the fine regulation of that threshold [80].

Thus, mature CCA anchor acto-myosin bundles [81] (Figure 3). Myosin IIb recruits actin filament along the junctions [82] and Myosin IXA supports the formation of actin bundles orthogonal to the junction [79]. Both myosin types ensure cell–cell contact integrity by resisting destructive orthogonal forces on the CCA.

Coupling of actin dynamics associated with CMA and CCA

The nucleation, stabilization, capture and disassembly of actin filaments have to be integrated at the cell level to ensure the stationary state of the entire network. The cytoskeletal forces applied on CCA and CMA also have to be balanced to ensure cell mechanical stability. These forces may be responsible for adhesion maturation as well as for their rupture or displacement in the membrane. The spatial distribution of forces in the actin network and the spatial arrangement of filament nucleation, bundle assembly and bundle stabilization processes may be responsible for CMA and CCA displacement away from each other. As cells come into contact and assemble CCA, traction force on CMA close to the contact region get turned into tugging force at cell–cell contacts that result into local CMA disassembly [43•]. The magnitude of the tugging force at cell–cell contacts is proportional to that of cell traction forces exerted through CMA [83•]. How the magnitude of these forces relate to CCA positioning with respect to CMA has been studied in a minimal system of two cells in which CMA is confined on ECM micropatterns of controlled geometry [84•]. In this system, CCA are subjected to high tugging forces when they are close to CMA sites and lower forces when positioned away from them [84•]. As a consequence, the contact plane is moved away from CMA sites and cells adopt a stationary position in which the cell–cell contact is as far as possible from CMA. Thereby the steady state of multicellular organizations corresponds to the minimization of the overall magnitude of tensional forces [84•].

How force production on CCA lead to such a controlled junction displacement and cell positioning remain to be elucidated. There are at least two ways to apply forces on CCA [85,86]. Contractile acto-myosin bundles can mediate forces orthogonal [71,87–90] or parallel to the junction [91]. Mechanical forces applied orthogonally to the CCA can be transmitted to the CMA sites through radial actin bundles (Figure 3). Such a configuration may occur in a flat epithelium such as the vascular endothelium [87,89]. This configuration could also occur at CCA close to basal surfaces of simple epithelia [71,88,51]. Since integrins may support higher forces than cadherin on comparable substrate stiffness [73•], mechanical force could lead to CCA disruption near CMA sites [92,51] (Figure 3). In addition, at the apical pole of epithelial cells, the retrograde movement of transverse arcs linked to radial bundles orthogonal to the CCA produces tensional forces on CCA [90,93•]. We speculate that the retrograde movement of transverse arcs and radial bundles from CMA (described above) exert forces on CCA responsible for their rupture and displacement away from CMA (Figure 3). Indeed, actin network dynamics has been shown to be responsible for a basal-to-apical flow of CCA in moving epidermal cells [94]; and apical enrichment of actin filaments is necessary for the maintenance of the apical localization of CCA in intestinal cells [70]. We suggest that the actin flow initiated by bundle formation at CMA sites and their retrograde movement

could pull CCA away from CMA. The accumulation of these contractile actin bundles at CCA distant from CMA could contribute to the strengthening and stabilization of CCA (Figure 3).

Conclusion

The complete mechanism supporting the spatial segregation of CCA and CMA remains elusive. Future insights should be expected from the analysis of actin network dynamics and its relationship with mechanical force production. In addition, the coupling between CCA components renewal at the membrane and force production [70,95] could play a key role in epithelial morphogenesis [96–99]. Unravelling the mechanisms supporting spatial segregation of cell adhesions during epithelial morphogenesis, which is tightly coupled to apico-basal polarity, could greatly improve our understanding of organogenesis and oncogenesis.

Acknowledgements

We thank Nicolas Borghi for many interesting discussions and constructive critical reading of our manuscript. We thank Peggy Raynaud, Gokul Kesavan, Bette Dzamba and Pedro Rifes for discussing and sharing images of their work. We apologize for authors whose results have been discussed in this opinion but whose main conclusions may not have been reported since the problematic we addressed was quite different from the central focus of their study.

References and recommended reading

Papers of particular interest, published within the period of review, have been highlighted as:

- • of special interest
- •• of outstanding interest

1. Vicente-Manzanares M, Choi CK, Horwitz AR: **Integrins in cell migration – the actin connection**. *J Cell Sci* 2009, **122**:1473.

2. Niessen CM, Leckband D, Yap AS: **Tissue organization by cadherin adhesion molecules: dynamic molecular and cellular mechanisms of morphogenetic regulation**. *Physiol Rev* 2011, **91**:691-731.

3. Papusheva E, Heisenberg C-P: **Spatial organization of adhesion: force-dependent regulation and function in tissue morphogenesis**. *EMBO J* 2010, **29**:2753-2768.

4. Solon J, Levental I, Sengupta K, Georges PC, Janmey PA: **Fibroblast adaptation and stiffness matching to soft elastic substrates**. *Biophys J* 2007, **93**:4453-4461.

5. Polte TR, Eichler GS, Wang N, Ingber DE: **Extracellular matrix controls myosin light chain phosphorylation and cell contractility through modulation of cell shape and cytoskeletal prestress**. *Am J Physiol Cell Physiol* 2004, **286**:C518-C528.

6. • Guo C-L, Ouyang M, Yu J-Y, Maslov J, Price A, Shen C-Y: **Long-range mechanical force enables self-assembly of epithelial tubular patterns**. *Proc Natl Acad Sci USA* 2012, **109**:5576-5582.
This study shows that ECM can propagate cell traction forces over several hundreds of microns and thereby direct the organization of multiple cells into large structures such as tubules.

7. Rozario T, DeSimone DW: **The extracellular matrix in development and morphogenesis: a dynamic view**. *Dev Biol* 2010, **341**:126-140.

8. Balzer EM, Tong Z, Paul CD, Hung W-C, Stroka KM, Boggs AE, Martin SS, Konstantopoulos K: **Physical confinement alters tumor cell adhesion and migration phenotypes**. *FASEB J* 2012 http://dx.doi.org/10.1096/fj.12-211441.

9. Pathak A, Kumar S: **Independent regulation of tumor cell migration by matrix stiffness and confinement**. *Proc Natl Acad Sci USA* 2012, **109**:10334-10339.

10. Vasilyev A, Liu Y, Mudumana S, Mangos S, Lam P-Y, Majumdar A, Zhao J, Poon K-L, Kondrychyn I, Korzh V *et al.*: **Collective cell migration drives morphogenesis of the kidney nephron**. *PLoS Biol* 2009, **7**:e9.

11. Li R, Pendergast AM: **Arg kinase regulates epithelial cell polarity by targeting β1-integrin and small GTPase pathways**. *Curr Biol* 2011, **21**:1534-1542.

12. Yu W, Shewan AM, Brakeman P, Eastburn DJ, Datta A, Bryant DM, Fan Q-W, Weiss WA, Zegers MMP, Mostov KE: **Involvement of RhoA, ROCK I and myosin II in inverted orientation of epithelial polarity**. *EMBO Rep* 2008, **9**:923-929.

13. Onodera T, Sakai T, Hsu JC-feng, Matsumoto K, Chiorini JA, Yamada KM: **Btbd7 regulates epithelial cell dynamics and branching morphogenesis**. *Science* 2010, **329**:562-565.

14. Zallen JA: **Planar polarity and tissue morphogenesis**. *Cell* 2007, **129**:1051-1063.

15. Yeaman C, Grindstaff K: **New perspectives on mechanisms involved in generating epithelial cell polarity**. *Physiol Rev* 1999, **79**:73-98.

16. Ewald AJ, Jorgens DM, Huebner RJ, Tauscher AN, Palsdottir H, Cheung KJ, Lee JK, Zena Werb, Perez MJ, Manfred Auer: **Mammary collective cell migration involves transient loss of epithelial features and individual cell migration within the epithelium**. *J Cell Sci* 2012, **125(Pt 11)**:2638-2654.

17. Weber GF, Bjerke MA, DeSimone DW: **Integrins and cadherins join forces to form adhesive networks**. *J Cell Sci* 2011, **124**:1183-1193.

18. Martinez-Rico C, Pincet F, Thiery J-paul, Dufour S: **Integrins stimulate E-cadherin-mediated intercellular adhesion by regulating Src-kinase activation and actomyosin contractility**. *J Cell Sci* 2010, **123**:712-722.

19. • Al-Kilani A, de Freitas O, Dufour S, Gallet F: **Negative feedback from integrins to cadherins: a micromechanical study**. *Biophys J* 2011, **101**:336-344.
This study demonstrates that the increase formation of CMA reduces the strength of CCA using cell spreading on micropatterned surfaces and cell attachment to cadherin coated beads.

20. Raynaud P, Carpentier R, Antoniou A, Lemaigre FP: **Biliary differentiation and bile duct morphogenesis in development and disease**. *Int J Biochem Cell Biol* 2011, **43**:245-256.

21. • Antoniou A, Raynaud P, Cordi S, Zong Y, Tronche F, Stanger BZ, Jacquemin P, Pierreux CE, Clotman F, Lemaigre FP: **Intrahepatic bile ducts develop according to a new mode of tubulogenesis regulated by the transcription factor SOX9**. *Gastroenterology* 2009, **136**:2325-2333.
This study describes the complete formation of new tubules during cell differentiation *in vivo* from assembly of new cell adhesions to cell polarization.

22. Kesavan G, Sand FW, Greiner TU, Johansson JK, Kobberup S, Wu X, Brakebusch C, Semb H: **Cdc42-mediated tubulogenesis controls cell specification**. *Cell* 2009, **139**:791-801.

23. Sakai T, Larsen M, Yamada KM: **Fibronectin requirement in branching morphogenesis**. *Nature* 2003, **423**:876-881.

24. Zovein AC, Luque A, Turlo KA, Hofmann JJ, Yee KM, Becker MS, Fassler R, Mellman I, Lane TF, Iruela-Arispe ML: **Beta1 integrin establishes endothelial cell polarity and arteriolar lumen formation via a Par3-dependent mechanism**. *Dev Cell* 2010, **18**:39-51.

25. Izu Y, Sun M, Zwolanek D, Veit G, Williams V, Cha B, Jepsen KJ, Koch M, Birk DE: **Type XII collagen regulates osteoblast polarity and communication during bone formation**. *J Cell Biol* 2011, **193**:1115-1130.

26. • Martins GG, Rifes P, Amândio R, Rodrigues G, Palmeirim I, Thorsteinsdóttir S: **Dynamic 3D cell rearrangements guided by a fibronectin matrix underlie somitogenesis**. *PLoS ONE* 2009, **4**:e7429.

This study and [27] show the complex cell choregraphy during somitogenesis and the fundamental role of CMA in the polarization of CCA and accretion of cells into rosette like structures delineating the future somites.

27. Rifes P, Thorsteinsdóttir S: **Extracellular matrix assembly and 3D organization during paraxial mesoderm development in the chick embryo**. *Dev Biol* 2012, **368**:370-381.

28. Davidson LA, Hoffstrom BG, Keller R, DeSimone DW: **Mesendoderm extension and mantle closure in Xenopus laevis gastrulation: combined roles for integrin alpha(5)beta(1), fibronectin, and tissue geometry**. *Dev Biol* 2002, **242**:109-129.

29. Dzamba BJ, Jakab KR, Marsden M, Schwartz MA, DeSimone DW: **Cadherin adhesion, tissue tension, and noncanonical Wnt signaling regulate fibronectin matrix organization**. *Dev Cell* 2009, **16**:421-432.

30. Ojakian GK, Ratcliffe DR, Schwimmer R: **Integrin regulation of cell-cell adhesion during epithelial tubule formation**. *J Cell Sci* 2000, **114**:941-952.

31. Tsai J, Kam L: **Rigidity-dependent cross talk between integrin and cadherin signaling**. *Biophys J* 2009, **96**:L39-L41.

32. Koenig A, Mueller C, Hasel C, Adler G, Menke A: **Collagen type I induces disruption of E-cadherin-mediated cell-cell contacts and promotes proliferation of pancreatic carcinoma cells**. *Cancer Res* 2006, **66**:4662-4671.

33. Giehl K, Menke A: **Microenvironmental regulation of E-cadherin-mediated adherens junctions**. *Front Biosci* 2008, **13**:3975-3985.

34. Chen XL, Nam J-ock, Jean C, Lawson C, Walsh CT, Goka E, Lim S-taek, Tomar A, Tancioni I, Uryu S *et al.*: **VEGF-induced vascular permeability is mediated by FAK**. *Dev Cell* 2012, **22**:146-157.

35. Avizienyte E, Wyke AW, Jones RJ, McLean GW, Westhoff MA, Brunton VG, Frame MC: **Src-induced de-regulation of E-cadherin in colon cancer cells requires integrin signalling**. *Nat Cell Biol* 2002, **4**:632-638.

36. Canel M, Serrels A, Miller D, Timpson P, Serrels B, Frame MC, Brunton VG: **Quantitative in vivo imaging of the effects of inhibiting integrin signaling via Src and FAK on cancer cell movement: effects on E-cadherin dynamics**. *Cancer Res* 2010, **70**:9413-9422.

37. Yamada S, Nelson WJ: **Localized zones of Rho and Rac activities drive initiation and expansion of epithelial cell-cell adhesion**. *J Cell Biol* 2007, **178**:517-527.

38. • Liu Z, Tan JL, Cohen DM, Yang MT, Sniadecki NJ, Alom S, Nelson CM, Chen CS: **Mechanical tugging force regulates the size of cell – cell junctions**. *Proc Natl Acad Sci USA* 2010, **107**:9944-9949.
This study combines tensional force measurement and cell shape control with micropattern to show that intra-cellular level of tension regulates the expansion of the cell–cell contact area.

39. Guilluy C, Garcia-Mata R, Burridge K: **Rho protein crosstalk: another social network?** *Trends Cell Biol* 2011, **21**:718-726.

40. Zandy NL, Playford M, Pendergast AM: **Abl tyrosine kinases regulate cell-cell adhesion through Rho GTPases**. *Proc Natl Acad Sci USA* 2007, **104**:17686-17691.

41. Sazonova OV, Lee KL, Isenberg BC, Rich CB, Nugent MA, Wong JY: **Cell-cell interactions mediate the response of vascular smooth muscle cells to substrate stiffness**. *Biophys J* 2011, **101**:622-630.

42. Wendt MK, Taylor MA, Schiemann BJ, Schiemann WP: **Down-regulation of epithelial cadherin is required to initiate metastatic outgrowth of breast cancer**. *Mol Biol Cell* 2011, **22**:2423-2435.

43. • McCain ML, Lee H, Aratyn-Schaus Y, Kléber AG, Parker KK: **Cooperative coupling of cell-matrix and cell-cell adhesions in cardiac muscle**. *Proc Natl Acad Sci USA* 2012, **109**:9881-9886.
This study directly demonstrates that the formation of CCA stimulates the local disassembly of CMA.

44. • Borghi N, Lowndes M, Maruthamuthu V, Gardel ML, Nelson WJ: **Regulation of cell motile behavior by crosstalk between cadherin- and integrin-mediated adhesions**. *Proc Natl Acad Sci USA* 2010, **107**:13324-13329.
This study use co-patterning of cadherin and integrin to investigate their crosstalk in controled and comparable conditions. It directly demonstrates the negative effect of CCA on CMA close by.

45. Schlippe MV, Marshall JF, Perry P, Stone M, Zhu AJ, Hart IR: **Functional interaction between E-cadherin and αv-containing integrins in carcinoma cells**. *J Cell Sci* 2000, **437**:425-437.

46. Livshits G, Kobielak A, Fuchs E: **Governing epidermal homeostasis by coupling cell-cell adhesion to integrin and growth factor signaling, proliferation, and apoptosis**. *Proc Natl Acad Sci USA* 2012, **109**:4886-4891.

47. Lehembre F, Yilmaz M, Wicki A, Schomber T, Strittmatter K, Ziegler D, Kren A, Went P, Derksen PWB, Berns A *et al.*: **NCAM-induced focal adhesion assembly: a functional switch upon loss of E-cadherin**. *EMBO J* 2008, **27**:2603-2615.

48. Eggers K, Werneburg S, Schertzinger A, Abeln M, Schiff M, Scharenberg MA, Burkhardt H, Mu M: **Polysialic acid controls NCAM signals at cell–cell contacts to regulate focal adhesion independent from FGF receptor activity**. *J Cell Sci* 2011, **124**:3279-3291.

49. Camand E, Peglion F, Osmani N, Sanson M, Manneville SE: **N-cadherin expression level modulates integrin-mediated polarity and strongly impacts on the speed and directionality of glial cell migration**. *J Cell Sci* 2012, **125(Pt 4)**:844-857.

50. Lefort CT, Wojciechowski K, Hocking DC: **N-cadherin cell-cell adhesion complexes are regulated by fibronectin matrix assembly**. *J Biol Chem* 2011, **286**:3149-3160.

51. Sperry RB, Bishop NH, Bramwell JJ, Brodeur MN, Carter MJ, Fowler BT, Lewis ZB, Maxfield SD, Staley DM, Vellinga RM *et al.*: **Zyxin controls migration in epithelial-mesenchymal transition by mediating actin-membrane linkages at cell-cell junctions**. *J Cell Physiol* 2010, **222**:612-624.

52. • le Duc Q, Shi Q, Blonk I, Sonnenberg A, Wang N, Leckband D, de Rooij J: **Vinculin potentiates E-cadherin mechanosensing and is recruited to actin-anchored sites within adherens junctions in a myosin II-dependent manner**. *J Cell Biol* 2010, **189**:1107-1115.
This study that the vinculin, more classical known to be involved in CMA, support the mechanosensation in CCA.

53. Zhang F, Saha S, Kashina A: **Arginylation-dependent regulation of a proteolytic product of talin is essential for cell-cell adhesion**. *J Cell Biol* 2012, **197**:819-836.

54. Todorović V, Desai BV, Patterson MJS, Amargo EV, Dubash AD, Yin T, Jones JCR, Green KJ: **Plakoglobin regulates cell motility through Rho- and fibronectin-dependent Src signaling**. *J Cell Sci* 2010, **123**:3576-3586.

55. • Weber GF, Bjerke MA, DeSimone DW: **A mechanoresponsive cadherin-keratin complex directs polarized protrusive behavior and collective cell migration**. *Dev Cell* 2012, **22**:104-115.
This study highlights the role of intermediate filament in the transmission of the local signal induced by tension on CCA to the opposite cell side where it stimulates CMA formation and formation of membrane protrusion.

56. Yu C-han, Law JBK, Suryana M, Low HY, Sheetz MP: **Early integrin binding to Arg-Gly-Asp peptide activates actin polymerization and contractile movement that stimulates outward translocation**. *Proc Natl Acad Sci USA* 2011, **108**:20585-20590.

57. Lutz R, Pataky K, Gadhari N, Marelli M, Brugger J, Chiquet M: **Nano-stenciled RGD-gold patterns that inhibit focal contact maturation induce lamellipodia formation in fibroblasts**. *PLoS ONE* 2011, **6**:e25459.

58. Wu C, Asokan SB, Berginski ME, Haynes EM, Sharpless NE, Griffith JD, Gomez SM, Bear JE: **Arp2/3 is critical for lamellipodia and response to extracellular matrix cues but is dispensable for chemotaxis**. *Cell* 2012, **148**:973-987.

59. Kuo J-C, Han X, Hsiao C-T, Yates JR, Waterman CM: **Analysis of the myosin-II-responsive focal adhesion proteome reveals a role for β-Pix in negative regulation of focal adhesion maturation**. *Nat Cell Biol* 2011, **13**:383-393.

60. Guilluy C, Swaminathan V, Garcia-Mata R, Timothy O'Brien E, Superfine R, Burridge K: **The Rho GEFs LARG and GEF-H1 regulate the mechanical response to force on integrins**. *Nat Cell Biol* 2011, **13**:724-729.

61. Parsons JT, Horwitz AR, Schwartz MA: **Cell adhesion: integrating cytoskeletal dynamics and cellular tension**. *Nat Rev Mol Cell Biol* 2010, **11**:633-643.

62. Shemesh T, Verkhovsky AB, Svitkina TM, Bershadsky AD, Kozlov MM: **Role of focal adhesions and mechanical stresses in the formation and progression of the lamellipodium-lamellum interface**. *Biophys J* 2009, **97**:1254-1264.

63. • Burnette DT, Manley S, Sengupta P, Sougrat R, Davidson MW, Kachar B, Lippincott-schwartz J: **A role for actin arcs in the leading-edge advance of migrating cells**. *Nat Cell Biol* 2011, **13**:371-381.
This study uses actin network photoconversion to highlight the transformation of actin meshwork in membrane protrusion into transverse arcs contributing to the production of traction forces on CMA.

64. Hotulainen P, Lappalainen P: **Stress fibers are generated by two distinct actin assembly mechanisms in motile cells**. *J Cell Biol* 2006, **173**:383-394.

65. Aratyn-Schaus Y, Oakes PW, Gardel ML: **Dynamic and structural signatures of lamellar actomyosin force generation**. *Mol Biol Cell* 2011, **22**:1330-1339.

66. Oakes PW, Beckham Y, Stricker J, Gardel ML: **Tension is required but not sufficient for focal adhesion maturation without a stress fiber template**. *J Cell Biol* 2012, **196**:363-374.

67. Vasioukhin V, Bauer C, Yin M, Fuchs E: **Directed actin polymerization is the driving force for epithelial cell–cell adhesion**. *Cell* 2000, **100**:209-219.

68. Hoelzle MK, Svitkina T: **The cytoskeletal mechanisms of cell-cell junction formation in endothelial cells**. *Mol Biol Cell* 2012, **23**:310-323.

69. Kovacs EM, Verma S, Ali RG, Ratheesh A, Hamilton NA, Akhmanova A, Yap AS: **N-WASP regulates the epithelial junctional actin cytoskeleton through a non-canonical post-nucleation pathway**. *Nat Cell Biol* 2011, **13**:934-943.

70. Bernadskaya YY, Patel FB, Hsu H-ting, Soto MC: **Arp2/3 promotes junction formation and maintenance in the Caenorhabditis elegans intestine by regulating membrane association of apical proteins**. *Mol Biol Cell* 2011, **22**:2886-2899.

71. Tang VW, Brieher WM: **α-Actinin-4/FSGS1 is required for Arp2/3-dependent actin assembly at the adherens junction**. *J Cell Biol* 2012, **196**:115-130.

72. Kris A, Kamm RD, Sieminski AL: **VASP involvement in force-mediated adherens junction strengthening**. *Biochem Biophys Res Commun* 2009, **375**:134-138.

73. • Ladoux B, Anon E, Lambert M, Rabodzey A, Hersen P, Buguin A, Silberzan P, Mège R-M: **Strength dependence of cadherin-mediated adhesions**. *Biophys J* 2010, **98**:534-542.
This study uses micropatterned cadherins on substrates on various stiffness to highlight the mechanosensation properties of CMA.

74. • Taguchi K, Ishiuchi T, Takeichi M: **Mechanosensitive EPLIN-dependent remodeling of adherens junctions regulates epithelial reshaping**. *J Cell Biol* 2011, **194**:643-656.
This study reveals how EPLIN regulates the switch between the two types of actin filament network architecture either parallel or orthogonal to cell–cell contact plane.

75. Chervin-Pétinot A, Courçon M, Almagro S, Nicolas A, Grichine A, Grunwald D, Prandini M-H, Huber P, Gulino-Debrac D: **Epithelial protein lost in neoplasm (EPLIN) interacts with α-catenin and actin filaments in endothelial cells and stabilizes vascular capillary network in vitro**. *J Biol Chem* 2012, **287**:7556-7572.

76. Abe K, Takeichi M: **EPLIN mediates linkage of the cadherin catenin complex to F-actin and stabilizes the circumferential actin belt**. *Proc Natl Acad Sci USA* 2008, **105**:13-19.

77. Sumida GM, Tomita TM, Shih W, Yamada S: **Myosin II activity dependent and independent vinculin recruitment to the sites of E-cadherin-mediated cell-cell adhesion**. *BMC Cell Biol* 2011, **12**:48.

78. de Rooij J, Kerstens A, Danuser G, Schwartz MA, Waterman-Storer CM: **Integrin-dependent actomyosin contraction regulates epithelial cell scattering**. *J Cell Biol* 2005, **171**:153-164.

79. Omelchenko T, Hall A: **Myosin-IXA regulates collective epithelial cell migration by targeting RhoGAP activity to cell-cell junctions**. *Curr Biol* 2012, **22**:278-288.

80. Warner SJ, Longmore GD: **Cdc42 antagonizes Rho1 activity at adherens junctions to limit epithelial cell apical tension**. *J Cell Biol* 2009, **187**:119-133.

81. Abreu-Blanco MT, Verboon JM, Parkhurst SM: **Cell wound repair in Drosophila occurs through three distinct phases of membrane and cytoskeletal remodeling**. *J Cell Biol* 2011, **193**:455-464.

82. Smutny M, Cox HL, Leerberg JM, Kovacs EM, Conti MA, Ferguson C, Hamilton NA, Parton RG, Adelstein RS, Yap AS: **Myosin II isoforms identify distinct functional modules that support integrity of the epithelial zonula adherens**. *Nat Cell Biol* 2010, **12**:696-702.

83. • Maruthamuthu V, Sabass B, Schwarz US, Gardel ML: **Cell-ECM traction force modulates endogenous tension at cell-cell contacts**. *Proc Natl Acad Sci USA* 2011, **108**:4708-4713.
This study reveals the mechanical homeostasis in connective cells by showing that the total traction forces on CMA were coupled and almost identical to the total tensional forces on CCA.

84. • Tseng Q, Duchemin-Pelletier E, Deshiere A, Balland M, Guillou H, Filhol O, Thery M: **Spatial organization of the extracellular matrix regulates cell-cell junction positioning**. *Proc Natl Acad Sci USA* 2012, **109**:1506-1511.
This study demonstrates that CMA regulates the positioning of CCA by modulating the tension they are submitted to. It also shows that multicellular arrangements can reach a stable configuration only if CCA can be positioned away from CMA.

85. Yonemura S, Itoh M, Nagafuchi A, Tsukita S: **Cell-to-cell adherens junction formation and actin filament organization: similarities and differences between non-polarized fibroblasts and polarized epithelial cells**. *J Cell Sci* 1995, **108(Pt 1)**:127-142.

86. Gomez GA, McLachlan RW, Yap AS: **Productive tension: force-sensing and homeostasis of cell-cell junctions**. *Trends Cell Biol* 2011, **21**:499-505.

87. Huveneers S, Oldenburg J, Spanjaard E, van der Krogt G, Grigoriev I, Akhmanova A, Rehmann H, de Rooij J: **Vinculin associates with endothelial VE-cadherin junctions to control force-dependent remodeling**. *J Cell Biol* 2012, **196**:641-652.

88. He L, Wang X, Tang HL, Montell DJ: **Tissue elongation requires oscillating contractions of a basal actomyosin network**. *Nat Cell Biol* 2010, **12**:1133-1142.

89. Millán J, Cain RJ, Reglero-Real N, Bigarella C, Ramiro BM-, Fernández-Martín L, Correas I, Ridley AJ: **Adherens junctions connect stress fibers between adjacent endothelial cells**. *BMC Biol* 2010, **8**:11.

90. Martin AC, Gelbart M, Fernandez-Gonzalez R, Kaschube M, Wieschaus EF: **Integration of contractile forces during tissue invagination**. *J Cell Biol* 2010, **188**:735-749.

91. Rauzi M, Verant P, Lecuit T, Lenne P-F: **Nature and anisotropy of cortical forces orienting Drosophila tissue morphogenesis**. *Nat Cell Biol* 2008, **10**:1401-1410.

92. Krishnan R, Klumpers DD, Park CY, Rajendran K, Trepat X, van Bezu J, van Hinsbergh VWM, Carman CV, Brain JD, Fredberg JJ *et al.*: **Substrate stiffening promotes endothelial monolayer disruption through enhanced physical forces**. *Am J Physiol Cell Physiol* 2011, **300**:C146-C154.

93. Roh-Johnson M, Shemer G, Higgins CD, McClellan JH, Werts AD,
• Tulu US, Gao L, Betzig E, Kiehart DP, Goldstein B: **Triggering a cell shape change by exploiting preexisting actomyosin contractions**. *Science* 2012, **335**:1232-1235.
This study shows that myosin-induced centripetal flow of actin filament requires a physical link to transmit mechanical forces to cell periphery and induce apical constriction.

94. Kametani Y, Takeichi M: **Basal-to-apical cadherin flow at cell junctions**. *Nat Cell Biol* 2007, **9**:92-98.

95. Kiyoshima D, Kawakami K, Hayakawa K, Tatsumi H, Sokabe M: **Force- and Ca^{2+}-dependent internalization of integrins in cultured endothelial cells**. *J Cell Sci* 2011, **124**:3859-3870.

96. Levayer R, Pelissier-Monier A, Lecuit T: **Spatial regulation of Dia and Myosin-II by RhoGEF2 controls initiation of E-cadherin endocytosis during epithelial morphogenesis**. *Nat Cell Biol* 2011, **13**:529-540.

97. Harris KP, Tepass U: **Cdc42 and Par proteins stabilize dynamic adherens junctions in the Drosophila neuroectoderm through regulation of apical endocytosis**. *J Cell Biol* 2008, **183**:1129-1143.

98. de Beco S, Gueudry C, Amblard F, Coscoy S: **Endocytosis is required for E-cadherin redistribution at mature adherens junctions**. *Proc Natl Acad Sci USA* 2009, **106**:7010-7015.

99. de Beco S, Amblard F, Coscoy S: **New insights into the regulation of e-cadherin distribution by endocytosis**. *Int Rev Cell Mol Biol* 2012, **295**:63-108.

0.3 Introduction to internal polarity of the cell

Striking feature of the epithelial organization is that the cells contained in an epithelial structure such as mammary gland acini, kidney tubule, intestine or pancreatic gland exhibit a concerted polarization (Figure 0.3 B). These cells are capable of individually responding to external cues and thus polarize in a fashion that collectively constitutes physiologically functioning units such as secretory lumens, tubules or absorptive ducts. The asymmetric organization of internal organelles in a cell is responsible for attributing its intrinsic polarity, which I will term as 'internal polarity' hereafter. This property of establishing intrinsic self-organization can be primarily revealed by relative location of the nucleus and centrosome. Centrosome of animal cells consists of pair of centriols surrounded by pericentriolar material (PCM). Microtubules are nucleated from the γ-tubulin ring complex (γ-TuRC), which is part of the PCM, and these microtubules eventually get anchored at the mother centriole (Figure 0.3 A). Centrosome location in the cell is important because Golgi apparatus is organized and actively maintained adjacent to centrosome and its position is dependent on both microtubules and dyneins (Rios and Bornens, 2002). In motile cells trans-golgi network (TGN) from which vesicles that are destined for plasma membrane are orientated towards the cell cortex, whereas the cis-Golgi is orientated inward (Figure 0.3 B). Extensive work performed using MDCK cell line model identified TGN as a major sorting station. TGN and recycling endosome (RE) sort apical and basolateral proteins and serve as important recycling routes (Deborde et al 2008). As a result of this organization, cell establishes intracellular axis of polarization, which can be defined by Nucleus-centrosome-golgi axis (also referred as NC axis). The idea of NC axis as structural axis was first conceived by Van Beneden in 1883 (Figure 0.3 C). One hundred and thirty two years after van Beneden's first proposition, it has been well established that centrosome functions as the main organelle responsible for non-random distribution of cellular transport owing to its microtubule organization property (Luxton and Gundersen, 2011; Théry et al., 2006). The NC axis orientation allows demarcation of cellular domains where the intracellular trafficking will be dominated e.g. NC axis orientated toward lumen and the secretion of milk proteins into lumen occurs from the apical side of mammary gland acini. As a result of which Nucleus-centrosome orientation is considered a faithful indicator of internal cell polarity (Figure 0.3 B). Concerted NC axis orientation is observed within cells of intestinal, kidney, mammary gland tissue. In various physiological events such as wound healing, fibroblast migration and immune response; NC vector is re-positioned demonstrating reorientation of cell's internal polarity (Dupin et al., 2009; Luxton and Gundersen, 2011; Reversat et al., 2015).

In a stable epithelial tissue, the polarization cues from cortical polarity (Figure 0.3 C) and internal polarity (Figure 0.3 C) are well coordinated to generate polarized epithelium. Live cell imaging of

Figure 0.4

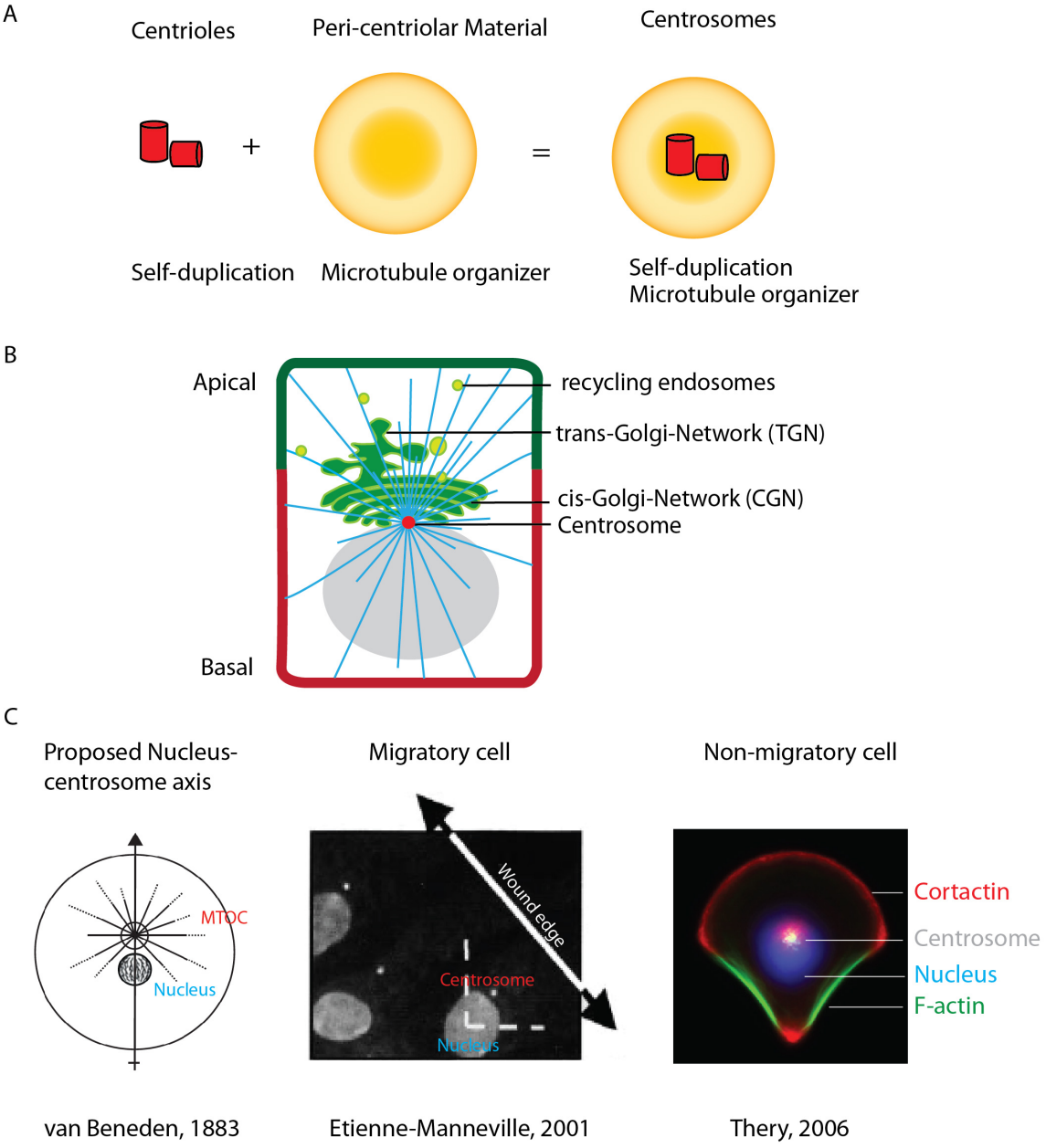

(A) Centriols and pericentriolar material make up the centrosome and provide ability of self-duplication and microtubule nucleation.
(B) Asymmetric positioning of nucleus and centrosome directs the intracellular trafficking in polarized epithelial cell
(C) Progressive establishement of 'NC axis' as the marker of internal polarity. In 1883, van Beneden proposed the concept of NC axis. Orietnation of NC axis in migratory cells in the direction of wound was shown by S. Etienne-Manneville. NC axis orientation along with membrane polarization in confined epithelial cell was demonstrated by M. Thery in 2006

Figure 0.5

A

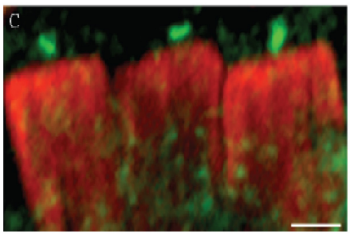

Hoppeler-Lebel ,JCS 2007

Epithelial cells

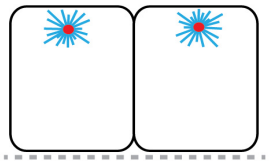

Basement
Membrane

B

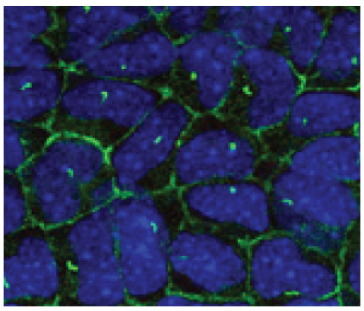

Blitzer, PNAS 2011

Planar polarity program

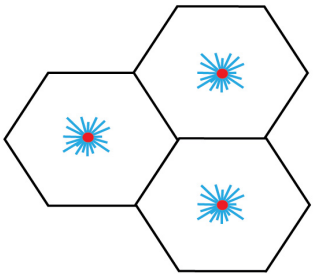

C

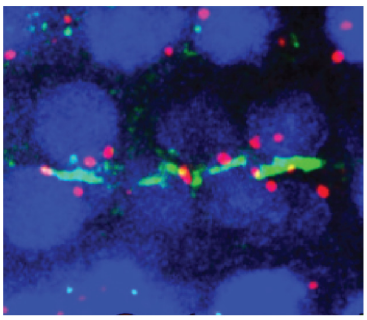

Feldman, CB 2012

Intestinal cells

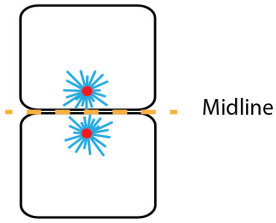

Centrosome position in epithelial tissues

(A) Pillar cells of inner ear labelled for centrosomal large CAP-Gly protein CAP350 (Green) and microtubules (red).
(B) Cells of mouse cornea stained for ZO-1and cilia (green)
(C) intestinal cells of developing c. elegans, centrosome (red) and Par3 (Green)

acini formation from single cell indicated that internal and cortical polarity are tightly coupled at every stage of acini development (Bryant et al., 2014; Wang et al., 2013). The presence of feedback loops between the polarity cues can be witnessed in several other examples wherein centrosome position seems highly modulated within epithelial tissue subjected to remodeling (Figure 0.5). Centrosome (Latin Centrum Sōma) has self-centering ability because of its microtubule -nucleating and -anchoring activity in tissue, cell, cytoplasts and the in artificial minimal systems (Bornens, 2008; Holy et al., 1997; Rodionov and Borisy, 1997). Despite having the self-centering ability, centrosome can be also found highly off-centered in stable epithelium and during in remodeling epithelium (Figure 0.5 A). In intestinal, respiratory, secretory epithelia centrosome is preferentially positioned close to apical/luminal side. In other instances like zebrafish gut formation, centrosome is located close to the midline while it is present at the cell-center in mouse cornea cells (Figure 0.5 B-C). (Blitzer et al., 2011; Feldman and Priess, 2012). The capacity of the centrosome movement can be attributed to microtubules anchored at the centrosome, which interact with the cell cortex as well as with other organelles and balance pulling and pushing forces to determine the final localization of centrosome within the cell (Zhu et al., 2010). A prominent example of microtubule and cortex interaction is spindle position orientation during cell division (Cowan and Hyman, 2004; Moore and Cooper, 2010). In non-dividing epithelial cells, microtubule arrays are organized in apical-basal direction close to cell cortex possibly by selective microtubule anchoring or stabilization at the cell cortex (Moss et al., 2007). Centrosome position within the cell can be modulated by variety of factors such as cortical pulling of microtubules, Pushing on cortex by growing microtubule +tips, microtubule sliding along the cortex, Pulling on microtubules by cytoplasmic organelles (Zhu et al., 2010). In addition number of microtubules nucleated at the centrosome, mechanical properties of microtubules, post-translational modification of tubulin can also affect the forces exerted on the centrosome by microtubules.

Over the next two chapters I will address the effect of cortical and internal polarity components on each other, which is mainly mediated by microtubules. We have studied two specific morphogenetic events to understand how microtubules mediate crosstalk between cells' interior and its periphery. Centrosome being the main microtubule organizer it acts as a good indicator of MTOC position and also of internal polarity orientation. In the first chapter, we have studied a human cancer model with centrosome abnormalities to understand how microtubules affect cell junction dynamics to trigger malignant phenotype of tumors. In second chapter, we have studied general mechanism of Epithelial-to-mesenchymal transition to understand how cell-cell junction remodeling is coupled by microtubules to cell's interior and affects centrosome position.

0.4 References

Blitzer, A.L., Panagis, L., Gusella, G.L., Danias, J., Mlodzik, M., and Iomini, C. (2011). Primary cilia dynamics instruct tissue patterning and repair of corneal endothelium. Proc. Natl. Acad. Sci. U. S. A. *108*, 2819–2824.

Bornens, M. (2008). Organelle positioning and cell polarity. Nat. Rev. Mol. Cell Biol. *9*, 874–886.

Bryant, D.M., Roignot, J., Datta, A., Overeem, A.W., Kim, M., Yu, W., Peng, X., Eastburn, D.J., Ewald, A.J., Werb, Z., et al. (2014). A molecular switch for the orientation of epithelial cell polarization. Dev. Cell *31*, 171–187.

Cowan, C.R., and Hyman, A.A. (2004). ASYMMETRIC CELL DIVISION IN *C. ELEGANS*: Cortical Polarity and Spindle Positioning. Annu. Rev. Cell Dev. Biol. *20*, 427–453.

Dupin, I., Camand, E., and Etienne-manneville, S. (2009). Classical cadherins control nucleus and centrosome position and cell polarity. *185*.

Feldman, J.L., and Priess, J.R. (2012). A role for the centrosome and PAR-3 in the hand-off of MTOC function during epithelial polarization. Curr. Biol. *22*, 575–582.

Holy, T.E., Dogterom, M., Yurke, B., and Leibler, S. (1997). Assembly and positioning of microtubule asters in microfabricated chambers. Proc. Natl. Acad. Sci. U. S. A. *94*, 6228–6231.

Luxton, G.W.G., and Gundersen, G.G. (2011). Orientation and function of the nuclear – centrosomal axis during cell migration GW Gant Luxton and Gregg G Gundersen. Curr. Opin. Cell Biol. *23*, 579–588.

Moore, J.K., and Cooper, J.A. (2010). Coordinating mitosis with cell polarity: Molecular motors at the cell cortex. Semin. Cell Dev. Biol. *21*, 283–289.

Moss, D.K., Bellett, G., Carter, J.M., Liovic, M., Keynton, J., Prescott, A.R., Lane, E.B., and Mogensen, M.M. (2007). Ninein is released from the centrosome and moves bi-directionally along microtubules. J. Cell Sci. *120*, 3064–3074.

Reversat, A., Yuseff, M.-I., Lankar, D., Malbec, O., Obino, D., Maurin, M., Penmatcha, N.V.G., Amoroso, A., Sengmanivong, L., Gundersen, G.G., et al. (2015). Polarity protein Par3 controls B-cell receptor dynamics and antigen extraction at the immune synapse. Mol. Biol. Cell *26*, 1273–1285.

Rios, R.M., and Bornens, M. (2002). The Golgi apparatus at the cell centre. Curr. Opin. Cell

Biol. *15*, 60–66.

Rodionov, V.I., and Borisy, G.G. (1997). Self-centring activity of cytoplasm. Nature *386*, 170–173.

Théry, M., Racine, V., Piel, M., Pépin, A., Dimitrov, A., Chen, Y., Sibarita, J.-B., and Bornens, M. (2006). Anisotropy of cell adhesive microenvironment governs cell internal organization and orientation of polarity. Proc. Natl. Acad. Sci. U. S. A. *103*, 19771–19776.

Wang, H., Lacoche, S., Huang, L., Xue, B., and Muthuswamy, S.K. (2013). Rotational motion during three-dimensional morphogenesis of mammary epithelial acini relates to laminin matrix assembly. Proc. Natl. Acad. Sci. U. S. A. *110*, 163–168.

Zhu, J., Burakov, A., Rodionov, V., and Mogilner, A. (2010). Finding the Cell Center by a Balance of Dynein and Myosin Pulling and Microtubule Pushing : A Computational Study. *21*, 4418–4427.

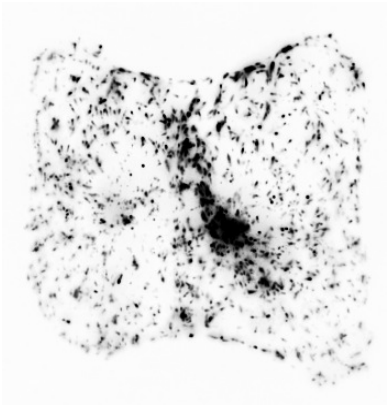
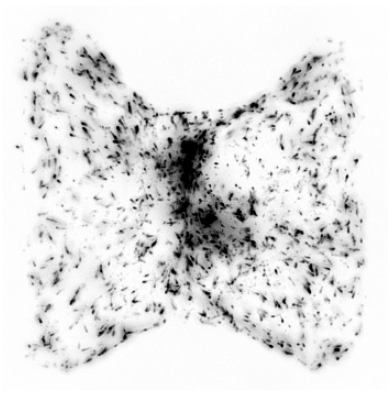

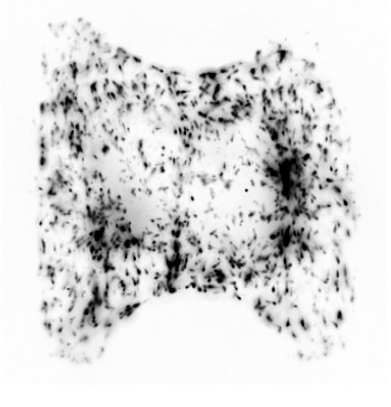

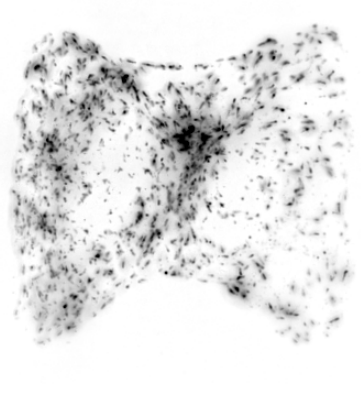
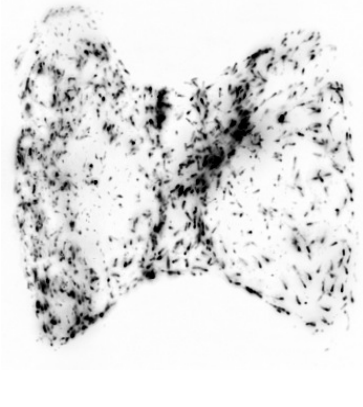


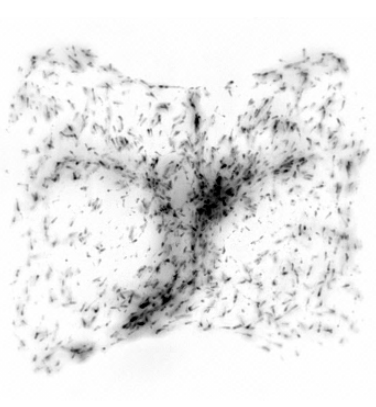
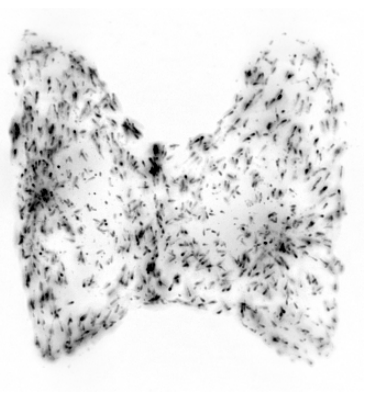
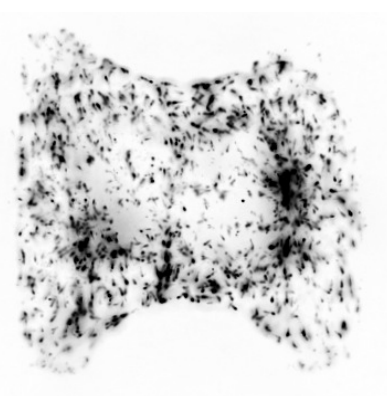

CHAPTER I

Effect of the Centrosome associated Microtubule Network on Cell-cell Adhesions

1.0 Effect of Centrosome Amplification on epithelial organization

The typical epithelial organization is severally altered in human carcinoma and is correlated with the occurrence of the centrosome amplification (CA). Centrosome suepernumery is the hallmark of human cancers and the centrosome cluster in these cells is highly mis-organized with several amplified centriols (Figure 1.1). A century ago, Boveri proposed that increased numbers of centrosomes cause cancer when he observed eggs harboring extra centrosomes underwent multipolar mitoses and divisions of cells to give aneuploid progeny (Boveri, 1887). Aneuploidy being another common feature of cancer, it was also thought to be responsible for generation of invasive structures. Whether chromosome segregation abnormalities cause cancer has been debated over 100 years (Godinho and Pellman, 2012). The model that centrosome amplification caused mis-segregation of chromosomes during mitosis, which triggered malignancy, was popular until late 1900. This model was supported by high occurrences of extra-centrosomes in tumorogenic cells however the important issue of whether chromosomal instability caused by amplified centrosomes leads to tumorogenesis was still unresolved. A report by R. Basto showed that tumorogenesis in flies caused by PLK4 overexpression is accompanied by only minor frequency of aneuploidy (Basto et al., 2009). Ganem et al., demonstrated the direct link between extracentrosomes and cause of centrosomal instability. The authors demonstrated that cells with amplified centrosomes rarely undergo multipolar division and instead undergo bipolar division by clustering of centrosome to constitute bipolar spindle (Ganem et al., 2009). The mitotic defects observed in these cells are result of lagging chromosomes because of the observed defects in chromosome number is result of merotely, where a single kinetochore attaches to microtubules emanating from different poles. This leads to lagging chromosomes during anaphase and results into aneuploid daughter cells, which often have tumorogenic potential. Furthermore study of breast tumors showed alteration of centrosome number, amplification of centrioles, accumulation of PCM, inappropriate phosphorylation of centrosomal protein, higher microtubule nucleation is associated with disorganized tissue structures like mammary gland acini (Lingle et al., 1998). Thus two important questions that were still unanswered about malignant tumors with amplified centrosomes were that was it the aneuploidy that is responsible for malignant phenotype of cells? Secondly, do higher microtubules nucleation and their interaction with cortex promoted the tissue disorganization that causes malignant behavior? To answer these questions, our collaborator Susana Godinho designed the experiments by generating a cell line model of human mammary gland cells (MCF10A) with inducible expression of polo-like-Kinase-4 (PLK-4) that is responsible for centrosome duplication.

Figure 1.1

A

Normal human mammary gland acini

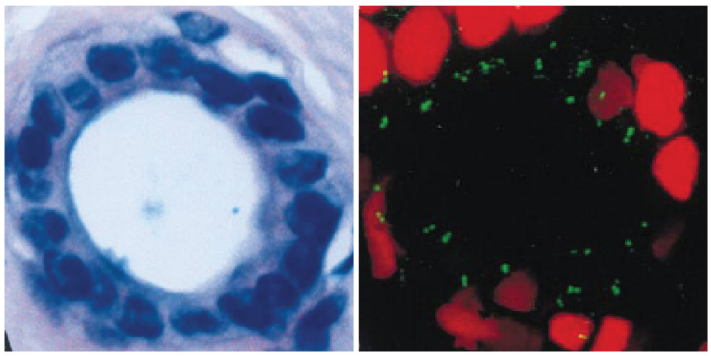

Centrin DNA

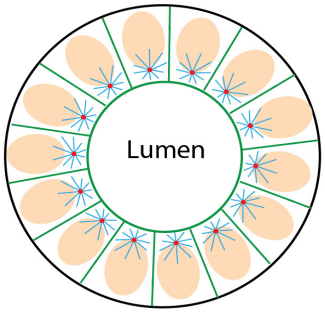

B

Mammary gland acini from human cancer tumors

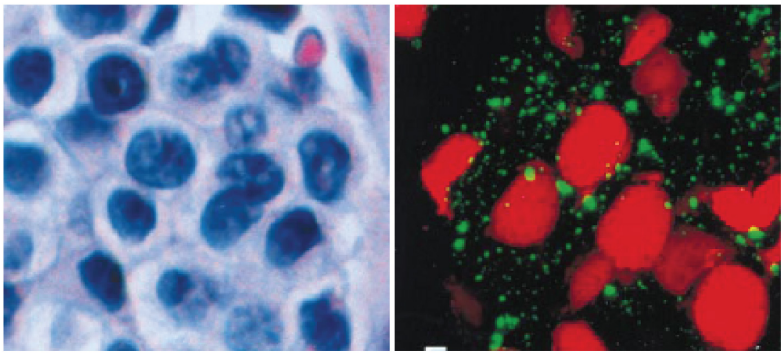

Centrin DNA

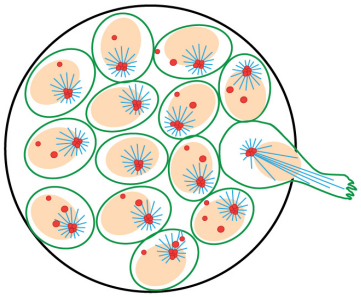

To dissect the effect of ploidy of the cell and presence of amplified centrosomes, aneuploid cells with normal centrosome number and diploid cells with amplified centrosomes were generated. The following article explains the methodology and experiments performed to demonstrate that the presence of extracentrosomes directly triggers cell invasion by microtubule interaction with cell-cell adhesions. This study reveals a new mechanism showing centrosome amplification and subsequent effect of microtubule- cell junction interaction can severally affect the stability of cell-cell junction and thus promotes metastatic behavior.

LETTER

doi:10.1038/nature13277

Oncogene-like induction of cellular invasion from centrosome amplification

Susana A. Godinho[1,2]†, Remigio Picone[1,2], Mithila Burute[3,4,5], Regina Dagher[1,2], Ying Su[6], Cheuk T. Leung[2]†, Kornelia Polyak[6], Joan S. Brugge[2], Manuel Théry[3,4] & David Pellman[1,2]

Centrosome amplification has long been recognized as a feature of human tumours; however, its role in tumorigenesis remains unclear[1]. Centrosome amplification is poorly tolerated by non-transformed cells and, in the absence of selection, extra centrosomes are spontaneously lost[2]. Thus, the high frequency of centrosome amplification, particularly in more aggressive tumours[3], raises the possibility that extra centrosomes could, in some contexts, confer advantageous characteristics that promote tumour progression. Using a three-dimensional model system and other approaches to culture human mammary epithelial cells, we find that centrosome amplification triggers cell invasion. This invasive behaviour is similar to that induced by overexpression of the breast cancer oncogene *ERBB2* (ref. 4) and indeed enhances invasiveness triggered by ERBB2. Our data indicate that, through increased centrosomal microtubule nucleation, centrosome amplification increases Rac1 activity, which disrupts normal cell–cell adhesion and promotes invasion. These findings demonstrate that centrosome amplification, a structural alteration of the cytoskeleton, can promote features of malignant transformation.

The centrosome is the major microtubule-organizing centre in mammalian cells and comprises of a pair of centrioles surrounded by the pericentriolar material[5]. Centrosome abnormalities, usually increased numbers, are common in human tumours[1] and have been positively associated with advanced tumour grade and metastasis[3], suggesting a possible role in tumour progression. This is somewhat surprising given the well-documented deleterious effects of centrosome amplification on cell proliferation[6]; such amplification can be lethal if it compromises the ability of cells to organize multiple centrosomes to generate pseudo-bipolar spindles[2]. These seemingly paradoxical observations suggest that centrosome amplification might enhance other aspects of tumorigenesis.

We have developed orthogonal approaches to generate genetically comparable cells that do or do not carry extra centrosomes[2]. Here we adapt these methods to determine how centrosome amplification influences epithelial organoid integrity, making use of the well characterized three dimensional (3D) culture model for MCF10A cells, a non-transformed human mammary epithelial cell line. This model recapitulates many aspects of breast glandular architecture[7].

We engineered MCF10A cells to enable the inducible overexpression of Polo-like kinase 4 (PLK4), an essential regulator of centrosome duplication, whose overexpression induces supernumerary centrosomes[8,9]. As a negative control, we transiently overexpressed a truncated form of PLK4 ($PLK4^{1-608}$) that retains kinase activity but does not induce centrosome amplification[10]. As expected, transient induction of PLK4, but not of $PLK4^{1-608}$, led to centrosome amplification (Fig. 1a and Extended Data Fig. 1). Strikingly, centrosome amplification induced by PLK4 resulted in the formation of invasive protrusions, cytoplasmatic extensions that invade the surrounding matrix (Fig. 1b and Extended Data Fig. 1f, g). Expression of centrin1–GFP to visualize the centrioles revealed that virtually all cells with invasive protrusions exhibited centrosome amplification (Fig. 1c). An independent approach, using an organotypic culture system to assay for fibroblast-led collective migration, confirmed that centrosome amplification promotes invasion, both of MCF10A cells and non-transformed keratinocytes (HaCaTs) (Fig. 1d and Extended Data Fig. 1h).

Cytokinesis failure was induced in MCF10A cells using dihydrocytochalasin B (DCB) to generate centrosome amplification without PLK4 overexpression. Newly generated tetraploid cells, with doubled centrosome content, were isolated by fluorescence-activated cell sorting (FACS). A control population of tetraploid cells in which extra centrosomes were spontaneously lost were generated, as previously described[2] (evolved tetraploids, 4N.evo, Extended Data Fig. 2a–e). Tetraploid cells with extra centrosomes were invasive in 3D cultures, whereas 4N.evo cells were not (Fig. 1e). PLK4 overexpression in 4N.evo cells induced centrosome amplification accompanied by invasive protrusions, demonstrating that 4N.evo cells still retained the ability to become invasive (Extended Data Fig. 2g, h).

Invasive protrusions are accompanied by the degradation of laminin-V (Fig. 1f) and collagen-I (Extended Data Fig. 1i), contain actin and microtubules (Extended Data Fig. 3a) and are surrounded by the extracellular matrix component fibronectin (Extended Data Fig. 3b). Consistent with centrosome amplification promoting matrix degradation, the invasive phenotype was partially suppressed by inhibition of metalloproteinases using marimastat (Extended Data Fig. 3c). Live-cell imaging showed that protrusions are highly dynamic, constantly extending and retracting (Supplementary Videos 1 and 2), which may partially explain why only a fraction of acini with extra centrosomes exhibits invasive protrusions at a given time (Fig. 1c). The formation of an initial protrusion provided a track for the collective migration of multiple cells out of the acinus and into the surrounding matrix (Extended Data Fig. 3d, e and Supplementary Video 3). This type of collective invasion resembles what has been observed in tumours *in vivo*. Indeed, many solid tumours typically exhibit collective invasion, which often involves the degradation of the extracellular matrix[11].

Invasion induced by centrosome amplification strongly resembled that induced by a bona fide breast cancer oncogene, *ERBB2* (ref. 4) (Extended Data Fig. 4). As in *ERBB2* tumours[12], cells with extra centrosomes retained the expression of E-cadherin (Extended Data Fig. 3f), suggesting that mechanisms other than a classical epithelial-to-mesenchymal transition account for the invasive phenotype. Importantly, when combined with ERBB2 overexpression, centrosome amplification enhanced the frequency of invasive acini (Fig. 1g).

The induction of invasive protrusions by extra centrosomes could be an indirect consequence of aneuploidy that results from chromosome missegregation[2,13]. To directly address this possibility, we depleted MCAK (also known as KIF2C), a kinesin important for chromosome segregation during mitosis[14], to induce a comparable degree of aneuploidy before (48 h after PLK4 induction) and after 4 days in 3D culture (Fig. 2a, b).

[1]Howard Hughes Medical Institute, Department of Pediatric Oncology, Dana-Farber Cancer Institute and Pediatric Hematology/Oncology, Children's Hospital, Boston, Massachusetts 02115, USA. [2]Department of Cell Biology, Harvard Medical School, Boston, Massachusetts 02115, USA. [3]Institut de Recherche en Technologie et Science pour le Vivant, UMR5168 CEA/UJF/INRA/CNRS, Grenoble, France. [4]Hôpital Saint Louis, Institut Universitaire d'Hematologie, U1160 INSERM/AP-HP/Université Paris Diderot, Paris 75010, France. [5]CYTOO SA, Grenoble 38054, France. [6]Department of Medical Oncology, Dana-Farber Cancer Institute, Harvard Medical School, Boston, Massachusetts 02115, USA. †Present addresses: Barts Cancer Institute, Queen Mary University of London, Charterhouse Square, London EC1M 6BQ, UK (S.A.G.); Department of Pharmacology, University of Minnesota, Minneapolis, Minnesota 55455, USA (C.T.L.).

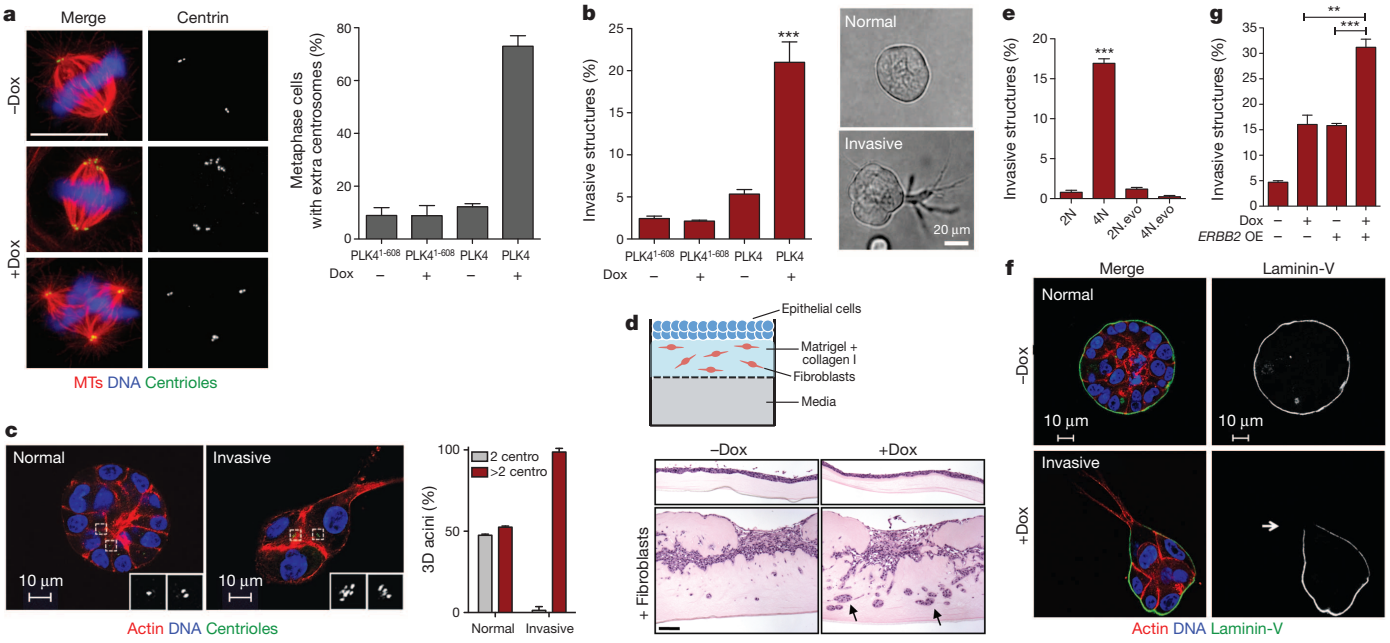

Figure 1 | Invasive behaviour of epithelial cells triggered by centrosome amplification. **a**, Cells stained for microtubules (α-tubulin, red), centrioles (centrin2, green) and DNA (Hoechst, blue). Scale bar, 10 µm. Histogram shows fraction of cells with centrosome amplification. Error bars represent mean ± s.e. from 3 independent experiments. **b**, Fraction of invasive acini in 3D cultures and representative images of normal acinus and an acinus with invasive protrusions. Scale bar, 10 µm. Error bars represent mean ± s.e. from 4 independent experiments. **c**, Cells stained for F-actin (red), centrioles (centrin1–GFP, green, inset white) and DNA (blue). Scale bar, 10 µm. Histogram shows fraction of acini with centrosome amplification after PLK4 overexpression. Error bars represent mean ± s.e. from 3 independent experiments. **d**, Scheme of the organotypic culture model used to assess invasion (top). Images show haematoxylin and eosin (H&E) staining of sections of MCF10A cells plated on the organotypic model, with and without fibroblasts (black arrows indicate highly invasive areas). Percentage of invasion (mean ± s.d.): −Dox = 11.7 ± 0.83; +Dox = 26.1 ± 6.5. Scale bar, 100 µm. **e**, Fraction of invasive acini in tetraploids. Error bars represent mean ± s.e. from 3 independent experiments. **f**, Acini stained for laminin-V (green), F-actin (red) and DNA (blue). White arrow indicates laminin-V degradation. Scale bar, 10 µm. **g**, Fraction of invasive acini in cells that overexpress *ERBB2*, with or without centrosome amplification. Error bars represent mean ± s.e. from 3 independent experiments. All *P* values were derived from unpaired two-tailed Student's *t*-test (***P* < 0.005; ****P* < 0.0005). OE, overexpression.

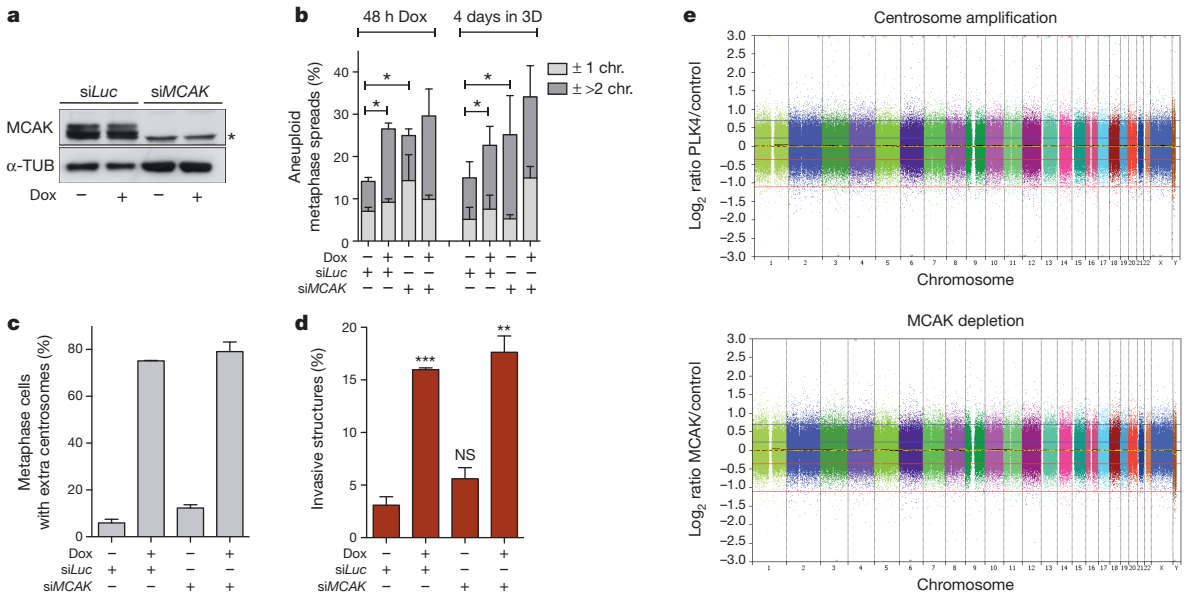

Figure 2 | The induction of aneuploidy does not generate invasive acini. **a**, Western blot showing depletion of MCAK by siRNA (48 h). The asterisk marks a non-specific band. **b**, Quantification of chromosome number, shown as the percentage deviation from the mode, in cells before adding to 3D cultures (48 h) and after 3D cultures (~100 spreads were scored per condition). Significance was determined by chi-squared testing to compare the frequencies of nominal variables (**P* < 0.05). si*Luc*, si luciferase control. **c**, Fraction of cells with centrosome amplification. Error bars represent mean ± s.e. from 3 independent experiments. **d**, Fraction of invasive acini. Error bars represent mean ± s.e. from 3 independent experiments. *P* value derived from unpaired two-tailed Student's *t*-test (***P* < 0.005, ****P* < 0.0005; NS, not significant). **e**, SNP analysis of cells with extra centrosomes and depleted of MCAK. Shown are $\log_2$ copy number ratios of the indicated samples relative to their controls.

Cells depleted of MCAK neither increased centrosome number nor exhibited a significant increase in invasive protrusions (Fig. 2c, d). Similarly, aneuploidy, generated by inhibition of the spindle assembly checkpoint kinase MPS1 (using the inhibitor reversine)[15] also failed to induce invasion (Extended Data Fig. 5a–c). In addition, although 4N.evo cells exhibit substantial aneuploidy, they did not form invasive acini (Fig. 1e and Extended Data Fig. 2f). Finally, single-nucleotide polymorphism analysis (SNP-arrays) demonstrated that neither cells with extra centrosomes nor depletion of MCAK accumulate a recurrent aneuploidy after 4 days in 3D culture (Fig. 2e and Extended Data Fig. 5d). Thus, aneuploidy per se is not responsible for the invasive behaviour.

Centrosome amplification also leads to altered cilia signalling[16] and to increased levels of p53 (ref. 17). However, we found that neither the parental MCF10A cells nor the derivatives with extra centrosomes formed detectable cilia after 4 days in 3D culture. Moreover, depletion of p53 did not alter centrosome amplification mediated invasion (Extended Data Fig. 6a–d). In a transplant model using asymmetrically dividing neuroblasts from *Drosophila melanogaster*, centrosome amplification induces tumours that, interestingly, are capable of metastasis[18]. Centrosome amplification in this system disrupts asymmetric cell division, resulting in stem cell expansion, potentially contributing to tumorigenesis. Because MCF10A cells do not undergo asymmetric cell division, this mechanism does not apply to our results. In the *Drosophila* neuroblasts, centrosome amplification may also disrupt cell polarization, which can trigger tumorigenesis in many systems. Although we cannot exclude effects on cell polarization in our system, we do note that MCF10A cells cannot form tight junctions and do not exhibit polarization of the apical Par3–Par6–aPKC complex[19]. Moreover, centrosome amplification does not impair the ability of MCF10A cells to asymmetrically position centrosomes, the main detectable polarization in these cells (Extended Data Fig. 6e, f).

Insight into why cells with extra centrosomes are invasive in 3D cultures first came from observing the adhesive properties of single cells after cell division. As expected because they are epithelial cells, following mitosis, MCF10As formed cell–cell contacts, and remained as apposed cell pairs. By contrast, cells with extra centrosomes 'scattered', resulting in a high fraction of individual cells (Extended Data Fig. 7a, b and Supplementary Videos 4 and 5), a characteristic associated with loss of cell–cell adhesion. Furthermore, live cell imaging in cells with a fluorescent membrane marker revealed that cell–cell contacts are not stable and often overlap in cells with extra centrosomes (Fig. 3a, Supplementary Videos 6 and 7). As a direct measure of cell–cell junction integrity, we plated cells onto fibronectin micropatterns that were specifically designed to promote the formation of adherens junctions at a stereotypical position between the two cells (Fig. 3b)[20]. Consistent with the cell scattering effect, centrosome amplification produced marked defects in cell–cell junction positioning and size (Fig. 3c, d). This effect of centrosome amplification is similar to that described for loss of p120 catenin, whose knockdown weakens cell–cell contacts[20], although centrosome amplification does not affect p120 levels (Extended Data Fig. 7c).

These phenotypic characteristics induced by centrosome amplification are similar to what has previously been observed upon activation of Rac1 (refs 21, 22), a small GTPase strongly associated with oncogenic signalling and with the induction of invasiveness and metastasis[23,24].

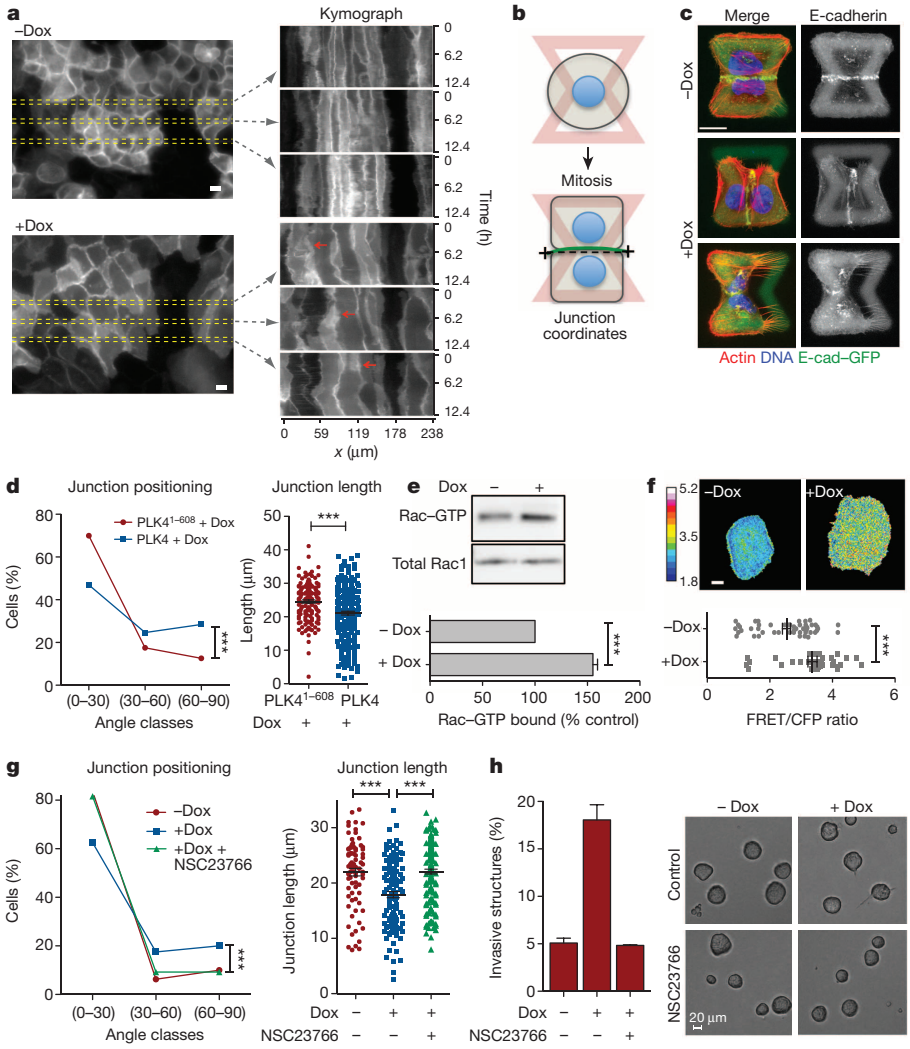

Figure 3 | Centrosome amplification disrupts normal cell–cell adhesion because of Rac1 activation. **a**, Kymograph analysis of cell–cell adhesion in live cells visualized with a plasma membrane marker (Raichu-Rac1, CFP fluorescence). Red arrows mark areas of increased dynamics of cell–cell contacts. **b**, Scheme of the micro-pattern used. **c**, Images of cells (after mitosis) on micro-patterns labelled for E-cadherin (GFP; green), F-actin (red), DNA (blue) and fibronectin micro-pattern (green). Normal sized junction with a normal position (narrow angle) (top); abnormal junction position (middle); smaller junction size (bottom). Scale bar, 10 μm. **d**, Distribution of the cell–cell junctions angles, as a measure of junction positioning, (left) and size (right). For –Dox, $n = 143$; +Dox, $n = 216$. Error bars represent mean ± s.e. **e**, Representative western blot from a pull-down experiment to detect GTP-bound Rac1. Histogram shows quantification from 3 independent pull-down experiments. Error bars represent mean ± s.e. **f**, Top shows examples of FRET ratiometric images; colour-coded scale represents the level of Rac1 activation. Scale bar, 10 μm. Bottom, levels of active Rac1 measured by FRET. For –Dox, $n = 50$; +Dox, $n = 38$. Error bars represent mean ± s.e. **g**, Inhibition of Rac1 with NSC23766 in cells plated on micro-patterns. For –Dox, $n = 80$; + Dox $n = 119$; +Dox + NSC23766, $n = 162$. **h**, Fraction of invasive acini after treatment with NSC23766 and images of control and NSC23766-treated acini. Scale bar, 20 μm. Error bars represent mean ± s.e. from 3 independent experiments. All P values were derived from unpaired two-tailed Student's t-test (***$P < 0.0005$).

This motivated the hypothesis that extra centrosomes might promote invasive-like effects through inappropriate activation of Rac1. Indeed, we found that centrosome amplification induced a consistent ~1.5-fold Rac1 activation using a biochemical pull-down assay to measure GTP-bound Rac1 in multiple cell lines. Maximal Rac1 activity induced by EGF in MCF10A cells is ~2-fold (Fig. 3e and Extended Data Fig. 7d, e). This was confirmed by monitoring Rac1 activation in single cells using the Raichu-Rac1 fluorescence resonance energy transfer (FRET) biosensor[25] (Fig. 3f and Extended Data Fig. 7f, g). Consistent with the commonly reported antagonism between Rac1 and RhoA, we found that cells with extra centrosomes have decreased active RhoA (Extended Data Fig. 7h). Thus, centrosome amplification in MCF10A cells activates Rac1.

Small molecule Rac1 inhibitor (NSC23766) inhibited Rac1 activation and partially rescued defects in cell–cell adhesion, suggesting that Rac1 activation is responsible for the cell–cell adhesion defect in cells with centrosome amplification, (Fig. 3g and Extended Data Fig. 7i). Similar results were obtained in tetraploid MCF10A cells (Extended Data Fig. 8a, b). Furthermore, treatment with CK-666, an inhibitor of the Arp2/3 complex, an actin nucleator and important downstream target of Rac1 (ref. 23), also partially rescued the defects in cell–cell adhesion induced by centrosome amplification (Extended Data Fig. 8c–e). These findings demonstrate that the cell–cell adhesion defects in cells with extra centrosomes are, to a substantial degree, caused by increased Arp2/3-dependent actin polymerization that occurs downstream of Rac1 signalling. In addition, we found that Rac1 inhibition blocked the formation of invasive acini without impairing the ability of cells to form normal acini (Fig. 3h).

Previous work has established that microtubule polymerization after nocodazole washout induces Rac1 activation. This activation appears to require dynamic microtubules because it is suppressed by the microtubule-stabilizing agent, paclitaxel[26]. We considered the possibility that centrosome amplification induces Rac1 activation through effects on centrosomal microtubule nucleation. As expected[27], MCF10A cells with extra centrosomes display elevated levels of centrosomal γ-tubulin (Extended Data Fig. 9a-c) and an increased capacity for microtubule-nucleation (Fig. 4a, note that amplified centrosomes are almost always clustered in interphase). Moreover, paclitaxel blocked the activation of Rac1 in cells with extra centrosomes (Fig. 4b), indicating a similar requirement for dynamic microtubules[26]. These results were independently confirmed when Rac1 activity was monitored by FRET (Fig. 4c). Finally, Rac1 activation measured by FRET was also observed in cells with extra centrosomes deprived of EGF (Extended Data Fig. 9d), indicating that this Rac1 activation is independent of any effects on growth factor signalling. Furthermore, induction of centrosome amplification (at 48 h) does not alter the cell cycle profile (Extended Data Fig. 9e) arguing against cell cycle effects as the cause for Rac1 activation in cells with extra centrosomes.

We next examined the impact of increased centrosomal microtubule nucleation on cell–cell adhesion and the development of invasive structures. To do so, centrosomal microtubule nucleation was moderately decreased by RNAi-mediated knockdown of *CEP192*, which encodes a centrosomal protein required for interphase recruitment of γ-tubulin to the centrosomes[28]. As described[28], this protocol decreases centrosomal γ-tubulin without affecting centrosome number (Extended Data Fig. 10a, b, d, e). Consistent with our hypothesis, the depletion of CEP192 inhibited Rac1 activation and restored normal cell–cell adhesion among cells with centrosome amplification (Fig. 4d–f). Most notably, partial depletion of CEP192 after short hairpin RNA (shRNA) treatment fully suppressed the invasive phenotype in cells with extra centrosomes without compromising cell viability or centrosome amplification, even after 4 days in 3D cultures (Fig. 4g and Extended Data Fig. 10c, f–h). These results indicate that increased centrosomal microtubule nucleation in cells with extra centrosomes triggers invasion. Although it remains unclear how dynamic microtubules activate Rac1 (ref. 29), our data

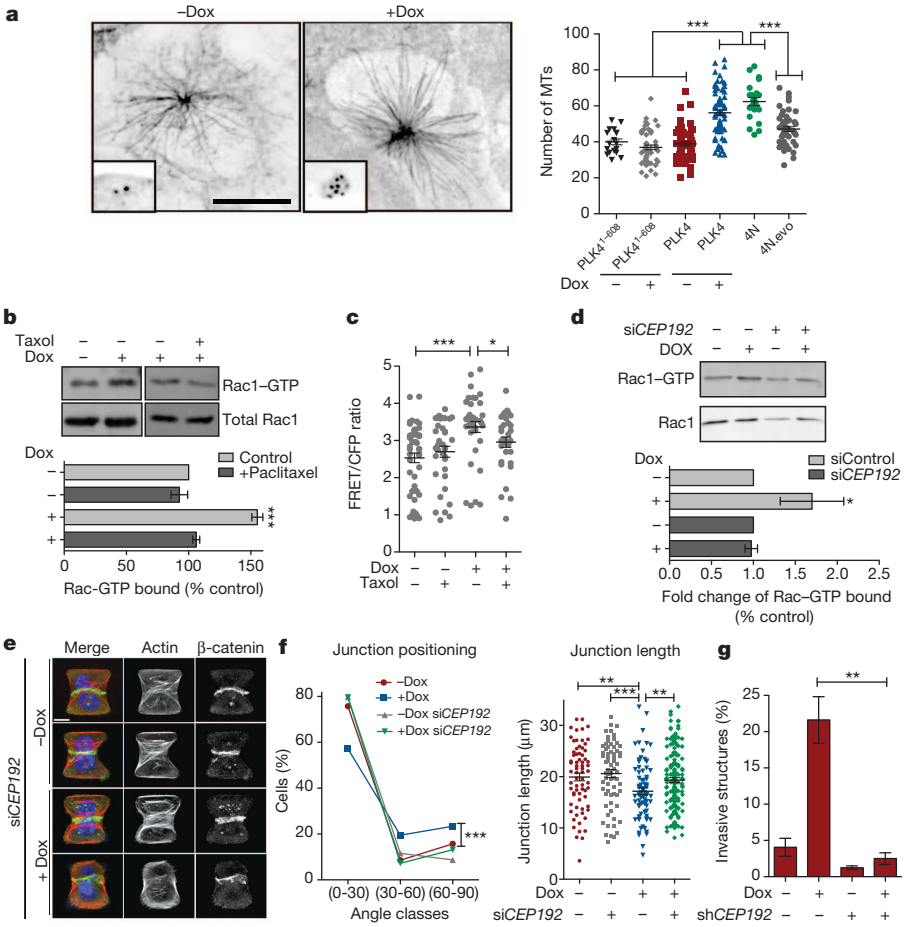

Figure 4 | Effects of centrosome amplification are mediated by increased nucleation of centrosomal microtubules. **a**, Images of microtubules (α-tubulin; insets, centrioles) in cells after microtubule re-growth. Graph shows microtubule numbers from the indicated cells. For PLK4$^{1-608}$ –Dox, $n = 18$; PLK4$^{1-608}$ +Dox, $n = 51$; PLK4 –Dox, $n = 66$; PLK4 +Dox, $n = 71$; 4N, $n = 22$; 4N.evo, $n = 49$. Error bars represent mean ± s.e. **b**, Pull-down assay to measure GTP-bound Rac1 after paclitaxel treatment and quantification of the levels of Rac1–GTP. Error bars represent mean ± s.e. from 3 independent experiments. **c**, FRET ratios for measuring active Rac1 in cells after the indicated treatments. For –Dox, $n = 50$; −Dox +Taxol $n = 38$; +Dox, $n = 38$; +Dox +Taxol, $n = 32$. Error bars represent mean ± s.e. **d**, Pull-down assay to measure GTP-bound Rac1 after CEP192 depletion by siRNA and quantification of the levels of Rac1–GTP. Error bars represent mean ± s.e. from 4 independent experiments. *P* value derived from Wilcoxon test (*$P < 0.05$). **e**, Images of cells depleted of CEP192 on micro-patterns labelled for β-catenin (green), F-actin (red), DNA (blue) and fibronectin micro-pattern (green). Scale bar, 10 μm. **f**, Angles and sizes of cell–cell junctions after depletion of CEP192 by siRNA. For control siRNA –Dox, $n = 71$; control siRNA +Dox, $n = 78$; *CEP192* siRNA −Dox $n = 69$; *CEP192* siRNA +Dox, $n = 150$. Error bars represent mean ± s.e. **g**, Fraction of invasive acini seen after depletion of CEP192 by shRNA. Error bars represent mean ± s.e. from 3 independent experiments. For panels **a**–**c**, **f** and **g**, *P* values were derived from unpaired two-tailed Student's *t*-test (*$P < 0.05$, **$P < 0.005$, ***$P < 0.0005$).

indicates that Rac1 activation downstream of microtubule nucleation plays a central role in this phenomenon.

Deregulated Rac1 activity has been implicated in the pathogenesis of many tumour types and is known to drive tumour invasion and metastasis[24]. Previous studies have demonstrated that Rac1 activation in tumours can be regulated by many mechanisms[24]. Our data indicate that centrosome amplification is probably another common mechanism for Rac1 activation during tumorigenesis, and that centrosome amplification may augment other oncogenic signals. In addition to Rac1 activation, additional mechanisms probably contribute to the effects of centrosome amplification. Gene expression analyses of 3D cultures showed that TGF-β pathway, involved in metastasis formation and associated with tumour aggressiveness[30], is strongly upregulated in cells with extra centrosomes (S.A.G. and D.P., unpublished data).

Many studies have noted a positive correlation between centrosome amplification and advanced-stage tumours, recurrence and poor survival[3], yet the mechanistic basis for this correlation has remained unclear. Here we provide evidence that centrosome amplification can mimic and accentuate the effects of oncogenes in triggering cellular invasion. These findings illustrate the integral relationship between cellular signalling and the cytoskeleton, underscoring the importance of this relationship to tumour progression.

METHODS SUMMARY

Human mammary epithelial MCF10A cells were maintained at 37 °C with 5% CO_2 atmosphere. PLK4 overexpression to induce centrosome amplification was induced by treatment with 2 μg ml^{-1} of doxycycline (48 h). Alternatively, centrosome amplification was induced by inhibition of cytokinesis with 4 μM of DCB (18 h) and tetraploid cells were isolated by FACS, as previously described[2]. A more detailed description of methods used can be found in the Methods section.

Online Content Any additional Methods, Extended Data display items and Source Data are available in the online version of the paper; references unique to these sections appear only in the online paper.

Received 24 July 2013; accepted 24 March 2014.

Published online 13 April; corrected online 2 May 2014 (see full-text HTML version for details).

1. Zyss, D. & Gergely, F. Centrosome function in cancer: guilty or innocent? *Trends Cell Biol.* **19,** 334–346 (2009).
2. Ganem, N. J., Godinho, S. A. & Pellman, D. A mechanism linking extra centrosomes to chromosomal instability. *Nature* **460,** 278–282 (2009).
3. Chan, J. Y. A clinical overview of centrosome amplification in human cancers. *Int. J. Biol. Sci.* **7,** 1122–1144 (2011).
4. Levental, K. R. *et al.* Matrix crosslinking forces tumor progression by enhancing integrin signaling. *Cell* **139,** 891–906 (2009).
5. Bettencourt-Dias, M. & Glover, D. M. Centrosome biogenesis and function: centrosomics brings new understanding. *Nature Rev. Mol. Cell Biol.* **8,** 451–463 (2007).
6. Sluder, G. & Nordberg, J. J. The good, the bad and the ugly: the practical consequences of centrosome amplification. *Curr. Opin. Cell Biol.* **16,** 49–54 (2004).
7. Debnath, J. & Brugge, J. S. Modelling glandular epithelial cancers in three-dimensional cultures. *Nature Rev. Cancer* **5,** 675–688 (2005).
8. Bettencourt-Dias, M. *et al.* SAK/PLK4 is required for centriole duplication and flagella development. *Curr. Biol.* **15,** 2199–2207 (2005).
9. Habedanck, R., Stierhof, Y. D., Wilkinson, C. J. & Nigg, E. A. The Polo kinase Plk4 functions in centriole duplication. *Nature Cell Biol.* **7,** 1140–1146 (2005).
10. Guderian, G., Westendorf, J., Uldschmid, A. & Nigg, E. A. Plk4 trans-autophosphorylation regulates centriole number by controlling βTrCP-mediated degradation. *J. Cell Sci.* **123,** 2163–2169 (2010).
11. Friedl, P., Locker, J., Sahai, E. & Segall, J. E. Classifying collective cancer cell invasion. *Nature Cell Biol.* **14,** 777–783 (2012).
12. Palacios, J. *et al.* Relationship between ERBB2 and E-cadherin expression in human breast cancer. *Virchows Archiv.* **427,** 259–263 (1995).
13. Silkworth, W. T., Nardi, I. K., Scholl, L. M. & Cimini, D. Multipolar spindle pole coalescence is a major source of kinetochore mis-attachment and chromosome mis-segregation in cancer cells. *PLoS ONE* **4,** e6564 (2009).
14. Maney, T., Hunter, A. W., Wagenbach, M. & Wordeman, L. Mitotic centromere-associated kinesin is important for anaphase chromosome segregation. *J. Cell Biol.* **142,** 787–801 (1998).
15. Santaguida, S., Tighe, A., D'Alise, A. M., Taylor, S. S. & Musacchio, A. Dissecting the role of MPS1 in chromosome biorientation and the spindle checkpoint through the small molecule inhibitor reversine. *J. Cell Biol.* **190,** 73–87 (2010).
16. Mahjoub, M. R. & Stearns, T. Supernumerary centrosomes nucleate extra cilia and compromise primary cilium signaling. *Curr. Biol.* **22,** 1628–1634 (2012).
17. Holland, A. J. *et al.* The autoregulated instability of Polo-like kinase 4 limits centrosome duplication to once per cell cycle. *Genes Dev.* **26,** 2684–2689 (2012).
18. Basto, R. *et al.* Centrosome amplification can initiate tumorigenesis in flies. *Cell* **133,** 1032–1042 (2008).
19. Fogg, V. C., Liu, C. J. & Margolis, B. Multiple regions of Crumbs3 are required for tight junction formation in MCF10A cells. *J. Cell Sci.* **118,** 2859–2869 (2005).
20. Tseng, Q. *et al.* Spatial organization of the extracellular matrix regulates cell-cell junction positioning. *Proc. Natl Acad. Sci. USA* **109,** 1506–1511 (2012).
21. Chen, X. & Macara, I. G. Par-3 controls tight junction assembly through the Rac exchange factor Tiam1. *Nature Cell Biol.* **7,** 262–269 (2005).
22. Xue, B., Krishnamurthy, K., Allred, D. C. & Muthuswamy, S. K. Loss of Par3 promotes breast cancer metastasis by compromising cell–cell cohesion. *Nature Cell Biol.* **15,** 189–200 (2013).
23. Jaffe, A. B. & Hall, A. Rho GTPases: biochemistry and biology. *Annu. Rev. Cell Dev. Biol.* **21,** 247–269 (2005).
24. Mack, N. A., Whalley, H. J., Castillo-Lluva, S. & Malliri, A. The diverse roles of Rac signaling in tumorigenesis. *Cell Cycle* **10,** 1571–1581 (2011).
25. Itoh, R. E. *et al.* Activation of Rac and Cdc42 video imaged by fluorescent resonance energy transfer-based single-molecule probes in the membrane of living cells. *Mol. Cell. Biol.* **22,** 6582–6591 (2002).
26. Waterman-Storer, C. M., Worthylake, R. A., Liu, B. P., Burridge, K. & Salmon, E. D. Microtubule growth activates Rac1 to promote lamellipodial protrusion in fibroblasts. *Nature Cell Biol.* **1,** 45–50 (1999).
27. Lingle, W. L. *et al.* Centrosome amplification drives chromosomal instability in breast tumor development. *Proc. Natl Acad. Sci. USA* **99,** 1978–1983 (2002).
28. Zhu, F. *et al.* The mammalian SPD-2 ortholog Cep192 regulates centrosome biogenesis. *Curr. Biol.* **18,** 136–141 (2008).
29. Stehbens, S. & Wittmann, T. Targeting and transport: how microtubules control focal adhesion dynamics. *J. Cell Biol.* **198,** 481–489 (2012).
30. Padua, D. & Massague, J. Roles of TGFβ in metastasis. *Cell Res.* **19,** 89–102 (2009).

Supplementary Information is available in the online version of the paper.

Acknowledgements We are grateful to S. Jhaveri-Schneider, S. Muthuswamy, M. Bettencourt-Dias, R. Basto, D. Calado, N. Ganem, A. Spektor, M. Kwon and B. Atkins for comments or discussion of the manuscript; the Nikon Imaging Center at Harvard Medical School; J. Waters, J. Rosenberg and H. Elliott from the Image and Data Analysis Core at Harvard Medical School for their help with FRET microscopy and analysis; L. Cameron of the Confocal and Light Microcopy Facility at Dana-Farber Cancer Institute; H. Li of SNP analysis; A. Bui for help establishing the 3D cultures; Q. Tseng for establishing MCF10A doublets on micropatterns; and C. Sproat and J. Marshall for help with the organotypic cultures. Reagents were kindly provided by L. Pelletier, J. Locarek, M. Matsuda, A. Hall and J. Marshall. S.A.G. is supported by an FCT grant HMSP-CT/SAU-ICT/0075/2009. M.T. is supported by the ERC grant 310472 and the ISI program of BPIFrance. D.P. is an HHMI investigator and is supported by an NIH grant GM083299-1.

Author Contributions S.A.G. and D.P. designed the experiments and wrote the manuscript. S.A.G. conceived, conducted and performed data analysis for most experiments. R.P. conceived and conducted all FRET experiments and Fig. 3a. M.T. and M.B. contributed with micro-pattern fabrication, Fig. 3d, Extended Data Fig. 6e, d and Extended Data Fig. 8c–e. R.D. contributed with Fig. 2b and Extended Data Fig. 5a. Y.S., K.P., C.T.L. and J.S.B. provided assistance with 3D cultures. All authors contributed with discussions and edited the manuscript.

Author Information The SNP data discussed in this publication have been deposited in NCBI's Gene Expression Omnibus and are accessible through accession number GSE55042. Reprints and permissions information is available at www.nature.com/reprints. The authors declare no competing financial interests. Readers are welcome to comment on the online version of the paper. Correspondence and requests for materials should be addressed to S.A.G. (s.godinho@qmul.ac.uk) or D.P. (david_pellman@dfci.harvard.edu).

METHODS

Cell culture. Human mammary epithelial MCF10A cells were maintained at 37 °C with 5% CO_2 atmosphere and cultured as previously described[31]. Briefly, MCF10A cells were grown in DMEM/F12 (Invitrogen) supplemented with 5% donor horse serum (Sigma), 20 ng ml^{-1} epidermal growth factor (EGF; Sigma), 10 μg ml^{-1} insulin (Invitrogen), 100 μg ml^{-1} hydrocortisone (Sigma), 1 ng ml^{-1} cholera toxin (Sigma), 100 U ml^{-1} penicillin and streptomycin (Invitrogen). The MCF10A cell line overexpressing the human *ERBB2* gene (MCF10A.ErbB2 or MCF10A.NeuN) was previously characterized[32,33]. For 3D cultures, cells were grown in the same medium with reduced horse serum (2%) and EGF (5 ng ml^{-1}). To assay invasion in 3D cultures, cells were grown in a mix of Matrigel:collagen-I, as previously described[34]. The addition of collagen-I to Matrigel facilitates invasion by increasing matrix stiffness[35]. We used growth factor-reduced Matrigel (BD Biosciences) lots with protein concentrations between 9 and 11 mg ml^{-1}. Collagen-I (BD Biosciences) was used at 1.6 mg ml^{-1}. Cells were grown for 4 days in 3D cultures before quantification of invasion. Between 200–300 acini were scored per condition for each experiment. To assess collagen-I degradation in 3D cultures, we added to the Matrigel: collagen-I mix 25 μg ml^{-1} of quenched DQ-collagen-I (Molecular Probes). After degradation, DQ-collagen-I becomes fluorescent.

To collect cells from 3D cultures, we incubated cells with Dispase (BD Biosciences) for 30–60 min at 37 °C, according to the manufacturer's instructions. Cell aggregates were then trypsinized to obtain single cells suspensions and processed either for western blotting or to prepare chromosome spreads.

The alveolar epithelial cell line 16HBE, provided by Alan Hall, was cultured in MEM (Invitrogen) supplemented with GlutaMAX, Earle's salts, 10% of FBS and 100 U ml^{-1} penicillin and streptomycin[36]. The non-transformed keratinocyte line (HaCaT), primary breast fibroblasts (1492N) and skin fibroblasts (HDFs) were provided by John Marshall. HaCats and HDFs were cultured in DMEM supplemented with 10% of FBS and 100 U ml^{-1} penicillin and streptomycin, 1492N were cultured in 50:50 Ham's F12:DMEM supplemented with 10% of FBS and 100 U ml^{-1} penicillin and streptomycin We used tetracyclin-free FBS (Hyclone) to grow the 16HBE and HaCaTs cells expressing the *PLK4* construct to inhibit *PLK4* expression in the absence of doxycycline.

Organotypic culture system. The organotypic culture system was adapted from previously described methods[37,38]. Briefly, 200 μl of culture media containing epithelial cells or epithelial cells plus fibroblasts was added on top of the polymerized Matrigel:collagen-I mixture in each well. Co-culture of epithelial cells with fibroblasts was carried out as follows: HaCaTs cells were grown with HDF fibroblasts and MCF10A cells were grown with human primary fibroblasts (1492N). 600 μl of culture media was added to the bottom of the transwell. Fibroblasts invade the Matrigel:collagen-I layer whereas most of the non-invasive epithelial cells grow on top of this layer. Medium was changed every 2 days. Cells were grown for 7 days before samples were fixed and stained.

Cells in transwells were fixed in formalin overnight at room temperature. Inserts were removed using scalpels and placed in 70% ethanol and processed for histology. Paraffin embedded inserts were sectioned and stained for haematoxylin and eosin (H&E). For both MCF10A and HaCaTs, the percentage invasion was calculated as the number of cells that entered the Matrigel:collagen-I layer relative to the total number of cells per each well.

Lentiviral and retroviral vectors. For the generation of the inducible *PLK4* overexpression system we used the lentiviral vectors pLenti-CMV-TetR-Blast (17492, Addgene) and pLenti-CMV/TO-Neo-Dest (17292, Addgene)[39]. Wild-type *PLK4* and *PLK4*$^{1-608}$ cDNAs were cloned using the Gateway system into the pLenti-CMV/TO-Neo-Dest vector. Cells were first infected with a lentivirus containing the TetR and selected with Blasticidin (10–5 μg ml^{-1}). After selection, cells were infected with the lentivirus containing the wild-type *PLK4* or *PLK4*$^{1-608}$ transgenes and selected with Geneticin (200–100 μg ml^{-1}). Note that no clones were selected at any point and that all the selected cells were pooled to make a population. All the cell lines generated were induced with 2 μg ml^{-1} of doxycycline for 48 h to induce the expression of the transgenes. pLKO.1 lentiviral vector containing Cep192 shRNA hairpin sequence was obtained from the RNAi consortium (TCR) at the Broad Institute (5′-CCCGG GAGGCATCAGTTAATACTGAT-CTCGAG-AT CAGTATTAACTGATGCCTCTTTTTTG-3′). pLKO.1 lentiviral vector expressing p53 shRNA was obtained from Addgene (19119)[40]. Lentilox Centrin1–eGFP construct was a gift from J. Loncarek. pLenti6/V5 lentiviral vector expressing H2B–GFP was cloned as previously described[2]. The Raichu-Rac1 biosensor, a gift from M. Matsuda, was subcloned into the retroviral vector pWZL-blast using the restriction sites EcoR1 and SalI.

Chemicals. Doxycycline (Sigma) was used at 2 μg ml^{-1}. The following doses of inhibitors were used: 25 μM NSC23766 (EMD Millipore), 50 μM CK-666 (Sigma), 0.1 μM Reversine (Cayman Chemical), 10 mM paclitaxel (Sigma), 4 μM of dihydrocytochalasin B (DCB; Sigma), 200 ng ml^{-1} doxorubicin (Sigma), and 5 μM and 10 μM of marimastat (BB-2516; Sigma).

2D indirect immunofluorescence microscopy. Cells plated in glass coverslips were washed in PBS and fixed with 4% of PFA for 15 min at room temperature (RT). For centriole/centrosome staining, cells were fixed with ice-cold methanol at −20 °C for 10 min. Following fixation, cells were permeabilized with PBS and 0.2% Triton X-100 for 5 min, blocked in PBST (PBS, 5%BSA, 0.1% Triton X-100) for 30 min, and then incubated with primary antibodies in PBST for 60 min. Cells were washed with PBS and incubated with species-specific fluorescent secondary antibodies (Alexa-conjugated, Molecular Probes). DNA was stained with Hoechst 33342 (1:5,000; Invitrogen) for 5 min in PBS. Coverslips were mounted with ProLong Antifade mounting medium (Molecular Probes). Antibodies used included anti α-tubulin DM1a (1:500; Sigma-Aldrich), anti-centrin2 (1:100; Santa Cruz), anti γ-tubulin GTU88 (1:500; Sigma-Aldrich) and anti β-catenin (1:500; Abcam). Phalloidin was used to stain F-actin (1:250; AlexaFluor 568; Invitrogen). Images were collected with a Yokogawa CSU-22 spinning disk confocal mounted on a Zeiss Axiovert microscope using 404, 488 and 561 nm laser light. Captured images from each experiment were analysed with Slidebook software (Intelligent Imaging Innovations). Measurement of centrosome number was performed in mitotic cells, ~100 were scored in each experiment.

3D indirect immunofluorescence microscopy. Immunofluorescence of 3D cultures was carried out as previously described[31]. Briefly, cells grown in 3D cultures were washed with 1× PBS and fixed in 5% of formalin (Sigma) in PBS for 20 min at 37 °C. After fixation cells were rinsed 3 times, 10 min each, with PBS:glycine (100 mM) and permeabilized with 0.5% Triton X-100 in PBS for 10 min. Cells were blocked with 10% of goat serum (Sigma) in IF buffer (130 mM NaCl, 7 mM Na_2HPO_4, 3.5 mM NaH_2PO_4, 7.7 mM NaN_3, 0.1% BSA, 0.2% Triton X-100, 0.05% Tween-20) for 1 h at room temperature and primary antibodies were incubated in the same solution over night at 4 °C. Cells were washed 3 times, 20 min each, with IF buffer. When required, cells were incubated with secondary antibodies for 1 h at room temperature (Alexa-conjugated, Molecular Probes). Cells were washed twice with IF buffer and once with PBS followed by incubation with Hoechst 33342 (1:2,500; Invitrogen) for 20 min. 3D cultures were then mounted in ProLong Antifade mounting medium (Molecular Probes). Antibodies used included anti α-tubulin FITC conjugated DM1a (1:100; Sigma), anti Laminin-V AlexaFluor 488 conjugated (1:100; Millipore), anti-acetylated-tubulin 611B-1 (1:100; Sigma), anti-fibronectin (1:100; BD Biosciences) and anti-Pericentrin (1:100; Abcam). Phalloidin was used to stain F-actin (1:100; AlexaFluor 568; Invitrogen). Images were collected with a Nikon A1R laser scanning confocal head mounted on a Nikon Ti-E motorized inverted microscope using 404, 488 and 561 nm laser light. Captured images from each experiment were analysed using NIS-Elements software (Nikon).

Long-term live-cell imaging. H2B–GFP expressing cells were grown on glass-bottom 12-well tissue culture dishes (MatTek) for 2D imaging or in Lab-Tek chambered coverglass for 3D imaging. Cells were imaged on a Nikon TE2000-E2 inverted microscope equipped with a cooled CCD camera (TE2000, Orca ER, Hamamatsu; Ti-E, Coolsnap HQ2, Photometrics), a precision motorized stage (Bioprecision, Ludl), and Nikon Perfect Focus. Microscope was enclosed within temperature- and CO_2-controlled environments that maintained an atmosphere of 37 °C and 3–5% humidified CO_2. GFP and bright field images were captured at multiple points every 4 min for 1–2 days with either 10× (0.3 NA) or 20× (0.5, 0.75 NA) objectives. Captured images from each experiment were analysed using NIS-Elements software.

Immunofluorescence quantification. Quantification of γ-tubulin fluorescence intensity associated with the centrosomes was performed as previously described[41]. Images were acquired with a 100× NA 1.45 Plan Apo objective. Stacks of 6 images with 0.6 μm step size were collected. Step size was calculated to have minimal pixel overlapping between steps. SUM intensity projections of the images were used to quantify fluorescence intensity using ImageJ. Computer generated 50 × 50 and 80 × 80 pixel regions were centred over each centrosomes (as shown in Extended Data Fig. 9). The intensity value measured for the 50 × 50 pixel region include both centrosome and background fluorescence. Background fluorescence was obtained by subtracting the integrated value of 50 × 50 pixel region from the larger 80 × 80 pixel region. Integrated centrosomal fluorescence intensity was calculated by subtraction of the background fluorescence intensity from total fluorescence intensity (Extended Data Fig. 9). The advantage of this approach is that it controls for the non-homogeneity in background fluorescence.

2D cell–cell adhesion analysis. MCF-10A cells expressing the Raichu-Rac (here used just to visualize the cell membrane), with and without centrosome amplification, were plated on glass-bottom tissue culture dishes (MatTek) coated with 20 μg ml^{-1} fibronectin (Sigma-Aldrich) for 20 min. Centrosome amplification was induced by 48 h PLK4 induction, as described above. To monitor the cell–cell contact dynamics, we acquired time-lapse series of images, visualizing the CFP moiety of the Raichu-Rac FRET reporter (Fig. 3a and Supplementary Videos 6 and 7) at 5 min intervals over 12.4 h. To illustrate differences in cell–cell contact dynamics, we generated kymographs (Fig. 3a). The kymograph was obtained by

sequentially mounting a 1 × 336 (pixel) region of interest from the videos, using ImageJ. Time-lapse series were collected with a Nikon inverted microscope with epi-fluorescence optics using a 40× plan Apo NA 1.4 objective. The microscope was equipped with a Nikon Perfect Focus System and a Hamamatsu ORCA ER cooled CCD camera and controlled with Nikon NIS-Element software. To reduce illumination intensity, minimizing phototoxicity and photobleaching, we used a ND8 (1/8 transmission) neutral density filter.

Western blotting. Cells were collected and ressuspended in Laemmli buffer and proteins were separated on sodium dodecyl sulphate polyacrylamide gel electrophoresis (SDS–PAGE) and transferred onto PVDF membranes. Antibodies used included anti α-tubulin DM1a (1:2,000; Sigma), anti-CEP192 (1:1,000; gift from L. Pelletier), anti-MCAK (1:1,000; Bethyl Laboratories), anti-p53 (1:1,000, Cell Signaling), anti-P-p53 (1:1,000, phospho-Ser15, Cell Signaling), E-cadherin (1:1,000, Invitrogen) and anti-Rac1 (1:1,000, BD Biosciences). Images were acquired using ImageQuant LAS4000 (GE Healthcare) and when required band intensity was quantified using ImageJ.

siRNA. siRNA was performed using Lipofectamine RNAiMax (Invitrogen) according to the manufacturer's instructions. 50 nM of *CEP192*, *MCAK* and luciferase (negative control) siRNA was used per well in a 6-well plate. After 6 h of incubation, transfected cells were washed and normal growth medium was added. Cells were analysed at 48 h after transfection. ON-Target plus SMART pools were used for *MCAK* and *CEP192* siRNA (Dharmacon). Human *KIF2C/MCAK* siRNA (L-004955-00-0005): GGCAUAAGCUCCUGUGAAU (J-004955); CCAACGCA GUAAUGGUUUA (J-004955-07); GCAAGCAACAGGUGCAAGU (J-004955-08); UGACUGAUCCUAUCGAAGA (J-004955-09). Human *CEP192* siRNA (L-032250-01-0005): UGUGAAGAAAUACGAGAUA (J-032250-09); GCUCAGC GGUAUUUGGGAA (J-032250-10); GUCUAGAACUCGAGAAUCA (J-032250-11); GGUUGAAGCAGUAGAGAGU (J-032250-12).

Single-nucleotide polymorphisms (SNP). Cells from 3D cultures were recovered after 4 days as described above (see Cell Culture section for details) and genomic DNA was prepared using DNA purification Kit (Qiagen) according to the manufacturer's instructions. Genomic DNA was used to perform analysis with genome-wide human SNP 6.0 arrays to determine copy number in MCF10A control cells, MCF10A after induction of centrosome amplification and MCF10A depleted of MCAK. SNP array data was analysed with the Nexus Copy Number Software (BioDiscovery; http://www.biodiscovery.com/software/nexus-copy-number/), using the 'Matched Paired Analysis' module. The SNP data discussed in this publication have been deposited in NCBI's Gene Expression Omnibus[42] and are accessible through GEO accession number GSE55042.

Microtubule polymerization assay. Cells plated in glass coverslips were transferred to ice cold medium and incubated 1 h on ice to depolymerize microtubules. Cells were then incubated with medium at 37 °C for 30 s to allow microtubules to polymerize and fixed immediately in ice-cold methanol for 10 min. Cells were stained for microtubules and centrioles (as described above) and microtubule number was quantified manually. Images of cells used in the analysis were acquired from 2 independent experiments.

qRT–PCR. PLK4 is highly unstable and we were not able to monitor its transient overexpression by western blotting. qRT–PCR was therefore used to analyse the extent of its expression. RNA was prepared using Qiagen RNAeasy kit according to the manufacturer's instructions. For 3D cultures, RNA was initially harvested using TRIzol, and after chloroform extraction, the upper aqueous phase was used to purify RNA using the RNAeasy kit. 300 ng of RNA was used to produce cDNA using qScript cDNA SuperMix kit (Quanta Bioscience), according to the manufacturer's instructions. For qRT–PCR, we used Power SYBR Green followed by analysis with ViiA PCR machine (Applied Biosystems).

Primers used to assess the levels of *PLK4* overexpression only amplify the exogenous wild-type *PLK4* or $PLK4^{1-608}$ sequences. The primers used for qRT–PCR were: *PLK4* forward: 5′-CAGGATTTGCCCGGGATGGCG-3′; *PLK4* reverse: 5′-AACCAGTGTGAATGGACTCAGCTCT-3′; *GAPDH* forward: 5′-TTAAAAG CAGCCCTGGTGAC-3′; *GAPDH* reverse: 5′-CTCTGCTCCTCCTGTTCGAC-3′.

Rac1–GTP pull-down. The Rac1–GTP pull-down assay was performed using the Rac1 activation kit (Cytoskeleton) according to the manufacturer's instructions. We used cells plated in one 10 cm dish per assay. Cells were resuspended in 400 µl of lysis buffer and 15 µl of CRIB/PBD beads were used to pull-down active Rac1. Extracts were incubated with the beads for 30 min. All the procedures were done at 4 °C and buffers were kept ice-cold. After washing, beads were resuspended in 15 µl of Laemmli buffer and processed for western blotting. To inhibit microtubule dynamics, cells were treated with 10 mM of paclitaxel for 1 h[26].

Generation of tetraploid cells with normal centrosome number. MCF10A cells were treated with 4 µM DCD for ~18 h, washed every 5 min over 30 min, and then FACS sorted by DNA content using Hoechst at 1:2,500 (Molecular Probes) to isolate tetraploid cells with extra centrosomes. To isolate tetraploid cells with normal centrosome number, cells with a DNA content of 8c (dividing tetraploid cells) were isolated and cultured for ~8 days before a second FACS sorting to re-isolate 8c cells. By sort 4, nearly 100% of tetraploid cells (as assessed by FACS and karyotyping) had two centrosomes[2].

Chromosome spreads. MCF10A cells were treated with 20 ng ml^{-1} colcemid (Gibco) for 4 h, trypsinized, resuspended in 75 mM of KCl and incubated for 30 min at 37 °C. Cells were then fixed with 3:1 ice-cold methanol:acetic acid, (Carnoy's solution) pelleted, and then washed three times more with methanol: acetic acid before being dropped on a pre-cleaned glass side. Cells were allowed to dry on the slide and were then stained for 3 min with Giemsa stain in 1× Gurr's buffer (Gibco). Following a wash in Gurr's buffer, coverslips were added to slides and sealed with Permount (Fisher). Images of spreads were taken with a 100× objective on a Zeiss upright microscope and chromosomes were counted manually using Adobe Photoshop. The chi squared test of independence for nominal variables was used to calculate the *P* value.

FACS. Cells were fixed with 70% ethanol at 4 °C followed by incubation with 250 µg ml^{-1} RNaseA and 10 µg ml^{-1} propidium iodide (Invitrogen) at 37 °C for 30 min. FACS analysis was performed with a FACSCalibur flow cytometer (Becton Dickinson) and data analysed with CellQuest software.

Micropatterning. Glass coverslip micropatterning was performed as previously described[43]. Coverslips were first spin-coated with adhesion promoter Ti Prime (MicroChemicals) and then with 1% polystyrene in toluene at 3,000 r.p.m. Polystyrene coated coverslips were oxidized through oxygen plasma (FEMTO; Diener Electronics) for 15 s at 30 W before incubating with 0.1 mg ml^{-1} PLL-PEG in 10 mM HEPES pH 7.4 for 30 min. After drying, coverslips were exposed to deep ultraviolet (UV) (UVO cleaner, Jelight) through a photomask (TOPPAN) for 5 min. Right after UV activation, coverslips were incubated with 20 µg ml^{-1} of fibronectin (Sigma), and 20 µg ml^{-1} of fluorescent fibrinogen conjugate (Invitrogen) solution in PBS for 30 min. Coverslips were washed 3 times with sterile PBS before plating cells. Approximately 0.5 million cells were seeded onto micropatterned chips and were washed after 30 min to remove non-attached cells, which almost always resulted in single cells per micropattern. Cells were allowed to divide for 16 h prior to fixation. For Rac1 and Arp2/3 inhibition, cells were treated with NSC27633 (25 µM) or CK-666 (50 µM), respectively, for 6 h, before fixation. For *CEP192* siRNA, cells were plated after 48 h of siRNA treatment. Images of cells used in the analysis were acquired from 2 independent experiments. The hourglass micropattern guides intracellular junction positioning as shown in Figure 3b, where most of the junction extremities are positioned in the region deprived of extracellular matrix (fibronectin). We measure the angle and size of the junctions to assess junction position and length in the different conditions.

Note that when the cells divide on these patterns, spindle orientation is completely random with respect to the geometry of the pattern. The cells also move after division before establishing normal cell–cell contacts, further altering the position of the prior division site relative to the site of eventual cell–cell contact. Thus, the final adhesion pattern is completely random relative to the initial (and random) orientation of the spindle, as previously described[20].

Rac1 FRET. For FRET experiments we used MCF10A cells stably expressing Raichu-Rac[25]. Centrosome amplification was induced with Dox for 48 h and ~10,000 cells per ml of control and extra-centrosomes cells were plated onto 20 µg ml^{-1} fibronectin (Sigma-Aldrich) coated glass-bottom dishes/plates (MatTek) for 6 h. For EGF depletion experiments cells incubated without EGF for 15 h.

FRET acquisition. Before acquisition, to increase the signal to noise, the culture medium was exchanged with 199 medium (Life Technologies) without serum and phenol red. For FRET imaging, cells were excited using a Nikon Intensilight source with a 430/24nm (for CFP) excitation filter with a dual band pass (ECFP/EYFP #89002) dichroic mirror and 470/24 (for CFP) and 535/40 (for FRET and YFP) emission filters from Chroma (Bellows Falls, VT). To reduce illumination intensity and thus minimize phototoxicity and photobleaching, we used a ND8 (1/8 transmission) neutral density filter. All images were collected with Nikon Ti inverted microscope with epi-fluorescence optics equipped with a ×40 plan Apo NA 1.4 object lens, perfect focus system and a Hamamatsu ORCA ER cooled CCD camera controlled with Nikon NIS-Element software.

The following steps were taken to calculate the average magnitude and spatial variation of the camera's noise for image correction of the acquired channels (CFP, FRET): (1) a sequence of 10 dark-current images were taken with 600 ms exposure time and 4 × 4 binning as the experimental images, but with no light incident on the CCD; (2) a sequence of 10 shade/illumination correction images for each channel (CFP and FRET) were taken with 600 ms exposure time and 4 × 4 binning as the experimental images, but acquired on a blank area without any objects. The average dark-current and shade images were calculated by averaging the acquired 10 images by using ImageJ. Single channel images (CFP, FRET) for each field view visualizing maximum four non-contacting cells were collected by using an exposure time of 600 ms, 4 × 4 binning, a ND8 (1/8 transmission) neutral density filter and illumination light shuttered between acquisitions.

FRET analysis. The Biosensor software from Dr. Gaudenz Danuser's laboratory (http://lccb.hms.harvard.edu/index.html) along with a series of automated ImageJ macros were used to calculate the FRET ratio images. The acquired CFP and FRET images were corrected for the average dark-current, shading and background subtracted by using Biosensor or ImageJ. Then, single-cell images from each channel (CFP and FRET) were segmented by using the ImageJ minimum and mean threshold method, and the relative regions of interest (ROIs) were recorded. Single cell mask images having background and foreground (cell image) pixel values equal to zero and one, respectively, were calculated from each cell ROI by ImageJ. To set the image background pixels to zero, CFP and FRET images were multiplied by the corresponding calculated image masks. Finally the FRET ratio images were obtained by dividing the processed FRET image by the CFP image.

Single cell average FRET/CFP values representing the Rac1 activation levels were obtained by calculating the mean pixel value of the FRET ratio images for each ROI (single cell). FRET/CFP values were collected from 2 independent experiments. An unpaired two-tailed Student's *t*-test statistical analysis was used to obtain level of significance between different experiment conditions.

31. Debnath, J. *et al.* The role of apoptosis in creating and maintaining luminal space within normal and oncogene-expressing mammary acini. *Cell* **111,** 29–40 (2002).
32. Schafer, Z. T. *et al.* Antioxidant and oncogene rescue of metabolic defects caused by loss of matrix attachment. *Nature* **461,** 109–113 (2009).
33. Gunawardane, R. N. *et al.* Novel role for PDEF in epithelial cell migration and invasion. *Cancer Res.* **65,** 11572–11580 (2005).
34. Xiang, B. & Muthuswamy, S. K. Using three-dimensional acinar structures for molecular and cell biological assays. *Methods Enzymol.* **406,** 692–701 (2006).
35. Paszek, M. J. & Weaver, V. M. The tension mounts: mechanics meets morphogenesis and malignancy. *J. Mammary Gland Biol. Neoplasia* **9,** 325–342 (2004).
36. Wallace S. W., Magalhaes A. & Hall A. The Rho target PRK2 regulates apical junction formation in human bronchial epithelial cells. *Mol Cell Biol.* **31,** 81–91 (2011).
37. Gaggioli, C. *et al.* Fibroblast-led collective invasion of carcinoma cells with differing roles for RhoGTPases in leading and following cells. *Nature Cell Biol.* **9,** 1392–1400 (2007).
38. Nyström, M. L. *et al.* Development of a quantitative method to analyse tumour cell invasion in organotypic culture. *J. Pathol.* **205,** 468–475 (2005).
39. Campeau, E. *et al.* A versatile viral system for expression and depletion of proteins in mammalian cells. *PLoS ONE* **4,** e6529 (2009).
40. Godar, S. *et al.* Growth-inhibitory and tumor-suppressive functions of p53 depend on its repression of CD44 expression. *Cell* **134,** 62–73 (2008).
41. Hoffman, D. B., Pearson, C. G., Yen, T. J., Howell, B. J. & Salmon, E. D. Microtubule-dependent changes in assembly of microtubule motor proteins and mitotic spindle checkpoint proteins at PtK1 kinetochores. *Mol. Biol. Cell* **12,** 1995–2009 (2001).
42. Edgar, R., Domrachev, M. & Lash, A. E. Gene expression and hybridization array data repository. *Nucleic Acids Res.* **30,** 207–210 (2002).
43. Azioune, A., Carpi, N., Tseng, Q., Thery, M. & Piel, M. Protein micropatterns: a direct printing protocol using deep UVs. *Methods Cell Biol.* **97,** 133–146 (2010).
44. Zhan, L., Xiang, B. & Muthuswamy, S. K. Controlled activation of ErbB1/ErbB2 heterodimers promote invasion of three-dimensional organized epithelia in an ErbB1-dependent manner: implications for progression of ErbB2-overexpressing tumors. *Cancer Res.* **66,** 5201–5208 (2006).
45. Yuan, K. *et al.* Primary cilia are decreased in breast cancer: analysis of a collection of human breast cancer cell lines and tissues. *J. Histochem. Cytochem.* **58,** 857–870 (2010).
46. Sonnen, K. F., Gabryjonczyk, A. M., Anselm, E., Stierhof, Y. D. & Nigg, E. A. Human Cep192 and Cep152 cooperate in Plk4 recruitment and centriole duplication. *J. Cell Sci.* **126,** 3223–3233 (2013).

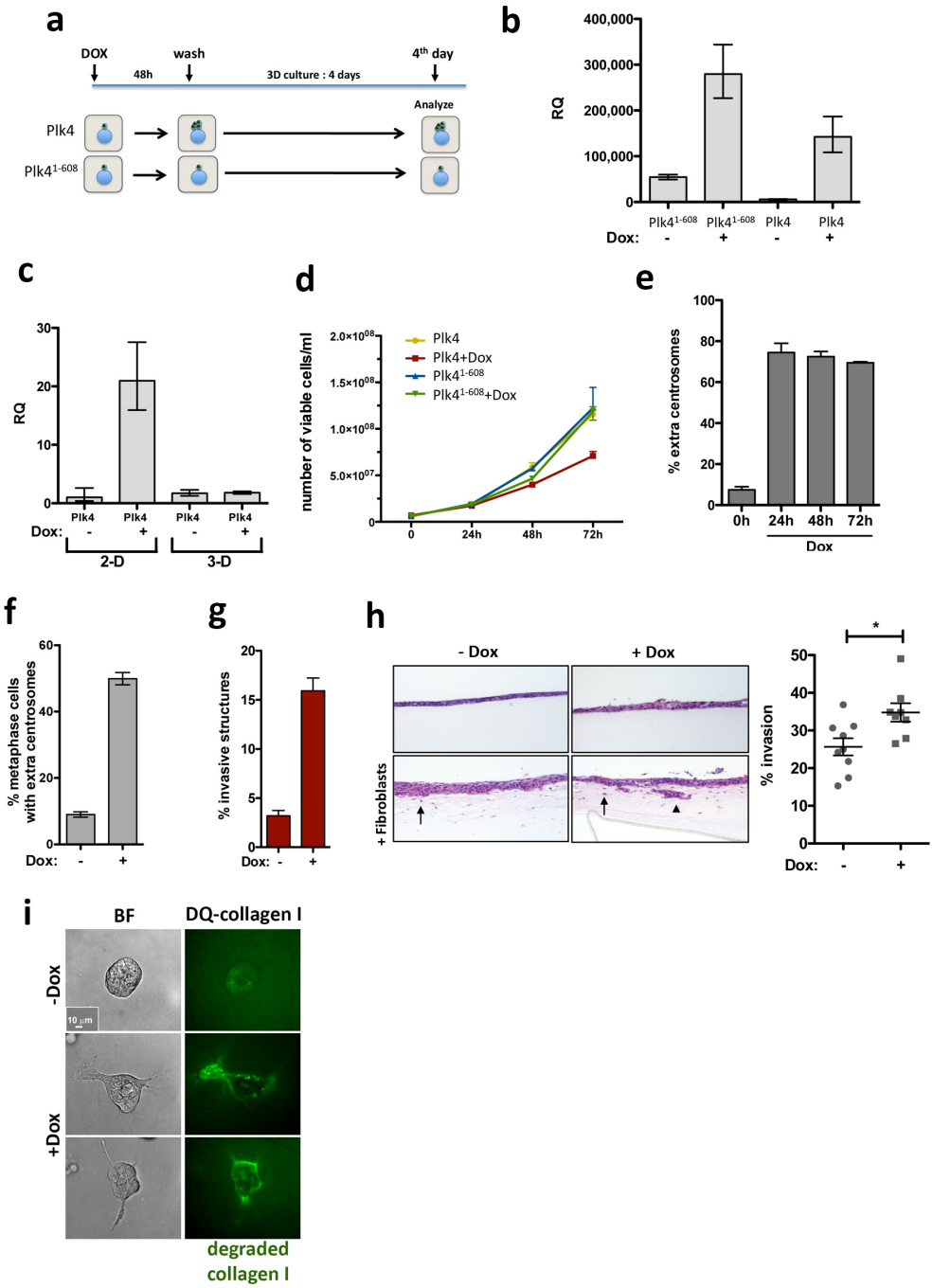

Extended Data Figure 1 | Characterization of cells after transient overexpression of PLK4 or PLK4$^{1-608}$. **a**, Scheme of the experimental design to induce centrosome amplification. Transient overexpression of PLK4 and PLK4$^{1-608}$ was achieved by addition of Dox for 48 h (2D culture) followed by removal of Dox and growth in 3D culture for 4 days in the absence of Dox. **b**, qRT–PCR showing the levels of induction of the *PLK4*$^{1-608}$ and wild-type *PLK4* transgenes in cells after 48 h of Dox. Error bars represent mean ± s.e. from 3 independent experiments. **c**, qRT–PCR showing the expression of *PLK4* after 48 h of Dox (2D) and after 4 days in 3D cultures (3D). Note that *PLK4* overexpression after 4 days in 3D cultures is down to control levels after Dox removal. Error bars represent mean ± s.e. from 3 independent experiments. **d**, Proliferation curve of cells after induction of PLK4 and PLK4$^{1-608}$ over 72 h. Centrosome amplification decreases cell proliferation. Error bars represent mean ± s.e. from 3 independent experiments. **e**, The fraction of cells with centrosome amplification at the indicated time points after PLK4 induction. Note that, because centrosome number is quantified in mitotic cells, this result demonstrates that cells with extra centrosomes can enter mitosis even after 72 h of Dox treatment. Error bars represent mean ± s.e. from 3 independent experiments. **f**, Fraction of cells with centrosome amplification in an independently generated MCF10A.PLK4 cell line. Error bars represent mean ± s.e. from 3 independent experiments. **g**, Corresponding fraction of invasive acini in 3D cultures. Error bars represent mean ± s.e. from 3 independent experiments. **h**, Centrosome amplification (PLK4 overexpression, +Dox) in non-transformed keratinocytes (HaCaTs) promotes invasion in the organotypic culture model. Images show H&E staining of sections of HaCaTs cells. Black arrows indicate cells invading the matrix. Note that the invasion of groups of cells was only detected in the +Dox condition (black arrowhead). Scale bar, 100 µm. Graph shows quantification of the percentage of cells that invade. Each dot in the graphic represents the percentage of invasion in each individual well per experiment analysed. The *P* value was derived from unpaired two-tailed Student's *t*-test *$P < 0.05$). **i**, Collagen-I degradation induced by centrosome amplification (green). Collagen degradation is visualized by DQ-Col-I, which becomes fluorescent after degradation because of fluorophore dequenching. Scale bar, 10 µm. See Methods for more details.

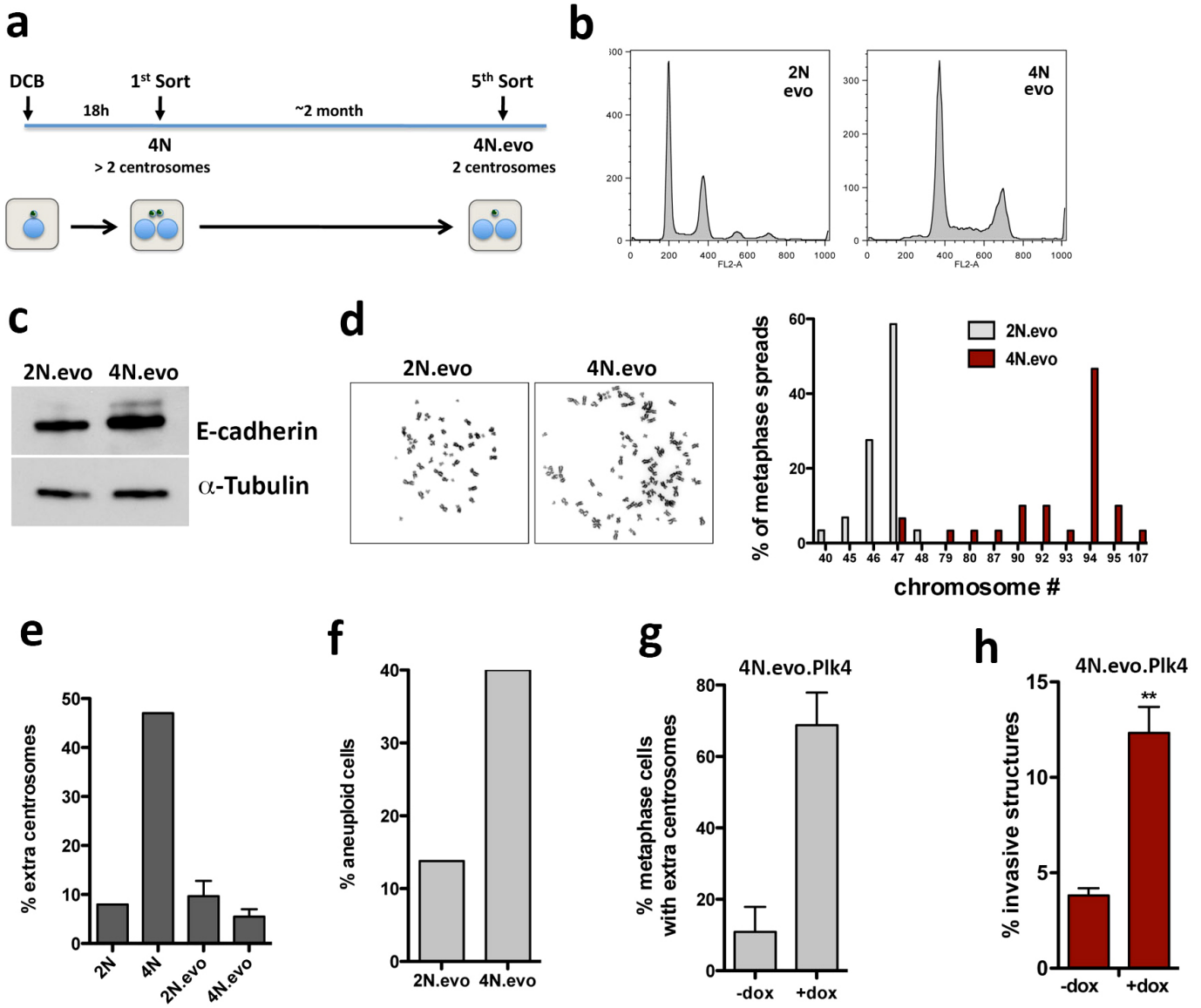

Extended Data Figure 2 | Characterization of evolved diploid and tetraploid cells. **a**, Scheme of the experimental design to obtain fresh MCF10A tetraploid cells with extra centrosomes (4N) and 'evolved' tetraploid cells that lost the extra centrosomes (4N.evo), as previously described[2]. **b**, FACS profiles of 'evolved' diploid (2N.evo) and tetraploid cells (4N.evo). **c**, Western blotting to detect E-cadherin in the 'evolved' cells indicates that 4N.evo maintain epithelial characteristics. **d**, Representative images of metaphase chromosome spreads of 2N.evo and 4N.evo and quantification of chromosome number by karyotyping (~30 chromosome spreads were quantified in each condition). 4N.evo cells have a near-tetraploid karyotype. **e**, Centrosome amplification in diploid cells (2N or 2N.evo) newly generated tetraploid cells (4N) and evolved tetraploid cells (4N.evo). **f**, Quantification of the percentage of aneuploid cells in the 'evolved' cells. The 4N.evo cells are aneuploidy despite their near-tetraploid genomes (~30 chromosome spreads were quantified in each condition). **g**, Quantification of centrosome amplification of 4N.evo cells overexpressing PLK4. Error bars represent mean ± s.e. from 3 independent experiments. **h**, Quantification of the invasive acini in 4N.evo cells after PLK4 overexpression. This experiment serves as a control to demonstrate that the 4N.evo cells retain their ability to amplify centrosomes and, after centrosome amplification, retain the capacity to form invasive acini. Error bars represent mean ± s.e. from 3 independent experiments. *P* value derived from unpaired two-tailed Student's *t*-test (**$P < 0.005$).

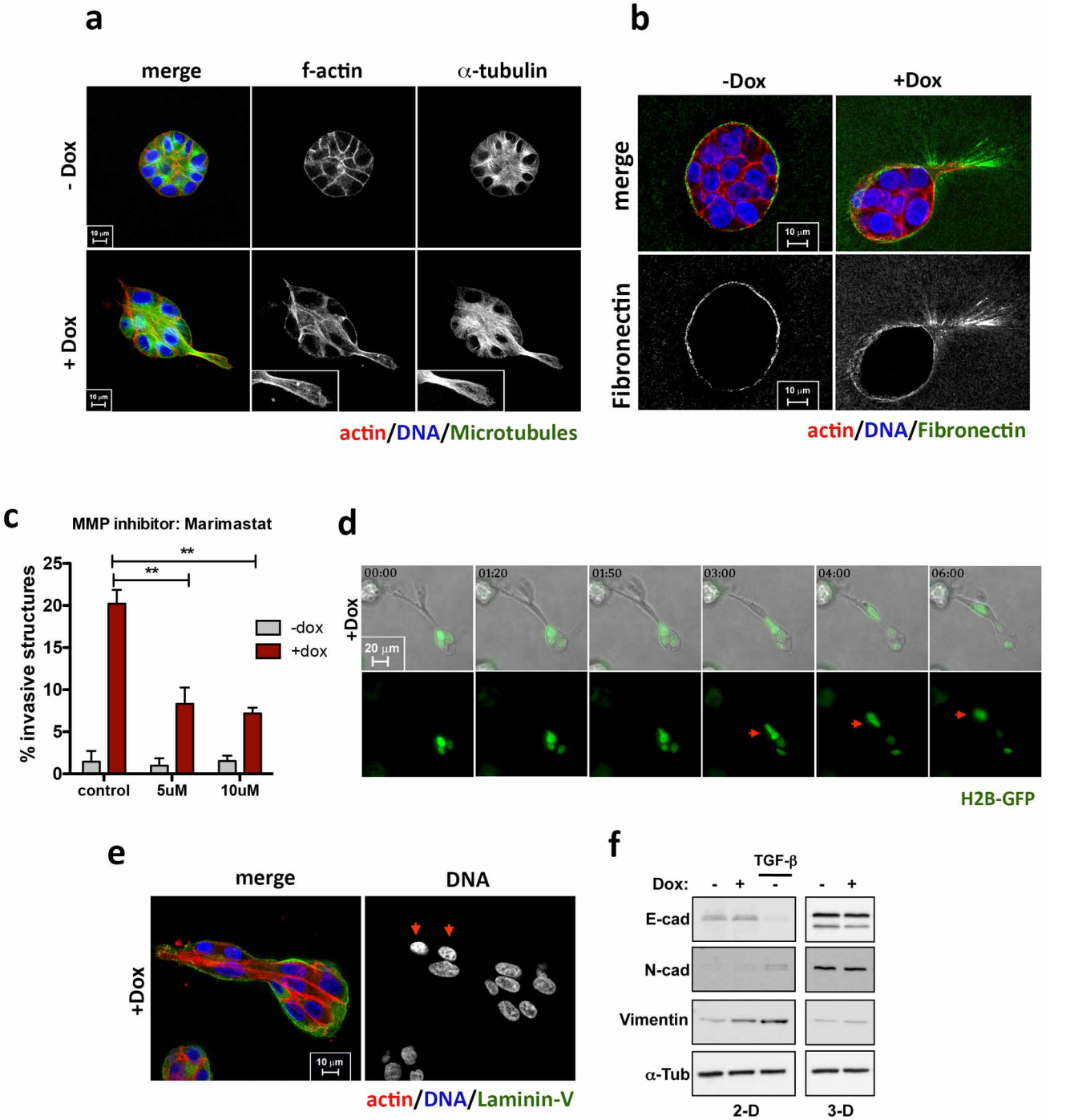

Extended Data Figure 3 | Characterization of invasive structures in cells with extra centrosomes. **a**, F-actin and microtubules in invasive protrusions: F-actin (red), microtubules (α-tubulin, green) and DNA (blue). Insets show higher magnification images of the invasive protrusions. Scale bar, 10 μm. **b**, Fibronectin at invasive protrusions: cells were stained for F-actin (red), fibronectin (green) and DNA (blue). Scale bar, 10 μm. **c**, Fraction of invasive acini in 3D cultures after treatment with the broad spectrum matrix metalloprotease (MMP) inhibitor, marimastat (BB-2516). Error bars represent mean ± s.e. from 3 independent experiments. *P* value derived from unpaired two-tailed Student's *t*-test (**$P < 0.005$). **d**, Images from videos of PLK4 overexpression cells (Supplementary Video 3), showing nuclei (labelled with H2B–GFP) migrating into an invasive protrusion (red arrows). Time scale shown as h:min. Scale bar, 20 μm. **e**, Multiple cells can migrate into invasive protrusions. Cells were stained for F-actin (red), laminin-V (green) and DNA (blue). Red arrows mark cells that migrated into the invasive protrusion. Scale bar, 10 μm. **f**, Western blot showing levels of E-cadherin, N-cadherin and vimentin in cells with (+Dox) and without (−Dox) extra centrosomes before and after 4 days in 3D culture. The western blots show that, unlike cells treated with TGF-β, cells with extra centrosomes do not acquire a canonical epithelial–mesenchymal transition (EMT) phenotype. We do note a small increase in the levels of vimentin in cells with extra centrosomes before plating in 3D cultures. Dox treatment was given for 48 h before 3D cultures in all experiments.

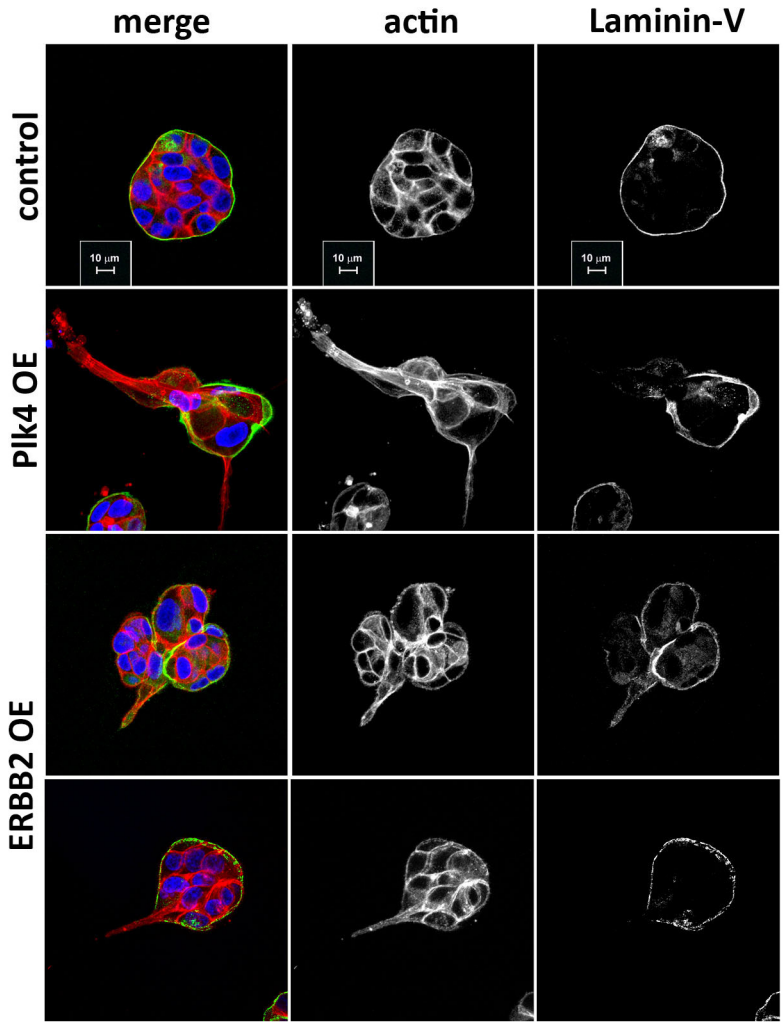

Extended Data Figure 4 | Similarity between cells with centrosome amplification and cells with oncogene-induced invasion. Cells were stained for F-actin (red), laminin-V (green) and DNA (blue). Similarity between the invasive protrusions of cells with extra centrosomes and the ones generated by cells overexpressing ERBB2, as previously reported[4,44]. In both conditions, invasive protrusions are characterized by the formation of actin-rich protrusions that are accompanied by degradation of the basement membrane. Scale bar, 10 μm.

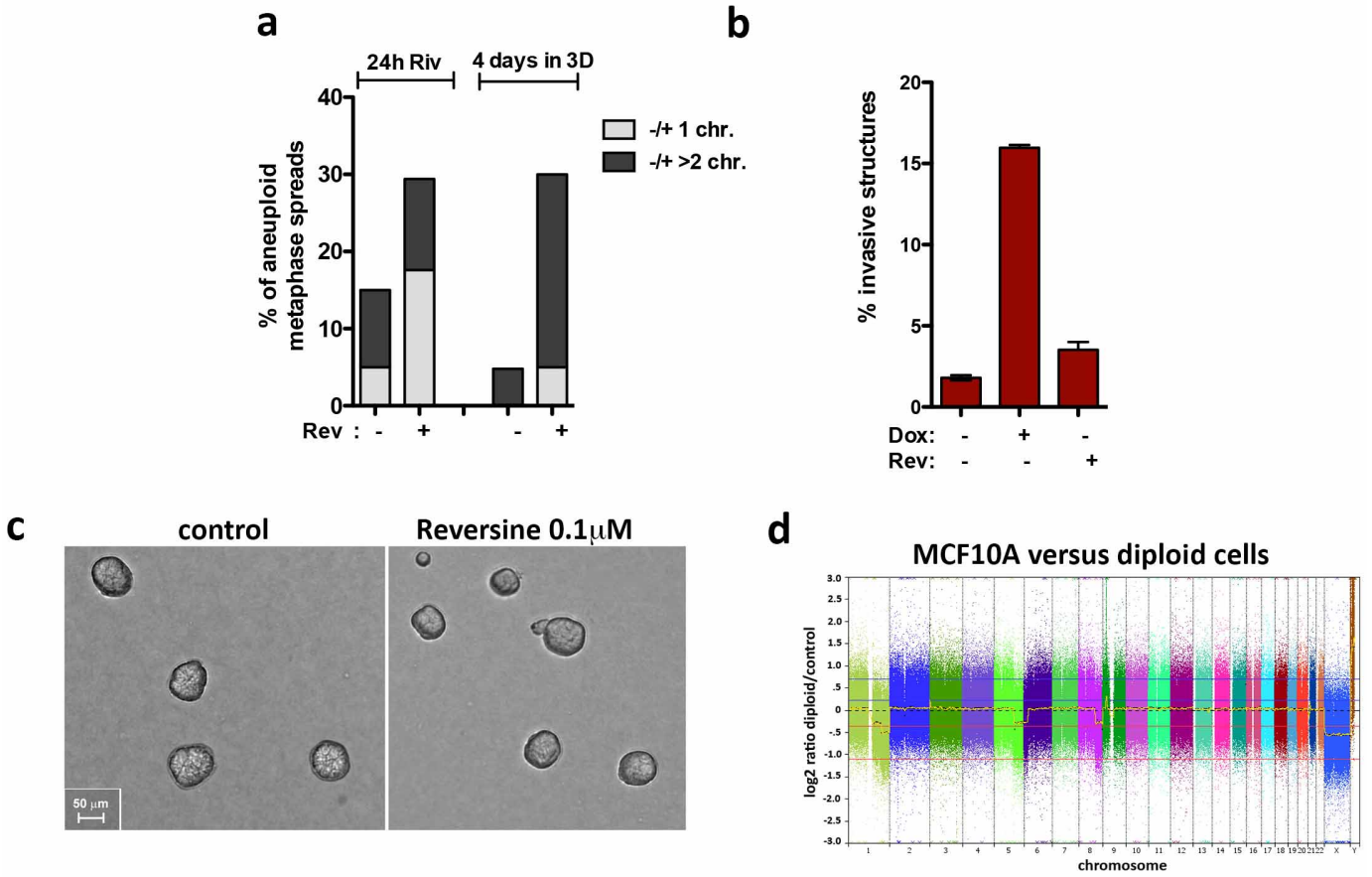

Extended Data Figure 5 | Reversine treatment induces aneuploidy but not invasive acini in MCF10A cells. **a**, Quantification of the chromosome number in cells after treatment with with 0.1 μM of reversine (Rev) for 24 h before and after 4 days in 3D cultures (~20 chromosome spreads were quantified in each condition). The concentration of reversine used does not induce cytokinesis failure and therefore would not induce centrosome amplification by inducing tetraploidy. **b**, Fraction of invasive acini after MCF10A cells are treated with reversine. Increased aneuploidy from reversine treatment does not induce invasion. Error bars represent mean ± s.e. from 3 independent experiments. **c**, Images of 3D cultures after treatment with reversine showing normal appearing acini. Scale bar, 50 μm. **d**, SNP analysis of MCF10A cells (without centrosome amplification) compared with Human Reference Genomic DNA 103 from Affymetrix. Previously reported genomic alterations in MCF10A cells can be detected in our analysis, namely: +5q, +6p and +8q.

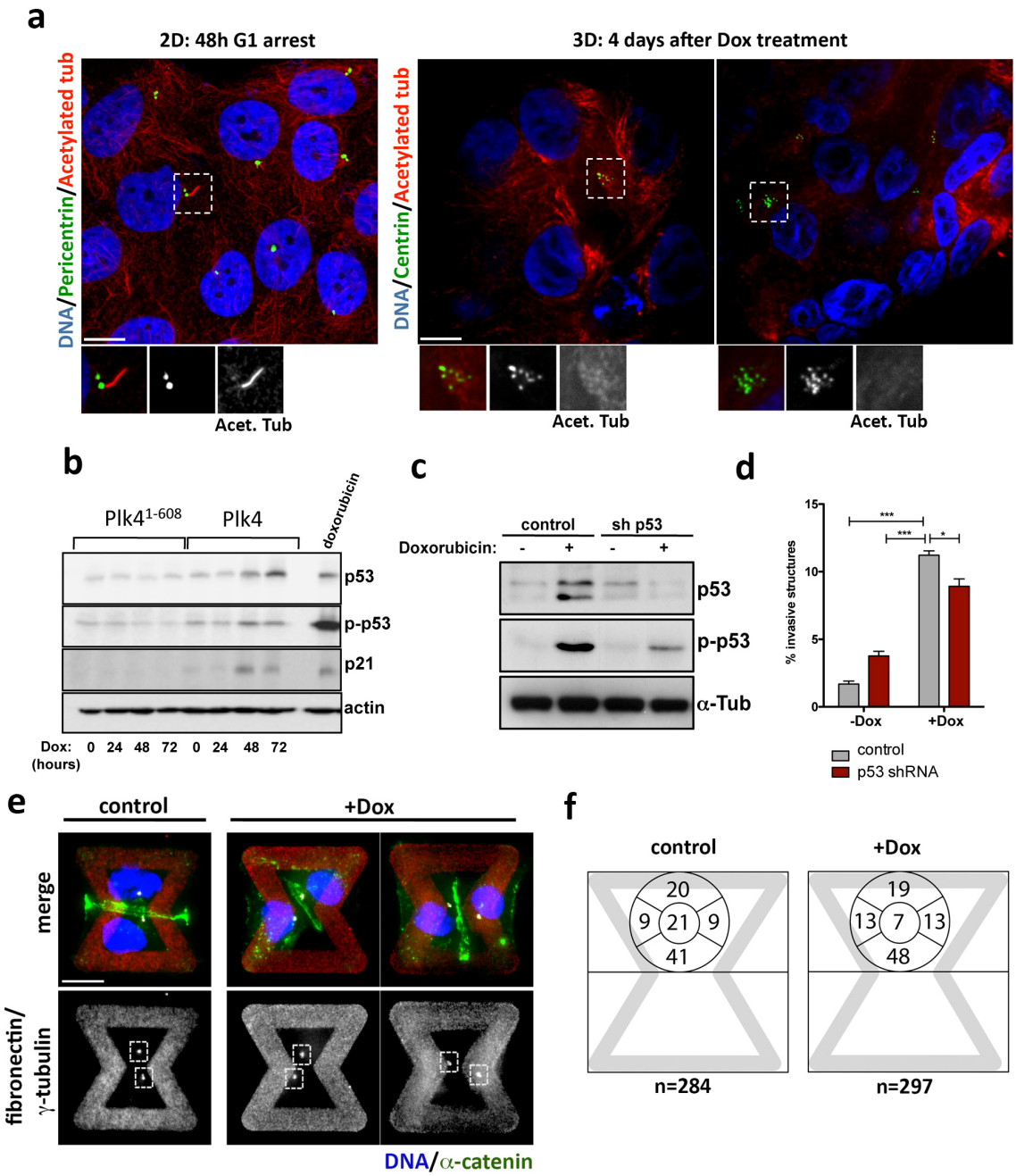

Extended Data Figure 6 | Invasive protrusions from 3D cultures of MCF10A cells with extra centrosomes are not an indirect consequence of altered cilia signalling, increased p53 expression or defects in centrosome polarization. **a**, Cells in 2D were stained for pericentrin (green, inset), acetylated tubulin (red, inset) and DNA (blue). Cells were arrested for 48 h in G1 to induce primary cilium formation. Note that even in this case most of the cells do not form cilia. This is expected because MCF10A cells have limited proficiency for cilia formation, with only ~7% of the cells assembling cilia even after 7 days of serum starvation[45]. Cells in 3D were stained for centrin (GFP, green inset), acetylated tubulin (red, inset) and DNA (blue). Cells do not form cilia after 4 days in 3D cultures. This is expected because, unlike MDCK cells, MCF10A cells do not have a discernable apical polarity and lumen after 4 days in 3D cultures and thus are unlikely to form primary cilium at this time. **b**, As expected[17], centrosome amplification in MCF10A cells induces modest p53 activation. Note that this degree of p53 activation has a minor effect on the proliferation of MCF10A cells (Extended Data Figure 1d). Expression of PLK4 and PLK4$^{1-608}$ was induced by Dox for the indicated times: 0, 24, 48 and 72 h. **c**, Western blotting showing the levels of induction of p53 after doxorubicin treatment (200 ng ml^{-1} for 4 h) in control and p53-depleted cells, demonstrating that the p53 shRNA efficiently prevents p53 activation. **d**, Fraction of acini with invasive protrusions from cells with (+Dox) or without (−Dox) centrosome amplification after depletion of p53. The ability of cells to form invasive acini is not significantly affected by their p53 status. Error bars represent mean ± s.e. from 3 independent experiments. *P* values were derived from unpaired two-tailed Student's *t*-test (***$P < 0.0005$; *$P < 0.05$). **e**, Cells were stained for α-catenin (green), γ-tubulin (red), DNA (blue) and the fibronectin micro-pattern visualized in red. Dashed boxes outline the centrosomes. Note that after PLK4 overexpression, extra centrosomes (clustered in interphase) are correctly positioned towards the cell–cell junction (similar to the control) even when the junction is defective, suggesting that centrosome amplification is not impairing the polarity axis of these cells. **f**, Centrosome positioning is not altered in cells with (+Dox) and without (control) extra centrosomes. Left image shows representative images of cells showing centrosomes (γ-tubulin) in relation to adherens junctions (α-catenin). Right image shows scheme with quantification of the fraction of centrosomes at the indicated positions on the micropatterns (see Fig. 3a). Note that the position of centrosomes in cells with centrosome amplification does not differ from that in control cells. Cells were plated on the patterns 48 h after induction of centrosome amplification with PLK4.

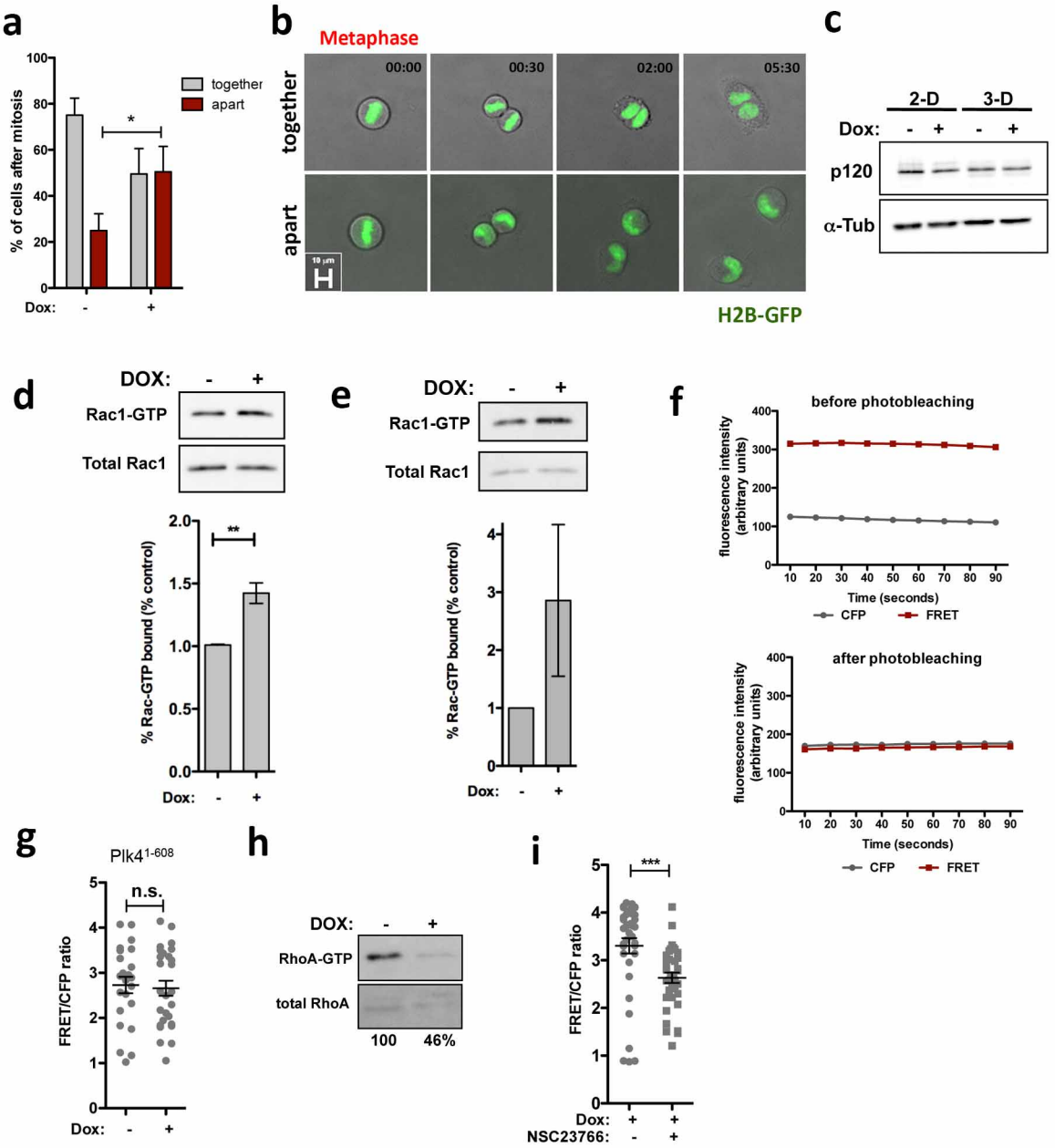

Extended Data Figure 7 | Centrosome amplification induces cell scattering and Rac activation. **a**, Quantification of number of cells with (+Dox) or without (−Dox) extra centrosomes that remain as pairs within 10 h time after mitosis. For –Dox $n = 180$; +Dox $n = 98$. Cell scattering occurred in most of the cases within the first 2 h after mitosis. Cells were imaged on 2D substratum. Similar results were obtained with fixed cells. Error bars represent mean ± s.e. from 3 independent experiments. **b**, Still images from videos showing examples of cells that stay together (−Dox) or move apart (+Dox). Time scale shown as h:min. **c**, Western blot showing levels of p120 catenin in cells with (+Dox) and without (−Dox) extra centrosomes in 2D and 3D cultures. **d**, Western blot from a pull-down experiment to detect GTP-bound Rac1 in HaCaTs cells. Graph shows quantification of active Rac1 from pull-down experiments. Error bars represent mean ± s.e. from 3 independent experiments. **e**, Western blot from a pull-down experiment to detect GTP-bound Rac1 in 16HBE cells. Graph shows quantification of active Rac1 from pull-down experiments. Error bars represent mean ± s.e. from 2 independent experiments. **f**, FRET control demonstrating increased CFP emission after photobleaching of the YFP fluorophore at an excitation wavelength of 510 nm for 10 min in MCF-10A single cells expressing Raichu-Rac. **g**, Levels of active Rac1 measured by FRET in cells overexpression $PLK4^{1-608}$. For –Dox, $n = 25$; +Dox, $n = 22$. Error bars represent mean ± s.e. **h**, Western blot from a pull-down experiment to detect GTP-bound RhoA in MCF10A cells showing decrease RhoA activity in cells with extra centrosomes. **i**, Levels of active Rac1 measured by FRET in cells with extra centrosomes treated with the Rac1 inhibitor NSC23766, demonstrating that NSC23766 inhibits Rac1 activation in cells with extra centrosomes. For −NSC23766, $n = 37$; +NSC23766, $n = 36$. Error bars represent mean ± s.e. All the P values were derived from unpaired two-tailed Student's t-test (***$P < 0.0005$; **$P < 0.005$; *$P < 0.05$). Scale bar, 10 µm.

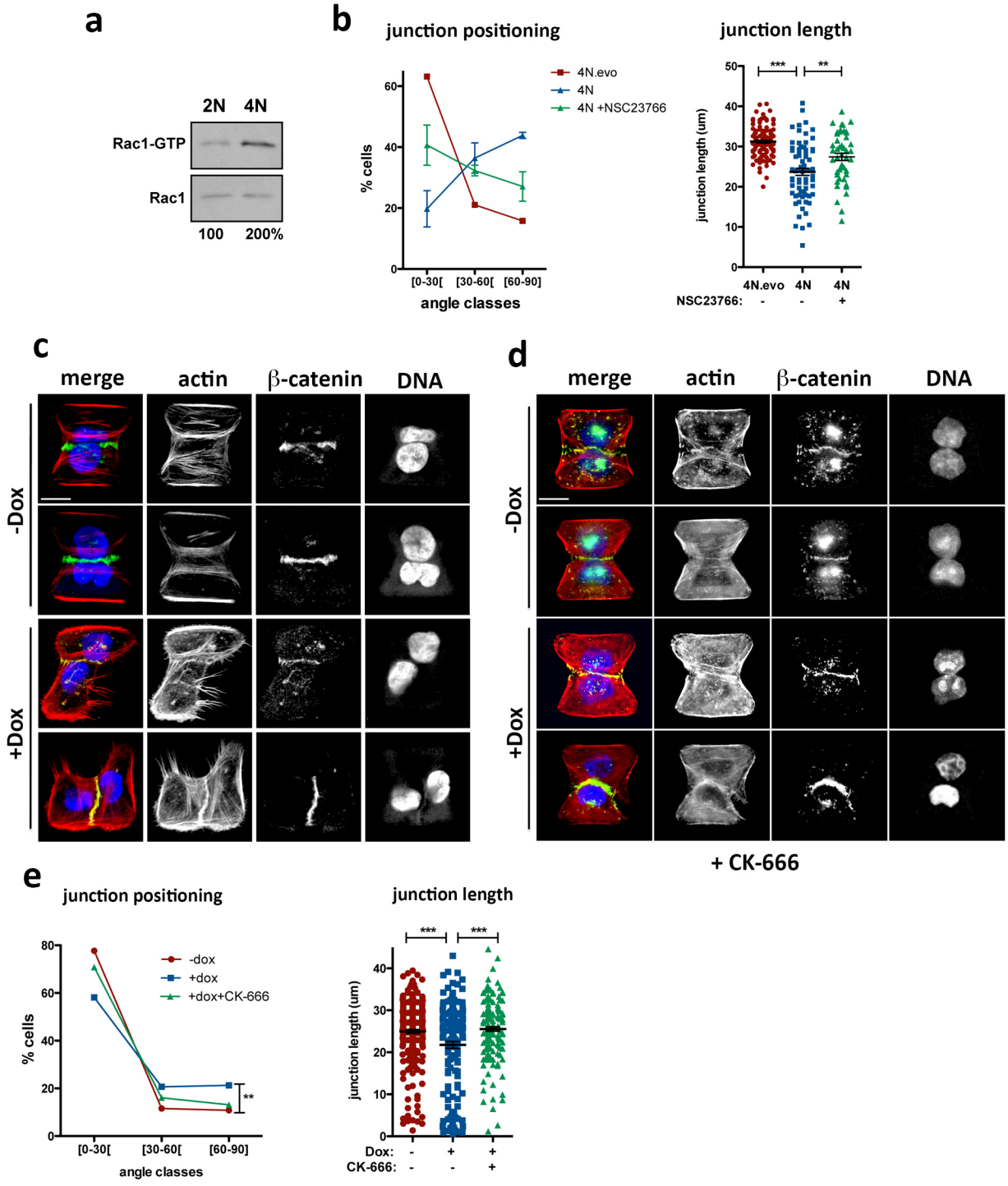

Extended Data Figure 8 | Cell–cell adhesion defects caused by centrosome amplification can be observed in tetraploid cells and can be suppressed by Arp2/3 complex inhibition. **a**, Western blot from a pull-down experiment to detect GTP-bound Rac1 in tetraploid MCF10A cells. **b**, Distribution of the cell–cell junction angles (left) and size (right) in the indicated tetraploid cells, with or without treatment with the Rac1 inhibitor, NSC23766. Note that tetraploid cells with extra centrosomes (4N) have a striking defect in junction positioning by comparison with tetraploid cells with normal centrosome number (4N.evo). This severe phenotype is only partially rescued by Rac1 inhibition. For 4N.evo, $n = 106$; 4N, $n = 70$; NCS23766, $n = 47$. Error bars represent mean ± s.e. **c**, Examples of cell doublets with (+Dox) or without (−Dox) centrosome amplification on the fibronectin micro-patterns. Cells were stained for F-actin (red), β-catenin (green), DNA (blue). **d**, Examples of cell doublets with (+Dox) or without (−Dox) centrosome amplification on the fibronectin micro-patterns treated with the Arp2/3 inhibitor (CK-666). Cells were stained for F-actin (red), β-catenin (green), DNA (blue). **e**, Distribution of the junction angle and quantification of the junction size in cells with extra centrosomes treated with 50 μM of Arp2/3 inhibitor (CK-666) for 6 h. Cells were analysed 48 h after Dox treatment. For –Dox, $n = 251$; +Dox, $n = 160$; CK666, $n = 168$. Error bars represent mean ± s.e. All the P values were derived from unpaired Student's two-tailed t-test (***$P < 0.0005$; **$P = 0.005$). Scale bar, 10 μm.

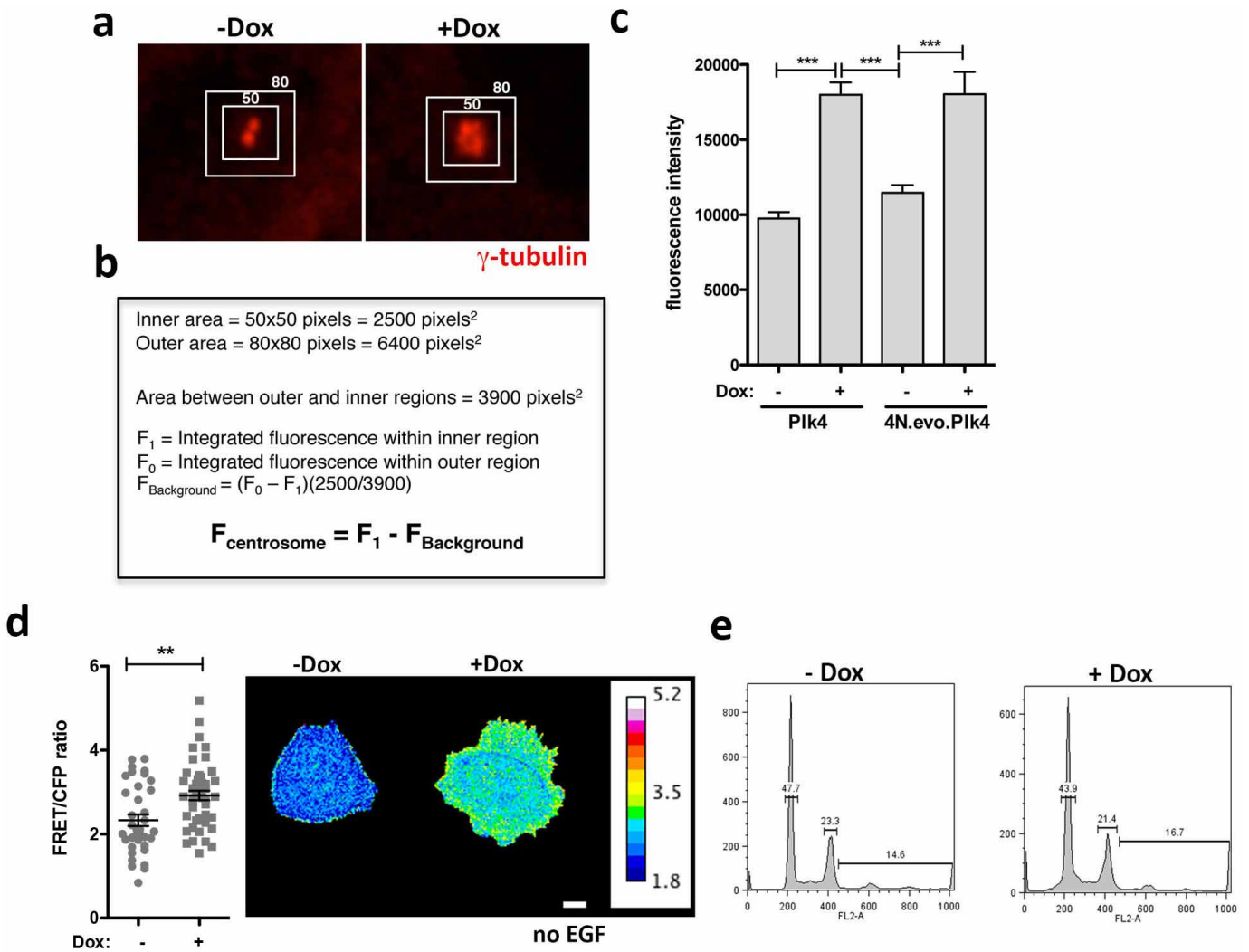

Extended Data Figure 9 | Quantification of centrosomal γ-tubulin in cells with extra centrosomes and levels of active Rac1 in the absence of EGF. **a**, Images of centrosomes from interphase MCF10A cells stained for γ-tubulin. Boxes represent the region for measurement of centrosomal γ-tubulin signal (inside) and background (area between inner and outer boxes). **b**, Method used to determine the integrated fluorescent intensity of centrosomal γ-tubulin, as previously described[41]. **c**, Measurement of γ-tubulin intensity at the centrosomes showing that in interphase, increased centriole number is sufficient to increase γ-tubulin levels at the centrosomes whereas increased ploidy *per se* does not (4Nevo). For PLK4 –Dox, $n = 60$; PLK4 +Dox, $n = 49$; 4N.evo. PLK4 –Dox, $n = 34$; 4N.evo. PLK4 +Dox, $n = 35$. Error bars represent mean ± s.e. **d**, Increased Rac1 activity in cells with extra centrosomes can be detected in arrested cells deprived of EGF. Quantification of Rac1 activity by FRET in single cells with (+Dox) and without (−Dox) extra centrosomes in the absence of EGF, and examples of FRET images of cells in the absence of EGF. For PLK4 −Dox, $n = 36$; PLK4 +Dox, $n = 47$. Error bars represent mean ± s.e. Scale bar, 10 μm. **e**, FACS profiles of control (−Dox) and cells with extra centrosomes (+Dox) after 48 h of Dox treatment showing that there is not major difference in the cell cycle profiles of these cells. Note that at this time point centrosome amplification does not produce a striking defect in cell proliferation (Extended Data Fig. 1d). All the *P* values were derived from unpaired two-tailed Student's *t*-test (**$P < 0.005$; ***$P < 0.0005$).

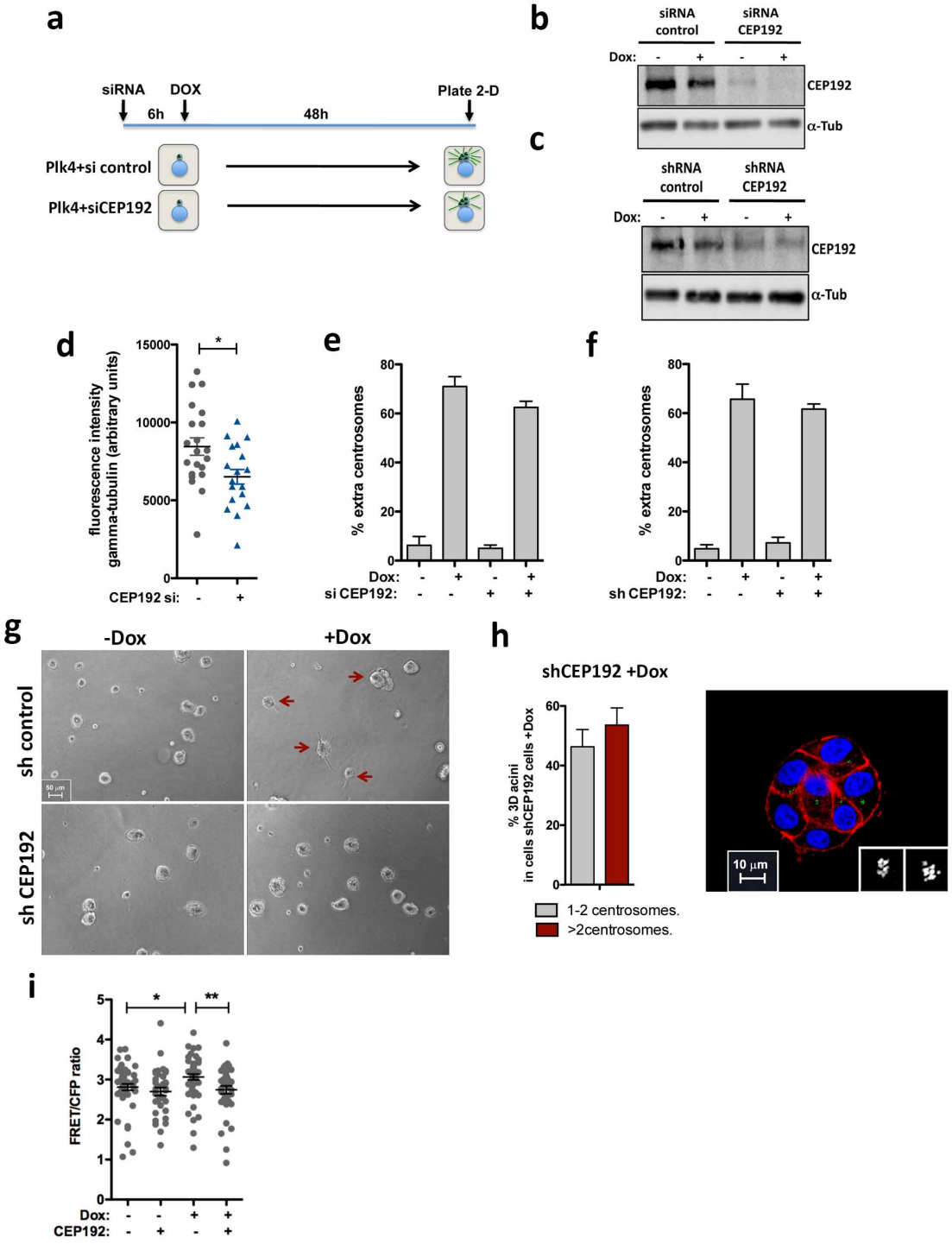

Extended Data Figure 10 | Depletion of CEP192 suppresses the invasive properties of cells with centrosome amplification. **a**, Scheme of the experimental design to induce centrosome amplification in cells depleted of CEP192 by siRNA. Transient overexpression of PLK4 is induced 6 h after siRNA to allow efficient centrosome overduplication. As expected, after depletion of CEP192 for 48 h, cells are partially compromised in their ability to overduplicate centrosomes after PLK4 overexpression[46]. **b**, Western blot showing efficient depletion of CEP192 after 48 h treatment of cells with *CEP192* siRNA. **c**, Western blot showing partial depletion of CEP192 by shRNA. **d**, Quantification of centrosomal γ-tubulin after depletion of CEP192 by siRNA for 48 h. Similar results were observed with CEP192 esiRNA (not shown). It is notable that at least for a three-day period, cells remain viable after CEP192 knockdown. For control siRNA, $n = 22$; *CEP192* siRNA, $n = 20$. Error bars represent mean ± s.e. Quantification of centrosome amplification after depletion of *CEP192* by siRNA (**e**) or shRNA (**f**). Error bars represent mean ± s.e. from 3 independent experiments. **g**, Bright field images of acini after 4 days in 3D culture, demonstrating that partial CEP192 depletion by shRNA does not significantly impair cell growth or the formation of acini. Red arrows indicate the invasive acini. **h**, Quantification of PLK4-mediated centrosome amplification in cells depleted of CEP192 after 4 days in 3D cultures showing that these cells still carry extra centrosomes. Error bars represent mean ± s.e. from 3 independent experiments. Images show normal acini displaying centrosome amplification after partial knockdown of CEP192. Cells were stained for F-actin (red), centrioles (centrin1-GFP, green) and DNA (blue). Scale bar, 10 µm. **i**, Levels of active Rac1 measured by FRET after CEP192 depletion. For ctr.siRNA –Doc, $n = 51$; ctr.siRNA +Dox, $n = 35$; CEP.siRNA –Dox, $n = 53$; CEP.siRNA +Dox, $n = 37$. Error bars represent mean ± s.e. All the *P* values were derived from unpaired two-tailed Student's *t*-test (*$P < 0.05$; **$P < 0.005$).

1.3 Short Q&A

Q. Can the invasive phenotype observed in PLK4 overexpressed cells possessing amplified centrosome be also the effect of kinase activity of PLK4?

A: Polo-like-kinase (PLK4) has catalytic kinase domain at its N terminal and non-catalytic domain at the C-terminal, which is responsible for localization of PLK4 to the centrosome. In this study truncated form of PLK4 (1-608) was used which had kinase domain but lacked the centrosome-targeting sequence. As centrosome duplication requires PLK4 at the centrosome, the truncated for of PLK4 did not induce centrosome amplification. Hence the control cells without centrosome amplification possess PLK4 kinase activity and do not show invasive protrusions while only the cells with full length PLK4 overexpression have amplified centrosomes and show invasiveness.

Q. Do cells with extra-centrosome involve epithelial-to-mesenchymal pathway for cell scattering?

A: Cells with extra-centrosomes did not show classical EMT markers such as E-cadherin reduction, increase of N-cadherin and vimentin. As E-cadherin levels in these cells are high which suggests that CCJ weakening did not occur because of lack of cell adhesion molecules. Thus we think that the scattering phenotype seen in the cells with amplified centrosomes occurs by non-canonical EMT pathway such as ERBB2-overexpressed human breast cancer. Tumors with ERBB2 also show invasive phenotype of tumors but maintain E-cadherin expression.

Q. Does cell division axis influences preferred configuration of cell daughter doublets on 'bowtie' pattern?

A: On 'bowtie' or 'hourglass' shaped micropattern, cells divide with random orientation of spindle position and so there is no preferential cell-division axis on this micropattern geometry. Daughter cells reposition their newly formed cell junction after the cell division. Thus the cell junction can move all over the micropattern. The cell junction then stabilizes to ECM-deprived region on the micropattern. Thus the final orientation of cell junction is independent from spindle pole orientation and cell division axis.

1.4 Comments

Does centrosome amplification confer advantages to the cancer cell?

Over the past decade mounting evidences have clearly implicated a robust correlation between centrosome amplification (CA) and malignant transformation (Godinho and Pellman, 2012). CA correlates with increased tumor grade, metastasis and recurrence in various types of cancer of the blood, bone, breast, cervix, kidney and prostrate (Chan, 2011). Given CA is a hallmark of cancer aggressiveness; it presumably confers advantages to the transformed cells, in terms of their migratory ability and invasive capability. Centrosome implements an extensive repertoire of molecular tools such as microtubule plus-end tracking proteins (+TIPS), Microtubule associated proteins (MAPs) to accomplish polarization that necessary for cancer cell migration (Ogden, 2008).

In this study we validated that over-amplified centrosomes accentuate filopodia formation machinery at the cell-cell adhesion (CCA), which are otherwise stable structures in epithelia. This mechanism was guided by abundance of growing MTs from clusters of amplified centrosomes. In addition to this mechanism, CA may provide other cytoskeleton advantages to the cancer cells that enhance their metastatic progression. Microtubule growing end harbors TIPs such as EB1, CLIP-170 and adenomatous polyposis (APC), which make contact with the cell cortex and can alter activities of cortex-associated components like focal adhesions, lipid rafts and actin-nucleation proteins (Ogden, 2013). Mesenchymal migrating cell establishes front-rear polarity by relocalizing the centrosome toward the leading edge (exceptions of lymphocytes, natural killer cells) with forward-orientated actin polymerizes and retrograde flow of actin toward cell center. Microtubules growth at the leading edge activates Rac1 and lamellopodial protrusion while microtubule turnover in the cell body activates RhoA-mediated stress fibre formation. In the model that we studied here, cells produced protrusions and escaped acini by maintaining their centrosome toward interior side (Figure 1C in (Godinho et al., 2014). This poses a possibility whether cells harboring amplified centrosome adapt the mode migration mode with the centrosome at the back of the cell. It is also possible that cells initially escape from acini by maintaining centrosome at their back and during invasion through stromal cells; they acquire centrosome toward the cell front. Current evidences also suggest that cancer cells employ amoeboid movement through extracellular matrix, which is a distinct mode of migration than the mesenchymal mode, which is dominated by lamellopodia formation (Liu et al., 2015). Rapid cancer cell migration within sites of pre-cleared matrix is achieved by collective mode of migration as also seen in 3D acini culture Figure S3 D-E in (Godinho et al., 2014). A stepwise

inspection of centrosome position through different stages, namely, within acini, degradation of basement membrane, escape from acini and single cell migration will reveal different modes of centrosome-assisted polarization. The presence of enlarged centrosome and depending on whether it is clustered or not can effect Golgi organization and ability to polarize the migrating cell.

Dialogue between centrosome and cell-cell junction

Microtubules are inherently polarized structures and in centrosome-nucleated aster organization they are capable of long-range interaction with cortex though their plus tips. Adherene junctions (AJ) associate with microtubules. Cadherin-homophilic interactions are sufficient to recruit microtubules and microtubule depolymerization can disrupt AJ organization (Harris and Tepass, 2010; Stehbens et al., 2006). Microtubules support CCA assembly by kinesin dependent trafficking of CCA components and also by targeting cellular components like APC, connexin-43 to their respective domains while CCA disassembly and remodeling is modulated by selective endocytosis (Harris and Tepass, 2010). Interestingly, small GTPases are also known to regulate CCA endocytosis during epithelial remodeling and we can not rule out the possibility that the weakening of CCA in centrosome amplified cells can result from increased endocytosis of CCA molecules. Inhibition of Rac1 and Arp2/3 complex recovered CCA stability in cells with CA (Figure S8 in (Godinho et al., 2014)) and generated non-invasive 3D structures confirming active role of Rac1 in CCA remodeling (Figure 3 in (Godinho et al., 2014)). On the other hand, small GTPases are also involved in cell-cell junction formation by generating E-cadherin rich filopodia, which rapidly engage in homophilic adhesion with opposing cell (Vasioukhin et al., 2000). Thus the optimal level of filopodia formation in the cell seems crucial in maintaining dynamics of cell junction. Actin regulators, Formins, which nucleate actin to generate unbranched parallel bundles of actin, also regulate the filopodia formation. Formins are as well regulated for their activity and localization by small GTPases. Particularly, MCF10A cells depleted for FMNL2 (Formin like-2) were impaired for contact formation but not for lamellopodia protrusion upon Rac1 activation, suggesting cell-cell adhesion specific role of the Formins (Grikscheit and Grosse, 2015). Additionally FMNLs are unregulated in some invasive colorectal cancer metastasis (Zeng et al., 2015). Hence it seems important to decipher the possible role of Rac1-Formin interaction in observed invasive behavior of cells with extra-centrosomes to understand mechanistic details, which could be mechanical or biochemical. Advances in light-induced activation/inactivation of small GTPases at intracellular precision will be helpful to dissect the spatial and temporal regulation of molecular mechanisms initiating cell protrusions (Wu et al., 2009).

Does centrosome control non-centrosomal MTOC organization?

Our study showed that cancer cells with CA maneuver their amplified centrosomes and achieve metastatic transformation. Higher number of microtubules nucleated from the amplified clustered centrosomes ensure the remodeling of CCA necessary for this transformation (Figure 4 in (Godinho et al., 2014). Surprisingly, in terminally differentiated cells like polarized epithelial cells and neurons the microtubule cytoskeleton is not focused at the centrosome. Particularly, in epithelial cells, non-centrosomal arrays of microtubules are observed in apical and lateral region (Figure 1.4A). The reassignment of the MTOC function from non-centrosomal site to the centrosome during malignant transformation can be correlated to intestinal cells of developing *C .elegans*. In post-mitotic intestinal cells, MTOC function is assigned to the apical membrane and the centrosome is required for specifying apical membrane as the new MTOC (Feldman and Priess, 2012). The required role of centrosome to generate the new MTOC sites could be guessed as to provide structural scaffold for assembly of PCM at the non-centrosomal sites. Although de novo PCM assembly is possible, which can be generated by action of microtubule-specific molecular motors acting towards microtubule reorganization (Khodjakov et al., 2000). Centrioles are still required for conferring efficiency to the de novo generated PCM for spindle poles and rapid nuclear division in early syncytial flies embryos contesting de novo PCM may not be functionally equivalent to centriol associated PCM (Stevens et al., 2007). Systematic cell fusion of interphase and mitotic intestinal cells of *C. elegans* cells showed that the centrosome acts as a dominant MTOC suggesting molecular signals which confirm this function (Feldman and Priess, 2012). Another elegant set up of centrosome free cytoplast used by Chausovosky and colleagues showed that non-centrosomal microtubules populate the epithelial cells with the density similar to that of cytoplasts with the centrosome. E- and N- cadherin expression is required for generating these non-centrosomal microtubules in centrosome-free cytoplasts; which again suggests that centrosome acts as a dominant MTOC in epithelial cells (Chausovsky et al., 2000). Similar approaches will be helpful to understand whether generation of non-centrosomal MT network in epithelial cells depends on the centrosome. It is widely believed that MTs in epithelial cells are released from the centrosome and anchored/organized at the apical and lateral sides. However, MT regrowth from cytoplasmic sites and self-organization microtubules still remain valid possibilities to explain MTs at apical/basal membrane. In my view, the correlation between apical localization of centrosome prior to apical-lateral organization of microtubules suggests a causal link. As suggested in (Figure 1.2 B), active relocalization of centrosome close to the apical region can be followed by capture/anchorage/stabilization of MTs on lateral/apical region by β-catenin dynein, Adherene junctions or MAPs (Bartolini and Gundersen, 2006). Finally their release from centrosome by MT pulling at the stabilization zone and/or MT release from

Figure 1.2

A

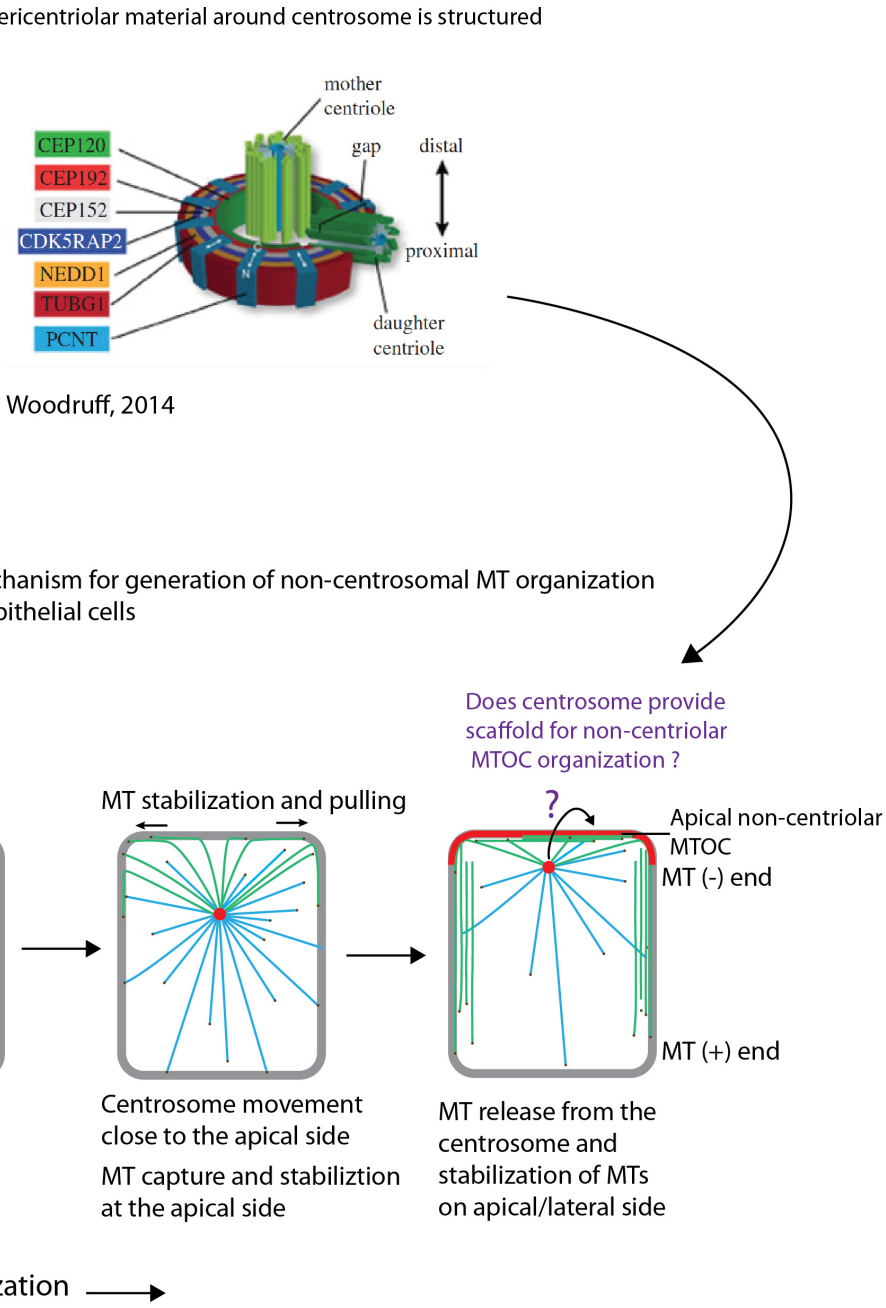
Pericentriolar material around centrosome is structured
mother centriole
CEP120
CEP192
CEP152
CDK5RAP2
NEDD1
TUBG1
PCNT
gap
distal
proximal
daughter centriole
Woodruff, 2014
B
Proposed mechanism for generation of non-centrosomal MT organization in polarized epithelial cells
Does centrosome provide scaffold for non-centriolar MTOC organization ?
MT stabilization and pulling
?
Apical non-centriolar MTOC
MT (-) end
MT (+) end
Centrosome aster
Centrosome movement close to the apical side
MT capture and stabiliztion at the apical side
MT release from the centrosome and stabilization of MTs on apical/lateral side
Epithelial polarization

centrosome seems a likely mechanism for generating in epithelial microtubule organization. Live imaging showed that MT could be released with its nucleating structure, which could act as a minus end cap (Keating and Borisy, 1999). This mechanism ensures apical pool of MTs as well directional organization of lateral MTs (-ve end towards apical) (Figure 1.2 B). Moreover, this orientation of non-centrosomal MTs seems crucial for lumen formation in mammary gland acini (Akhtar and Streuli, 2013). Systematic analysis of centrosome position and its MTOC activity during course of polarization can address the interconnection between centrosome and non-centrosomal sites. In addition, the capacity of centrosome to crosstalk at distance locations in cell is complemented by molecular signals. For example, the dominant role of centrosome as MTOC is assured by phsophorylation of SPD-2/CEP192 by Cyclin-dependent kinases for recruitment γ-tubulin at the centrosome (Yang and Feldman, 2015).

Centrosome as the structural and molecular hub

"*Several principles of construction of a microscopically small device for locating the directions of signal sources in microscopic dimensions. It appears that the simplest and smallest device that is compatible with the scrambling influence of thermal fluctuations as are demonstrated by Brownian motion is a pair of cylinders oriented at right angle to each other*"- Guenter Albrecht-Buehler 1981.

Guenter Albrecht-Buehler claimed that the centrosome could act as cell's angular detector by virtue of its 9-fold symmetry, precisely oriented blades (centriole microtubule arrangement) and -orthogonal arrangement of centrioles (Albrecht-Buehler, 1981). Although not conclusively proven, the intriguing symmetry of centrioles, template based duplication and tight control of centriole number had prompted researchers to call this organelle as 'Conspicuous'. Hundred years after Boveri's suggestion it was shown that microtubule asters were result of centroplasm (PCM) rather than centrioles themselves. With the advances of new 3D structured illumination microscopy (3D-SIM) sub-diffraction light microscopy techniques allowed to image PCM organization (Sonnen et al., 2012). Similar studies revealed that PCM, which was termed as amorphous cloud, is rather a structured complex. As shown in the (Figure 1.2 A), PCM possess radial symmetry which extends from centriole cylinder and concentric rings in layers around centriole (Figure 1.2 A). This may be partly explains why in the absence of centrioles de novo assembled PCM at spindle poles lacks the efficiency. So it is likely that centrosome is important in generating structured PCM for mitosis and in interphase cell, which is conserved across species as well (Lüders, 2012). Comparison of non-centrosomal PCM and centrosome-PCM will

indicate whether non-centrosomal PCM assembly is also assisted by the centrosome as explained above for hand-over MTOC function.

The PCM also contains hundreds of proteins including important cell cycle regulators and signaling molecules and many proteins that help to organize and nucleate microtubules (Arquint et al., 2014). The age of the centrioles is important because of PCM associated with it. The difference between PCM proteins of mother and daughter centrioles decides MT nucleating properties of centriols. Malignant cells have non-orthogonal centrioles and the centriolar number is altered (as in centrosome amplification) and the associated PCM assembly is altered too. These evidences suggest that PCM is structurally and functionally modified during morphogenetic events like cancer progression.

A study showed that β-catenin is present at the centrosome along with its interacting partners GSK3β, Axin and APC upon Wnt signaling (Huang et al., 2007). Modulation of β-catenin levels can affect centrosome maturation, organization and MT nucleating capacity. β-catenin, which is known for its multifunctional roles, shuttles between CCA and centrosome and effectively affect centrosome position, MT nucleation at the centrosome and mitotic progression (Bertrade et al., 2013; Ligon et al., 2001). In the context of cancer progression, two known tumor suppressors, BRCA1 and p53 have been found to localize at the centrosome of mammalian cells and it has been speculated that part of their tumor suppressor function takes place at the centrosome (Lingle and Salisbury, 2000). BRCA1 protein is associated with centrosome during mitosis and thought to contribute to genome instability in tumorogenic cells (Brown et al., 1994). While p53 that has cell cycle checkpoint function is partly localized to centrosome in addition to its nuclear portion. There is strong correlation between depletion of p53, centrosome amplification and genome instability and thus possible role of p53 at the centrosome controlling microtubule related function is highly anticipated. Cells lacking Cep192 show enhanced MT nucleation from Golgi apparatus which showed that PCM proteins at centrosome directly or indirectly result into MT nucleation ability at non-centrosomal sites (O'Rourke et al., 2014). Electron dense spots around centriols seen by electron microscopy studies are now referred to as "centriolar satellites", which move along the microtubules to minus end direction towards the centrosome and accumulate there (Bärenz et al., 2011). Growing knowledge on 'centrosomal satellites' is now shining some light on understanding how protein complexes at the centrosome are formed, maintained and exchanged. Further investigations of dynamic regulation of signaling at the centrosome will help to integrate different pieces of evidences showing centrosome crosstalk with cytoplasmic and cell cortex components.

1.5 References

Akhtar, N., and Streuli, C.H. (2013). An integrin-ILK-microtubule network orients cell polarity and lumen formation in glandular epithelium. Nat. Cell Biol. *15*, 17–27.

Albrecht-Buehler, G. (1981). Does the geometric design of centrioles imply their function? Cell Motil. *1*, 237–245.

Arquint, C., Gabryjonczyk, A.-M., and Nigg, E. a (2014). Centrosomes as signalling centres. Philos. Trans. R. Soc. Lond. B. Biol. Sci. *369*, 20130464 – .

Bärenz, F., Mayilo, D., and Gruss, O.J. (2011). European Journal of Cell Biology Centriolar satellites : Busy orbits around the centrosome. *90*, 983–989.

Bartolini, F., and Gundersen, G.G. (2006). Generation of noncentrosomal microtubule arrays. J. Cell Sci. *119*, 4155–4163.

Bertrade, M., Nelson, W.J., and Angela, B. (2013). NIH Public Access. *35*, 804–809.

Brown, C.R., Doxsey, S.J., White, E., and Welch, W.J. (1994). Both viral (adenovirus E1B) and cellular (hsp 70, p53) components interact with centrosomes. J. Cell. Physiol. *160*, 47–60.

Chan, J.Y. (2011). A clinical overview of centrosome amplification in human cancers. Int. J. Biol. Sci. *7*, 1122–1144.

Chausovsky, A., Bershadsky, A.D., and Borisy, G.G. (2000). Cadherin-mediated regulation of microtubule dynamics. Nat. Cell Biol. *2*, 797–804.

Feldman, J.L., and Priess, J.R. (2012). A role for the centrosome and PAR-3 in the hand-off of MTOC function during epithelial polarization. Curr. Biol. *22*, 575–582.

Godinho, S. a., and Pellman, D. (2012). Causes and consequences of aneuploidy in cancer. Nat. Publ. Gr. *13*, 189–203.

Godinho, S. a., Picone, R., Burute, M., Dagher, R., Su, Y., Leung, C.T., Polyak, K., Brugge, J.S., Théry, M., and Pellman, D. (2014). Oncogene-like induction of cellular invasion from centrosome amplification. Nature *510*, 167–171.

Grikscheit, K., and Grosse, R. (2015). Formins at the Junction. Trends Biochem. Sci. *41*, 148–159.

Harris, T.J., and Tepass, U. (2010). Adherens junctions: from molecules to morphogenesis. Nat Rev Mol Cell Biol *11*, 502–514.

Huang, P., Senga, T., and Hamaguchi, M. (2007). A novel role of phospho-beta-catenin in microtubule regrowth at centrosome. Oncogene *26*, 4357–4371.

Keating, T.J., and Borisy, G.G. (1999). Centrosomal and non-centrosomal microtubules. Biol. Cell *91*, 321–329.

Khodjakov, a, Cole, R.W., Oakley, B.R., and Rieder, C.L. (2000). Centrosome-independent mitotic spindle formation in vertebrates. Curr. Biol. *10*, 59–67.

Ligon, L.A., Karki, S., Tokito, M., and Holzbaur, E.L.F. (2001). Dynein binds to β -catenin and may tether microtubules at adherens junctions. *3*, 913–917.

Liu, Y.J., Le Berre, M., Lautenschlaeger, F., Maiuri, P., Callan-Jones, A., Heuzé, M., Takaki, T., Voituriez, R., and Piel, M. (2015). Confinement and low adhesion induce fast amoeboid migration of slow mesenchymal cells. Cell *160*, 659–672.

Lüders, J. (2012). The amorphous pericentriolar cloud takes shape. Nat. Cell Biol. *14*, 1126–1128.

O'Rourke, B.P., Gomez-Ferreria, M.A., Berk, R.H., Hackl, A.M.U., Nicholas, M.P., O'Rourke, S.C., Pelletier, L., and Sharp, D.J. (2014). Cep192 controls the balance of centrosome and non-centrosomal microtubules during interphase. PLoS One *9*.

Ogden, Angela, Rida, Padmashree Aneja, R. (2013). NIH Public Access. October *32*, 269–287.

Sonnen, K.F., Schermelleh, L., Leonhardt, H., and Nigg, E.A. (2012). 3D-structured illumination microscopy provides novel insight into architecture of human centrosomes. Biol. Open *1*, 965–976.

Stehbens, S.J., Paterson, A.D., Crampton, M.S., Shewan, A.M., Ferguson, C., Akhmanova, A., Parton, R.G., and Yap, A.S. (2006). Dynamic microtubules regulate the local concentration of E-cadherin at cell-cell contacts. J. Cell Sci. *119*, 1801–1811.

Stevens, N.R., Raposo, A.A.S.F., Basto, R., St Johnston, D., and Raff, J. (2007). From Stem Cell to Embryo without Centrioles. Curr. Biol. *17*, 1498–1503.

Vasioukhin, V., Bauer, C., Yin, M., and Fuchs, E. (2000). Directed actin polymerization is the driving force for epithelial cell-cell adhesion. Cell *100*, 209–219.

Wu, Y.I., Frey, D., Lungu, O.I., Jaehrig, A., Schlichting, I., Kuhlman, B., and Hahn, K.M. (2009). A genetically encoded photoactivatable Rac controls the motility of living cells. Nature *461*, 104–108.

Yang, R., and Feldman, J.L. (2015). SPD-2/CEP192 and CDK Are Limiting for Microtubule-Organizing Center Function at the Centrosome. Curr. Biol. *25*, 1924–1931.

Zeng, Y.F., Xiao, Y.S., Lu, M.Z., Luo, X.J., Hu, G.Z., Deng, K.Y., Wu, X.M., and Xin, H.B. (2015). Increased expression of formin-like 3 contributes to metastasis and poor prognosis in colorectal carcinoma. Exp. Mol. Pathol. *98*, 260–267.

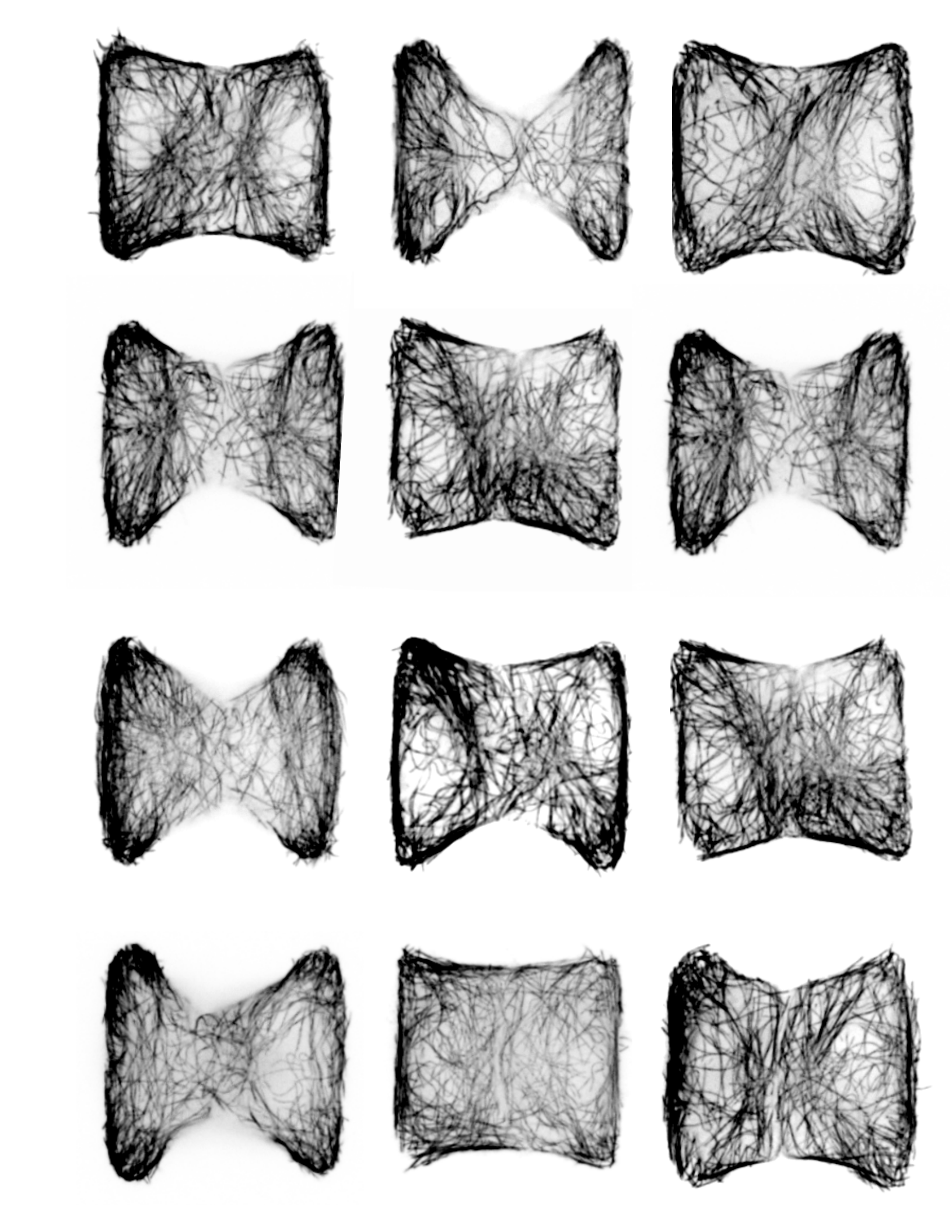

CHAPTER II

Effect of the Cell-cell Adhesions on Centrosome Position

2.1 Introduction to the polarity reversal

The epithelial plasticity is the prerequisite for driving tissue remodeling. As described in Chapter I, instances like branching morphogenesis involve local modification of cell polarity to form clefts and invaginations within the tissue. These events are initiated by Epithelial-to-Mesenchymal transition (EMT) where cells can switch between non-motile to migratory states to move across the cell layers. It is quite evident that the processes like gastrulation, tubulogenesis and mammary gland branching are guided using positional information within the tissue. As discussed in the introduction of the thesis the cellular compass that holds the positional information and directs the cells is mainly composed of internal polarity of cells, which responds to external environmental cues by dynamically interacting with cell cortex through cytoskeleton network. Morphogenetic events involve drastic remodeling of extracellular matrix within the tissue and this change is transmitted to cell interior through cell adhesions and cytoskeleton network engaged at these adhesions. The literature on EMT is vast and there are many studies dedicated to understand remodeling of cell adhesions accompanied by actin and microtubule network modification. There is plethora of molecules involved in mediating the crosstalk between cell adhesion and cytoskeleton network. However the question of how internal polarity within the cell is actively reoriented during EMT is still unclear. And the subsequent question of whether organelle asymmetry in generating this polarity is required for allow precise embryonic movements within an embryo still remains unanswered. How positional information is set up, how it is recorded and how is it interpreted by cells during pattern formation? Here I describe different mechanisms involved in the whole organisms, tissues as well as at the cellular level to guide directional growth, movements and pattern formation.

Polarity reversal - a feature of cell's positional information

In early stages of metazoan embryos and also in the primitive metazoan animal, hydra, positional information is set up by gradients of morphogens. Early graft experiments with hydra showed polarity reversal of the whole animal after regeneration (Figure 2.1 A). Initially it was thought that the nerve stem cells within hydra were responsible for the polarity reversal of the organism. When nerve cells from hydra were experimentally removed, the organism still retained the property of polarity reversal after the graft and thus it was clear that epithelial cells resting within the organism were responsible for polarity cues and regeneration of the organism (Marcum et al., 1977). Hydra is categorized as eumetazoan since it has true tissue layers, neurons and the embryo goes through gastrula stages. Study of hydra provides some important aspects of evolution of epithelium and its plasticity. Epithelial cells in hydra form two layers,

Figure 2.1

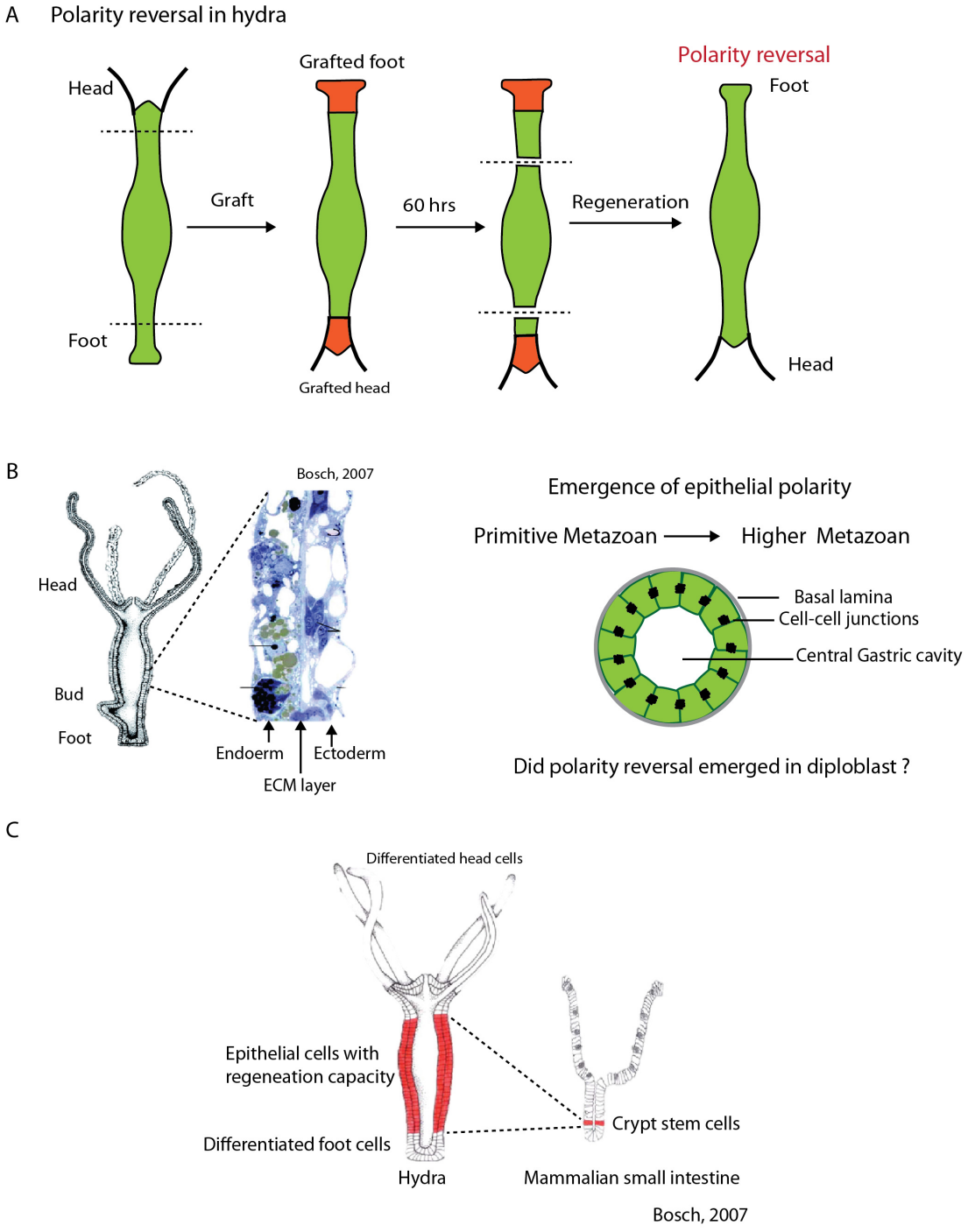

(A) Occurance of polarity reversal during regeneration of hydra after head and foot graft.
(B) Epithelial organization in hydra (left), definition of epithelial polarity- in hydra and higher metazoa animals(right).
(C) Comparison betwen hydra and mammalian intestine for presence of cells with regeneration capacity.

endoderm and ectoderm, which are separated by an ECM layer called mesoglea and it is composed of laminin, collagen and fibronectin like molecules (Figure 2.1B). Interestingly, this ECM layer is not only required for epithelial cells to maintain their polarity but also to retain their stem cell-ness which is essential for regeneration (Bosch, 2007). In addition, the remodeling of epithelial cells involves majority of classical EMT-signalling pathways such as Wnt, Mitogen Activation Kinase, Ras and PI3-kinase pathways (Bosch, 2007). Regeneration of hydra at the ultrastructure level is described as wound healing process initiated by the endoderm cells similar to that of wound healing by EMT process. Thus given that the definition of epithelial polarity emerged from the first occurrence of sealed cell-cell junctions in lower metazoans like hydra along with presence of molecular pathways employed for epithelial remodeling during regeneration (in hydra) and EMT (in higher metazoans), it is plausible that common features like polarity reversal are conserved in the higher metazoans to provide positional information to cells while undergoing pattern formation. In addition, events like gastrulation where cells move in the directions away from their current location, must involve complete re-orientation of polarity. We looked for evidences of polarity reversal, which involved either inversion of cell cortex features such as filopodia formation, dissolution of tight junction or inversion of position of the internal organelles, especially centrosome and golgi during course of morphogenesis.

One of the earliest demonstration of the correlation between the intracellular position of the Golgi apparatus and cell movement in an epithelium comes from the work of Cajal (1914) who showed that ganglion cells extend migratory process from their basal poles only after the golgi has moved from the apical to the basal pole (Bentivoglio, 1999). Investigation of ultrastructure of thyroid follicles maintained in suspension cultures showed intermediate stages of polarity reversal when cells were subjected to higher serum concentration. As serum contains several growth factors such as EGF and TGF-β, which can induce epithelial transformations, the study suggested that initial stages of follicles morphogenesis involve polarity reversal without the collapse of the lumen (Nitsch and Wollman, 1980). An elegant study of developing chick auditory system by Carney and Couve in 1989 provided clear evidences of polarity reversal wherein epithelial cells from otic structure progressively internalize cilia, reposition golgi and form filopodia at the basal surface (Carney and Couve, 1989). Systematic analysis of 7-26 stages of chick development and quantification of organelle position revealed that otic placode invagination is accompanied by inversion of organelle position within the cells with acquisition of mesenchymal phenotype (Figure 2.2 A). Authors of this study hypothesized that basal position of the Golgi towards basal surface could be related to the directed secretion of components, which today is designated as the secretion Metalloproteases for degradation of the basement membrane. The development of in-vitro 3-D culture assay using reconstituted basement membrane provided a powerful tool to study epithelial morphogenesis. Extensive studies of epithelial organization and change of polarity of cells by Mostov and colleagues

Figure 2.2

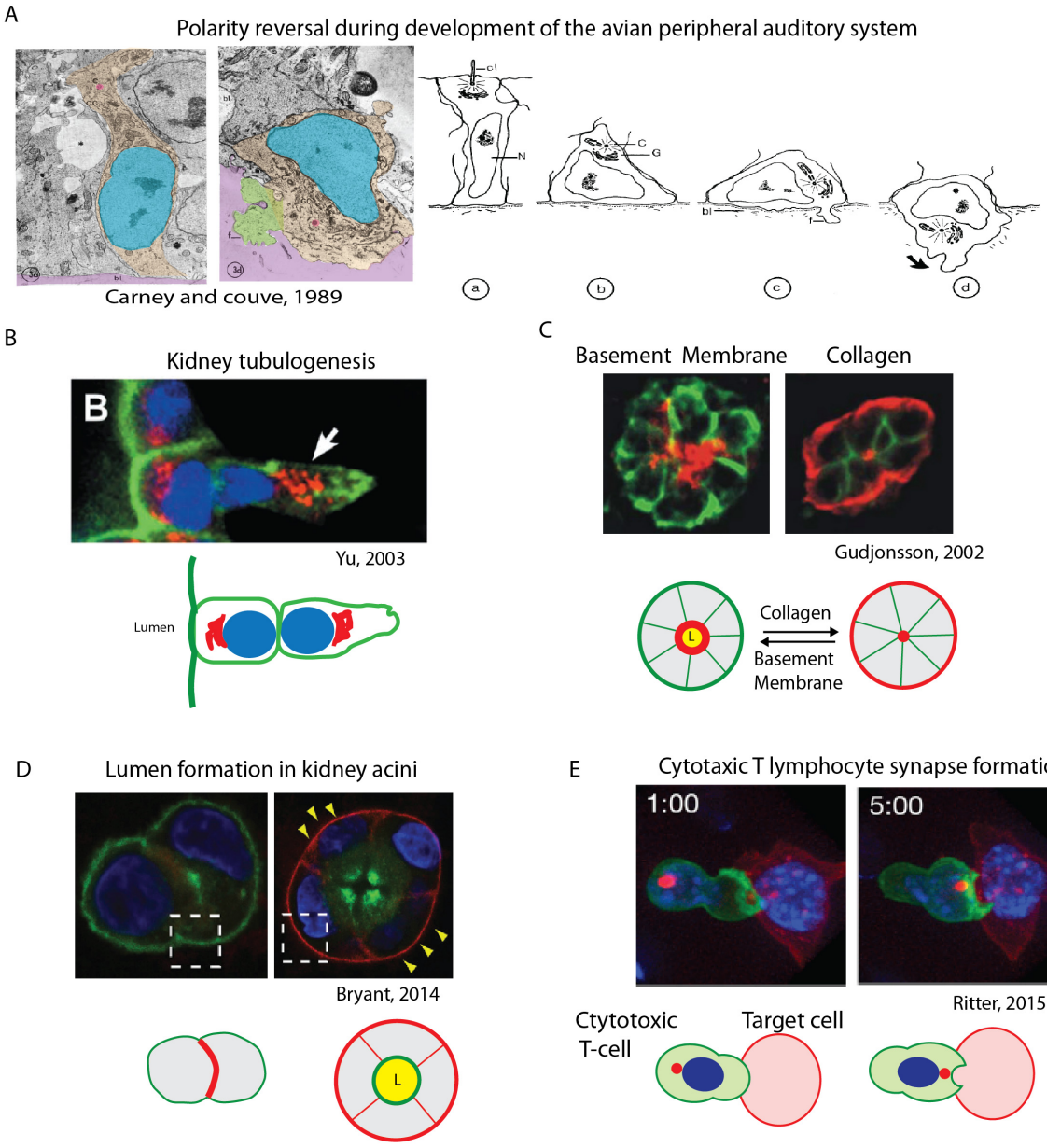

Examples of polarity reversal during different morphogenetic processes. (A) Development of chick auditory sytem. Electron micrograph images are false colored for whole cell (orange), nucleus(blue), filopodia (green), centrosome (red), basmement lamina (purple)
(B) MDCK tubulogeneis with golgi(red), actin(green)
(C) Breast luminal epithelial cells grown in 3D basement membrane substrate and collagen stained for sialomucin(Red) and ESA(green)
(D) Lumen development in MDCK cells Podocalyxin (Green) and active β1-integrin (red)
(E) Immune synapse formtion between T-cell and target cell with actin (green), centrosome(red)

showed transient polarity changes occur in cells forming branches to form kidney tubules (Figure 2.2B). Change of Laminin to collagen rich basement membrane in the presence of Hepatocyte-growth factor (HGF) and increased serum concentration was sufficient to induce tubulogenesis in MDCK 3D acini (Yu et al., 2003). Similar studies were conducted in mammary gland cells cultured in 3D matrix. Mere change of basement membrane from laminin to collagen completely reverted apical and basal cortex within the acini. Collagen matrix promoted localization of the apical cortex outside with disappearance of the lumen (Figure 2.2 C). This study also provided crucial information about the role of myoepithelial cells in imparting correct mammary gland acini organization and causing changes in surrounding matrix, which may promote breast cancer (Gudjonsson et al., 2002). Recent investigation of kidney acini formation revealed that at early stage, two kidney cells have apical markers extending over all over the cell cortex. Progressive cell divisions and phosphorylation of the membrane lipids guide transcytosis of the apical membrane proteins to interior side of the cells in a spheroid causing formation of distinct apex and lumen (Bryant et al., 2014). Interestingly, immunological response by T-cell forming an immune synapse also showed relocalization of the centrosome towards the immune synapse. This relocalization of the centrosome was required to release cytolytic granules to destroy the target cell. The repositioning of centrosome towards the membrane area reduced in actin density and phospholipid PIP2 takes place within 5 minutes suggesting centrosome repositioning is an early event and affected by actin and membrane lipids (Ritter et al., 2015).

Does polarity reversal occur during Epithelial-to-mesenchymal transition ?

All the above examples unambiguously demonstrate the presence of polarity reversal mechanisms involving active repositioning of the internal organelles of cells for achieving various functions. Although EMT has been studied extensively in the context of development and cancer progression wherein severe alteration of cell adhesion takes place but there isn't any evidence about how cells rearrange internal polarity to achieve their reorientation within the tissue to allow scattering during instances like cell ingression, mesoderm movement, mammary gland branching. Instances like kidney tubulogenesis involve alteration of the organelle positioning for the tube extension but it does not include cell scattering like in EMT (Pollack et al., 1998). Thus it is still unexplored whether the rearrangement of internal organelle positions precedes cells separation of mesenchymal cells after the EMT. The report from Carney and Couve suggested that a epithelial remodeling program controlling centrosome, golgi, nucleus repositioning alongwith filopodia formation underlies at developmental stages (Carney and Couve, 1989). This report was an eminent evidence for the existence of mechanisms that are responsible for organelle positioning during developmental EMT. However 27 years later, the

clear description of the proposed mechanisms is still missing. Simple geometric constrains and cell orientations required during EMT-induced morphogenesis suggest that polarity reversal is required, may be transiently to modulate internal polarity to follow tissue transformation. In order to first investigate whether polarity reversal exists within the context of EMT, we looked at the nucleus-centrosome axis orientation during gastrulation and mammary gland branching in mouse. We found evidences of polarity reversal in very localized areas of embryo and tissue structures indicating that these cells have probably coupled EMT with polarity reversal. As the polarity changes involved centrosome repositioning, we hypothesized that centrosome and associated microtubule network had important role in governing cell's internal polarity as well as for coupling changes of cell-cell and cell-Matrix adhesions to cells' interior. In the following article we have revealed for the first time the presence of polarity reversal during process of EMT using mouse model, 3D organoid and 2-D cell line models. This polarity reversal was not only the consequence of EMT as it took place at the early stages of EMT induction and in addition, the reorganization of MT network was necessary for separation of resulting mesenchymal cells. We approached the problem of understanding complex EMT processes by breaking the tissue model to smaller scale, which can be considered as minimal unit of tissue. By studying the smallest fundamental unit of tissue, which is made up two cells, we observed robust phenotype of cells with polarity reversal. How far can we extrapolate the two-cell model to understand tissue remodeling, is a matter of debate and I will discuss in the final discussion of the thesis. Whether the mechanisms that were revealed by this study of EMT are truly global and applicable to all different types of EMT during embryonic development and cancer progression requires further investigations.

Polarity Reversal Primes Cell Scattering during Epithelial to Mesenchymal Transition

Mithila Burute [1,2,3], Magali Prioux [1], Sandrine Truchet [4], Guillaume Blin [5], Gaëlle Letort [1], Qingzong Tseng [1], Thomas Bessy [3], Joanne Young [2], Odile Filhol-Cochet [6], Manuel Théry [1,3*]

[1] Laboratoire de Physiologie Cellulaire et Végétale, Biosciences & Biotechnology Institute of Grenoble, UMR5168, CEA/INRA/CNRS/Université Grenoble-Alpes, Grenoble, France.
[2] CYTOO SA, 7 Parvis Louis Néel, BP50 38040, Grenoble, France
[3] Unité de Thérapie Cellulaire, Hôpital Saint Louis, Institut Universitaire d'Hématologie, UMRS1160, INSERM/AP-HP/Université Paris Diderot, Paris, France.
[4] INRA, UMR1313 Génétique Animale et Biologie Intégrative, F-78350, Jouy-en-Josas, France
[5] MRC Centre for Regenerative Medicine, Institute for Stem Cell Research, School of Biological Sciences, University of Edinburgh, United Kingdom
[6] Laboratoire de Biologie du Cancer et de l'Infection, Biosciences & Biotechnology Institute of Grenoble, UMRS1036, CEA/INSERM/Université Grenoble-Alpes, Grenoble, France.
*Correspondence: manuel.thery@cea.fr

Abbreviations: CCJ- cell-cell adhesions, CMA- cell matrix adhesions, EMT- epithelial to mesenchymal transition, HGF- Hepatocyte growth factor, TGF-β - Transforming growth factor-beta, ECM-extracellular matrix, EB1- end binding protein 1.

Summary

During epithelial to mesenchymal transition (EMT), cells lining the tissue periphery break up their cohesion to migrate within the tissue. This dramatic reorganization involves a poorly characterized remodeling of the baso-apical polarity of static epithelial cells into the front-rear polarity of migrating mesenchymal cells. We monitored centrosome positioning during this transition in developing mouse embryos and mammary gland, in cultured 3D cell aggregates and in micro-patterned cell doublets. In all conditions, centrosomes left their peripheral localization next to cell-cell junctions (CCJ) to reposition at the cell center, while nuclei moved away from cell-matrix adhesions (CMA). This resulted in a complete cell polarity reversal, accompanied by a redistribution of intracellular tensional forces. Sequential release of cell confinement using dynamic micropatterns showed that polarity reversal promotes cell disengagement and scattering. These results reveal that polarity is not lost during EMT and on

the contrary that cytoskeletal remodeling and polarity reorientation are highly controlled and coordinated to direct cell scattering across the basement membrane.

Introduction

Epithelia line the periphery of organs that lie at the interface with the outer medium, such as the airways, intestinal track or secretory tubular glands. During specific developmental stages, and later during adult development, these peripheral cell layers invaginate to expand their contact area or develop internal tissues (Kalluri and Weinberg, 2009). As they do so, some epithelial cells convert into mesenchymal cells, which migrate into and populate the underlying interstitial tissues. This topological tissue remodeling, during which peripheral cells become internal cells, is accompanied by dramatic intra-cellular reorganization (Lamouille et al., 2014). Epithelial cells disassemble the tight junctions they had with their neighbors and that were ensuring the interface permeability. As they move in the organ, they lose the contact-free edge they had toward the outer medium and get fully surrounded by cells and extra-cellular matrix. Their secretory and endocytic functions, which were directed by the presence of this contact-free interface get redistributed toward adhesive edges (Akhtar and Streuli, 2013). Therefore the epithelial-to-mesenchymal transition (EMT) not only involves reorganization of cell position and acquisition of a migratory phenotype but also implies a reorientation of cell function and polarity (Godde et al., 2010; Huang et al., 2012; Rodriguez-Boulan and Macara, 2014).

Cell polarity is an intrinsic bias in internal cell organization which is spatially adapted to extra-cellular cues and which direct cell functions (Bornens, 2008). In epithelia, cell-cell junctions (CCJ) form a diffusion barrier between distinct plasma membrane domains and thus define the apical pole, toward the outer medium, and the basal pole, toward the extra-cellular matrix (ECM) that cells are attached to (Dickinson et al., 2011). The spatial segregation of cell-matrix adhesion (CMA) and CCJ, and thus the physical separation of the signaling and anchoring proteins they are associated with (Burute and Théry, 2012; Rodriguez-Boulan and Macara, 2014), defines the baso-apical orientation of epithelial cell polarity from ECM toward the contact free edge (Figure S1) (Yeaman et al., 1999). Microtubule orientation along the CMA-CCJ axis directs intra-cellular trafficking and establishment of the cell apical pole away from the basement membrane (Akhtar and Streuli, 2013). In mesenchymal cells, CCJ are much weaker and don't define membrane domains as in epithelial cells. Instead, it is the cell migration machinery that directs cell polarity (Etienne-Manneville, 2013). Here also, mutual exclusion of signaling pathways segregate actin network polymerization at the advancing cell edge and actin

contraction at the retracting edge and thereby define the mesenchymal front-rear polarity axis. Thus, during EMT the baso-apical polarity axis is converted into a front-rear axis (Godde et al., 2010; Nelson, 2009; Xu et al., 2009). The mechanism supporting this conversion has not been specifically addressed.

As epithelial cells disassemble CCJ, the apical pole components become free to mix with the rest of the plasma membrane. Therefore the transition from apico-basal to front-rear polarity has often been designated as a "loss of polarity" (Thiery, 2002; Thiery et al., 2009; Zavadil and Böttinger, 2005) (Figure S1). This widely accepted nomenclature echoes the parallel between physiological EMT and the initiation of metastasis during which the tight control of the epithelial program is lost, polarity is disorientated and cancer cells acquire migration capacities allowing them to scatter through surrounding tissues (Huber et al., 2005; Micalizzi et al., 2010; Spaderna et al., 2008; Thiery et al., 2009; Xu et al., 2009). However, it seems unlikely that key developmental stages involving EMT, such as gastrulation, neural crest induction or mammary branch network development, pass through an uncontrolled step during which polarity would be ill-defined.

Simple geometrical considerations rather suggest that during EMT the epithelial polarity toward the contact-free edge is literally inverted toward the underlying basement membrane that mesenchymal cells digest as they move inward (Figure S1). It is possible that the complexity of multi-cellular arrangements may have disguised the determinism of a well-controlled polarity reversal as a transient loss of polarity. Indeed genuine polarity reversals have been observed within simplified epithelia in vitro, in response to conditions that are close to the changes that occur during EMT. Thus, modifying the composition of the extra-cellular matrix surrounding epithelial cyst, or modulation of integrins activation state, can induce the relocalization of polarity surface markers from the outside surface to the internal lumen and vice versa (Akhtar and Streuli, 2013; Gudjonsson et al., 2002; Mauchamp et al., 1979; Ojakian and Schwimmer, 1994; Rodríguez-Fraticelli et al., 2012; Wang et al., 1990; Yu et al., 2005). While the characterization of the mechanism supporting surface marker inversion has been addressed (Bryant et al., 2014), the reorganization of intracellular organization has not yet been studied. Interestingly, analyses of intermediate stages of developing chick auditory system and neural network, as well as observations of branching kidney tubules and inversion of thyroid follicles in culture have suggested the existence of concerted repositioning of internal organelles such as nucleus, Golgi apparatus, lysosomes and centrosome (Carney and Couve, 1989; Das and Storey, 2014; Nitsch and Wollman, 1980; Pollack et al., 1998).

The microtubule network regulates the organization and trafficking of the endomembrane network (de Forges et al., 2012). As such, the position of the centrosome, the main microtubule-organizing center, is central to the establishment of an asymmetric microtubule array directing cell polarity (Bornens, 2008). In epithelial cells, the centrosome is

off-centered toward the actin-rich apical pole (Hebert et al., 2012). Although the underlying process supporting this peripheral positioning is still unknown, it plays a key role in the proper assembly of the primary cilium in the apical pole (Tang and Marshall, 2012) and the orientation of intracellular trafficking toward the primary cilium and the apical pole (Nelson, 2009; Rodriguez-Boulan and Macara, 2014). In mesenchymal cells, centrosome positioning toward the cell front and the associated asymmetric microtubule network organization is pivotal for the establishment and maintenance of the front-rear polarity axis of migrating cells (Etienne-Manneville, 2013; Luxton and Gundersen, 2011). Microtubules notably regulate the turnover and trafficking of adhesion components that are required to trigger and direct cell motion (Paul et al., 2015). These considerations suggest that centrosome position and the associated asymmetric geometry of the microtubule network may be modulated during the early stages of EMT and actively contribute to the reorientation of cell function and polarity.

Here we use in-vitro models of mammary gland development (Debnath et al., 2003) and kidney tubulogenesis (Pollack et al., 1998) to study cell polarity during epithelial morphogenesis. In order to distinguish the effect of cell neighbors, cell migration, cell spreading and adhesion remodeling on cell polarization, we use micropatterns to control the shape and position of cells forming doublets. We show that polarity reversal occurs in response to TGF-β in mammary gland and as a response to both TGF-β and HGF in MDCK cells by nucleus-centrosome axis reorientation. Polarity reversal was a consequence of centrosome repositioning, which appeared to be modulated by a change in microtubule number and the localization of Partitioning defective protein Par3 at CCJ. This polarity reversal occurred along with an increase of cellular contractility and redistribution of inter and intra-cellular forces that primes cells for scattering. Finally, we show that polarity inversion by centrosome repositioning occurs prior to cell scattering and was necessary for cell dissociation during EMT.

Results

Polarity reversal during EMT in mouse development

Several key developmental stages involve EMT and thus could display the polarity reversal we hypothesize. The first EMT event occurs at gastrulation, 5-6 days post fertilization. The primitive streak forms at the future posterior end of the embryo wherein a subset of epiblast cells differentiate into primary mesenchyme and ingress between the epiblast and endoderm layer (Acloque et al., 2009; Tam and Behringer, 1997). Epiblast cells are marked by expression of nuclear T-Brachyury along with breakdown of Collagen IV (Figure 1A). Using g-tubulin as a marker for centrosome, we investigated polarity of cell populations destined for different cell fates. The centrosome in epiblast cells was localized close to the amniotic cavity, resulting in a nucleus-centrosome axis oriented toward the cavity. The epiblast cells undergoing EMT showed higher T-Brachyury expression and were positioned farther from the cavity. In these cells, centrosomes appeared relocated away from the cavity and the nucleus-centrosome axis pointed toward the endoderm layer. This supported our hypothesis that upon the onset of EMT, when epiblast cells move inward to form the primitive streak, the nucleus-centrosome axis gets inverted.

Later, at puberty, the ductal network within the mouse mammary gland expands by invading the surrounding fat pad. At this stage, specialized structures called terminal end buds appear at the end of the primary ducts (Hinck and Silberstein, 2005). EMT induces complex reorganization of cell arrangement and polarity and promotes the collective migration of cells to drive ductal morphogenesis (Ewald et al., 2008, 2012; Godde et al., 2010). Cell polarity axis orientation was inferred from the orientation of the Golgi apparatus with respect to the nucleus. In luminal cells, the Golgi apparatus was positioned toward the duct (Figure 1B) as in the case of lactating acini (Akhtar and Streuli, 2013). Interestingly, a few cells at the tip of the growing terminal end buds showed complete inversion of the nucleus-golgi axis (Figure 1B). Other cells near the tip displayed a mispositioned Golgi apparatus suggestive of intermediate stages of polarity reversal (Figure 1B).

We thus found indications of nucleus-centrosome axis inversion at two distinct stages of mouse development, supporting our working hypothesis of polarity reversal occurring during EMT. Investigating the mechanics of polarity inversion in vivo at single cell resolution remains technically challenging. In order to obtain further insights into this process we used simpler and more accessible working systems to study the induction and consequences of those polarity reversals where parameters of interest could be better controlled.

Polarity reversal in 3D mammary gland cell culture

Self-organized mammary acini in 3D gels recapitulate numerous features of native tissue, including epithelial cell polarization (Debnath and Brugge, 2005; Underwood et al., 2006) and constitute a robust system amenable to induction of morphogenesis by the addition of growth factors (Debnath et al., 2003; Montesano et al., 2007; Nelson and Bissell, 2005; Seton-Rogers et al., 2004). We used MCF10A 3D cultures as a model of mammary gland acini to investigate polarity changes that may occur upon induction of EMT by TGF-β (Xu et al., 2009; Zhang et al., 2014) (Figure S2A-C). After seven days culture in 3D gels of laminin-rich basement membrane (commercialized as Matrigel), MCF10A show acini-like structures with enriched apical actin indicating the site of a future lumen (O'Brien et al., 2001) (Figure 1C). Nontreated cysts showed a regular arrangement of nuclei in a single layer and were placed equidistant from the acinus center (Figure 1C). This regular geometric organization was lost in cysts treated with TGF-β1 (5 ng/ml) for 5 days. The severe disorganization of cell arrangement in cysts was also associated with misorientation of the polarity axes (Figure 1D). We found a similar disorganization of acini assembled from MDCK cells of kidney origin upon treatment with HGF (Figure S2D-F). Thus, cell mispositioning and polarity axes disorientation are closely connected in these 3D architectures. This complex interplay between cell shape, position and polarity raised a few central questions that are difficult to address in 3D culture systems. How does cell mislocalization impact polarity axis orientation? Does the cell internal polarization mechanism no longer orient properly with respect to external cues or is it responding normally in a perturbed context due to mispositioning of neighboring cells? Furthermore, cell migration is known to actively regulate both epithelial (Wang et al., 2013) and mesenchymal (Luxton and Gundersen, 2011) cell polarities. Is TGF-β-induced motility involved in the reorientation of cell polarity in these 3D cysts?

Centrosome repositioning is associated with cell scattering

The structural complexity and lack of reproducibility of multicellular systems are recurrent limitations precluding the precise dissection and analysis of polarity reorientations in response to changes in cell microenvironment. This prompted us to adapt a simpler but more controlled cell culture model, which can still recapitulate important aspects of morphogenesis, to the study of cell migration and polarity (Théry, 2010). We first aimed at eliminating the variable effect due to the presence of multiple neighbors while keeping the possibility for cells to stay in contact or dissociate and move away from each other. We designed a minimal system comprised of only two cells on a micropatterned-ECM-track of finite length to constrain cell migration in a reproducible manner. We first monitored daughter cell motion following cell division by video microscopy in three distinct epithelial cell lines (Movie S1, S2). In most cases, control (CTR) epithelial cells stayed in contact after cell division whereas the vast majority of TGF-β or HGF

treated cells separated after division (Figure S3A,B). Importantly, nontreated cells which maintain their intercellular junction, tend to polarize toward their neighbor, whereas TGF-β treated cells which move away from each other, tend to polarize in the opposite direction, toward their newly created front edge (Figure S3C). These observations support the view that EMT-induced migration is intimately coupled to polarity reversal although we couldn't distinguish whether polarity reversal was a cause or a consequence of cell migration.

Polarity reversal is an early feature of EMT

To solve the ambiguity of polarity reversal contribution to cell scattering, we looked for micropattern geometries that could prevent cell migration. Restricting micropattern size is not sufficient to prevent cell motion because cells can exchange their positions and rotate within the micropatterned area (Huang et al., 2005; Tseng et al., 2012). Square-shaped micropatterns could not prevent the rotation of normal epithelial cells and were even less able to constrain that of TGF-β-induced mesenchymal cells (Figure 2A-i). Bowtie-shaped micropatterns stabilized the position of epithelial cells but could not prevent mesenchymal cell motion (Figure 2A-ii). H-shaped micropattern could block both epithelial (Tseng et al., 2012) and mesenchymal cell motion, placing them in similar and thus comparable conditions (Figure 2A-iii). Hence H-shaped micropatterns were used in further experiments to compare epithelial and mesenchymal cell polarity.

Single MCF10A or MDCK cells were plated on H-shaped micropatterns and fixed 24 hour later to give them enough time to divide once and form daughter cell doublets. Nucleus-centrosome vector orientations were measured with respect to the nucleus-nucleus axis pointing toward the adjacent cell (Figure 2C). Nucleus-centrosome distances were normalized with respect to nucleus size (Figure 2C). Thus, positive coordinates corresponded to nucleus-centrosome axes pointing toward adjacent cells and large values to highly eccentric centrosome positions. Both epithelial MCF10A (cultured in defined medium) and MDCK cells (cultured in classical growth medium with serum) displayed marked polarization toward the CCJ formed between adjacent cells (Figure 2D). Strikingly, MCF10A cells treated with TGF-β for 5 days and MDCK cells treated with HGF for 3 days both displayed the opposite polarity orientation, although confined daughter cells could not migrate away from each other (Figure 2D). This polarity reversal was also quantified by measuring the centrosome X coordinate along the nucleus-nucleus axis, hereafter referred to as the cell polarity index toward CCJ. The coordinate sign change attests to the centrosome repositioning from the nucleus side oriented toward the CCJ to the side oriented toward CMA (Figure 2E). Interestingly, in MCF10A treated with TGF-β, this polarity reversal was due to both centrosomes moving away from the CCJ to the cell center and nuclei moving away from CMA toward CCJ (Figure 2E, Figure S4A). By contrast, in MDCK,

nuclei positioning was not affected by HGF treatment, and centrosome repositioning alone contributed to polarity reversal (Figure 2E).

Progressive reversal of cell polarity

TGF-β treatment is known to take several days to induce a full EMT although the very first changes appear a few hours after TGF-β addition (J. D'Souza et al., 2014). We thought to evaluate the timing of cell polarity reversal with respect to the entire EMT process. Cells were first plated on micropatterns and then treated with TGF-β for increasing periods of time. In MCF10A, polarity was reversed in less than 24 hours (Figure 2F). In MDCK, TGF-β effects were detectable after 4 hours of treatment and polarity was reversed after 8 hours only. HGF effects on MDCK were even faster; polarity changed almost immediately and was reversed completely within 4 hours (Figure 2F). These data imply that centrosome repositioning and polarity reversal are early signs of EMT concomitant with the first changes in protein expression following TGF-β addition (J. D'Souza et al., 2014).

Cell shape and contractility in polarity reversal

Actin dynamics at the cell front have been shown to be involved in organelles, and notably centrosome and nucleus positioning (Dupin et al., 2009; Gomes et al., 2005; Hale et al., 2011; Rodríguez-Fraticelli et al., 2012). This raised the possibility that nucleus and centrosome repositioning during early EMT stages are consequences rather than causes of actin network remodeling. Interestingly, inhibition of acto-myosin contractility with blebbistatin (or inactivation of MLCK with Y-27632) could reinforce cell polarization toward CCJ in control MDCK cells and revert polarization toward CMA in MDCK treated with HGF by acting on nucleus but not on centrosome positioning (Figure S4C,D). Hence, nucleus repositioning away from CMA and toward CCJ, at least in MDCK, appeared to depend directly on acto-myosin contractility. On the contrary, centrosome repositioning toward CMA and away from CCJ was independent of cell contractility.

Cell size usually increases during EMT (Lamouille and Derynck, 2007) but this could not happen in our conditions in which cells were confined in micropatterns. Since cell shape extension has been shown to induce polarity reversal in MDCK (Rodríguez-Fraticelli et al., 2012) we tested whether it could further contribute to polarity reversal during EMT. Indeed we found that allowing MCF10A and MDCK cells to spread on larger micropatterns (1600 or 2200 μm^2 instead of 1100 μm^2) reduced epithelial cell polarization toward CCJ and amplified cell polarity reversal in TGF-β and HGF-treated cells (Figure S5A).

Matrix stiffness promotes polarity reversal

We further investigated polarity orientation changes in other classical models of EMT. NMuMG and EpH4 are luminal mammary cells that are known to be highly sensitive to EMT induction (Lamouille and Derynck, 2007; Montesano et al., 2007) (Figure S2G,H). To our surprise, when plated on micropatterns, both cell types were polarized toward CMA (mesenchyme-like polarity) and not toward CCJ. Since TGF-β was absent from the growth factor-defined serum-free culture medium, we reasoned that EMT might have been induced by the cell culture substrate. Indeed, matrix stiffness is a potent EMT inducer (Markowski et al., 2012; Wei et al., 2015). Cells were thus plated on micropatterned poly-acrylamide gels of controlled stiffness (Vignaud et al., 2014). On such soft substrates, cell doublets spread to a lesser extent and adopted a more compact geometry. When cultured on 10kPa gels, EpH4 displayed a typical epithelial polarity with the nucleus-centrosome axis oriented toward CCJ, opposite to their polarization on glass, the stiffness of which is of the order of gigapascals (Figure 3A). Stiffness had to be further reduced to 1 kPa for NMuMG to recover a typical epithelial-like polarity (Figure 3B). These results show that matrix stiffness is sufficient to induce polarity reversal in the absence of TGF-β and thereby predispose epithelial cells to a mesenchyme transition. They also revealed that polarity reversal is quite reactive to EMT factors and that it can be easily induced in sensitive epithelial cells in response to mechanical and/or biochemical stimulations.

Matrix stiffness modulates CMA turnover and the production of traction forces on ECM (Levental et al., 2009; Paszek et al., 2005) suggesting that activation of CMA during EMT might be sufficient to promote polarity reversal independently of the concurrent remodeling of CCJ. However, modulation of matrix composition by using different combinations and concentrations of ECM protein coatings was not sufficient to induce epithelial polarity reversal (Figure S5B). Furthermore, single MCF10A cells plated on asymmetric micropatterns did not increase the orientation of their nucleus-centrosome axis toward CMA at the cell front in response to TGF-β stimulation (Figure S4B). These observations suggest that the presence and remodeling of CCJ during EMT played an important role in polarity reversal.

Microtubule network remodeling accompany centrosome re-centering

Since centrosome positioning mostly depends on the microtubule network (Mimori-Kiyosue, 2011; Tang and Marshall, 2012), we compared microtubule network architectures before and after induction of EMT to gain further insight in the mechanism supporting centrosome repositioning. TGF-β treatment induced a drastic drop in the total amount of microtubules (Figure 4A). This reduction was even more drastic at the CCJ along which

microtubules are concentrated when cells are in their epithelial state (Figure 4A). These changes could be quantified by the diminution of polymerized a-tubulin intensity (Figure 4A) as well as the reduction in the number of EB1 comets (Figure 4B). Those differences could be explained by a reduction of centrosomal microtubules, as suggested by the reduction in g-tubulin intensity (Figure 4C) and the number of EB1 comets at the centrosome (Figure 4B). These observations suggest, in addition to the classical view that dynein associated to Par3/Par6 and b-catenin at CCJ pulls on the centrosome contributing to its off-centering (Harris and Peifer, 2005, 2007; Ligon and Holzbaur, 2007; Ligon et al., 2001; Schmoranzer et al., 2009), that the increase in the amount of microtubules may also be involved. We tested this new hypothesis by performing numerical simulations with Cytosim (Nedelec and Foethke, 2007) in which the number of microtubules was modulated. Asters were constrained to grow in a confined space similar to the cell shape obtained on square micropatterns. Cytoplasmic dyneins were scattered throughout the cytoplasm so that their minus-end directed motion could promote aster centering by exerting pulling forces on microtubules (Wu et al., 2011). Microtubules were allowed to glide along and to push on cell edges as they grow. Interestingly, at low microtubule numbers (10-100), asters moved and stabilized at the cell center whereas with higher numbers of microtubules (200-350), the pushing forces exceeded the centering force and moved the centrosome off-center, toward the cell edge (Figure 4D, movie S3 and S4). Measuring centrosome final position in relation to the number of microtubules confirmed this observation (Figure 4E). Importantly, this behavior was quite robust and did not depend on centrosome initial position (Figure 4F). Accordingly, microtubule network disassembly in response to TGF-β could actively contribute to centrosome displacement from CCJ to cell center. These results suggest that both the amount of polymerized tubulin and the local stabilization of microtubules along CCJ were involved in the transition from an off-centered microtubule network in epithelial cells to a centered conformation in mesenchymal cells.

Par3 regulates centrosome repositioning during EMT

To further understand the molecular mechanism allowing CCJ to modulate microtubule network asymmetry and centrosome off-centering, we quantified the changes in CCJ composition during the early stages of EMT. We first confirmed in our minimalist model of multicellular organization that the classical markers of EMT followed the trends described in physiological conditions (Xue et al., 2012). As expected, the concentration of E-cadherin at the CCJ decreased while the level of N-cadherin increased upon induction of EMT (Figure 5A). Interestingly, levels of a and β-catenin were strongly reduced, suggesting that the strength of the CCJ was diminished although cells were forced to stay in contact.

Partitioning defective proteins (PAR) polarity complexes Par3/Par6/aPKC are associated to CCJ and have ben shown to regulate centrosome positioning in a wide range of cell types

(Feldman and Priess, 2012; Oliaro et al., 2010; Schmoranzer et al., 2009; Solecki et al., 2009; St Johnston and Sanson, 2011). Par3 is notably involved in centrosome translocation from central to apical positioning during mesenchyme-to-epithelium transitions during neurulation (Hong et al., 2010). It was therefore likely to be involved in centrosome repositioning during EMT. After 5-day treatment of TGF-β, Par3 localization at CCJ was drastically reduced (Figure 5B). Interestingly the junction density of Par3 appeared related to centrosome positioning. Direct measurement of the distance separating centrosome and CCJ was sometimes made difficult by the curvy and non-vertical shape of the junction. Therefore, the measurement of the distance separating the two centrosomes was used instead as it also reflects centrosome positioning with respect to the interface between the two cells. These measures revealed a clear correlation between Par3 concentration and centrosome distance to CCJ: the higher the concentration of PAR3 at CCJ, the closer the centrosome (Figure 5B). Inhibition of signaling downstream of TGF-β type I receptor by SB431542 (Inman et al., 2002) restored Par3 levels at CCJ, centrosome off-centering and cell polarity index toward CCJ, showing that Par3-mediated centrosome repositioning was a direct outcome of TGF-β signaling (Figure 5B).

We further tested the direct role of Par3 by modulating its cellular concentration. Down-regulation of Par3 levels by Pard3 siRNA in MCF10A cells increased the inter-centrosome distance. The overall polarity index however remained unaffected, because nuclei were also further separated due to junction weakening and cell separation (Figure 5C). More strikingly, overexpression of Par3b in TGF-β treated cells, restored centrosome positioning close to CCJ along with cell polarization towards CCJ, suggesting that Par3 down-regulation at the junction was actually responsible for centrosome repositioning at the cell center during polarity reversal (Figure 5D).

Cell-cell and Cell-Matrix force redistribution upon EMT

To understand further how CCJ remodeling and centrosome-microtubule network reorganization in static and contacting cells could impact subsequent EMT physical processes such as cell separation and cell migration, we looked next at the cell contractile machinery, which is a central regulator of EMT (O'Connor and Gomez, 2014). We first quantified the localization of several structural components of contractile structures by taking advantage of normalized cell shapes to average immuno-stainings and calculate the spatial distributions of filamentous actin (F-actin), phosphorylated-myosin II and paxillin. TGF-β induced an increase of F-actin in stress fibers connecting the peripheral CMA, along the vertical H bars, and newly formed CMA next to CCJ, along the horizontal H bar (Figure 6A). This remodeling was accompanied by a relocalization of myosins along these fibers and a very strong increase of paxillin concentration on both previous and newly formed CMA (Figure 6B). All these changes suggested an increase of traction forces on the ECM and a redistribution of intra-cellular

tensional forces. We measured those forces by applying traction force microscopy to micropatterned cells on poly-acrylamide gels (Butler et al., 2002; Martiel et al., 2015). When applied to cell doublets, this method allowed the quantification of both traction forces on ECM and inter-cellular tensional forces since the sum of both should be null in each cell and the sum of traction forces for the entire doublet should be null as well (Liu et al., 2010). As expected from the immuno-stainings, TGF-β treated MCF10A cells showed overall higher total traction forces compared to control cells (Figure 6C). To our surprise, average inter-cellular forces were not reduced in those cells despite the apparent weakening of CCJ (Figure 5A). However, we detected a clear decrease of inter-cellular tension to extra-cellular traction ratio in individual cells in response to TGF-β treatment (Figure 6 C). The overall increase of cell contractility upon TGF-β treatment was consistent with our previous observation of a global disassembly of the microtubule network since both phenomenon are intimately linked (Guilluy et al., 2011; Rape et al., 2011). The specific increase of mechanical forces on CMA, while tension on CCJ remained unchanged, suggests that any subsequent separation and scattering processes would be mostly promoted by biochemical and mechanical activation of CMA, rather than by the weakening of CCJ (Rooij et al., 2005).

The observed redistribution of actin dynamics and balance of forces away from CCJ and toward CMA was reminiscent of the changes observed during neural crest cell repulsion and scattering (Scarpa et al., 2015). In both cases, traction forces on CMA appear to promote cell migration away from each other. This reinforces our hypothesis that polarity reversal in static cells is instrumental in the subsequent induction of cell scattering.

Polarity reversal is necessary for cell scattering

Our previous experiments showed that polarity reversal was not just a consequence of cell migration since it could be induced in non-migrating cells. Furthermore, they suggested that polarity reversal was coupled to the redistribution of traction forces, which could prime cell scattering. However, direct evidence for polarity reversal being at the origin of cell scattering is still lacking since it was difficult to temporally and spatially dissect these two phenomenons. Indeed, on micropatterned lines, TGF-β treated cells separated and reversed polarity synchronously (Figure S3C). On small micropatterns, cells could revert polarity but couldn't move, preventing any conclusion about the role of polarity reversal on cell motion (Figure 2). To directly test the potential upstream effect of polarity reversal on cell motion we decided to use dynamic micropatterning to first allow polarity reversal and then trigger the spatial release of previously confined cells. Thus, we could compare the scattering of cells with pre-established epithelial or inverted polarities.

Dynamic micropatterning relies on the use of click chemistry to graft RGD peptides to the PEG chains preventing cell adhesion around micropatterns (van Dongen et al., 2013). The mild conditions of the azide-alkyne cycloaddition offer the possibility to graft a RGD-alkyne compound to a PEG-azide chain in the presence of living cells (Figure 7A). Thus, micropatterned cells can start migrating out of the micropattern upon addition and grafting of RGD groups to the PEG chains.

We first confirmed the expected outcomes of EMT induction i.e. that most MCF10A epithelial cells remain in contact with each other while TGF-β treated cells tend to separate within 4 hour after cell release by addition of RGD (Figure 7B). Interestingly, not all TGF-β treated cells separated. Considering that all cells did not fully revert their polarity in response to TGF-β (Figure 2C, D), we hypothesized that scattering ability could be linked to the occurrence of polarity reversal. To challenge this hypothesis, we segregated the TGF-β treated cell population on the basis of their nucleus-centrosome orientation toward CCJ or CMA (Figure 7C). For this, we used the larger Golgi apparatus rather than small centrosome markers to facilitate their detection by live cell microscopy. We saw a clear difference in scattering behavior of TGF-β treated and transiently expressing Golgi apparatus marker cells depending upon the initial orientation of their polarity axis (Figure 7C, movie S5, S6). Cells with the polarity axis pointing toward CCJ (similar to non-treated epithelial cells) had less propensity (24%, n=25) to separate from each other compared to cells with a polarity axis pointing toward CMA (69%, n=43). This experiment conclusively proved that, upon TGF-β induced EMT, cells which maintained their polarity toward CCJ behaved like epithelial cells with less scattering potential while cells with inverted polarity are primed for cell scattering. Hence, we establish that EMT induction involves polarity reversal by centrosome repositioning away from inter-cellular junctions to promote cell separation and single cell migration.

Discussion

These results have revealed the existence of a global intra-cellular rearrangement occurring in the few hours following the addition by TGF-β, which therefore appeared as one of the earliest morphological sign of EMT that precedes complete inter-cellular junction disassembly. Microtubule network geometry and centrosome position rapidly adapt to early modifications of CCJ composition and notably to the reduction of Par3 concentration. Decreases in microtubule nucleation and polymerization in addition to the decrease of selective microtubule stabilization along the CCJ lead to centrosome displacement from the CCJ to the cell center. These changes were coupled to a relative increase of traction forces on the extra-cellular matrix compared to inter-cellular tensions. This redistribution of intra-cellular forces moves the nucleus back toward CCJ and thereby leads to an effective complete reversal of cell internal polarity with nucleus-centrosome axis switching from an orientation toward CCJ to an orientation toward CMA. The internal rearrangement and associated redistribution of mechanical forces put cells in an appropriate conformation to then separate and move away from each other (Figure 7D).

The difficulty to follow cytoskeleton reorganization at a subcellular scale in vivo, and the disordered and poorly reproducible arrangements of multi-cellular aggregates in 3D culture have somehow hidden the systematic repositioning of the centrosome toward the cell edge in contact with ECM during EMT. The use of micropatterned lines or square shapes to control cell number and position, with or without the possibility to migrate, shined some light on this central cell response during early stages of EMT. Polarity was not lost but physically reversed from the lumen toward the basement membrane by both centrosome and nucleus repositioning. Moreover, dynamic micropatterning, to sequentially confine and then release cells, allowed us to demonstrate that polarity reversal was not a consequence of cell migration but instead actively promoting it.

The centrosome-microtubule network appears to act as an extensive and sensitive spatial integrator of cell adhesion cues. Subtle variations of inter-cellular adhesion maturation, as revealed by the level of Par3 for example, were directly translated into modulations of centrosome positioning. Thereby, the centrosome-microtubule network allows the orientation of cell internal polarity to adapt to changes in the spatial organization of cell adhesion. How the centrosome adopts an off-center position toward CCJ in epithelial cells is not well understood. Our observations fit with two types of mechanisms: selective pulling forces along the CCJ and global pushing along cell edges. Presence of Par3 at the CCJ and the local accumulation of cortical microtubules are consistent with the local production of pulling forces on the centrosome as it has been described during immune synapse formation (Yi et al., 2013), planar cell polarity establishment (Jiang et al., 2015; Sipe et al., 2013), intestinal cell polarization

(Feldman and Priess, 2012), neurulation (Buckley et al., 2012; Hong et al., 2010) and spindle orientation (Hao et al., 2010). The ability of Par3 to recruit dynein, which captures and pulls on microtubules, would be consistent with this interpretation (Ligon et al., 2001; Schmoranzer et al., 2009). The reduction of Par3 and cortical microtubules at the CCJ are also consistent with the centrosome moving back to the center upon EMT induction. Interestingly, Par3 downregulation was sufficient to re-center the centrosome in epithelial cells but inefficient to act upon nucleus positioning and thus could not trigger polarity reversal, which probably requires other pathways down-stream of TGF-β. Nucleus positioning toward the future back of the cell is likely to depend on the development of actin retrograde flow from activated CMA (Dupin et al., 2009; Gomes et al., 2005; Théry et al., 2006). The shape and spatial organization of microtubules also suggest another interpretation in which microtubules that are longer than the cell size push the centrosome away from the center, as it has been observed in lymphoblastic cells (Bornens et al., 1989) and in reconstituted microtubule networks in lipid vesicles (Pinot et al., 2009) or microfabricated chambers (Faivre-Moskalenko and Dogterom, 2002). Our numerical simulations show that a high number of microtubules should have similar off-centering effects. This is in line with the recent observation of off-centered centrosomes in cells bearing excessive microtubules (Godinho et al., 2014). Microtubule capture and stabilization at CCJ (Chausovsky et al., 2000; Shahbazi et al., 2013; Shtutman et al., 2008), without any specific production of tensile forces, could bias this off-centering (Harris and Peifer, 2007; Sugioka and Sawa, 2012; Sumigray et al., 2011). This interpretation would be consistent with our observation that centrosome centering after EMT induction is associated with a reduction in the number of microtubules nucleated from the centrosome. Noteworthy, the reductions of g-tubulin, ninein and EB1 at the centrosome suggest that TGF-β not only acts on the microtubule network geometry via its effect on actin network organization but also modulates centrosome composition.

Importantly, our results show that centrosome-microtubule network geometry adapts to but also actively feedbacks to the adhesion-actin network configuration. Centrosome repositioning away from CCJ and toward CMA was required for cell scattering and migration. TGF-β treated cells that did not undergo polarity reversal could not separate upon the release of spatial constraint suggesting that the centrosome stabilizes CCJ as long as it stays close to it and promotes the migration machinery as it comes close to CMA at the cell front. Indeed microtubules interact and feedback with both CCJ and CMA (Akhmanova and Stehbens, 2009). The centrosome and CCJ exchange materials: some centrosomal proteins transit from centrosome to CCJ allowing microtubule anchoring and stabilization at CCJ (Gavilan et al., 2015; Lechler and Fuchs, 2007; Moss et al., 2007; Sumigray et al., 2011). In return, microtubules stabilize CCJ (Meng et al., 2008), notably by the dynein-dependent recruitment of CCJ components like occludin (Glotfelty et al., 2014). Some translocated centrosomal proteins even

promote CCJ reinforcement and epithelial cell acquisition of a columnar shape (Gavilan et al., 2015). Similarly, as the centrosome leaves CCJ and comes closer to CMA, microtubule density increases close to CMA and can promote actin polymerization and CMA turnover and thereby foster cell migration (Etienne-Manneville, 2013). Interestingly, during epithelial scattering occludin and Par3 have been shown to relocalize from CCJ to the cell front where they promote leading edge protrusion and cell migration (Du et al., 2010). Par3 relocalization was also observed in our working conditions on micropatterns. These considerations account for the capacity of centrosome relocalisation from CCJ toward CMA to actively weaken inter-cellular interaction and promote the cell migration machinery even before effective cell displacement and thereby primes cell scattering.

It is noteworthy that some forms of EMT, such as zebrafish lateral line development (Revenu et al., 2014) are not associated with centrosome inversion. In such cases, the centrosome stays at the migrating cell rear as in many other examples of amoeboid-like type of cell migration (Doyle et al., 2009; Pouthas et al., 2008; Ratner et al., 1997). These counter examples, in which centrosome position is not inverted prior to cell migration, suggest that the polarity reversal we describe here may be specific to the acquisition of a mesenchymal type of migration.

Whether early stages of cancer cell disengagement and dissemination from tumors proceed through polarity reversal is a question that needs to be further investigated. It does not seem to be required for epithelial cells with extra-centrosomes to break through their basement membrane (Godinho et al., 2014). But this particular case should not be taken as a rule for other types of tumor transformation since those cells have specific defects in the regulation of the microtubule network. Indeed, the loss of Par3, which was sufficient to induce centrosome repositioning away from CCJ in our conditions, has been shown to promote breast cancer metastasis (Xue et al., 2012).

Our results reveal the key role of centrosome-microtubule and actin network interplay in the geometrical and mechanical regulation of complex tissue remodeling such as EMT. They should prompt us to investigate further the mechanism supporting their biochemical and physical interactions in various morphogenetic processes.

Materials and Methods

MCF10A cells were cultured in Lonza MEGM medium (Lonza #CC3150) as described by ATCC protocol. MDCK, NMuMG and EpH4 cells were cultured as described in extended experimental procedures. EMT was induced by addition of 5 ng/ml TGF-β1 to MCF10A for 5 days, 2 ng/ml to NMuMG & EpH4 for 3 days and 10 ng/ml of HGF for MDCK for 3 days. Micropatterns on glass were fabricated as described previous ly (Azioune et al., 2010). Cell seeding was optimized to achieve single cell attachment per micropattern and cells were fixed 24 hours after. MCF10A 3D cultures were prepared as described previously (Debnath et al., 2003). Micropatterning on soft substrate and Traction force microscopy was performed for measuring cellular forces using Fourier transform traction cytometry analysis as described (Martiel et al., 2015; Vignaud et al., 2014). Dynamic micropatterning was performed using Azide-PLL-PEG and BCN-RGD (van Dongen et al., 2013).

Supplemental Information

Supplemental Information includes Supplemental Experimental Procedures, five figures, and five movies.

Authors' contribution

M.B performed most experimental work and data analyses. M.P performed most experiments with MDCK. S.T. performed experiments on mouse mammary glands. G.B performed experiments on mouse embryos. Q.T. performed initial experiments, stainings on Fig 6A-B and contributed to software developments for analysis of nucleus-centrosome polarity quantification and for traction force microscopy. G.L. performed numerical simulations and developed image analysis tools. O.F.C. designed experiments on 3D cell culture and provided key information about EMT to the consortium. J.Y. provided critical comments about the work and edited the manuscript. M.T. directed the project and wrote the manuscript.

Acknowledgments

We thank Priscilla Soulie for providing EpH4 cells, James Sillibourne for providing human-Ninein antibody, Matthieu Piel for providing APP & BCN-RDG compounds and advices for dynamic patterning and Benoit Vianay for his help with microscopy. We also thank Laurent Blanchoin for his useful comments throughout the project.

Figure 1

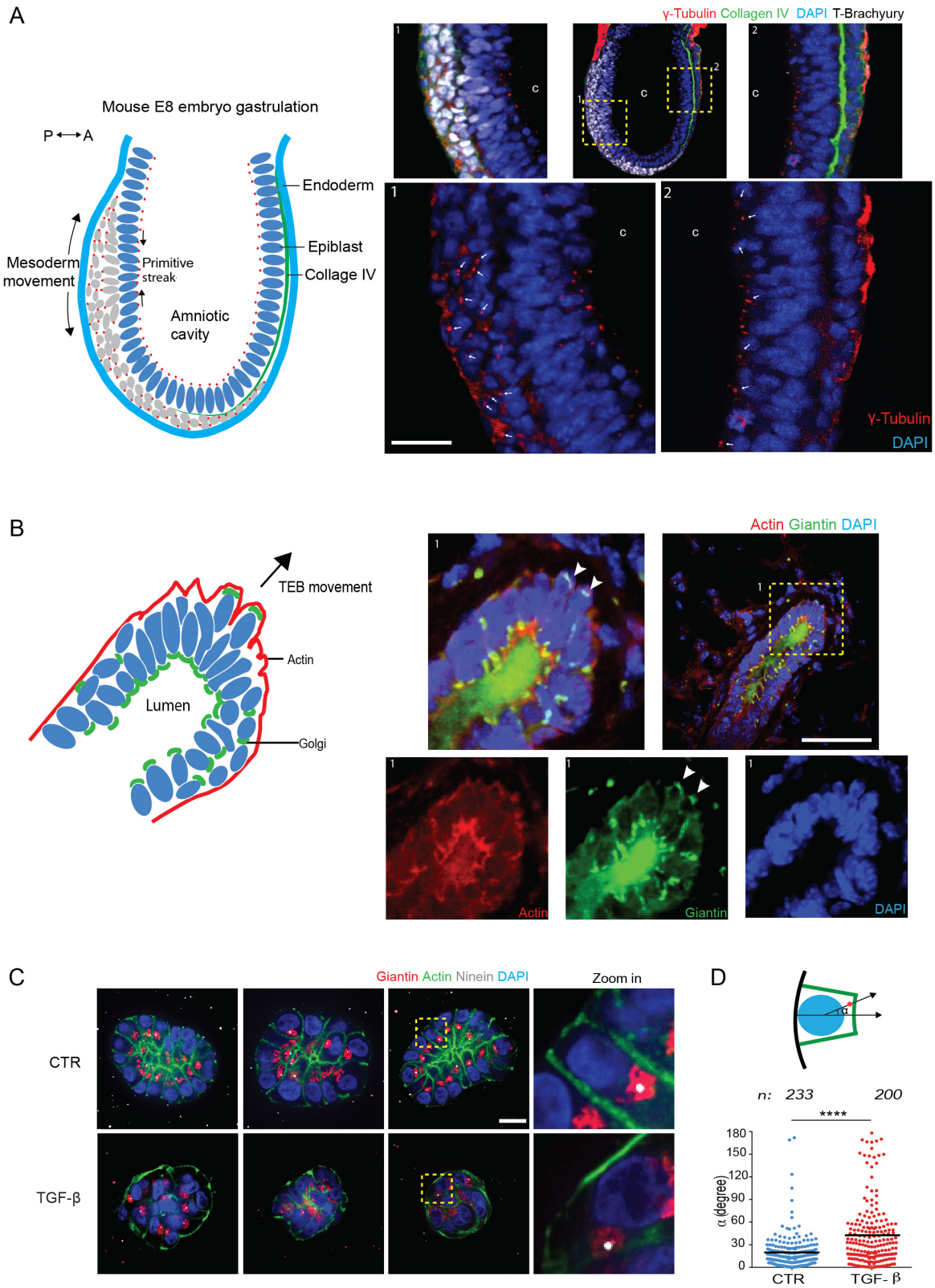
A
Mouse E8 embryo gastrulation
P ⟷ A
Endoderm
Epiblast
Collage IV
Primitive streak
Mesoderm movement
Amniotic cavity
γ-Tubulin Collagen IV DAPI T-Brachyury
γ-Tubulin
DAPI
B
TEB movement
Actin
Lumen
Golgi
Actin Giantin DAPI
Actin
Giantin
DAPI
C
Giantin Actin Ninein DAPI
Zoom in
CTR
TGF-β
D
n: 233 200
****
α (degree)
180
150
120
90
60
30
0
CTR
TGF- β

Figure 2

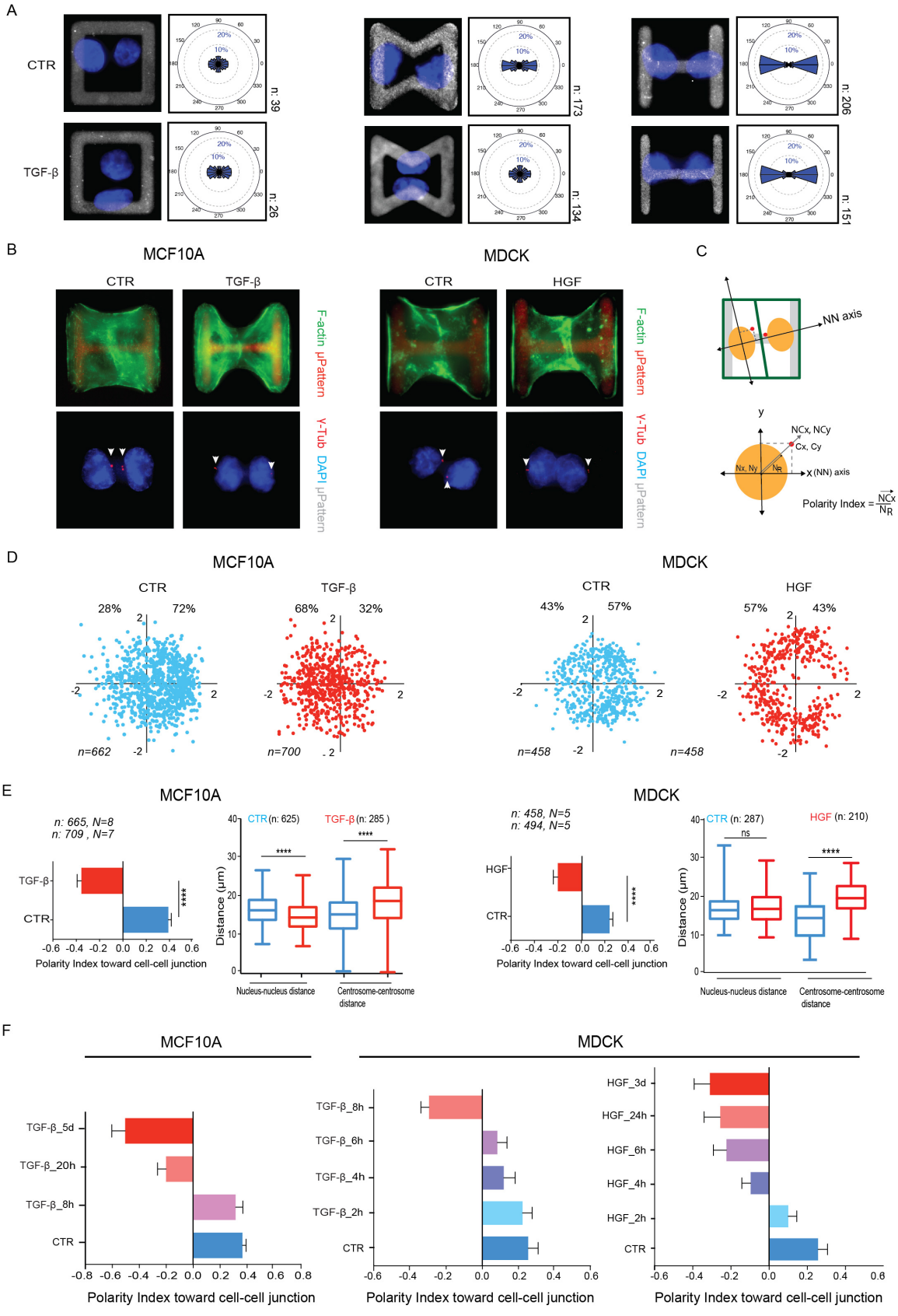
A
CTR
TGF-β
n: 39
n: 26
n: 173
n: 134
n: 206
n: 151
B
MCF10A
CTR
TGF-β
MDCK
CTR
HGF
F-actin µPattern
γ-Tub DAPI µPattern
C
NN axis
y
NCx, NCy
Cx, Cy
Nx, Ny
NR
x (NN) axis
Polarity Index = NCx / NR
D
MCF10A
CTR
28%
72%
n=662
TGF-β
68%
32%
n=700
MDCK
CTR
43%
57%
n=458
HGF
57%
43%
n=458
E
MCF10A
n: 665, N=8
n: 709 , N=7
TGF-β
CTR
Polarity Index toward cell-cell junction
CTR (n: 625)
TGF-β (n: 285)
Distance (µm)
Nucleus-nucleus distance
Centrosome-centrosome distance
MDCK
n: 458, N=5
n: 494, N=5
HGF
CTR
Polarity Index toward cell-cell junction
CTR (n: 287)
HGF (n: 210)
ns
F
MCF10A
TGF-β_5d
TGF-β_20h
TGF-β_8h
CTR
Polarity Index toward cell-cell junction
MDCK
TGF-β_8h
TGF-β_6h
TGF-β_4h
TGF-β_2h
CTR
Polarity Index toward cell-cell junction
HGF_3d
HGF_24h
HGF_6h
HGF_4h
HGF_2h
CTR
Polarity Index toward cell-cell junction

Figure 3

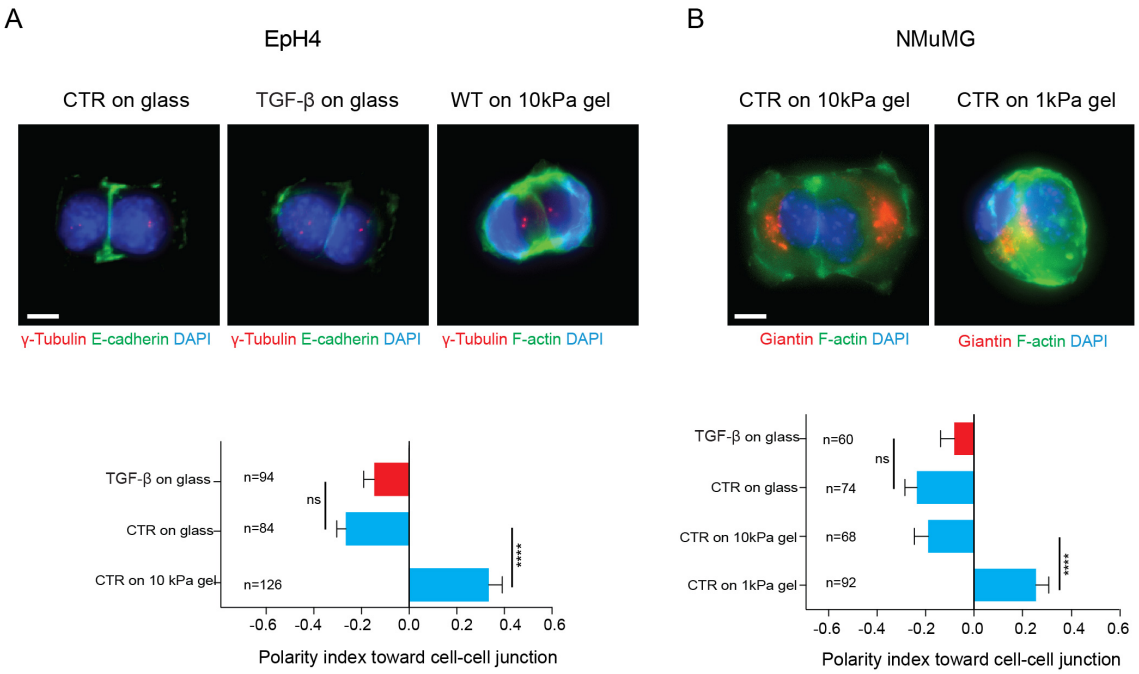
A
EpH4
CTR on glass
TGF-β on glass
WT on 10kPa gel
γ-Tubulin E-cadherin DAPI
γ-Tubulin E-cadherin DAPI
γ-Tubulin F-actin DAPI
TGF-β on glass
CTR on glass
CTR on 10 kPa gel
n=94
n=84
n=126
ns
****
-0.6 -0.4 -0.2 0.0 0.2 0.4 0.6
Polarity index toward cell-cell junction
B
NMuMG
CTR on 10kPa gel
CTR on 1kPa gel
Giantin F-actin DAPI
Giantin F-actin DAPI
TGF-β on glass
CTR on glass
CTR on 10kPa gel
CTR on 1kPa gel
n=60
n=74
n=68
n=92
ns
****
-0.6 -0.4 -0.2 0.0 0.2 0.4 0.6
Polarity index toward cell-cell junction

Figure 4

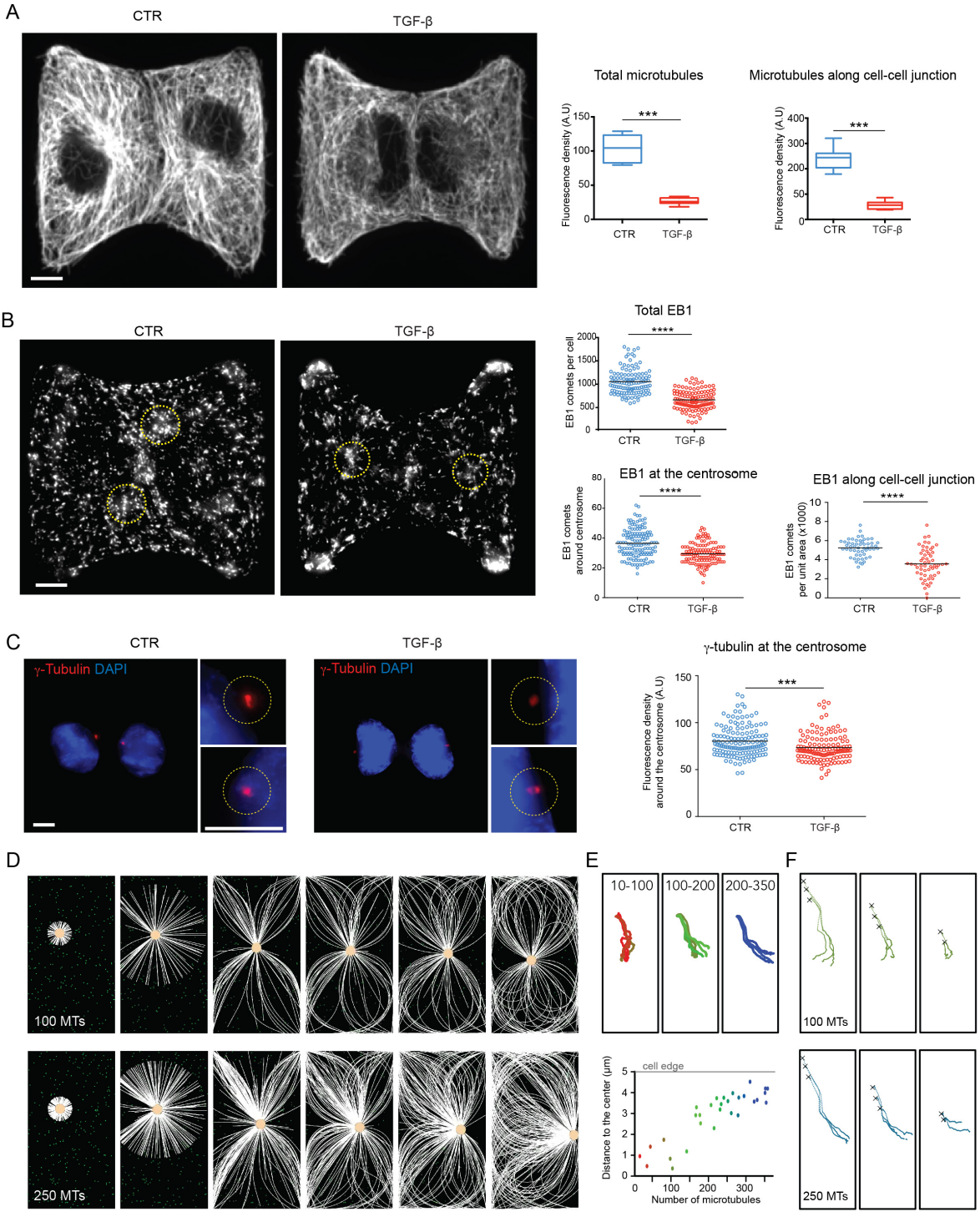
A
CTR
TGF-β
Total microtubules
Microtubules along cell-cell junction
Fluorescence density (A.U)
***
CTR
TGF-β
B
CTR
TGF-β
Total EB1
EB1 comets per cell
****
EB1 at the centrosome
EB1 comets around centrosome
EB1 along cell-cell junction
EB1 comets per unit area (x1000)
C
CTR
TGF-β
γ-Tubulin DAPI
γ-tubulin at the centrosome
Fluorescence density around the centrosome (A.U)
D
100 MTs
250 MTs
E
10-100
100-200
200-350
cell edge
Distance to the center (µm)
Number of microtubules
F
100 MTs
250 MTs

Figure 5

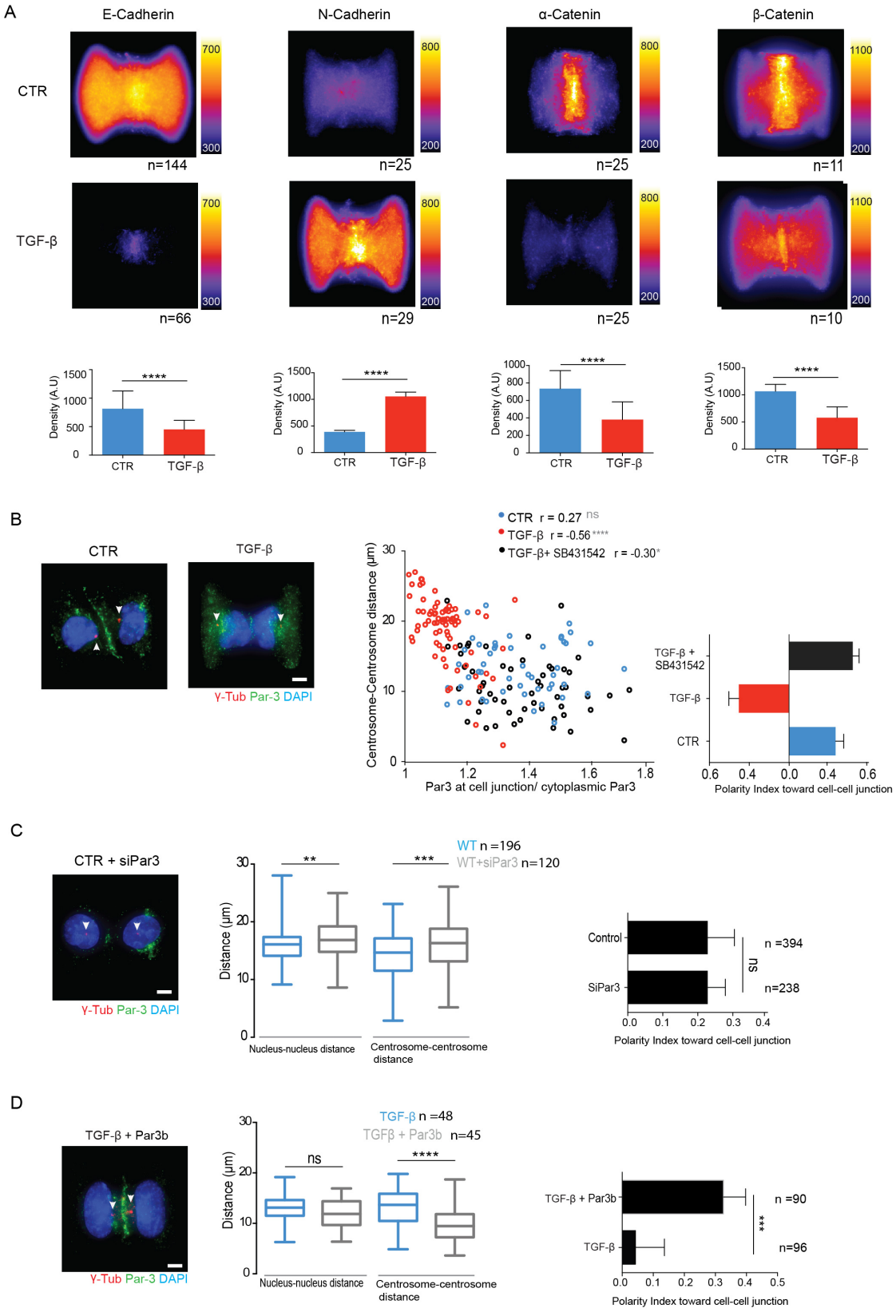
A
E-Cadherin
N-Cadherin
α-Catenin
β-Catenin
CTR
TGF-β
n=144
n=25
n=25
n=11
n=66
n=29
n=25
n=10
Density (A.U)
****
B
CTR
TGF-β
γ-Tub Par-3 DAPI
CTR r = 0.27 ns
TGF-β r = -0.56 ****
TGF-β+ SB431542 r = -0.30 *
Centrosome-Centrosome distance (µm)
Par3 at cell junction/ cytoplasmic Par3
TGF-β + SB431542
Polarity Index toward cell-cell junction
C
CTR + siPar3
γ-Tub Par-3 DAPI
WT n =196
WT+siPar3 n=120
Distance (µm)
Nucleus-nucleus distance
Centrosome-centrosome distance
Control
SiPar3
n =394
n=238
ns
D
TGF-β + Par3b
γ-Tub Par-3 DAPI
TGF-β n =48
TGFβ + Par3b n=45
n =90
n=96

Figure 6

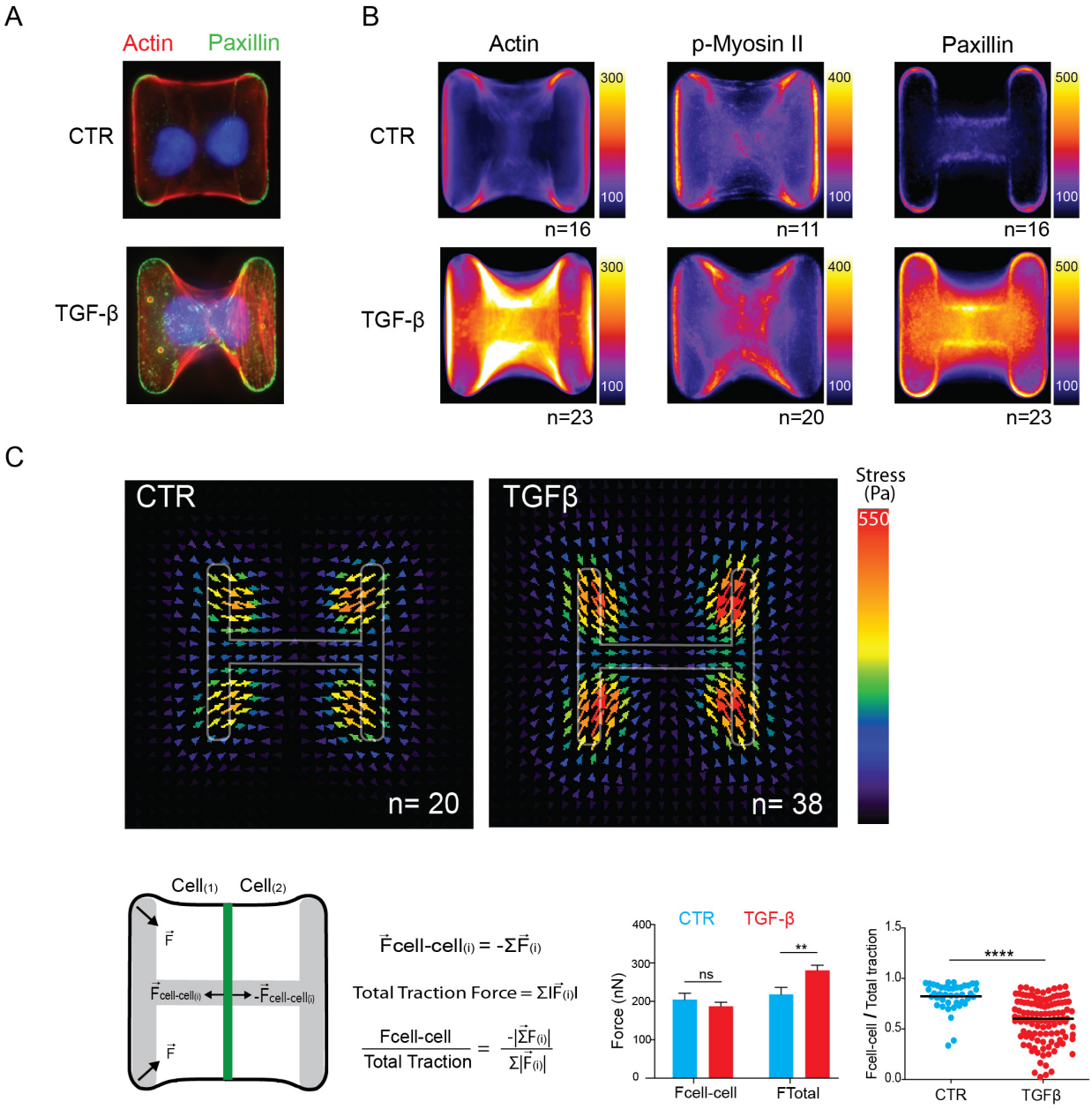
A
Actin
Paxillin
CTR
TGF-β
B
Actin
p-Myosin II
Paxillin
CTR
TGF-β
300
100
400
500
n=16
n=11
n=16
n=23
n=20
n=23
C
CTR
TGFβ
n= 20
n= 38
Stress (Pa)
550
Cell(1)
Cell(2)
Fcell-cell(i) = -ΣF(i)
Total Traction Force = Σ|F(i)|
Fcell-cell / Total Traction = -|ΣF(i)| / Σ|F(i)|
CTR
TGF-β
Force (nN)
ns
**
Fcell-cell
FTotal
Fcell-cell / Total traction
****
CTR
TGFβ

Figure 7

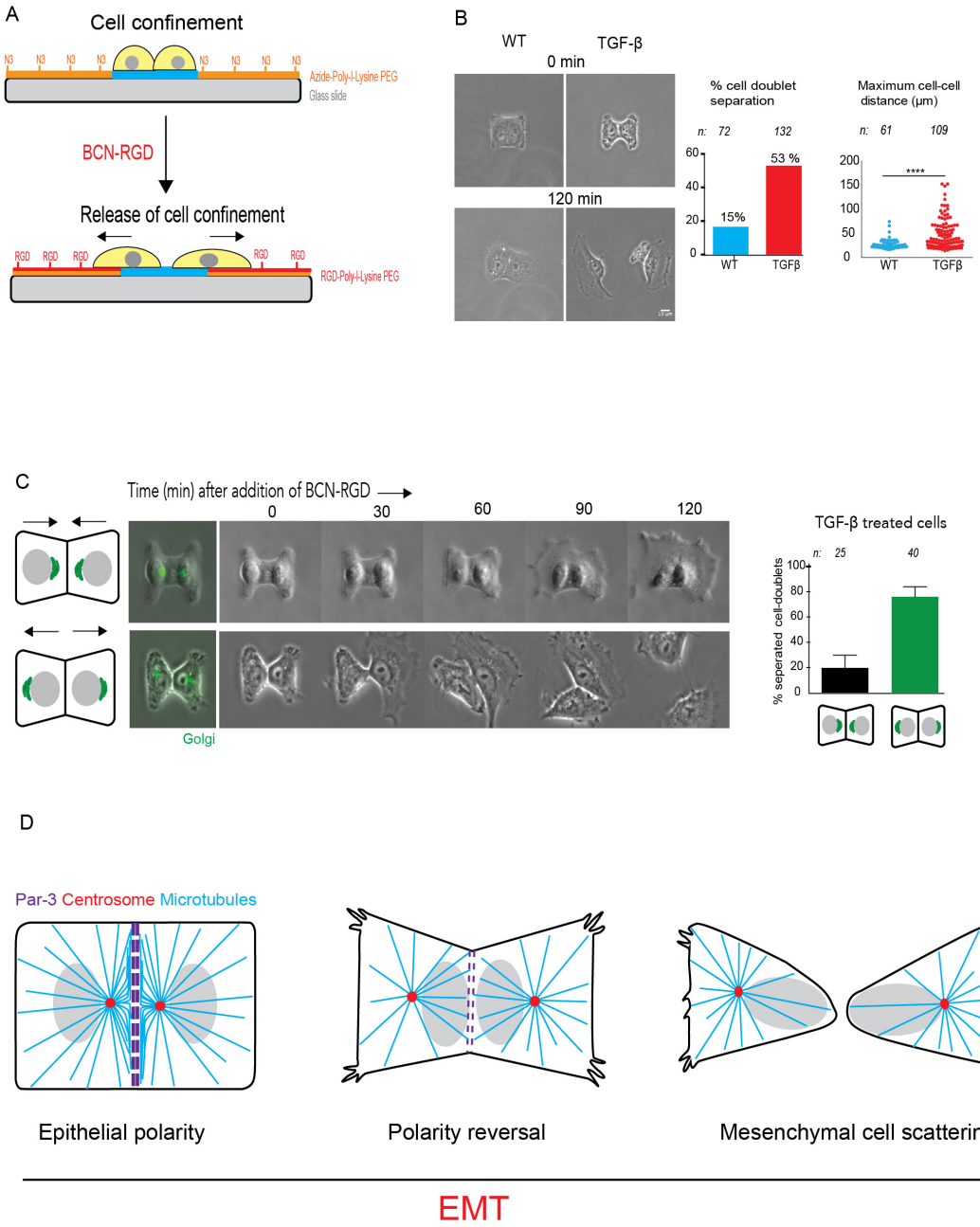
A
Cell confinement
N3
Azide-Poly-l-Lysine PEG
Glass slide
BCN-RGD
Release of cell confinement
RGD
RGD-Poly-l-Lysine PEG
B
WT
TGF-β
0 min
120 min
% cell doublet separation
n: 72 132
53 %
15%
WT
TGFβ
Maximum cell-cell distance (µm)
n: 61 109
****
C
Time (min) after addition of BCN-RGD
0
30
60
90
120
Golgi
TGF-β treated cells
n: 25 40
% seperated cell-doublets
D
Par-3 Centrosome Microtubules
Epithelial polarity
Polarity reversal
Mesenchymal cell scattering
EMT

Figure S1

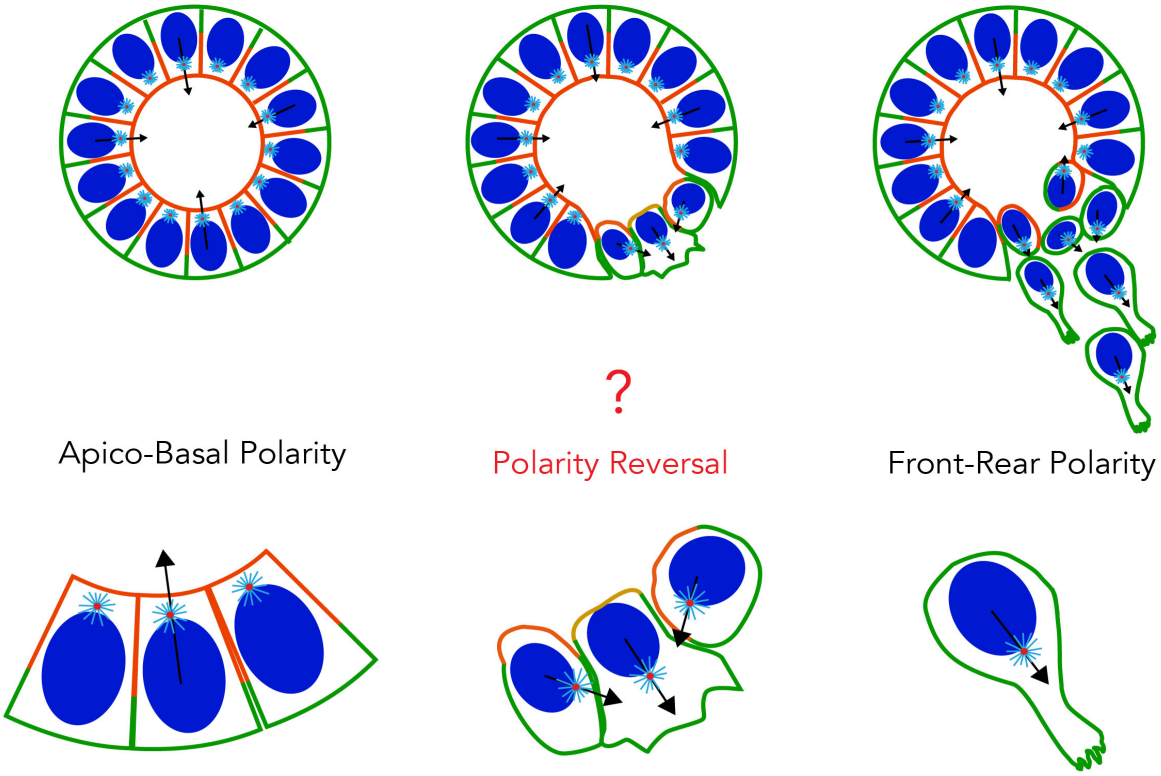
?
Apico-Basal Polarity
Polarity Reversal
Front-Rear Polarity

Figure S2

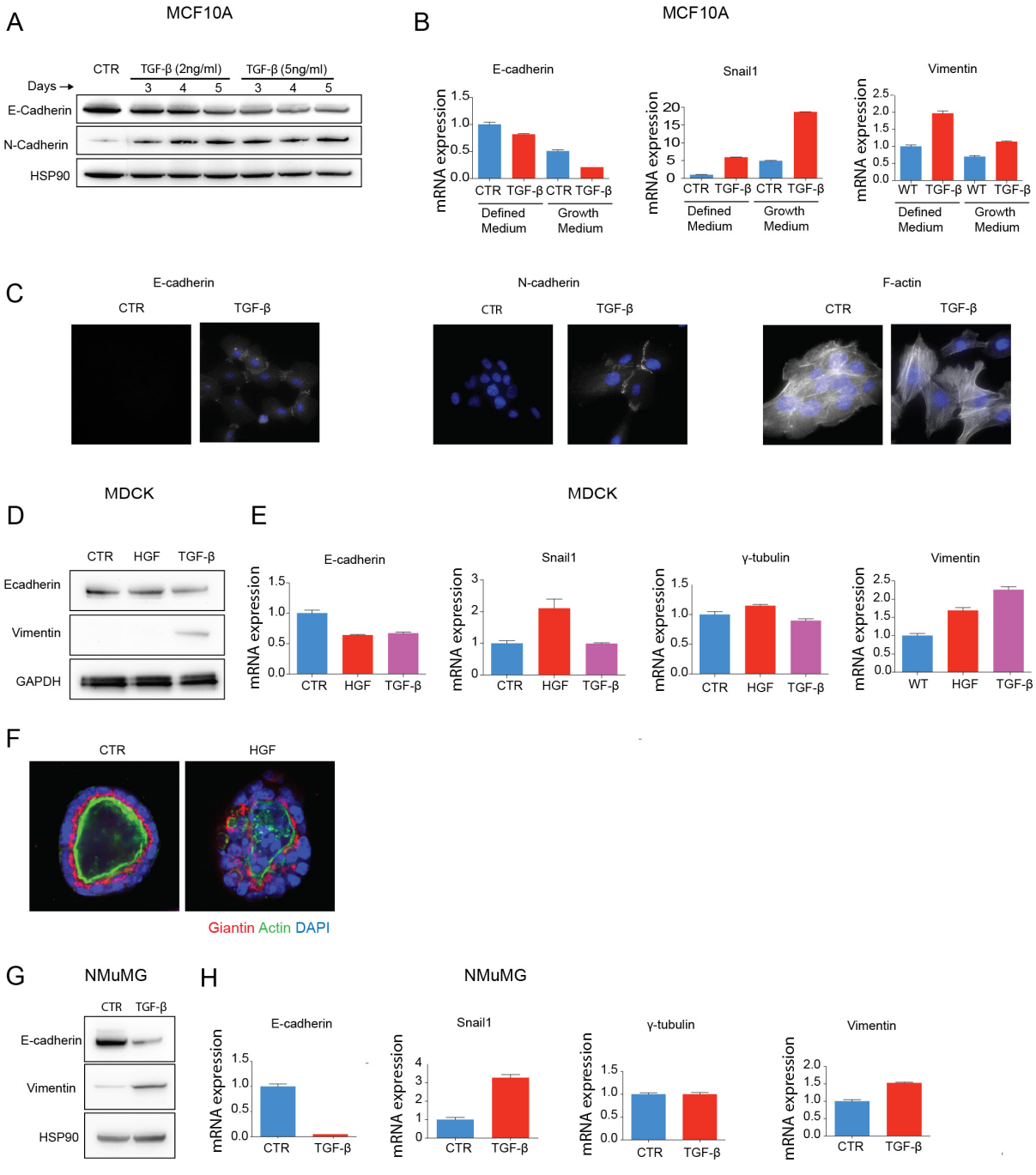
A
MCF10A
CTR
TGF-β (2ng/ml)
TGF-β (5ng/ml)
Days →
3 4 5 3 4 5
E-Cadherin
N-Cadherin
HSP90
B
MCF10A
E-cadherin
Snail1
Vimentin
mRNA expression
CTR TGF-β CTR TGF-β
Defined Medium
Growth Medium
WT TGF-β WT TGF-β
C
E-cadherin
N-cadherin
F-actin
CTR
TGF-β
D
MDCK
CTR HGF TGF-β
Ecadherin
Vimentin
GAPDH
E
MDCK
E-cadherin
Snail1
γ-tubulin
Vimentin
mRNA expression
CTR HGF TGF-β
WT HGF TGF-β
F
CTR
HGF
Giantin Actin DAPI
G
NMuMG
CTR TGF-β
E-cadherin
Vimentin
HSP90
H
NMuMG
E-cadherin
Snail1
γ-tubulin
Vimentin
mRNA expression
CTR TGF-β

Figure S3

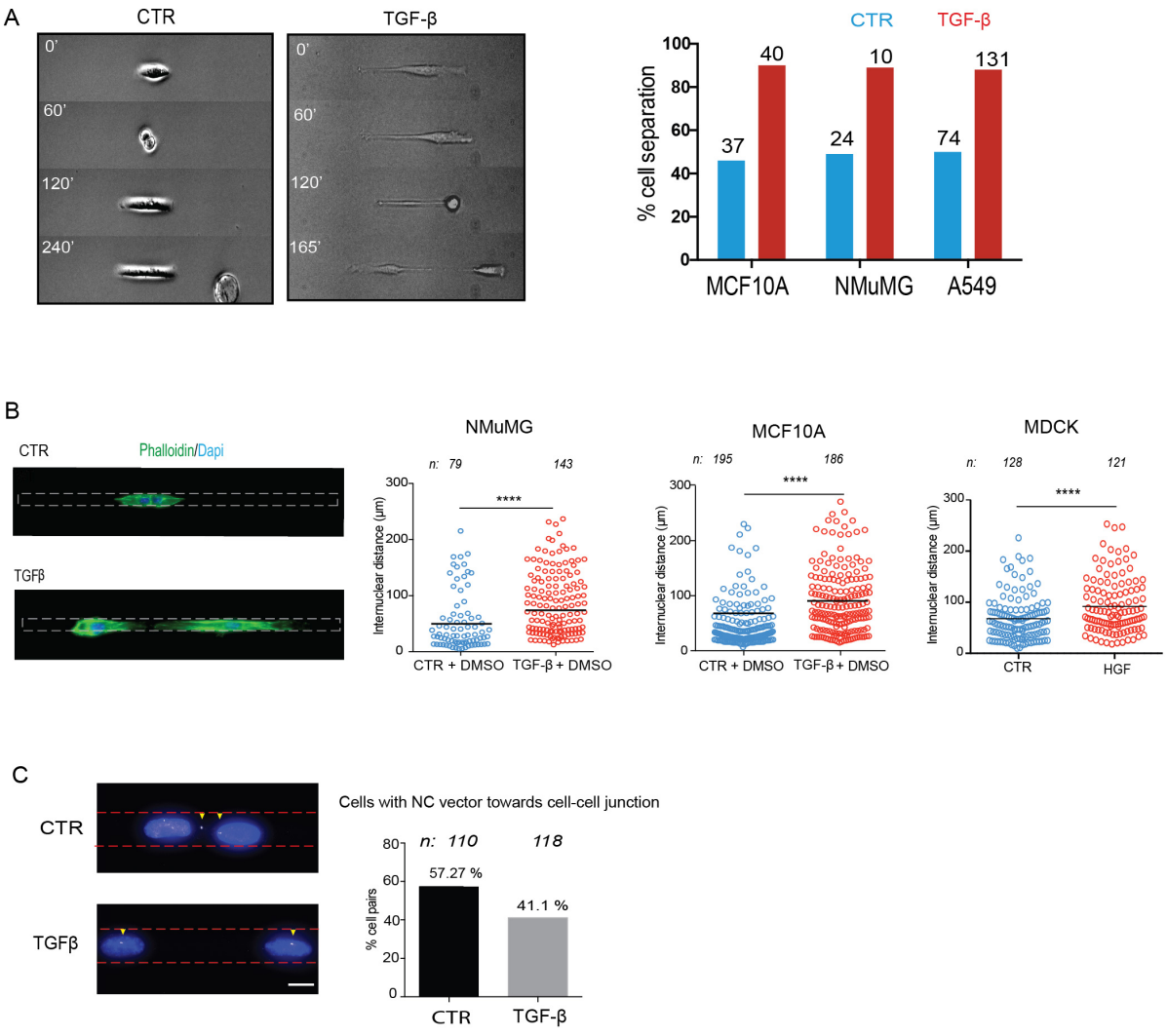
A
CTR
TGF-β
0'
60'
120'
240'
165'
% cell separation
MCF10A
NMuMG
A549
37
40
24
10
74
131
B
CTR
Phalloidin/Dapi
TGFβ
NMuMG
MCF10A
MDCK
Internuclear distance (μm)
CTR + DMSO
TGF-β + DMSO
HGF
****
C
CTR
TGFβ
Cells with NC vector towards cell-cell junction
% cell pairs
57.27 %
41.1 %

Figure S4

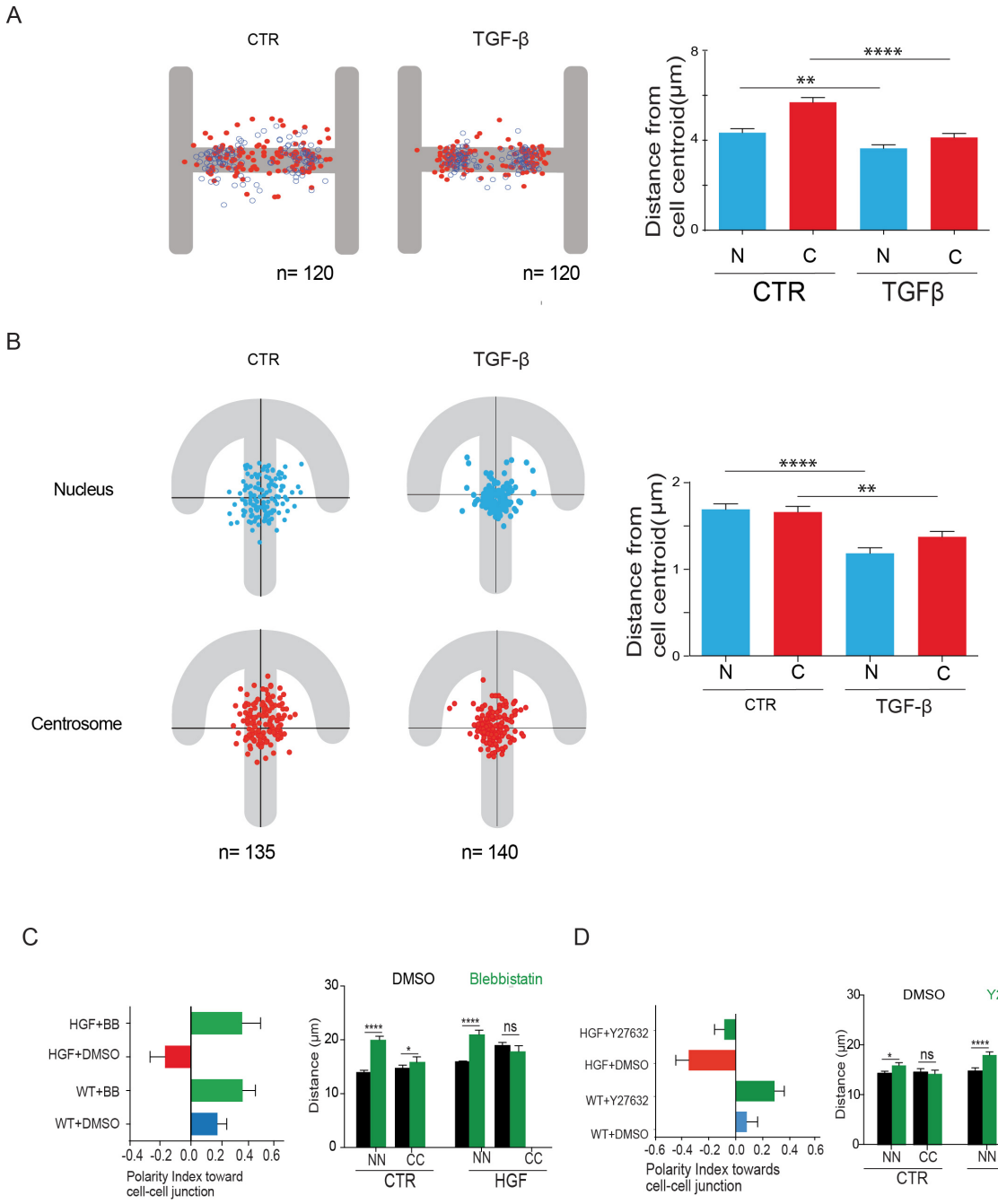
A
CTR
TGF-β
n= 120
n= 120
Distance from cell centroid(µm)
****
**
N
C
N
C
CTR
TGFβ
B
CTR
TGF-β
Nucleus
Centrosome
n= 135
n= 140
Distance from cell centroid(µm)
****
**
N
C
N
C
CTR
TGF-β
C
HGF+BB
HGF+DMSO
WT+BB
WT+DMSO
Polarity Index toward cell-cell junction
DMSO
Blebbistatin
Distance (µm)
NN
CC
NN
CC
CTR
HGF
D
HGF+Y27632
HGF+DMSO
WT+Y27632
WT+DMSO
Polarity Index towards cell-cell junction
DMSO
Y27632
Distance (µm)
NN
CC
NN
CC
CTR
HGF

Figure S5

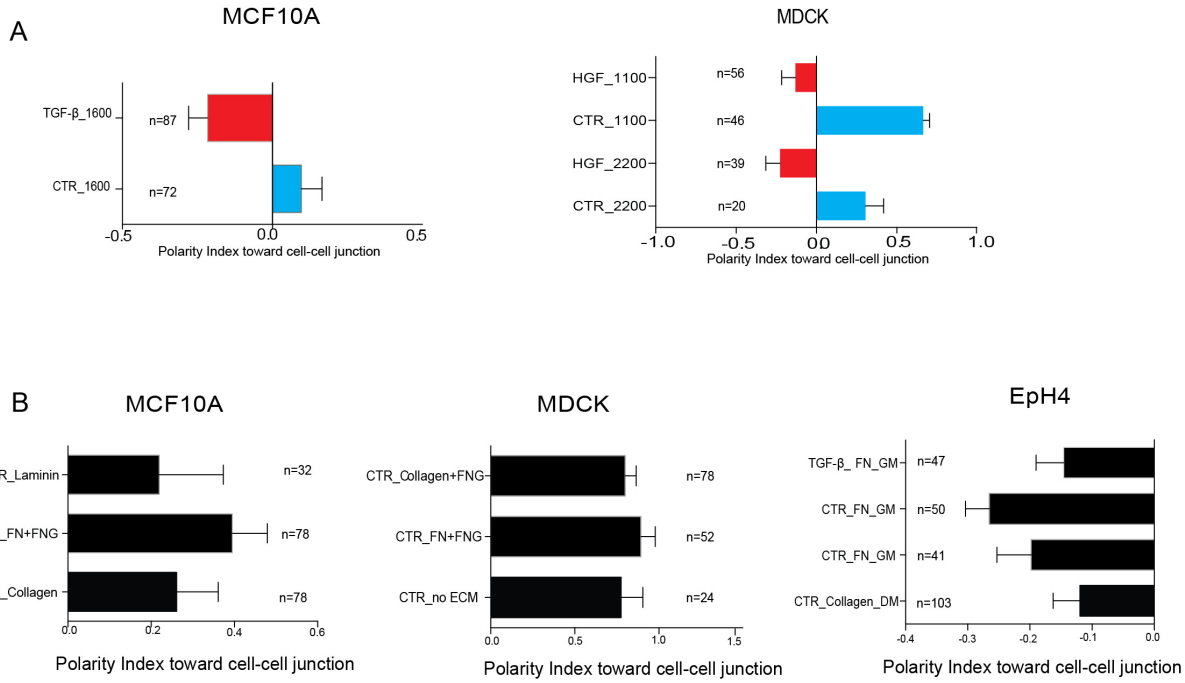
A
MCF10A
TGF-β_1600
n=87
CTR_1600
n=72
-0.5
0.0
0.5
Polarity Index toward cell-cell junction
MDCK
HGF_1100
n=56
CTR_1100
n=46
HGF_2200
n=39
CTR_2200
n=20
-1.0
-0.5
0.0
0.5
1.0
Polarity Index toward cell-cell junction
B
MCF10A
CTR_Laminin
n=32
CTR_FN+FNG
n=78
CTR_Collagen
n=78
0.0
0.2
0.4
0.6
Polarity Index toward cell-cell junction
MDCK
CTR_Collagen+FNG
n=78
CTR_FN+FNG
n=52
CTR_no ECM
n=24
0.0
0.5
1.0
1.5
Polarity Index toward cell-cell junction
EpH4
TGF-β_ FN_GM
n=47
CTR_FN_GM
n=50
CTR_FN_GM
n=41
CTR_Collagen_DM
n=103
-0.4
-0.3
-0.2
-0.1
0.0
Polarity Index toward cell-cell junction

Figure Legends

Figure 1. Evidence of polarity reversal at various stages of mouse development and within 3D organotypic cell culture

(A) Scheme representing germ layers of E8 mouse embryo, site of primitive streak formation and deduced nucleus-centrosome orientations from images in inset 1,2. Inset 1: Posterior end of embryo stained for T-Brachyury(white), γ-tubulin(red) and DAPI (blue). Arrows indicate cells expressing T-Brachyury with nucleus-centrosome axis (white arrows) orientated away from amniotic cavity (marked c). Inset2: Anterior end of E8 mouse showing cells without T-Brachyury and nucleus-centrosome axis pointing toward the amniotic cavity. Scale bar represents 20 μm.

(B) Scheme representing nucleus-Golgi apparatus axis of cells in growing terminal end bud of female mouse mammary gland at 6-7 weeks of age. Inset 1: Merged image of terminal end bud stained for Golgi apparatus (green), F-actin (red) and nucleus (blue). Images of separate channels are below. Scale bar represents 50 μm.

(C) Examples of control and TGF-β treated MCF10A 3D cultures (Day7) labeled for Golgi apparatus (green), centrosome (white), F-actin (green) with zoomed and cropped image showing nucleus-centrosome orientation on the right. Scale bar represents 20 μm.

(D) Scheme represents angle a contained by normal to cell base and nucleus-centrosome vector. Scatter plots show quantification of angle a for control and TGF-b treated MCF10A cells. N represents total number of cells quantified from CTR (n=23) and TGF-β (n=25) acini. Two tailed-non-parametric Mann-Whitney test was used, ****: $p<0.0001$.

Figure 2. Polarity reversal is an early feature of EMT

(A) Images of nuclei (blue) of MCF10A cell doublets on square (i), bowtie (ii) and H-shaped (iii) microcropatterns (grey). Graphs represent angular distribution of nucleus-nucleus axis (NN axis) orientation of cell doublets on micropatterns. n indicates number of cell doublets.

(B) MCF10A and MDCK cell doublets on H-shaped micropattern were stained for and F-actin (green) (top) or centrosome (red) and DNA (blue) (bottom).

(C) Axes system defined by NN axis (X axis) passing through center of nuclei of cell doublets on micropattern and an axis perpendicular to NN axis (Y axis). Normalized nucleus-centrosome vector coordinates (NCx, NCy) were calculated by subtracting coordinates of centrosome (Cx, Cy) from Nucleus (Nx, Ny) and normalized by the length of nucleus radius (NR).

(D) Scatter plot of normalized NC vector of MCF10A Control and TGF-β cells on left and MDCK, control and HGF treated cells on right. The total number of cells and the respective proportions (%) on positive and negative x-axis are indicated.

(E) Horizontal histograms show the quantification of polarity index, ie of normalized X

coordinate of NC vectors, for control (blue) and TGF-β (red) treated MCF10A cells, and for control and TGF or HGF-treated (red) MDCK cells. N indicates the number of independent experiments, whereas n indicates the total number of single cells. Vertical box plots show the quantification of inter-nuclear and inter-centrosome distance of MCF10A and MDCK.
(F) Polarity index toward cell-cell junction in control (blue) MCF10A cells after varying the duration of TGF-β treatment (pink to red, left graph). Polarity index of MDCK cells treated with TGF-β or HGF for different durations (middle and right graphs). h indicates hours and d indicates days.
Two tailed-non-parametric Mann-Whitney tests were used. ****: $p<0.0001$. Errors bar indicate SEM.

Figure 3. Matrix stiffness promotes polarity reversal

(A) Images of control (left) and TGF-β treated (middle) EpH4 cell doublets on H-shaped glass micropattern stained for E-cadherin (green), centrosome (red) and DNA (blue). Cell doublets on 10kPa Polyacrylamide gel (right) were stained for F-actin (green).
(B) Control NMuMG cells on glass and polyacrylamide gels are stained for Giantin (Golgi apparatus marker) (red), F-actin(green) and DNA (blue). Horizontal histograms show quantification of polarity index toward cell-cell junction. Scale bars represent 5 μm. Errors bar indicate SEM.

Figure 4. Microtubule network remodeling accompanies centrosome re-centering during EMT

(A) Images of control and TGF-β treated MCF10A cell-doublets on H-shaped micropattern stained for a-tubulin. Box plot shows quantification of total microtubule density and density at cell-cell junction based on fluorescence intensity in Z-stacks projections (arbitrary fluorescence units).
(B) Images of control and TGF-β treated MCF10A cell-doublets stained for EB1. Scatter plots show quantification of total EB1 comet count and density at cell-cell junction. A circular region of interest of 1.5 μm radius (yellow dotted circle) was used to count EB1 comets at the centrosome.
(C) Images of control and TGF-β treated MCF10A cell-doublets on H-shaped micropattern labeled for g-tubulin (red) and DNA (blue). Scatter plots show quantification of g-tubulin fluorescence intensity within the selected area (yellow circle) around centrosome.
(D) Numerical simulation showing microtubules (white) and centrosome (yellow) motion in response to varying microtubules number in a rectangular cell. Green dots correspond to cytoplasmic dynein (green).
(E) Effect of varying microtubule number on centrosome trajectory and final position. Different

colors represent different number of microtubules. The graph shows the relationship between the number of microtubules and the final position of the centrosome relative to cell center.
(F) Centrosome trajectories when starting from various initial positions (marked by cross) for either 100 (top) or 250 (bottom) microtubules.
Two tailed-non-parametric Mann-Whitney tests were used. ***: $p<0.001$, ****: $p<0.0001$.

Figure 5. Par3 regulates centrosome positioning during EMT

(A) Averaged images of E-cadherin, N-cadherin, α-catenin, β -catenin staining before (CTR) and after EMT induction by TGF-β of MCF10A cells on H-micropattern. Number of images used to obtain averaged image is indicated. Intensity at cell-cell junction per unit area (density in arbitrary units) of images was measured for CTR (blue) and TGF-β (red) treated cells.
(B) Par3 (green), g-tubulin (red) and DNA (blue) stainings of control and TGF-β treated MCF10A cells on H-micropattern. Central graph shows the relationship between Par3 enrichment at cell-cell junction and inter-centrosome distance. Pearson's correlation test r, ****: $p<0.001$, *: $p<0.1$, ns>0.1. Vertical histograms show measurement of polarity index toward cell-cell junction of control (blue), TGF-β (red) or TGF-β and SB3451542 treated cells (black).
C) Image of control cell doublet on H-shaped micropattern treated with Par3 siRNA and labelled for Par3 (green), g-tubulin (red) and DNA (blue). Box plots show quantification of nucleus-nucleus distance and inter-centrosome distance within cell doublets in control (blue) and siPar3 treated cells (grey). Horizontal histogram shows quantification of cell polarity index toward cell-cell junction.
(D) Same as (C) to measure the effect of exogenous Par3b over-expression in TGF-β treated MCF10A cells.
Arrows point at centrosomes. Scale bars represent 5 μm. Errors bar indicate SEM. Two tailed-non-parametric Mann-Whitney test were used **:$p<0.01$, ***:$p<0.001$, ****:$p<0.0001$, ns: $p>0.1$.

Figure 6. Cell-cell and cell-matrix forces redistribution upon EMT

(A) Immuno-stainings of F-actin (red), paxillin (green) and DNA (blue) in control and TGF-β treated MCF10A cells spread on H-micropattern.
(B) Averaged stainings of F-actin, phospho-myosin II, and paxillin in control and TGF-β treated MCF10A cells. Fluorescence intensity scales are displayed with colored LUT in arbitrary units. Numbers of images used to obtain averaged images are indicated.
(C) Average stress field (in Pascal) of MCF10A cell doublets on H-shaped micropattern.
(D) Schematic of cell-pair on micropattern with force balance measurement of intercellular (Fcell-cell) and total traction (Ftotal) forces in MCF10A cell doublets.

Figure 7. Polarity reversal is necessary for cell scattering

(A) Schematic depicting principle of dynamic micropatterning with azide-PLL-PEG (orange) and cell motion on BCN-RGD modified substrate (red).

(B) Time-lapse sequence images of cells on H-shaped micropattern in response to BCN-RGD addition in transmitted light. Histograms show measurement of the proportion of cell separation and maximum inter-nuclear distance between the MCF10A cells two hours after addition of BCN-RGD.

(C) Time-lapse sequence images of TGF-β treated MCF10A cells expressing Golgi apparatus markers (visualized in green at t=0) in response to the addition of BCN-RGD. Histogram shows measurement of the proportion of cell separation depending on their initial polarity orientation.

(D) Schematic description of centrosome repositioning along with microtubule reorganization and Par3 reduction at CCJ in the course of EMT.

Supplemental Experimental Procedures

Cell Culture and EMT Induction

Michigan Cancer foundation (MCF10A) human mammary gland cells (ATCC #CRL-10317) were maintained at 37°C at 5% CO_2 in Lonza Mammary Epithelial Growth Medium (Lonza MEGM bullet kit #CC3150 without Gentamycin) in the presence of 100 ng/ml of cholera toxin (Sigma #C-8052) and 0.5% antibiotic-antimycotic (Life Technologies #15240062). Cells were harvested by TrypLE™ (Life technologies #12605036) treatment for 12 min. An equal volume of soybean defined trypsin inhibitor (Life Technologies #R007100) was added followed by centrifugation at 200xg for 4 min. Cells were subcultivated in ratios less than 1:5 to maintain a stable epithelial phenotype. Medium was renewed every 2-3 days. 8000 cells/cm^2 were treated with 5 ng/ml TGF-β1 (R&D systems #240-B-002) in complete medium containing DMEM/F12 (Life Technologies #31331093), 5% horse serum (Gibco #16050-122), 25 ng/ml EGF (Peprotech TEBU #100-15), 100 ng/ml of cholera toxin, 10 μg/ml insulin (Sigma #I-1882), 500 ng/ml hydrocortisone (Sigma #H-0888), 0.5% antibiotic-antimycotic. Cells were passaged after 3 days and cultured for another 2 days in the presence of TGF-β. At the end of 5 days, cells were harvested for further experiments. Madin Darby Canine Kidney (MDCK) cells were maintained in DMEM-High glucose (Life Technologies #31966047) containing 10% fetal bovine serum (Invitrogen). EMT was induced by addition of 10ng/ml Hepatocyte Growth factor (Gibco #PHGO254) or 5ng/ml TGF-β for different durations ranging from 1 h to 3 days. EpH4 cells (Clone J3B1A) were a gift from Priscilla Soulie. Cells were maintained in DMEM containing 10% decomplemented Donor Bovine Serum (Gibco #16030-074). NMuMG cells (ATCC #CRL-1636) were cultured in DMEM containing 10% decomplemented fetal bovine serum and 10 μg/ml of insulin. EMT was induced in both cell lines by addition of TGF-β to the medium at 2 ng/ml for up to 3 days.

3D Acini Culture and Immunofluorescence Microscopy

Tip boxes, pipettes, eppendorf tubes, culture plates were pre-chilled at 4°C before the start of the experiment to prevent Matrigel polymerization. 50 μl of Matrigel (Sigma #E1270) was spread at the bottom of chamber slides-8 well (VWR #734-0088). MCF10A cells were trypsinized and resuspended in DMEM/F12 Glutamax medium (Life Technologies #31331093) supplemented with 2% horse serum, 500 ng/ml of hydrocortisone, 100 ng/ml of cholera toxin, 10 μg/ml of insulin, 5 ng/ml of EGF and 2% Matrigel. 4000 cells were seeded per well in 400 μl of medium. Medium was changed every 3 days. A similar procedure was performed for MDCK cells except using Minimal Essential Medium (Gibco #11140035) supplemented with 4% fetal bovine serum and 2% Matrigel. Acini were cultured for 8-10 days and fixed in 2% PFA for 20 min at room temperature. Acini were permeabilized with 0.5% Triton X-100 in PBS for 10 min at

4°C followed by 3 washes with 100 mM Glycine in PBS (Wash solution). Cells were saturated with 0.1% BSA in the presence of 0.2% Triton X-100 and 0.05% Tween-20 in PBS (Saturation solution) for 1 h at RT. Acini were incubated with primary antibody diluted in Saturation solution for 3 h followed by 3 washes of 15 min each at room temperature. Secondary antibody was diluted in Saturation solution and acini were incubated in it for 2 h followed by 3 washes of Wash solution. Acini were mounted on a coverslip with Prolong gold antifade reagent (Molecular Probes #P36935).

Mouse Mammary Gland Tissue and Immunofluorescence

C3H mice were bred at INRA (UE0907 IERP, Jouy-en-Josas, France). Mice were euthanized by cervical dislocation at 6-7 weeks of age, and the inguinal mammary glands were immediately excised. All ethical aspects of animal care complied with the relevant guidelines and licensing requirements laid down by the French Ministry of Agriculture and the procedures used were approved by the local ethics committee (*Comethea* Jouy-en-Josas/AgroParisTech). Mammary fragments were rinsed in PBS and fixed with 4% PFA in PBS for 10-15 min at 4°C. Fixed tissues were infused for 16-24 h at 4°C in 40% sucrose in PBS, embedded in Tissue-Tek (VWR #25608-930), frozen in liquid nitrogen and stored at -80°C. Ten micrometer sections were rinsed with PBS at room temperature, permeabilized with 0.2% Triton-X100 in PBS and saturated with 3% bovine serum albumin (BSA) in PBS for 1 h. Incubation with the primary antibody (anti-giantin rabbit pAb, Abcam ab24586, 1:300 dilution) was allowed overnight at 4°C followed by four washes (10 min each) with PBS. Tissue sections were incubated with an Alexa Fluor 488-conjugated donkey anti-rabbit IgG (Molecular Probes #A-21206, 1:1000) secondary antibody for 1.5 h at room temperature and then washed with PBS as above. Actin was stained using Rhodamine Phalloidin (Molecular Probes #R415, 1:300 dilution in PBS) for 15 min at RT. Slides were mounted with Vectashield containing DAPI (Vector Laboratories #H-1200) and stored at 4°C until observation. Primary and secondary antibodies were all diluted in 2% BSA. Each experiment was performed at least twice and included control sections without primary antibody. Images were acquired with CSUX1-A1N Nikon Spinning Disk confocal microscope (Yokogawa) and EMCCD evolve 512 camera (Photometrics) using plan apochromat 40x, 1.3 NA oil objective.

Mouse Embryo Whole Mount Immunofluorescence

Wild type, outbred MF1 mice were maintained on a 12-h-light/12-h-dark cycle. For timed matings, noon on the day of finding a vaginal plug was designated E0.5. Dissections of post-implantation embryos were performed as described in (Copp AJ et al., Prog Neurobiol. 1990). Post-implantation mammalian embryos were costained (overnight incubation of antibodies) for g-Tubulin (Abcam #ab11316, 1:250), T-brachyury (R&D #AF2085, 1:200),

Collagen IV (Abcam #ab6586, 1:400) and counterstained with Dapi. Confocal microscopy was performed after dehydration through a PBS/methanol series (10 min each), three 5 min washes in 100% methanol, clearing in 1:1 v/v methanol/BA:BB (2:1 benzyl alcohol:benzyl benzoate), and two washes in BA:BB. Embryos were imaged directly in BA:BB using a Leica Sp8 confocal microscope and a 40X oil objective.

Micropattern Fabrication and Cell Seeding

Fabrication of micropatterns on glass

A glass plate 10 x10 cm (Schott #1304369) was cleaned using an air pistol and the surface of the glass plate was coated with adhesion promoter, TI Prime (Microchemicals) using a spin-coater (Laurell #WS-650m2-23NPPB) at 3000 rpm for 30s. The glass plate was baked at 120°C for 2 min on a hot plate. The glass plate was then coated with 1% solution of polystyrene (MW 260,000 Acros Organic # 178891000) in toluene (Sigma #179418) using a spin-coater at 1000 rpm. The polystyrene layer was further oxidized with an air plasma treatment (Plasma Etch #PE-30) for 20 s at 30W under vacuum at a 10 cc/min flow rate of air and incubated with Poly-l-Lysine-Polyethylenglycol (PLL(20)-g[3.5]-PEG(2) SurfaceSolutionS, Switzerland) in 10mM HEPES, pH 7.4 at room temperature for 30 min. PLL-PEG coated slides were placed in contact with an optical mask (Toppan Photomask) containing the transparent micropatterns using a vacuum chamber, then exposed to deep UV light using UVO cleaner (Model No. 342A-220, Jelight, USA) for 4 min at power 6mW/cm2, λ 190nm at a distance of 1cm from the lamp. Micropatterned slides were subsequently incubated with a PBS solution containing 20 µg/mL fibronectin (Sigma #F1141) or laminin (Sigma #L2020) or collagen (Life Technologies, #A1048301) along with 20 µg/mL Alexa 647-fibrinogen (Gibco #F135200) for 30 min followed by 3 washes of PBS. Coverslips were dried and then rinsed in sterile PBS before cell seeding.

Fabrication of micropatterns on PAA gel

To achieve compliant substrates for cell attachment, micropatterns were prepared on a polyacrylamide gel attached to a glass coverslip. For a detailed protocol, refer to Mask method (Vignaud et al., 2014). Briefly, a photomask was plasma treated and coated with PLL-PEG using surface activation as explained above. The mask was exposed to UV light for 4 min. The fibronectin and fibrinogen mixture was prepared in sodium bicarbonate buffer, 100 mM, pH 8.3 and incubated on the mask for 30 min. The solution was allowed to flow by keeping the mask vertical. A mixture of acrylamide and bis-acrylamide was freshly prepared for desired rigidity (Tse and Engler, 2010) and was degassed for 30 min. TEMED at 0.1% of total volume and 10% APS at 1% total volume were added to the acrylamide solution. 25 µl of acrylamide was placed onto the photomask where protein was adsorbed. A silanized glass coverslip was placed gently

to spread the drop and the gel was allowed to polymerize for 30 min. The coverslip was removed gently with a scapel and was placed into PBS solution with micropatterns facing up.

Dynamic micropatterning

Azide-PLL-PEG was coated onto a coverslip in a similar manner as for PLL-PEG. Micropatterns were etched by UV irradiation. Cells were seeded onto the coverslip and allowed to form cell doublets after 16 h. Cells were released from confinement by addition of 20 µM BCN-RGD dissolved in 1x PBS. (van Dongen et al., 2013). Note that micropatterns were not coated with any ECM protein to facilitate cell movement onto the RGD-coated surface upon addition of BCN-RGD.

Cell seeding

Approximately 0.5 million cells were seeded onto micropatterned chips of 20x20 mm size and non-adhered cells were washed off after 30 min, which almost always resulted in single cell attachment per micropattern. Cells were allowed to divide over 24 h prior to fixation.

Cell Scattering on Line Micropatterns and Video Microscopy

For video microscopy, glass coverslips were patterned without the layer of polystyrene and then plated with 150,000 cells per 20x20 mm coverslip. Medium was changed once enough cells were attached to the coverslip. Coverslips were mounted on Chamlide chmabers (CM-s20-1). Cells were then recorded with a Nikon Eclipse Ti-E with 10x phase contrast objective in transmitted light and a 15 min interval was set between pictures. The number of cell separation events after a single cell division was then counted manually.

Indirect Immunofluorescence

Cells plated on glass coverslips were fixed with 4% parafomaldehyde in Cytoskeleton buffer (10mM HEPES pH 6.1, 138 mM KCl, 3 mM MgCl2, 2 mM EGTA) containing 0.01% Triton-X100 for 15 min. Autofluorescence was quenched by treatment with 1 mg/ml sodium borohydrate in PBS for 7 min. For centrosome staining, cells were fixed with ice-cold methanol at -20°C for 5 min. Coverslips with cells were incubated in primary antibody diluted in 1.5% BSA containing 0.1% Tween-20 for 60 min. After 2 washes of PBS, the coverslip was incubated with specific secondary antibodies (Alexa Fluor Conjugated, Thermo Fischer Scientific) diluted in 1.5% BSA containing 0.1% Tween-20 for 30 min in the dark. DNA was stained with DAPI (1:5000, Sigma #D9542) for 2 min in PBS. Coverslips were mounted with Mowiol 4-88 (Sigma #81381). Antibodies used included γ-tubulin (1:5000, abcam #ab11317), giantin (1:500 abcam #24586), α-tubulin (1:500, Sigma #T6557), Par-3 (Millipore 07-330), E-cadherin (1:500, BD Biosciences #610181), N-Cadherin (1:500, BD Biosciences #610920), p-MLC (1:100, Cell Signalling #3671),

EB1 (1:200, BD Biosciences #610534), Paxillin (1:200, abcam #ab32084) and human ninein (1:100) was a gift from James Sillibourne.

Chemical Treatments

Blebbistatin (Sigma #B0560) and Y-27632 (Selleckchem #S1049) were added onto cell doublets on micropatterns formed 16 h after seeding at 25 μM and at 20 μM respectively for 6 h. Smad pathway inhibitor SB431542 was added to MCF10A cells along with TGF-β (Selleckchem #S1067) for 5 days. DMSO vehicle was added to control samples at an equivalent volume.

Microscopy and Image Analysis

Fixed and fluorescently labelled cells were imaged using an epi-fluorescence Olympus microscope (up-right BX61) with 100x NA 1.4 oil objective. Stacks of images spanning 12 μm z-distance were acquired using a piezo motor at the same illumination setting for control (CTR) and TGF-β treated sample. Image analysis for centrosome positioning was performed using a series of Macros in Image J. Briefly, z-projection of each color channel was obtained using 'maximum z-projection' plugin followed by merging the 4 channels to obtain a composite image. Using Pattern Alignment plugin (https://sites.google.com/site/qingzongtseng/template-matching-ij-plugin) images were aligned with the reference micropattern image. Nuclei in DAPI channel were detected using image thresholding and object size criteria. Centrosomes were detected with similar thresholding and by using nuclei Region Of Interest (ROI) as spatial reference. Finally nucleus-centrosome vector was computed by subtracting co-ordinates of centrosome from nucleus co-ordinates and was normalized by the nucleus radius as indicated in Figure 3.

EB1 Comet Quantification

Z-projected images of EB1 comets were obtained as described above. Background substraction was performed using a rolling ball radius of 50. For analyzing nucleation capacity of the centrosome, ROI of 1.5 μm radius was drawn around the centrosome labeled by ninein. EB1 comets were detected in the selected ROI by 'Find Maxima' Process.

Microtubule Intensity Quantification

Images of microtubules were acquired using CSUX1-A1N Nikon Spinning Disk microscope (Yokogawa) with 100X, 1.3 NA objective and Evolve 512 EMCCD camera (Photometrics). Z-projected images 'Maximum z intensity' of alpha-tubulin staining were obtained as described above. A ROI 46x46 μm was selected containing the cell pair on <H> micropatterns. Total intensity of the image was measured in Image J for each image to quantify total microtubule density in each cell-pair. To quantify microtubule density at the cell-cell junction, a ROI of 3.2

μm thickness was drawn along the cell-cell junction and intensity of alpha-tubulin staining was measured.

Generating Averaged Images

Images of E-cadherin, N-cadherin, b-catenin and α-catenin, actin, phospho-myosin II and paxillin were averaged using Z project. Cell-doublets on H-shaped micropatterns were stained for junction proteins and images were aligned using 'Pattern Alignment plugin' with reference to the micropattern. Average intensity at each pixel of the image was calculated using the 'average intensity' projection type in Image J.

Three-dimentional Acini Quantification

Images of acini were acquired on a Nikon Spinning Disk microscope at 60x oil objective with a z-step of 500 nm. To determine angle alpha formed between normal to cell periphery and the nucleus-centrosome vector (Figure 1), 4-5 central planes of acini images were selected to obtain single layers of cells at the center of the acini. A normalizing line was drawn to the basal surface of cells, which was marked by phalloidin staining. Using the 'angle' measurement in Image J, the value of alpha (0-180°) was determined providing the angle formed by vectors in the same plane. Only the central plane of acini was considered for these measurements in order to have a planar distance of cells to the center of the acini.

Traction Force Microscopy

Passivation of beads with poly-ethylene-glycol (PEG)

Fluorescent beads were PEG passivated to avoid cell attachment and intake of the beads by cells. Carboxylated polystyrene beads, 200 nm, dark red (660/680), 2% solids (Molecular Probes #F-8807) were diluted to 1:4 in 10 mM MES buffer pH 5.5 containing 8 mg/ml of N-hydroxysuccinimide (NHS) (Sigma #1130672) and 4 mg/ml 1-ethyl-3-[3-dimethylaminopropyl]carbodiimide hydrochloride (EDC) (Molecular Probes #E-2247). This solution was mixed with 4 mg/ml PLL-PEG prepared in 10 mM HEPES buffer pH8.5. The mixture was incubated on a rotator for 2 h at RT. The beads were finally spun down and resuspended in 10 mM HEPES buffer, pH 7.4 in 2x the original bead volume. NHS and EDC solutions were prepared freshly and the mixing step with PLL-PEG was performed within 30 sec to avoid formation of bead aggregates. PEG passivated beads were stored at 4°C over 1-2 months and before every use beads were sonicated for 5 min to remove small aggregates.

Silanization of coverslips

20x20mm glass coverslips were plasma cleaned for 3 min, 30W, 10 cc/min gas level with plasma cleaner (Plasma Etch #PE-30). Coverslips were treated for 10 min in solution containing 2% 3-

trimethoxymethylsilane (Sigma #M6514) and 1% (v/v) acetic acid in ethanol. Coverslips were rinsed with ethanol and dried with air-gun followed by baking at 120°C for 1 h.

Fabrication of micropatterns on PAA with fluorescent beads

10 kPa polyacrylamide gels were prepared using 5% acrylamide and 0.3% bis-acrylamide solution. The solution was degassed for 15 min in a vacuum bell. Quartz mask (Toppan) was washed with soap followed by milliQ water and dried using nitrogen gas flow. The surface of the quartz mask was activated by plasma treatment at 100W for 3 min in air plasma cleaner. A drop of PLL-PEG solution (0.1 mg/ml, 10 mM, pH 7.4) was added onto the chromium side of the mask at the region of interest (ROI) and was covered with a clean 20x20 mm glass coverslip. After 30 min of incubation at RT, the mask was tilted to let the coverslip flow off with excess solution and the mask was allowed to dry by dewetting. The mask was UV insulated with the chromium side facing the UV lamp (UVO cleaner Model No. 342A-220, Jelight, USA) for 4 min at power 6mW/cm2, λ 190nm at a distance of 1cm from the lamp. The ROI on the mask was coated with 20 µg/ml of fibronectin (Sigma #F1141) and fibrinogen Alexa Fluor 647 (Molecular Probes #F135200) dissolved in 100 mM of sodium bicarbonate buffer, pH 8.3 and was incubated for 30 min at RT. At the end of the incubation, excess solution was allowed to flow off the mask which was then gently rinsed once with sodium bicarbonate buffer. PEG passivated polystyrene beads were sonicated in a water bath for 5 min and immediately added to Acrylamide-bis-acrylamide solution to 1:16 dilution (0.06% solid beads) and mixed well with the help of a pipette. Once the mask was dried, 25 µl of Acrylamide and Bis-acrylamide solution was put onto the ROI on the mask and was immediately covered with a silanized glass coverslip while making sure there was no bubble introduced in the gel. After 25 min of polymerization, the polyacrylmide gel with coverslip was flooded with sodium bicarbonate buffer to facilitate detachment of the gel. The gel was detached gently from the mask using a sharp scapel. The silanized coverslip containing polymerized gels with micropatterns was stored at 4°C in PBS solution with micropatterns facing up until further use.

Cells were seeded onto micropatterns on PAA as described for glass substrates. A glass coverslip with PAA gel and cells was mounted in a magnetic chamber (Live Cell Instrument, Chamlide CMS). Images of fluorescent beads were acquired at 63X, 1.4 NA Plan Apochromat VC (Nikon) on CSUX1-A1N Nikon Spinning Disk microscope (Yokogawa) and Evolve 512 EMCCD camera (Photometrics). Stacks of five images with 0.5 µm z-distance were acquired around the topmost focused beads plane. Cells were trypsinized at 37°C in the chamlide chamber with extreme care so as to not move the chamber on the microscope. Cells were washed away with the help of the pipette after 10 min. Images of the beads were acquired at the positions registered before.

Calculations of cellular forces

Image analysis macros and plugins and tutorial for Image J for traction force microscopy analysis can be found at (https://sites.google.com/site/qingzongtseng/piv). Briefly, the best-focused and top-most plane of bead images of before and after trypsinzation of cells was selected. Images of beads from independent cell doublets were aligned using normalized cross-correlation algorithm of the plugin-'Align slices in stack' and with the micropattern as a reference. The dDisplacement field was computed from bead movements using iterative Particle Image velocimetry (PIV) algorithm. Parameters used for Iterative PIV were 3 interrogation window 204, 25, 12 pixel and correlation 0.6 Traction forces were calculated from displacement field using Fourier Transform Traction Cytometry (FTTC) algorithm. Parameters used for FTTC were, Young's Modulus 10000 Pa, Regularization factor of 10^-9, Poisson ratio 0.5. The stress field values were obtained in Pascal units. The product of unit grid area (3.2x3.2 μm) and the traction stress vector generated the traction force vector (nN).

Force vectors at each position were averaged over several images to obtain averaged force fields for cell-pairs. Cell-cell force (Fcell-cell) was computed by from the vector sum of traction forces for each cell on H-micropatterns and negative imbalanced force was designated as Fcell-cell. The sum of magnitudes of the each traction force exerted at each point was obtained as total Traction force.

Transient Cell Transfection

250,000 MCF10A cells were seeded in a single 6 well plate. Par3 siRNA was added to the defined MEBM medium to 10 nM along with RNAiMax reagent (Invitrogen #13778030). After 24 h, cells were seeded onto micropatterns and were allowed to divide for another 24 h before fixation. On-Target plus SMART pool was used for Par3 siRNA (Dharmacon L-015602-00-0005) J-015602-05, AAGCAUGGAUUUAGGUAUA, J-015602-06 AGACUAAACUCAAUACAGU, J-015602-07 CGAUAAAGACAGACUGGUA, J-015602-08 GAUGGCGACCUUCGAAAUA. Control siRNA (Qiagen #SI03650318) was used at 10 nM. MCF10A cells were transfected with pk-myc-Par3b construct (Addgene #19388) using Plus Reagent (Invitrogen #11514015) according to manufacturer instructions. 24 h after transfection cells were treated with TGF-β and seeded onto micropatterns 24 h after. Following one cell division, cells on micropatterns were fixed. Cells used for dynamic micropatterning were seeded at a density of 125,000 the previous day followed by addition of 2 μl of CellLight Golgi-GFP BacMam 2.0 (Molecular Probes #C10592) per 10,000 cells. Cells were imaged after 30-48 h of incubation.

Quantitative PCR

qRT-PCR was used to analyze mRNA expression levels of E-cadherin, snail1, vimentin and g-

Tubulin. RNA was extracted in TRIzol (Ambion 15596-026) and chloroform extraction. RNA quantity was measured using Nanodrop2000. cDNA was synthesized using Affinity script qPCR synthesis kit (Stratagene #600559). The reagents used were SYBR® Green PCR Master Mix and SYBR® Green RT-PCR Reagents Kit (CFX96 Touch™ Real-Time PCR Detection System from BioRad).

Primers for MDCK cells (Dog origin)
E-Cadherin F: 5′-TGACAGCTACACGTTCACCG-3′ R: 5′-TTCAAAACTCACCCTGCCCA-3
Snail1 F 5′-AAGATGCACATCCGAAGCCA-3′ R 5′-CTTCTCACCGGTGTGGGTC-3,
Vimentin F 5′-AAATGGCTCGTCACCTTCGG-3′ Vimentin R 5′-GAGCAATCCTGCTCTCCTCG-3′,
U6 F 5′GCAAGATGGCGGACAAAGAG-3′ U6 R 5′-TCGAACCCCTTCAAGATGCC-3′
g-Tubulin F 5′-CCGGTACCTGAGGAGCGAT-3′ R 5′-TTCCAGAACTCGAACCCAATCTG-3′
Primers used for NmuMG (Mouse)
Vimentin F 5′-TGCACGATGAAGAGATCCAGG -3′ , R 5′-AGGCTTGGAAACGTCCACAT -3′
g-Tubulin forward 5′-GGAGCGATGCCGAGAGAAAT-3′R 5′-CCAGAACTCGAACCCAATCTGA -3′
Snail1 5′-TGTGTGGAGTTCACCTTCCAG-3′ Snail1 R 5′-AGAGAGTCCCAGATGAGGGT -3′
g-Tubulin forward 5′-GGAGCGATGCCGAGAGAAAT-3′
g-Tubulin-reverse 5′-CCAGAACTCGAACCCAATCTGA -3′
E-Cadherin F 5′-GAAGGCTTGAGCACAACAGC -3′, R 5′-CCCTGATACGTGCTTGGGTT -3′
U6 F 5′-TGTGCTGTTGACGAGGACTT-3′, R 5′-GTTCCACAGATGCTCAGGTCA-3′

Primer used for MCF10A (Human origin)
E-Cadherin F 5′-CCCACCACGTACAAGGGTC-3′ R 5′-CTGGGGTATTGGGGGCATC-3′
Snail1 F 5′-AGGCAGCTATTTCAGCCTCCTGTT R 5′=TGACAGCCATTACTCACAGTCCCT-3′
Vimentin F 5′-AGAACCTGCAGGAGGCAGAAGAAT,R 5′-TTC CAT TTC ACG CAT CTG GCG TTC-3′
U6 F 5′-CTCGCTTCGGCAGCAGA-3′, R 5′-AACGCTTCAGGAATTTGCGT-3

Western Blot

For immunoblot analyses of proteins, cell lysates were prepared in RIPA lysis buffer (10 mM Tris-HCl [pH 7.4], 150 mM NaCl, 1% (v/v) Triton X-100, 0.1% (v/v) SDS, 0.5% (v/v) DOC and 1 mM EDTA) containing a protease inhibitor cocktail (Sigma P8340), phosphatase inhibitor cocktails 1 and 2 (Sigma-Aldrich P2850, P5726), and were cleared by centrifugation. Equivalent amounts of protein were processed to SDS-PAGE electrophoresis and transferred to nitrocellulose or PVDF membrane (Hybond-P, Amersham Biosciences). Immunoblotting was performed using the primary antibodies (anti-E-cadherin, anti-N-cadherin from BD Biosciences Pont de Claix, France;

anti-HSP90 (Cell Signalling), anti-vimentin (clone Vim13.2) was from Sigma-Aldrich (Lyon, France), anti-GAPDH from (Invitrogen). The blocked membranes were incubated overnight with primary antibodies, washed with TBST and incubated with secondary antibodies conjugated to horseradish peroxidase. Detection was achieved by using Enhanced chemiluminescence method (ECL Plus, GE Healthcare).

Numerical Simulations using Cytosim Software

Simulations were performed using the Cytosim software (www.cytosim.org). Microtubules are considered as elastic fibers surrounded by a viscous fluid following Langevin dynamics (Nedelec and Foethke, 2007). We simulated only microtubules nucleated from and anchored to a centrosomal complex. New nucleation of microtubules, microtubules unbinding from centrosome or steric interactions between microtubules are not taken into account. Microtubules can grow at a force-dependent speed (Dogterom, 1997), can undergo catastrophe events and shrink, and can undergo rescue events. Their bending elasticity is modelled following Euler's buckling description. Microtubules are initially uniformily distributedaround the centrosome and can freely rotate around it. They are constrained into a rectangular space with an Hookean rappel force and will push against this border but can glide freely along it. Cytoplasmic dyneins are modeled as immobile objects spread into the cellular space that can bind/unbind microtubules and move toward the MT minus end when bound, thus generating a pulling force on the centrosome.

Main parameters:

Name	Value	Description
General		
Cell confinement	18 * 10 μm^2	Rectangular space
Cell viscosity	1 $pN.s.\mu m^{-2}$	(Kimura and Onami, 2010)
Simulated time	400 s	
Time step	0.05 s	Compromise exactitute / simulation time
Temperature	25°C	Room temperature
Centrosome		
Anchoring stiffness	500 pN/µm	Stiffness of each MT minus_end anchoring to centrosmal complex
Radius	0.5 µm	~ centrosome radius
Microtubules MT		
MT segmentation	0.5 µm	Compromise exactitude / simulation time
MT persistence length	5200 µm	(Gittes et al., 1993)
Polymerization force	5 pN	(Dogterom, 1997)

Polymerisation (resp. shrinking) speed	0.13 (resp. -0.27) $\mu m.s^{-1}$	(Burakov, 2003)
Rescue rate	0.064 s^{-1}	(Burakov, 2003)
Catastrophe rate	0.01, 0.04 s^{-1}	Free and stalled catastrophe rate, Janson 2003
Initial MT length	0.75 µm (+-0.05)	Initial length distribution of Mts around centrosome (mean and standard deviation)
Dyneins		
Dynein stall force	1.1 pN	(Soppina et al., 2009), (Gross et al., 2000)
Dynein max speed	1.5 µm/s	(Soppina et al., 2009), (Gross et al., 2000)
Dynein stiffness	10 pN/µm	Strength of dynein anchoring to their cytoplasmic position
Binding rate	5 s^{-1}	Binding rate of a free dynein within binding range of MT
Binding range	0.1 µm	Distance to MT from which dynein can bind it
Unbinding rate	0.05 s^{-1}	Unbinding rate of bound dynein
Unbinding force	2 pN	Opposite force that will make dynein unbind MT
Dynein density	~1.5 dyn/μm^2	Estimated in (Zhu et al., 2010)

Statistical Analysis

Mann-Whitney non-parametric test was used to compare differences between the samples. Error bars indicate standard error mean (SEM). N indicates numbers of experiments while n indicates sample size.

Supplemental Figure Legends

Figure S1. Two models of polarity changes during EMT progression

Possible models for driving changes from epithelial (apico-basal) polarity to mesenchymal (front-rear) polarity. Intermediate states involve either loss of polarity (top) or polarity reversal (bottom). Nuclei (dark blue), centrosome (red dot), basolateral (green) and apical membrane (red) are depicted.

Figure S2. Molecular characterization of EMT induction in MCF10A, MDCK and NMuMG

(A) Western blot of MCF10A cell lysate probed for E-cadherin, N-cadherin and loading control, HSP90 at different concentrations of TGF-β treatment over 3-5 days.
(B) Quantitative-PCR to analyze mRNA expression of E-cadherin, Snail1 and vimentin for cells cultured in defined growth medium.
(C) Images of MCF10A cells stained for E-cadherin, N-cadherin and F-actin before (CTR) and after TGF-β treatment.
(D) Western blot of MDCK cell lysate probed for E-cadherin, vimentin and GAPDH loading control.
(E) Quantitative-PCR to analyze mRNA expression of E-cadherin, Snail1, g-tubulin, vimentin using U6 as control mRNA of MDCK cells.
(F) Images of MDCK acini immune-stained for Golgi apparatus (red), F-actin (green) and nuclei (blue) in control and HGF treated cells.
(G) Western blot of NMuMG cells probed for E-cadherin, vimentin and loading control HSP90.
(F) Quantitative-PCR to analyze mRNA expression of E-cadherin, Snail1, g-tubulin, vimentin using U6 as a control mRNA of NMuMG cells.

Figure S3. Centrosome repositioning is associated with cell scattering

(A) Time-lapse sequence of control and TGF-β treated NMuMG cells on micro-patterned lines. Histograms show quantification of the proportion of cell separation in control and TGF-β treated cells for various cell types. Numbers indicate the number of cell division events measured before cell separation.
(B) Images of fixed NMuMG cells stained for F-actin (green) and nucleus (blue) on micropatterned lines. Scale bar represent 30 μm. Histograms show the quantification of inter-nuclear distance between two NMuMG, MCF10A and MDCK cells occupying the same micropatterned line 24 hours after cell plating.
(C) Images of control and TGF-β treated MCF10A cells on micropatterned lines stained for g-tubulin (white) and DNA (blue). Histogram shows the proportion of cells with polarity index

oriented toward CCJ in control and TGF-β treated cells. Scale bar represents 10 μm.

Figure S4. Nucleus-centrosome repositioning in single and cell-doublets after EMT

(A) Distribution of nucleus (blue) and centrosome (red) positions in MCF10A cell doublet spread on H-micropattern (grey). Histograms show quantification of nucleus and centrosome distance from cell center of mass (cell centroid) in control and TGFb treated cells.
(B) Distribution of nucleus (blue) and centrosome (red) positions in single MCF10A cell spread on crossbow-micropattern (grey). Histograms show quantification of nucleus and centrosome distance from cell center of mass (cell centroid) in control and TGFb treated cells.
(C) Horizontal histograms shows measurements of polarity index of control or HGF-treated MDCK cells after blebbistatin (BB) treatment. Vertical histograms show inter-nuclear (NN) and inter-centrosome (CC) distance within cell pairs after blebbistatin treatment (green).
(D) Horizontal histograms shows measurements of polarity index of control or HGF-treated MDCK cells after Y-27632 treatment. Vertical histograms show inter-nuclear (NN) and inter-centrosome (CC) distance within cell pairs after Y-27632 treatment (green).

Figure S5. Effect of cell spreading and different ECM proteins on cell polarity

(A) Quantification of the polarity index of cells spread on micropatterns of 1600μm^2 (MCF10A), 1100μm^2 and 2200μm^2 (MDCK) before and after EMT.
(B) Effect of different ECM proteins coated on micropatterns on cell polarity in MCF10A, MDCK and EpH4.

Movie S1. Movie showing control NMuMG cells migrating on line micropatterns of 10 μm thickenss.
Movie S2. Movie showing TGF-β treated NMuMG cells migrating on line micropatterns of 10 μm thickeness.
Movie S3. Cytosim simulation showing 100 microtubules emanating from MTOC (yellow circle) and effect of their interaction with cell border and cytoplasmic dynein (green dots) on centrosome trajectory and final position.
Movie S4. Cytosim simulation showing 250 microtubules emanating from MTOC (yellow circle) and effect of their interaction with cell border and cytoplasmic dynein (green dots) on centrosome trajectory and final position.
Movie S5. TGF-β treated MCF10A cells with nucleus-centrosome axis toward CCJ are released from confinement by addition of BCN-RGD.
Movie S6. TGF-β treated MCF10A cells with nucleus-centrosome axis toward CMA are released from confinement by addition of BCN-RGD

2.3 Short Q&A

Q. Why are the cell culture mediums switched from Defined medium to Growth medium during EMT induction of MCF10A cells?

A. Classical growth mediums contain 10% fetal bovine serum. The serum contains growth factors including TGF-β. Nanomolars of TGF-β concentrations in the serum can induce mesenchymal characteristics and initiate branching morphogenesis in 3-D cultures of mouse mammary gland (Montesano et al., 2007). Secondly, when cultured in GM, we had troubles to get reproducible results over independent experiments. So in order to restrain from the use of serum we adapted the defined cell culture medium from Lonza. The cells did show reproducible polarity orientations over several experiments as compared to when they were cultured in growth medium. However, TGF-β treatment was not efficient in defined medium suggesting other growth factors in serum were required for TGF-β treatment. Hence we switched the medium during EMT induction. Please note that Lonza medium is not completely defined, as Pituitary gland extract from the kit, is not a defined component.

Q. Why did we choose MCF10A as the main epithelial cell line model?

A: MCF10A cells are of human origin and thus they were the first choice for development of the 'EMT kit' (Chapter III), which was developed with the aim to screen anti-cancer drugs against human cancers. Secondly, the cell line has normal chromosome number and is widely used as a model of mammary gland. We chose this cell line primarily to develop EMT kit for screening drugs against human cancers. However, MCF10A cells show phenotype of basal (myoepithelial) cells as characterized by their cytokeratin expression. EpH4 (mouse origin) are clonally selected and thus would show lesser variation in phenotype. In addition EpH4 cells are very sensitive to TGF-β and thus would be more suited to study EMT.

Q. Why different cell lines of mammary gland show difference in polarity behavior on different substrates?

A: This was a genuine surprise to us in the beginning to observe drastically different polarity orientations of mammary gland cells, MCF10A, NMuMG and EpH4. One major difference could be the integrin expression of these cell lines. Secondly, the source of cell line generation can be heterogeneous. MCF10A and NMuMG cells are established from human and mouse tissue respectively but the cell population is not homogenous. While EpH4 clone we received from Priscilla soulie is selected for their ability to form 3-D cultures (Montesano et al., 1998)

2.4 Comments

In the two projects (Chapter I and II) I studied different mechanisms that enable the cell to communicate and respond to the cues for undergoing transformations. I described the mechanisms by subdividing polarity into two groups, cortical and internal polarity. In this thesis I have emphasized on cell-cell adhesion that make up part of cortical polarity and their interaction with internal polarity cues. However, another important element of cortical polarity is Cell-Matrix adhesion and the discussion of thesis will be incomplete without describing how cell adhesions formed with extra-cellular matrix affects internal polarity and direct tissue formation.

Microtubule and Cell-Matrix adhesion interaction for polarity establishment

In the physiological environment, cells of the tissue are in contact with the basement membrane and extracellular matrix (ECM). Cells can sense and modify the chemical composition, assembly, stiffness and other mechanical properties of ECM. This can be mediated by interaction of cells with their ECM through various receptors, such as integrins, dystroglycan and proteoglycan. Massive changes of tissue microenvironment including changes in deposition, degradation and structural organization of ECM components provide cues for cell survival, proliferation, migration, differentiation and polarization during normal development as well as at the onset of cancer. As we saw in Chapter II, Figure 2.1 that mere change of ECM matrix from collagen to reconstituted basement membrane was sufficient to invert the acini organization (Gudjonsson et al., 2002). Also a complete polarity inversion of the nucleus-centrosome axis by merely changing matrix stiffness clearly suggested that CMA provides vital cues for orientation of internal cell polarity (Figure 3, Burute et al.,).

Microtubule organization is crucial link between cell internal components and cell cortex. Microtubules are involved in orientation of centrosome, nucleus, golgi, directed trafficking as well as formation and maturation of CCA and CMA, actin polymerization and contractility. MTs also interact with the third major cytoskeleton component, intermediate filaments. Thus MTs interact with all the major cellular components and are essential for polarity program. Hence it is not surprising to see that CMA also communicates with MTs for polarity guidance. However, the molecular players that mediate CMA-MT interaction remain mostly elusive. A study from Akhtar and Streuli showed that during mammary gland development, integrin linked kinase (ILK) is required for generating polarized microtubules array (minus end toward basolateral surface) in apical-basal direction, which are responsible for targeting apical complex proteins to the apical side of the acini. Orientation of microtubules is likely to be driven by EB1 capture and microtubule anchorage at the Integrins (Akhtar and Streuli, 2013). This study shows an exclusion

mechanism by which apical surface protein, which are at the basement membrane are selectively transported to apical surface. Similar exclusion mechanism of apical markers from basal surface is observed in MDCK cells while forming 3D acini. At the initial stages, cells have apical plasma membrane protein Podocalyxin/gp135 decorating entire cell surface. Deposition of β1-integrin signaling initiated phosphorylation cascade by RhoA, which removes gp135 from basal surface and trancytoses it to the opposite end where lumen formation begins (Bryant et al., 2014). The authors argue that MDCK acini formation although involves exclusion mechanism like in mammary gland acini formation, the process is not mediated by microtubules and thus tissue-type differences in polarization mechanism may therefore exist. Notably, mammary gland and kidney have different germ layer origins. Mammary gland is derived from ectoderm while kidney is a result of mesoderm. Hence the kidney cells have undergone EMT during gastrulation and formed the organ by reverse process of MET. Thus it is possible that mesoderm-derived tissues retain the feature of mesenchyme-origins involving contractility based mechanisms. Surprisingly, in our study we also observed that contractility inhibition of HGF-induced MDCK cells reversed the polarity to epithelial-like phenotype while polarity of MCF10A cells was not altered by contractility inhibition (Figure s4). These results support the hypothesis that mesoderm and ectoderm derived tissues could employ different polarization mechanisms.

Link between Actin and Microtubule network

A very interesting report by Joo and Yamada revealed a missing link between microtubule and contractility involved in morphogenesis. Using a branching morphogenesis model of submandibular gland mice tissue, authors demonstrated that Myosin phosphatase 1 acts as intermediate link for microtubule acetylation and myosin light chain phosphorylation in a competitive manner. Acetylated microtubules enhance α5β1 recycling and decrease cell migration and thus inhibit branching morphogenesis. An increase of contractility can counterbalance this phenotype. Thus, cellular contractility is inversely regulated by microtubule acetylation through myosin phosphatase and HDAC6 (Histone Deacetylase-6) (Joo and Yamada, 2014). Previously, the actin-microtubule crosstalk was mainly described by polymerization/depolymerization via availability of signaling components such as Rac1 and Rho-A GTPases, their regulators, GEFs and GAPs (Etienne-Manneville and Hall, 2002; Rodriguez et al., 2003). This study by Yamada group provided the evidence for post-polymerization crosstalk between actin and microtubules. Another study by Deakin and colleagues reported that HDAC6 inhibition by paxillin is responsible for microtubule acetylation and golgi organization. The outcome of this interaction affects final cell migration and invasive capacity (Deakin and Turner, 2014). Traditionally, HDAC6 was known as a chromatin modifier and now with its role in cytoskeleton reorganization further dominates its importance for cancer therapeutics.

Control of the cell architecture by photoactivation technology

In our system of MCF10A cell doublets we did not observe any clear difference in polarity upon inhibition of HDAC6 by tubacin or pan-HDAC inhibitor Trichostatin A. However, this does not rule out the possibility of microtubule acetylation playing an active role in centrosome position. The cytoskeleton inhibitor approach is powerful to answer some key question such as whether global contractility affects organization of acini. Acetylated tubulin staining in MCF10A epithelial doublets was preferentially located close to cell-cell junction (Figure 2.3A). Thus there is a possibility that selective acetylated tubulin at the cell-cell junction could affect centrosome position by changing mechanical force transmitted to the centrosome or by molecular motors selectively interacting with acetylated tubulin. Global inhibition of HDAC6 acetylates majority of the microtubules in the cell, which abolishes local asymmetry of forces that could be involved in affecting centrosome position and thus we do not see any net effective change. Similar limitation was faced with Myosin II isoform repartition within the cell after EMT induction. We observed local differences in Myosin IIA and IIB decoration within cells, which is important for invasiveness of cells after TGF-β treatment (Figure 2.3B) (Beach et al., 2011). It is possible that balance between inter- and intracellular forces which we saw (Figure 6, Burute et al.,) after EMT could be result of difference in local contractility guided by different myosin isoforms. Inhibition of overall contractility by chemical inhibition like Blebbistatin or siRNA knockdown masks the effect of local changes. Recent advances in light-induced recruitment of molecular motors or activation of small GTPase have provided tools to answer these types of questions (van Bergeijk et al., 2015). Proteins that change conformation in response to light can be adapted to regulate a wide array of activities of genes, proteins, protein-complexes and sub-cellular organelle positioning (Tischer and Weiner, 2014). Light-oxygen-voltage-sensitive domains isolated from several organisms are sensitive to blue light (440-473nm) and are successfully used as optogenetic tools (Figure 2.4A). For example, a cell line expressing photosensitive LOV peptide linked to tubulin acetyltransferase (TAT1) and complementary ePDZ linked to E-cadherin can be used to activate the TAT1 recruitment specifically to E-cadherin, whose expression in epithelial cell is enriched at the cell-cell junction (Figure 2.4A). Selective recruitment of TAT1 close to the CCA would acetylate microtubules that are close to the CCA and thus its subsequent effect on centrosome position can be studied. On the other hand, Rab11 recycling endosomes localize to pericentriolar material via microtubule-dependent transport. During interphase, Rab11 localizes to the mother centriole and proteins associated with the mother centriole regulate Rab11 localization and their activity (Hehnly et al., 2012). In addition, during mitosis, dynein dependent Rab11 endosome localization to spindle pole increases γ-tubulin and astral microtubules(Hehnly and Doxsey, 2014). Thus photo-activation of dynein-mediated transport of Rab11 can increase MT nucleation at the centrosome while kinesin-mediated transport would decrease MT nucleation at the centrosome (Figure 2.4B). Kinesin-mediated activation is also likely to increase

Figure 2.4

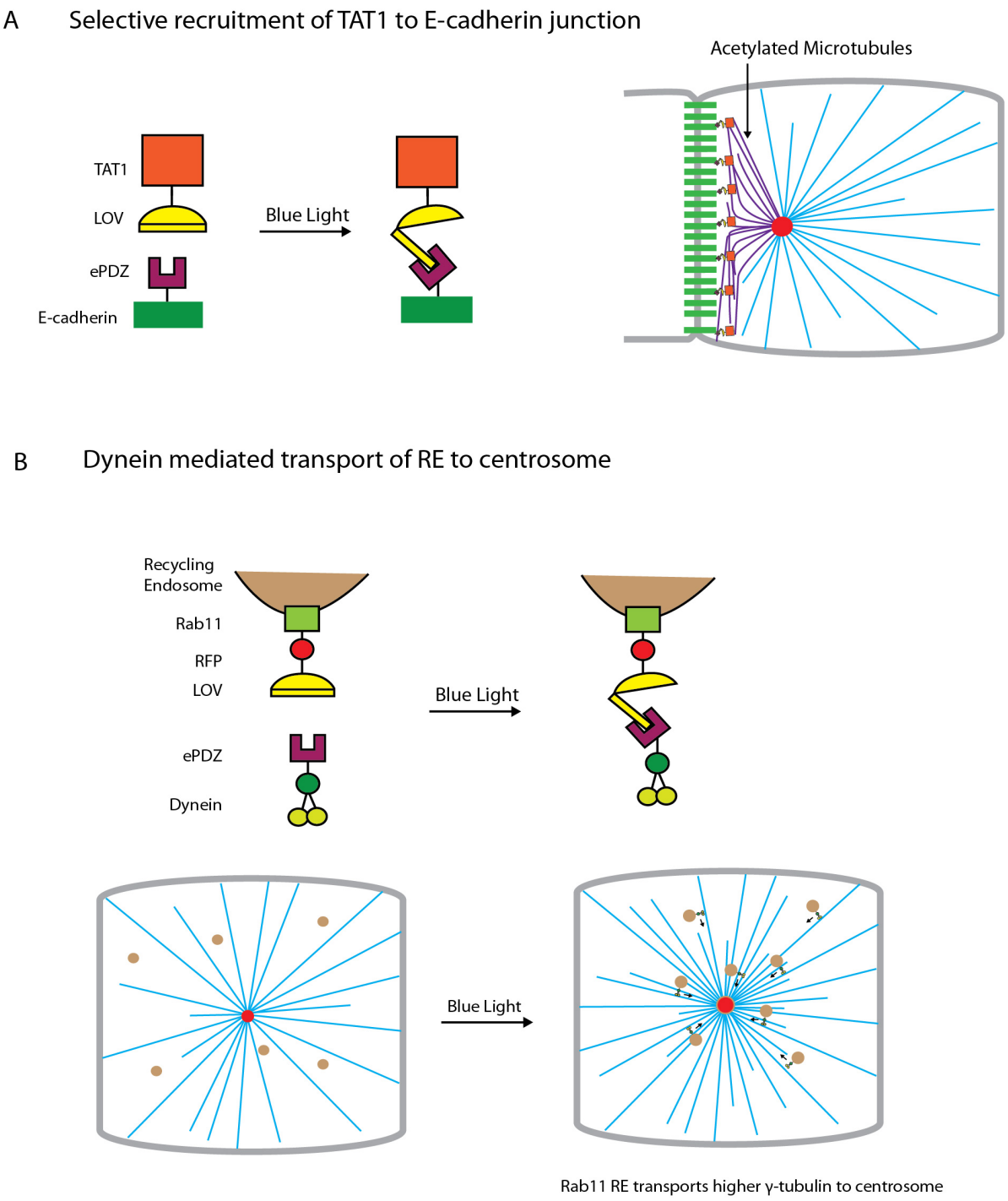

(A) Recrutiment of Tubulin acetylatransferase to cell-cell junction using light-activation set-up
(B) Modulation of Peri-centriolar material by light-induced transport of recycling endosomes

γ-tubulin localization at CCJ where +tip of MTs are anchored (Figure 2.4B). Temporal and spatial control of organelle positioning using light-controlled activation technology holds a great promise incoming years to reveal cellular architecture.

Dialogue between Cell-Matrix adhesion and centrosome

In chapter I discussion, I described the cell-cell junction molecules which are found at the centrosome and have a regulatory function. Similarly focal-adhesion proteins; Paxillin is also found at the centrosome (Herreros et al., 2000; Robertson and Ostergaard, 2011). Paxillin is a multidomain adapter protein and is enriched at integrin-focal adhesion but also present in cytosol and can be membrane-associated. Paxillin is associated with the α-tubulin network and also present at the immune synapse of T-lymphocyte, which do not form focal-adhesions. Tyrosin phosphorylated Paxillin in T cells is recruited to MTOC and responds to ERK signaling upon TCR stimulation. It is constitutively localized at the MTOC upon engagement of CTL with the target cell and helps orientation of MTOC in the direction of immune synapse so that supramolecular activation complex (SMAC) could be released precisely at the target cells for its destruction (Robertson and Ostergaard, 2011). In adherent cell lines, where integrins are involved in formation of focal adhesion, they can regulate microtubule nucleation at the centrosome. Inhibition of signaling through cytoplasmic tail of β1-integrin reduced microtubule nucleation at the centrosome and it is controlled by MEK/ERK signaling pathway probably by affecting γ -tubulin accumulation (Colello et al., 2012). In our study we saw that EMT induced mesenchymal cells had reduced microtubule nucleation capacity along with reduction of γ -tubulin accumulation at the centrosome. Hence within the context of EMT, it will important to understand how different pathways such as Smad, MEK, Ras etc. affect MTOC activity of the centrosome and thereby affect the polarity reversal and cell-separation. Another study by the same group revealed that these cells with non-functional β1-integrin tail also forms multipolar spindles and have cytokinetic failure (Reverte et al., 2006). Furthermore, β1 integrin null mice have severely fragmented centrosomes, which affects polarization of cells during wound healing response. Inhibition β1-integrin function by blocking antibody also perturbed centrosome integrity in Brain, muscle and skin cells dissociated from 18 day embryonic chick thus suggesting the integrin regulation of centrosome integrity is not tissue-specific (Peng et al., 2013). These evidences are very important to realize multifaceted role of centrosome during interphase and during cell division. As described in chapter I, defects in centrosome morphology is associated with errors in chromosome segregation and aneuploidy. Focal adhesion proteins could affect the centrosome integrity by signaling molecules activated at the cytoplasmic integrin tails or by selective transport of molecules via FA-associated MTs to the centrosome. It will be important

to validate whether inhibition of β1-integrin function during EMT directly affects MTOC activity of the centrosome which can give a clue about mechanisms that control centrosome composition and microtubule nucleating activity (Figure 4 Burute et al).

2.5 References

Acloque, H., Adams, M.S., Fishwick, K., Bronner-fraser, M., and Nieto, M.A. (2009). Review series Epithelial-mesenchymal transitions : the importance of changing cell state in development and disease. *119*.

Akhmanova, A., and Stehbens, S.J. (2009). Touch , Grasp , Deliver and Control : Functional Cross-Talk Between Microtubules and Cell Adhesions. Traffic 1–7.

Akhtar, N., and Streuli, C.H. (2013). An integrin-ILK-microtubule network orients cell polarity and lumen formation in glandular epithelium. Nat. Cell Biol. *15*, 17–27.

Azioune, A., Carpi, N., Tseng, Q., Théry, M., and Piel, M. (2010). Protein micropatterns: A direct printing protocol using deep UVs. Methods Cell Biol. *97*, 133–146.

Beach, J.R., Hussey, G.S., Miller, T.E., Chaudhury, a., Patel, P., Monslow, J., Zheng, Q., Keri, R. a., Reizes, O., Bresnick, a. R., et al. (2011). Myosin II isoform switching mediates invasiveness after TGF- -induced epithelial-mesenchymal transition. Proc. Natl. Acad. Sci. *108*, 17991–17996.

Bentivoglio, M. (1999). The discovery of the Golgi apparatus. J Hist Neurosci. *8*, 202–208.

van Bergeijk, P., Hoogenraad, C.C., and Kapitein, L.C. (2015). Right Time, Right Place: Probing the Functions of Organelle Positioning. Trends Cell Biol. *xx*, 1–14.

Bornens, M. (2008). Organelle positioning and cell polarity. Nat. Rev. Mol. Cell Biol. *9*, 874–886.

Bornens, M., Paintrand, M., and Celati, C. (1989). The cortical microfilament system of lymphoblasts displays a periodic oscillatory activity in the absence of microtubules: implications for cell polarity. J. Cell Biol. *109*, 1071–1083.

Bosch, T.C.G. (2007). Why polyps regenerate and we don't: Towards a cellular and molecular framework for Hydra regeneration. Dev. Biol. *303*, 421–433.

Bryant, D.M., Roignot, J., Datta, A., Overeem, A.W., Kim, M., Yu, W., Peng, X., Eastburn, D.J., Ewald, A.J., Werb, Z., et al. (2014). A molecular switch for the orientation of epithelial cell polarization. Dev. Cell *31*, 171–187.

Buckley, C.E., Ren, X., Ward, L.C., Girdler, G.C., Araya, C., Green, M.J., Clark, B.S., Link, B. a, and Clarke, J.D.W. (2012). Mirror-symmetric microtubule assembly and cell interactions drive lumen formation in the zebrafish neural rod. EMBO J. 1–15.

Burakov, a. (2003). Centrosome positioning in interphase cells. J. Cell Biol. *162*, 963–969.

Burute, M., and Théry, M. (2012). Spatial segregation between cell-cell and cell-matrix adhesions. Curr. Opin. Cell Biol. 1–9.

Butler, J.P., Tolić-Nørrelykke, I.M., Fabry, B., and Fredberg, J.J. (2002). Traction fields, moments, and strain energy that cells exert on their surroundings. Am. J. Physiol. Cell Physiol. *282*, C595–C605.

Carney, P.R., and Couve, E. (1989). Cell polarity changes and migration during early development of the avian peripheral auditory system. Anat. Rec. *225*, 156–164.

Chausovsky, A., Bershadsky, A.D., and Borisy, G.G. (2000). Cadherin-mediated regulation of microtubule dynamics. Nat. Cell Biol. *2*, 797–804.

Colello, D., Mathew, S., Ward, R., Pumiglia, K., and LaFlamme, S.E. (2012). Integrins regulate microtubule nucleating activity of centrosome through mitogen-activated protein kinase/extracellular signal-regulated kinase kinase/extracellular signal-regulated kinase (MEK/ERK) signaling. J. Biol. Chem. *287*, 2520–2530.

Das, R.M., and Storey, K.G. (2014). Apical abscission alters cell polarity and dismantles the primary cilium during neurogenesis. Science (80-.). *343*, 200–204.

Deakin, N.O., and Turner, C.E. (2014). Paxillin inhibits HDAC6 to regulate microtubule acetylation, Golgi structure, and polarized migration. J. Cell Biol. *206*, 395–413.

Debnath, J., and Brugge, J.S. (2005). Modelling glandular epithelial cancers in three-dimensional cultures. Nat. Rev. Cancer *5*, 675–688.

Debnath, J., Muthuswamy, S.K., and Brugge, J.S. (2003). Morphogenesis and oncogenesis of MCF-10A mammary epithelial acini grown in three-dimensional basement membrane cultures. Methods *30*, 256–268.

Dickinson, D.J., Nelson, W.J., and Weis, W.I. (2011). A Polarized Epithelium Organized by - and -Catenin Predates Cadherin and Metazoan Origins. Science (80-.). *331*, 1336–1339.

Dogterom, M. (1997). Measurement of the Force-Velocity Relation for Growing Microtubules. Science (80-.). *278*, 856–860.

van Dongen, S.F.M., Maiuri, P., Marie, E., Tribet, C., and Piel, M. (2013). Triggering cell adhesion, migration or shape change with a dynamic surface coating. Adv. Mater. *25*, 1687–1691.

Doyle, A.D., Wang, F.W., Matsumoto, K., and Yamada, K.M. (2009). One-dimensional topography underlies three-dimensional fibrillar cell migration. J. Cell Biol. *184*, 481–490.

Du, D., Xu, F., Yu, L., Zhang, C., Lu, X., Yuan, H., Huang, Q., Zhang, F., Bao, H., Jia, L., et al. (2010). The tight junction protein, occludin, regulates the directional migration of epithelial

cells. Dev. Cell *18*, 52–63.

Dupin, I., Camand, E., and Etienne-manneville, S. (2009). Classical cadherins control nucleus and centrosome position and cell polarity. *185*.

Etienne-Manneville, S. (2013). Microtubules in cell migration. Annu. Rev. Cell Dev. Biol. *29*, 471–499.

Etienne-Manneville, S., and Hall, A. (2002). Rho GTPases in cell biology. Nature *420*, 629–635.

Ewald, A.J., Brenot, A., Duong, M., Chan, B.S., and Werb, Z. (2008). Collective Epithelial Migration and Cell Rearrangements Drive Mammary Branching Morphogenesis. Dev. Cell *14*, 570–581.

Ewald, A.J., Jorgens, D.M., Huebner, R.J., Tauscher, A.N., Palsdottir, H., Cheung, K.J., Lee, J.K., Zena Werb, Perez, M.J., and Manfred Auer (2012). Mammary collective cell migration involves transient loss of epithelial features and individual cell migration within the epithelium. J. Cell Sci.

Faivre-Moskalenko, C., and Dogterom, M. (2002). Dynamics of microtubule asters in microfabricated chambers: the role of catastrophes. Proc. Natl. Acad. Sci. U. S. A. *99*, 16788–16793.

Feldman, J.L., and Priess, J.R. (2012). A role for the centrosome and PAR-3 in the hand-off of MTOC function during epithelial polarization. Curr. Biol. *22*, 575–582.

de Forges, H., Bouissou, A., and Perez, F. (2012). Interplay between microtubule dynamics and intracellular organization. Int. J. Biochem. Cell Biol. *44*, 266–274.

Gavilan, M.P., Arjona, M., Zurbano, A., Formstecher, E., Bornens, M., and Rios, R.M. (2015). Alpha-catenin-Dependent Recruitment of the Centrosomal Protein CAP350 to Adherens Junctions Allows Epithelial Cells to Acquire a Columnar Shape. 1–31.

Gittes, F., Mickey, B., Nettleton, J., and Howard, J. (1993). Flexural rigidity of microtubules and actin filaments measured from thermal fluctuations in shape. J. Cell Biol. *120*, 923–934.

Glotfelty, L. a, Zahs, A., Iancu, C., Shen, L., and Hecht, G. a (2014). Microtubules Are Required for Efficient Epithelial Tight Junction Homeostasis and Restoration. Am. J. Physiol. Cell Physiol.

Godde, N.J., Galea, R.C., Elsum, I. a, and Humbert, P.O. (2010). Cell polarity in motion: redefining mammary tissue organization through EMT and cell polarity transitions. J. Mammary Gland Biol. Neoplasia *15*, 149–168.

Godinho, S. a., Picone, R., Burute, M., Dagher, R., Su, Y., Leung, C.T., Polyak, K., Brugge, J.S., Théry, M., and Pellman, D. (2014). Oncogene-like induction of cellular invasion from centrosome amplification. Nature *510*, 167–171.

Gomes, E.R., Jani, S., and Gundersen, G.G. (2005). Nuclear Movement Regulated by Cdc42, MRCK, Myosin, and Actin Flow Establishes MTOC Polarization in Migrating Cells. Cell *121*, 451–463.

Gross, S.P., Welte, M.A., Block, S.M., and Wieschaus, E.F. (2000). Dynein-mediated Cargo Transport In Vivo: A Switch Controls Travel Distance. J. Cell Biol. *148*, 945–955.

Gudjonsson, T., Rønnov-Jessen, L., Villadsen, R., Rank, F., Bissell, M.J., and Petersen, O.W. (2002). Normal and tumor-derived myoepithelial cells differ in their ability to interact with luminal breast epithelial cells for polarity and basement membrane deposition. J. Cell Sci. *115*, 39–50.

Guilluy, C., Swaminathan, V., Garcia-Mata, R., Timothy O'Brien, E., Superfine, R., and Burridge, K. (2011). The Rho GEFs LARG and GEF-H1 regulate the mechanical response to force on integrins. Nat. Cell Biol. *13*, 724–729.

Hale, C.M., Chen, W.-C., Khatau, S.B., Daniels, B.R., Lee, J.S.H., and Wirtz, D. (2011). SMRT analysis of MTOC and nuclear positioning reveals the role of EB1 and LIC1 in single-cell polarization. J. Cell Sci.

Hao, Y., Du, Q., Chen, X., Zheng, Z., Balsbaugh, J.L., Maitra, S., Shabanowitz, J., Hunt, D.F., and Macara, I.G. (2010). Par3 Controls Epithelial Spindle Orientation by aPKC-Mediated Phosphorylation of Apical Pins. Curr. Biol. *20*, 1809–1818.

Harris, T.J.C., and Peifer, M. (2005). The positioning and segregation of apical cues during epithelial polarity establishment in Drosophila. J. Cell Biol. *170*, 813–823.

Harris, T.J.C., and Peifer, M. (2007). aPKC controls microtubule organization to balance adherens junction symmetry and planar polarity during development. Dev. Cell *12*, 727–738.

Hebert, A.M., Duboff, B., Casaletto, J.B., Gladden, A.B., and McClatchey, A.I. (2012). Merlin/ERM proteins establish cortical asymmetry and centrosome position. Genes Dev. *26*, 2709–2723.

Hehnly, H., and Doxsey, S. (2014). Rab11 Endosomes Contribute to Mitotic Spindle Organization and Orientation. Dev. Cell *28*, 497–507.

Hehnly, H., Chen, C.T., Powers, C.M., Liu, H.L., and Doxsey, S. (2012). The centrosome regulates the Rab11- dependent recycling endosome pathway at appendages of the mother centriole. Curr. Biol. *22*, 1944–1950.

Herreros, L., Rodríguez-Fernández, J.L., Brown, M.C., Alonso-Lebrero, J.L., Cabañas, C., Sánchez-Madrid, F., Longo, N., Turner, C.E., and Sánchez-Mateos, P. (2000). Paxillin localizes to the lymphocyte microtubule organizing center and associates with the microtubule cytoskeleton. J. Biol. Chem. *275*, 26436–26440.

Hinck, L., and Silberstein, G.B. (2005). Key stages in mammary gland development: the mammary end bud as a motile organ. Breast Cancer Res. *7*, 245–251.

Hong, E., Jayachandran, P., and Brewster, R. (2010). The polarity protein Pard3 is required for centrosome positioning during neurulation. Dev. Biol. *341*, 335–345.

Huang, R.Y.-J., Guilford, P., and Thiery, J.P. (2012). Early events in cell adhesion and polarity during epithelial-mesenchymal transition. J. Cell Sci. 4417–4422.

Huang, S., Brangwynne, C.P., Parker, K.K., and Ingber, D.E. (2005). Symmetry-breaking in mammalian cell cohort migration during tissue pattern formation: role of random-walk persistence. Cell Motil. Cytoskeleton *61*, 201–213.

Huber, M.A., Kraut, N., and Beug, H. (2005). Molecular requirements for epithelial–mesenchymal transition during tumor progression. Curr. Opin. Cell Biol. *17*, 548–558.

Inman, G.J., Nicolás, F.J., Callahan, J.F., Harling, J.D., Gaster, L.M., Reith, A.D., Laping, N.J., and Hill, C.S. (2002). SB-431542 is a potent and specific inhibitor of transforming growth factor-beta superfamily type I activin receptor-like kinase (ALK) receptors ALK4, ALK5, and ALK7. Mol. Pharmacol. *62*, 65–74.

J. D'Souza, R.C., Knittle, A.M., Nagaraj, N., van Dinther, M., Choudhary, C., ten Dijke, P., Mann, M., and Sharma, K. (2014). Time-resolved dissection of early phosphoproteome and ensuing proteome changes in response to TGF- . Sci. Signal. *7*, rs5–rs5.

Jiang, T., Mckinley, R.F.A., Mcgill, M.A., Angers, S., Harris, T.J.C., Jiang, T., Mckinley, R.F.A., Mcgill, M.A., Angers, S., and Harris, T.J.C. (2015). Report A Par-1-Par-3-Centrosome Cell Polarity Pathway and Its Tuning for Isotropic Cell Adhesion Report A Par-1-Par-3-Centrosome Cell Polarity Pathway and Its Tuning for Isotropic Cell Adhesion. Curr. Biol. 1–8.

Joo, E.E., and Yamada, K.M. (2014). MYPT1 regulates contractility and microtubule acetylation to modulate integrin adhesions and matrix assembly. Nat. Commun. *5*, 3510.

Kalluri, R., and Weinberg, R. a (2009). Review series The basics of epithelial-mesenchymal transition. J. Clin. Invest. *119*, 1420–1428.

Kimura, A., and Onami, S. (2010). Modeling Microtubule-Mediated Forces and Centrosome Positioning in Caenorhabditis elegans Embryos. Methods Cell Biol. *97*, 437–453.

Lamouille, S., and Derynck, R. (2007). Cell size and invasion in TGF-beta-induced epithelial to mesenchymal transition is regulated by activation of the mTOR pathway. J. Cell Biol. *178*, 437–451.

Lamouille, S., Xu, J., and Derynck, R. (2014). Molecular mechanisms of epithelial-mesenchymal transition. Nat. Rev. Mol. Cell Biol. *15*, 178–196.

Lechler, T., and Fuchs, E. (2007). Desmoplakin: an unexpected regulator of microtubule organization in the epidermis. J. Cell Biol. *176*, 147–154.

Levental, K.R., Yu, H., Kass, L., Lakins, J.N., Egeblad, M., Erler, J.T., Fong, S.F.T., Csiszar, K., Giaccia, A., Weninger, W., et al. (2009). Matrix crosslinking forces tumor progression by enhancing integrin signaling. Cell *139*, 891–906.

Ligon, L. a, and Holzbaur, E.L.F. (2007). Microtubules tethered at epithelial cell junctions by dynein facilitate efficient junction assembly. Traffic *8*, 808–819.

Ligon, L.A., Karki, S., Tokito, M., and Holzbaur, E.L.F. (2001). Dynein binds to β -catenin and may tether microtubules at adherens junctions. *3*, 913–917.

Liu, Z., Tan, J.L., Cohen, D.M., Yang, M.T., Sniadecki, N.J., Ruiz, S.A., Nelson, C.M., and Chen, C.S. (2010). Mechanical tugging force regulates the size of cell-cell junctions. Proc. Natl. Acad. Sci. U. S. A. *107*, 9944–9949.

Luxton, G.G., and Gundersen, G.G. (2011). Orientation and function of the nuclear-centrosomal axis during cell migration. Curr. Opin. Cell Biol. 1–10.

Marcum, B.A., Campbell, R.D., and Romero, J. (1977). Polarity reversal in nerve-free hydra. Science *197*, 771–773.

Markowski, M.C., Brown, A.C., and Barker, T.H. (2012). Directing epithelial to mesenchymal transition through engineered microenvironments displaying orthogonal adhesive and mechanical cues. J. Biomed. Mater. Res. - Part A *100 A*, 2119–2127.

Martiel, J.-L., Leal, A., Kurzawa, L., Balland, M., Wang, I., Vignaud, T., Tseng, Q., and Théry, M. (2015). Measurement of cell traction forces with ImageJ. Methods Cell Biol. *125*, 269–287.

Mauchamp, J., Margotat, A., Chambard, M., Charrier, B., Remy, L., and Michel-Bechet, M. (1979). Polarity of three-dimensional structures derived from isolated hog thyroid cells in primary culture. Cell Tissue Res. *204*, 417–430.

Meng, W., Mushika, Y., Ichii, T., and Takeichi, M. (2008). Anchorage of microtubule minus ends to adherens junctions regulates epithelial cell-cell contacts. Cell *135*, 948–959.

Micalizzi, D.S., Farabaugh, S.M., and Ford, H.L. (2010). Epithelial-mesenchymal transition in cancer: parallels between normal development and tumor progression. J. Mammary Gland Biol. Neoplasia *15*, 117–134.

Mimori-Kiyosue, Y. (2011). Shaping microtubules into diverse patterns: Molecular connections for setting up both ends. Cytoskeleton *68*, 603–618.

Montesano, R., Soriano, J. V, Fialka, I., and Orci, L. (1998). Isolation of EpH4 mammary epithelial cell subpopulations which differ in their morphogenetic properties. In Vitro Cell. Dev.

Biol. Anim. *34*, 468–477.

Montesano, R., Carrozzino, F., and Soulié, P. (2007). Low concentrations of transforming growth factor-beta-1 induce tubulogenesis in cultured mammary epithelial cells. BMC Dev. Biol. *7*, 7.

Moss, D.K., Bellett, G., Carter, J.M., Liovic, M., Keynton, J., Prescott, A.R., Lane, E.B., and Mogensen, M.M. (2007). Ninein is released from the centrosome and moves bi-directionally along microtubules. J. Cell Sci. *120*, 3064–3074.

Nedelec, F., and Foethke, D. (2007). Collective Langevin dynamics of flexible cytoskeletal fibers. New J. Phys. *9*.

Nelson, W.J. (2009). Remodeling epithelial cell organization: transitions between front-rear and apical-basal polarity. Cold Spring Harb. Perspect. Biol. *1*, a000513.

Nelson, C.M., and Bissell, M.J. (2005). Modeling dynamic reciprocity : Engineering three-dimensional culture models of breast architecture , function , and neoplastic transformation. Semin. Cancer Biol. *15*, 342–352.

Nitsch, L., and Wollman, S.H. (1980). Ultrastructure of intermediate stages in polarity reversal of thyroid epithelium in follicles in suspension culture. J.Cell Biol. *86*, 875–880.

O'Brien, L.E., Jou, T., Pollack, A.L., Zhang, Q., Hansen, S.H., and Mostov, K.E. (2001). Rac1 orientates epithelial apical polarity through effects on basolateral laminin assembly. Nat. Cell Biol. *3*, 831–838.

O'Connor, J.W., and Gomez, E.W. (2014). Biomechanics of TGFβ-induced epithelial-mesenchymal transition: implications for fibrosis and cancer. Clin. Transl. Med. *3*, 23.

Ojakian, K.G., and Schwimmer, R. (1994). Regulation of epithelial cell surface polarity reversal by beta 1 integrins. J. Cell Sci. *107*, 561–576.

Oliaro, J., Van Ham, V., Sacirbegovic, F., Pasam, A., Bomzon, Z., Pham, K., Ludford-Menting, M.J., Waterhouse, N.J., Bots, M., Hawkins, E.D., et al. (2010). Asymmetric Cell Division of T Cells upon Antigen Presentation Uses Multiple Conserved Mechanisms. J. Immunol. *185*, 367–375.

Paszek, M.J., Zahir, N., Johnson, K.R., Lakins, J.N., Rozenberg, G.I., Gefen, A., Reinhart-King, C. a, Margulies, S.S., Dembo, M., Boettiger, D., et al. (2005). Tensional homeostasis and the malignant phenotype. Cancer Cell *8*, 241–254.

Paul, N.R., Jacquemet, G., and Caswell, P.T. (2015). Endocytic Trafficking of Integrins in Cell Migration. Curr. Biol. *25*, R1092–R1105.

Peng, H., Ong, Y.M., Shah, W.A., Holland, P.C., and Carbonetto, S. (2013). Integrins regulate centrosome integrity and astrocyte polarization following a wound. Dev. Neurobiol. *73*, 333–

353.

Pinot, M., Chesnel, F., Kubiak, J.Z., Arnal, I., Nedelec, F.J., and Gueroui, Z. (2009). Effects of confinement on the self-organization of microtubules and motors. Curr. Biol. *19*, 954–960.

Pollack, A.L., Runyan, R.B., and Mostov, K.E. (1998). Morphogenetic Mechanisms of Epithelial Tubulogenesis : MDCK Cell Polarity Is Transiently Rearranged without Loss of Cell – Cell Contact during Scatter Factor / Hepatocyte Growth. Dev. Biol. *79*, 64–79.

Pouthas, F., Girard, P., Lecaudey, V., Ly, T.B.N., Gilmour, D., Boulin, C., Pepperkok, R., and Reynaud, E.G. (2008). In migrating cells, the Golgi complex and the position of the centrosome depend on geometrical constraints of the substratum. J. Cell Sci. *121*, 2406–2414.

Rape, A.D., Guo, W.-H., and Wang, Y.-L. (2011). Microtubule depolymerization induces traction force increase through two distinct pathways. J. Cell Sci.

Ratner, S., Sherrod, W.S., and Lichlyter, D. (1997). Microtubule retraction into the uropod and its role in T cell polarization and motility. J. Immunol. *159*, 1063–1067.

Revenu, C., Streichan, S., Donà, E., Lecaudey, V., Hufnagel, L., and Gilmour, D. (2014). Quantitative cell polarity imaging defines leader-to-follower transitions during collective migration and the key role of microtubule-dependent adherens junction formation. Development 1282–1291.

Reverte, C.G., Benware, A., Jones, C.W., and LaFlamme, S.E. (2006). Perturbing integrin function inhibits microtubule growth from centrosomes, spindle assembly, and cytokinesis. J. Cell Biol. *174*, 491–497.

Ritter, A.T., Asano, Y., Stinchcombe, J.C., Dieckmann, N.M.G., Chen, B.C., Gawden-Bone, C., van Engelenburg, S., Legant, W., Gao, L., Davidson, M.W., et al. (2015). Actin Depletion Initiates Events Leading to Granule Secretion at the Immunological Synapse. Immunity *42*, 864–876.

Robertson, L.K., and Ostergaard, H.L. (2011). Paxillin associates with the microtubule cytoskeleton and the immunological synapse of CTL through its leucine-aspartic acid domains and contributes to microtubule organizing center reorientation. J. Immunol. *187*, 5824–5833.

Rodriguez, O.C., Schaefer, A.W., Mandato, C. a, Forscher, P., Bement, W.M., and Waterman-Storer, C.M. (2003). Conserved microtubule-actin interactions in cell movement and morphogenesis. Nat. Cell Biol. *5*, 599–609.

Rodriguez-Boulan, E., and Macara, I.G. (2014). Organization and execution of the epithelial polarity programme. Nat. Rev. Mol. Cell Biol. *15*, 225–242.

Rodríguez-Fraticelli, A.E., Auzan, M., Alonso, M. a, Bornens, M., and Martín-Belmonte, F. (2012). Cell confinement controls centrosome positioning and lumen initiation during epithelial

morphogenesis. J. Cell Biol. *198*, 1011–1023.

Rooij, J. De, Kerstens, A., Danuser, G., Schwartz, M.A., and Waterman-storer, C.M. (2005). Integrin-dependent actomyosin contraction regulates epithelial cell scattering. October *171*, 153–164.

Scarpa, E., Szabó, A., Bibonne, A., Theveneau, E., Parsons, M., and Mayor, R. (2015). Cadherin Switch during EMT in Neural Crest Cells Leads to Contact Inhibition of Locomotion via Repolarization of Forces. Dev. Cell *34*, 421–434.

Schmoranzer, J., Fawcett, J.P., Segura, M., Tan, S., Vallee, R.B., Pawson, T., and Gundersen, G.G. (2009). Par3 and dynein associate to regulate local microtubule dynamics and centrosome orientation during migration. Curr. Biol. *19*, 1065–1074.

Seton-Rogers, S.E., Lu, Y., Hines, L.M., Koundinya, M., LaBaer, J., Muthuswamy, S.K., and Brugge, J.S. (2004). Cooperation of the ErbB2 receptor and transforming growth factor beta in induction of migration and invasion in mammary epithelial cells. Proc. Natl. Acad. Sci. U. S. A. *101*, 1257–1262.

Shahbazi, M.N., Megias, D., Epifano, C., Akhmanova, A., Gundersen, G.G., Fuchs, E., and Perez-Moreno, M. (2013). CLASP2 interacts with p120-catenin and governs microtubule dynamics at adherens junctions. J. Cell Biol. *203*, 1043–1061.

Shtutman, M., Chausovsky, A., Prager-khoutorsky, M., Schiefermeier, N., Boguslavsky, S., Kam, Z., Fuchs, E., Geiger, B., Borisy, G.G., and Bershadsky, A.D. (2008). Signaling function of α-catenin in microtubule regulation ND ES SC RIB. 2377–2383.

Sipe, C.W., Liu, L., Lee, J., Grimsley-Myers, C., and Lu, X. (2013). Lis1 mediates planar polarity of auditory hair cells through regulation of microtubule organization. Development *140*, 1785–1795.

Solecki, D.J., Trivedi, N., Govek, E.-E., Kerekes, R. a, Gleason, S.S., and Hatten, M.E. (2009). Myosin II motors and F-actin dynamics drive the coordinated movement of the centrosome and soma during CNS glial-guided neuronal migration. Neuron *63*, 63–80.

Soppina, V., Rai, A.K., Ramaiya, A.J., Barak, P., and Mallik, R. (2009). Tug-of-war between dissimilar teams of microtubule motors regulates transport and fission of endosomes. Proc. Natl. Acad. Sci. U. S. A. *106*, 19381–19386.

Spaderna, S., Schmalhofer, O., Wahlbuhl, M., Dimmler, A., Bauer, K., Sultan, A., Hlubek, F., Jung, A., Strand, D., Eger, A., et al. (2008). The Transcriptional Repressor ZEB1 Promotes Metastasis and Loss of Cell Polarity in Cancer. Cancer Res. *68*, 537–544.

St Johnston, D., and Sanson, B. (2011). Epithelial polarity and morphogenesis. Curr. Opin. Cell Biol. 540–546.

Sugioka, K., and Sawa, H. (2012). Formation and functions of asymmetric microtubule organization in polarized cells. Curr. Opin. Cell Biol. 1–9.

Sumigray, K.D., Chen, H., and Lechler, T. (2011). Lis1 is essential for cortical microtubule organization and desmosome stability in the epidermis. J. Cell Biol. *194*, 631–642.

Tam, P.P., and Behringer, R.R. (1997). Mouse gastrulation: the formation of a mammalian body plan. Mech. Dev. *68*, 3–25.

Tang, N., and Marshall, W.F. (2012). Centrosome positioning in vertebrate development. J. Cell Sci. *125*, 4951–4961.

Théry, M. (2010). Micropatterning as a tool to decipher cell morphogenesis and functions. J. Cell Sci. *123*, 4201–4213.

Théry, M., Racine, V., Piel, M., Pépin, A., Dimitrov, A., Chen, Y., Sibarita, J.-B., and Bornens, M. (2006). Anisotropy of cell adhesive microenvironment governs cell internal organization and orientation of polarity. Proc. Natl. Acad. Sci. U. S. A. *103*, 19771–19776.

Thiery, J.P. (2002). Epithelial–mesenchymal transitions in tumour progression. Nat. Rev. Cancer *2*, 442–454.

Thiery, J.P., Acloque, H., Huang, R.Y.J., and Nieto, M.A. (2009). Epithelial-mesenchymal transitions in development and disease. Cell *139*, 871–890.

Tischer, D., and Weiner, O.D. (2014). Illuminating cell signalling with optogenetic tools. Nat. Rev. Mol. Cell Biol. *15*, 551–558.

Tse, J.R., and Engler, A.J. (2010). Preparation of hydrogel substrates with tunable mechanical properties. Curr. Protoc. Cell Biol. 1–16.

Tseng, Q., Duchemin-Pelletier, E., Deshiere, A., Balland, M., Guillou, H., Filhol, O., and Théry, M. (2012). Spatial organization of the extracellular matrix regulates cell-cell junction positioning. Proc. Natl. Acad. Sci. U. S. A. *109*, 1506–1511.

Underwood, J.M., Imbalzano, K.M., Weaver, V.M., Fischer, A.H., Imbalzano, A.N., and Nickerson, J.A. (2006). The Ultrastructure of MCF-10A Acini. J. Cell. Physiol. *148*, 141–148.

Vignaud, T., Ennomani, H., and Théry, M. (2014). Polyacrylamide Hydrogel Micropatterning. Methods Cell Biol. *120*.

Wang, H., Lacoche, S., Huang, L., Xue, B., and Muthuswamy, S.K. (2013). Rotational motion during three-dimensional morphogenesis of mammary epithelial acini relates to laminin matrix assembly. Proc. Natl. Acad. Sci. U. S. A. *110*, 163–168.

Wang, Z.A., Ojakian, K.G., and Nelson, W.J. (1990). Steps in the morphogenesis of a polarized epithelium II. Disassembly and assembly of plasma membrane domains during reversal of

epithelial cell polarity in multicellular epithelial (MDCK) cysts. J. Cell Sci. *95*, 153–165.

Wei, S.C., Fattet, L., Tsai, J.H., Guo, Y., Pai, V.H., Majeski, H.E., Chen, A.C., Sah, R.L., Taylor, S.S., Engler, A.J., et al. (2015). Matrix stiffness drives epithelial–mesenchymal transition and tumour metastasis through a TWIST1–G3BP2 mechanotransduction pathway. Nat. Cell Biol. *17*, 678–688.

Wu, J., Misra, G., Russell, R.J., Ladd, A.J.C., Lele, T.P., and Dickinson, R.B. (2011). Effects of dynein on microtubule mechanics and centrosome positioning. Mol. Biol. Cell *22*, 4834–4841.

Xu, J., Lamouille, S., and Derynck, R. (2009). TGF-beta-induced epithelial to mesenchymal transition. Cell Res. *19*, 156–172.

Xue, B., Krishnamurthy, K., Allred, D.C., and Muthuswamy, S.K. (2012). Loss of Par3 promotes breast cancer metastasis by compromising cell-cell cohesion. Nat. Cell Biol. *15*, 1–14.

Yeaman, C., Grindstaff, K.K., and Nelson, W.J. (1999). New Perspectives on Mechanisms Involved in Generating Epithelial Cell Polarity. Physiol. Rev. *79*, 73–98.

Yi, J., Wu, X., Chung, A.H., Chen, J.K., Kapoor, T.M., and Hammer, J. a (2013). Centrosome repositioning in T cells is biphasic and driven by microtubule end-on capture-shrinkage. J. Cell Biol. *202*, 779–792.

Yu, W., O'Brien, L.E., Fei, W., Henry, B., Mostov, K., and Zegers, M.M.P. (2003). Hepatocyte Growth Factor switches orientaion of polarity and mode of movement during morphogenesis of multicellular epithelial structures. Mol. Biol. Cell *14*, 2559–2569.

Yu, W., Datta, A., Leroy, P., O'Brien, L.E., Mak, G., Jou, T.-S., Matlin, K.S., Mostov, K.E., and Zegers, M.M.P. (2005). Beta1-integrin orients epithelial polarity via Rac1 and laminin. Mol. Biol. Cell *16*, 433–445.

Zavadil, J., and Böttinger, E.P. (2005). TGF-β and epithelial-to-mesenchymal transitions. Oncogene *24*, 5764–5774.

Zhang, J., Tian, X.-J., Zhang, H., Teng, Y., Li, R., Bai, F., Elankumaran, S., and Xing, J. (2014). TGF-β-induced epithelial-to-mesenchymal transition proceeds through stepwise activation of multiple feedback loops. Sci. Signal. *7*, ra91.

Zhu, J., Burakov, A., Rodionov, V., and Mogilner, A. (2010). Finding the Cell Center by a Balance of Dynein and Myosin Pulling and Microtubule Pushing : A Computational Study. *21*, 4418–4427.

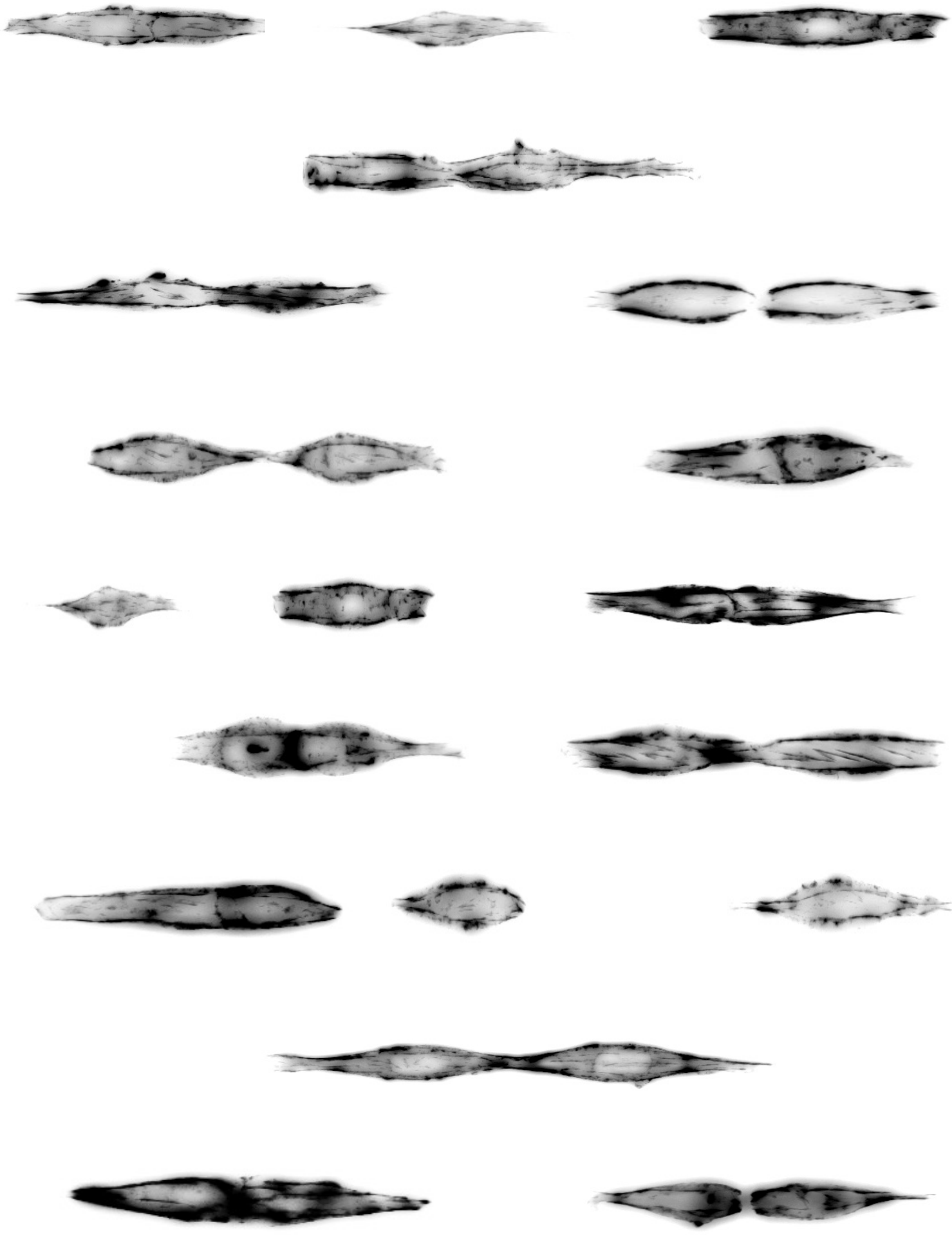

CHAPTER III

Development of the “EMT Kit”

3.1 Introduction

Need for developing a new assay to detect EMT

The 'War on Cancer' was declared in 1971 that led to National Cancer Act (1971) because of the lack of cures for cancer malignancies. Metastasis, which is the spread of cancer cells from site of origin to other parts of the body accounts for 90% of deaths in cancer patients (Cavallo et al., 2011; Nixon and Act, 1973). Tumor metastasis is a multistep process in which tumor cells disseminate into surrounding tissue and form secondary tumors at a distance site. Metastasis occurs through a series of steps: invasion, intravasation, transport, extravasation and colonization. Metastasis of primary tumor is associated with secretion of cytokines, growth factors and metalloproteases (MMPs) in the surrounding tissue. Epithelial to mesenchymal transition is thought to play a critical role in promoting metastasis in epithelium-derived carcinoma (Kalluri and Weinberg, 2009; Tsai and Yang, 2013).

The process of EMT was originally described in the context of normal cell differentiation during developmental processes (Hay, 1995; Thiery, 2002). Mesenchymal cell dissociation is observed at early stages of vertebrate gastrulation, neural plate formation, branching morphogenesis of mammary gland (Micalizzi Neoplasia 2010). For more than a decade EMT has been proposed as a potential mechanism for cancer progression (Thiery, 2002). Cancer patients have higher levels of growth factors such as Insulin-growth factor (IGF-1), Transforming growth factor (TGF-β), Epidermal growth factor (EGF) and Hepatocyte growth factor (HGF) in the blood, which are also the key drivers of EMT during development (Huang et al., 2012). Despite the vast available knowledge on EMT and cancer, the discovery of anticancer drugs remains a highly challenging endeavor. A typical drug development program requires progressive selection of drugs depending upon their anticancer activity (Figure 3.1A). In the 1930s, the drug developmental programs were small scale and based on rational selection of chemical compounds (up to 10-1000). These early strategies of drug screening were mostly focused on the end point phenotype of cancer. For example, inhibition of cell migration by targeting matrix metalloproteases (MMPs). With the mounting knowledge of the active role of EMT in cancer progression, new strategies for cancer drug screening are being based on exploiting the anti-EMT activity of chemical compounds. EMT induction elicits the action of several downstream molecular pathways, wherein subcellular changes occur at the level of transcription, post-translational and cytoskeleton level. The effect of EMT inducers can be observed starting from 5 minutes with protein phosphorylation to changes in proteome profile over days (J. D'Souza et al., 2014). To comprehend these molecular complexities a range of drug screening strategies are employed (Figure 3.1B). Beginning with rational design where the highest

Figure 3.1

A

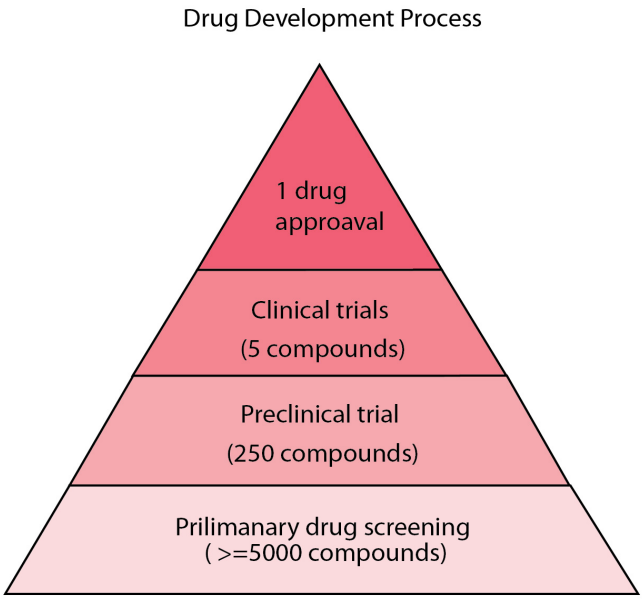

B

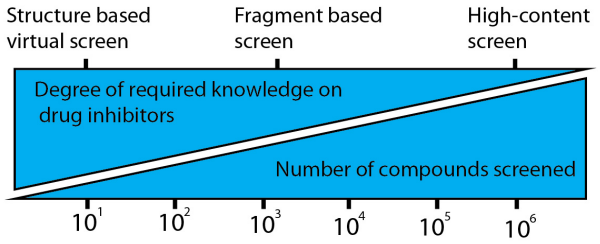

Hoelder, 2012

C

Apllication workflow for development of the "EMT kit"

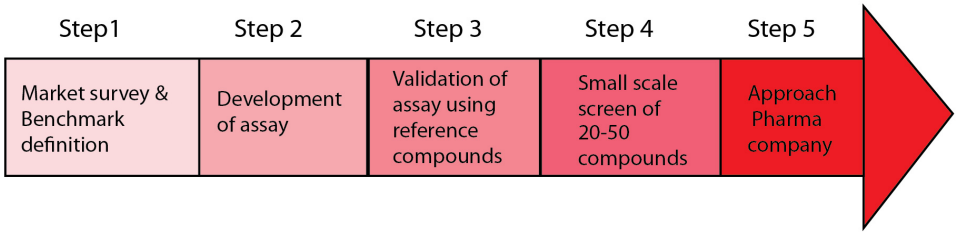

(A) Key steps in the Drug development process (B) Comparision of required knowledge on compounds and number of compounds screened with different screening methods (C) Different steps of application workflow for development of the 'EMT kit'

degree of knowledge of inhibitors is required to high-throughput screening (HTS) where up to a million compounds can be screened per week with minimum knowledge of inhibitors required (Hoelder et al., 2012). Another advantage of HTS is that it is a relatively unbiased approach and can identify compounds with novel modes of action. Immortalized cell lines are commonly used in cell-based drug screening assays because of their controlled growth behavior, ease of handling, low maintenance costs and ability to divide in culture forever. Thus, the combination of HTS using cell-based arrays provides a promising approach for testing large-scale compound libraries comprising hundreds of thousands of molecules. High content screening (HCS) combines HTS with the power of cell imaging. Complex cellular behavior can be studied at a phenotypic level using the advances provided by fluorescent probes and high-throughput microscopy (Zanella et al., 2010).

Current cell based screening assays used for cancer drug screening are based on detecting molecular changes of EMT-induced cells such as vimentin expression, E-cadherin reduction, increase of smooth-muscle actin (SMA) along with changes in cell morphology such as weak cell-cell junctions and cell migration ability. Quantification of the extent of cell dispersion upon addition of an EMT-inducer is termed a 'Cell scattering assay' and this specific assay is widely used in the pharmaceutical industry (Graham et al., 2008). Standardization of cell seeding methods and quantification of different morphological parameters such as cell dispersion index and loss of cell adhesion provide a promising assay that can be used for HCS (Chua et al., 2012; Loerke et al., 2012). Having said that, the inherent sensitivity of cell behavior to different experimental assay parameters poses problems for achieving reproducible behavior of cells. For example, rate of cell growth, E-cadherin expression and strength of cell-cell junctions can vary depending upon the density of cell seeding. Even automation of cell seeding can still result in variable cell island densities used in cell scattering assays (Cichon et al., 2015). In addition, several studies aimed at generating a HCS EMT assay, selected well-established but rather specific model systems (MDCK and DU-145 cell lines stimulated by HGF or a single cell line induced to undergo EMT initiated by different growth factors) which does not promise whether the assay could be adapted to other different cell lines and/or EMT inducers (Chua et al., 2012; Loerke et al., 2012).

Previously in Chapter II we saw that two different cell lines (NMuMG, EPH4) originated from mouse showed different sensitivity and polarity markers in response to TGF-β (Figure 3, Burute et al,). Use of different methods to generate cell lines from human tissues and lack of clonal selection pose severe questions about homogeneity of model cell lines and is probably part of the reason for non-reproducible behavior of cell lines. In addition, EMT is considered as a

Abbreviations: **EMT**: Epithelial to Mesenchymal Transition, **HCS**: High Content Screening, **HTS**: High Throughput screening

multi-cellular phenomenon and the majority of methods employed for developing drug screening assays have involved multi-cellular structures. Previously, we could recapitulate important aspects of epithelial polarity using a minimal-tissue model of two cells (Chapter II) and it seemed likely that a similar model could be used to develop a robust assay to detect EMT. As I was working in an academic lab of Manuel Thery at CEA and partly at CYTOO, it was ideal for me to exploit the ideas and assays developed in the lab and assess them for their utility as an EMT assay and a future marketable product in the form of a kit. The use of micropattern arrays on a chip had already demonstrated advantages for automated quantification, which was the critical need for developing an assay for industrial use (Degot et al., 2010). Thus, to circumvent problems faced by the classical scattering assay, we decided to develop an EMT assay using micropattern geometries and a minimal-model of tissue comprised of two cells. In addition, CYTOO as a start-up company has the main goal of developing cell-based assays compatible with High Content Screening (HCS). The EMT assay development task was part of a bigger project called Evolved Tissue Inspired Cell System (ETICS) funded by Bpifrance (Banque Publique d'Investissement). Guidance from Joanne Young and Sebastien Dêgot at CYTOO helped me to understand critical considerations for a developing an assay for the industrial screening purpose. The main consideration of developing the assay was to choose the suitable parameter, which is simple to quantify and represents general phenotype of the EMT. Earlier in Chapter II, we had observed occurrence of polarity reversal upon EMT induction by centrosome repositioning that precedes cell separation. There was a possibility to directly use nucleus-centrosome vector (NC axis) orientation as a parameter to detect EMT, although we had seen that NC axis orientation was sensitive to matrix rigidity in EpH4 and NMuMG cell lines (Figure 3, Chapter II). In addition, NC axis determination would have required centrosome detection, which limits the use of lower magnification (below 40x) objectives because of its small size (about 0.6 µm radius with γ-tubulin label). Interestingly, we had observed reproducible cell-cell junction destabilization upon EMT induction as well during centrosome amplification (Chapter I&II) and there was a possibility of using orientation of nucleus-nucleus axis within a cell pair spread on bow-tie micropattern as indicator of EMT. However, cell-cell junction destabilization is an early event during EMT progression, which is followed by cell separation of mesenchymal cells. Thus instead of using early markers of EMT induction such as NC vector and NN axis orientation, we decided to choose a parameter, which directly represents EMT cell scattering phenotype. Thus we designed the EMT detection assay to avoid inherent limitations of classical cell scattering assay in addition to allow automated high throughput imaging and analysis.

3.2 Experimental Methods

Cell Culture and EMT Induction

Michigan Cancer foundation (MCF10A) human mammary gland cells (ATCC #CRL-10317) were maintained at 37°C at 5% CO_2 in Lonza Mammary Epithelial Growth Medium (Lonza MEGM bullet kit #CC3150 without Gentamycin) in the presence of 100 ng/ml of cholera toxin (Sigma #C-8052) and 0.5% antibiotic-antimycotic (Life Technologies #15240062). Cells were harvested by TrypLE™ (Life technologies #12605036) treatment for 12 min. An equal volume of soybean defined trypsin inhibitor (Life Technologies #R007100) was added followed by centrifugation at 200xg for 4 min. Cells were subcultivated in ratios less than 1:5 to maintain a stable epithelial phenotype. Medium was renewed every 2-3 days. 8000 cells/cm^2 were treated with 5 ng/ml TGF-β1 (R&D systems #240-B-002) in complete medium containing DMEM/F12 (Life Technologies #31331093), 5% horse serum (Gibco #16050-122), 25 ng/ml EGF (Peprotech TEBU #100-15), 100 ng/ml of cholera toxin, 10 μg/ml insulin (Sigma #I-1882), 500 ng/ml hydrocortisone (Sigma #H-0888), 0.5% antibiotic-antimycotic. Cells were passaged after 3 days and cultured for another 2 days in the presence of TGF-β. At the end of 5 days, cells were harvested for further experiments. Madin Darby Canine Kidney (MDCK) cells were maintained in DMEM-High glucose (Life Technologies #31966047) containing 10% fetal bovine serum (Invitrogen). EMT was induced by addition of 10ng/ml Hepatocyte Growth factor (Gibco #PHGO254) or 5ng/ml TGF-β for different durations ranging from 1 h to 3 days.

Micropattern Fabrication and Cell Seeding

Fabrication of micropatterns on glass

A glass plate 10x10 cm (Schott #1304369) was cleaned using an air pistol and the surface of the glass plate was coated with adhesion promoter, TI Prime (Microchemicals) using a spin-coater (Laurell #WS-650m2-23NPPB) at 3000 rpm for 30s. The glass plate was baked at 120°C for 2 min on a hot plate. The glass plate was then coated with 1% solution of polystyrene (MW 260,000 Acros Organic # 178891000) in toluene (Sigma #179418) using a spin-coater at 1000 rpm. The polystyrene layer was further oxidized with an air plasma treatment (Plasma Etch #PE-30) for 20 s at 30W under vacuum at a 10 cc/min flow rate of air and incubated with Poly-l-Lysine-Polyethylenglycol (PLL(20)-g[3.5]-PEG(2) SurfaceSolutionS, Switzerland) in 10mM HEPES, pH 7.4 at room temperature for 30 min. PLL-PEG coated slides were placed in contact with an optical mask (Toppan Photomask) containing the transparent micropatterns using a vacuum chamber, then exposed to deep UV light using UVO cleaner (Model No. 342A-220, Jelight,

USA) for 4 min at power 6mW/cm2, λ 190nm at a distance of 1cm from the lamp. Micropatterned slides were subsequently incubated with a PBS solution containing 20 µg/mL fibronectin (Sigma #F1141) or laminin (Sigma #L2020) or collagen (Life Technologies, #A1048301) along with 20 µg/mL Alexa 647-fibrinogen (Gibco #F135200) for 30 min followed by 3 washes of PBS. Coverslips were dried and then rinsed in sterile PBS before cell seeding.

Fabrication of micropatterns in 96 well plate format

The micropatterns and protein coating in 96 well plates were manufactured by CYTOO.

Cell seeding on coverslips

Approximately 0.5 million cells were seeded onto micropatterned chips of 20x20 mm size and non-adhered cells were washed off after 30 min, which almost always resulted in single cell attachment per micropattern. Cells were allowed to divide over 24 h prior to fixation.

Cell seeding in 96-well plates

Wells were prefilled with 50 µl of cell culture medium using a multichannel pipette. Cells were trypsinized and resuspended to 40,000 cells/ml. Fifty µl of volume was seeded in each well and cells were fixed after 24 hours.

Chemical Treatments

Smad pathway inhibitor SB431542 and MAPK pathway inhibitor (U0126) was added to NMuMG and MCF10A cells respectively along with TGF-β (Selleckchem #S1067) to 10 µM concentration for 5 days. DMSO vehicle was added to control samples at 0.05%.

Indirect Immunofluorescence

Cells plated on glass coverslips were fixed with 4% parafomaldehyde in Cytoskeleton buffer (10 mM HEPES pH 6.1, 138 mM KCl, 3 mM MgCl2, 2 mM EGTA) containing 0.01% Triton-X100 for 15 min. Autofluorescence was quenched by treatment with 1 mg/ml sodium borohydrate in PBS for 7 min. For centrosome staining, cells were fixed with ice-cold methanol at -20°C for 5 min. Actin was stained using Alexa-488 Phalloidin (Molecular Probes #A12379 1:300 dilution in

PBS) for 30 min at RT. DNA was stained with DAPI (1:5000, Sigma #D9542) for 2 min in PBS. Coverslips were mounted with Mowiol 4-88 (Sigma #81381).

Cell Scattering assay (Figure 4.3A)

20,000 MCF10A cells were seeded on 20X20mm glass coverslip in Defined medium (referred above) Cells were allowed to grow for 3 days so that isolated colonies of cells were formed. Coverslips were mounted onto Chamlide chambers. TGF-β was added to 5 ng/ml in one chamber in DMEM complete medium. The other chamber was used as a control. Images were acquired from both the coverslips simultaneously using a dual chamber holder on a Nikon Spinning disk microscope. Images were acquired in transmitted light at 30 minute intervals using 10x phase contrast objective. Cells were images for 20 h. Positions of cells in a colony were manually selected and added to a ROI manager. Using a macro and formula indicated on Figure 4.3A, the scatter factor for each colony was computed.

Microscopy and Image Analysis

Fixed and fluorescently labeled cells were imaged using an epi-fluorescence Olympus microscope (up-right BX61) with 40x objective. Stacks of images spanning 10 µm z-distance were acquired. Image analysis for internuclear distance was performed using a series of Macros in Image J. Briefly; z-projection of each color channel was obtained using 'maximum z-projection' plugin followed by merging the 2 channels to obtain a composite image. Using a macro with inputs from the User a standard sized rectangle was placed around micropattern with two visible nuclei in DAPI channel. A hyper-stack of selected images with only two nuclei on single micropattern was created. Nuclei were detected using image thresholding and object size criteria. Internuclear distance was calculated using co-ordinates of center of mass of two nuclei.

Statistical Analysis

Mann-Whitney non-parametric test was used to compare differences between the samples. Error bars indicate standard error mean (SEM). n indicates sample size. For classical scattering assay in figure 4.6 A, the fraction of single cells against the total number of cells in the field of view were plotted. Positive hits are any siRNAs that caused all three experiments to fall above the 95% confidence interval for the line describing the behavior of the cells transfected with the non-targeting control smart pool. Knockdown of the positive control, CTNND1, caused all points to fall above this line.

3.3 Results

Definition of the Benchmark and the application workflow

As a first step in defining goals for development of a product, CYTOO performed a market survey for evaluating the demand and criteria necessary for a cell-based assay that can be used for screening anti-cancer drugs within the context of EMT. Pharmaceutical companies were currently using the 'classical scattering assay', which quantifies the dispersion of cell islands in response to EMT inducers (Figure 3.2 A). This assay provided advantages of allowing direct use of market available 96-well plates for seeding the cells. Ability of anti-cancer drugs to inhibit cell dispersion could be easily scored using this set up. However, one of the major disadvantages of this system was the variability of the initial cell island size that formed. The cell density is a crucial parameter and it affects several cellular processes including cell proliferation, cell migration and expression of epithelial markers (Cichon et al., 2015; Varelas et al., 2010). The image analysis of cell groups is complex since it requires development of algorithms suitable for detecting individual cells with the cell-cluster. In addition, on 2D surfaces, cells from different islands on same the coverslip/well can mix because of cell migration after EMT induction and pose a trouble in correctly identifying cells that belong to the initial island of cells.

The market survey by CYTOO in 2011 revealed that a new assay that takes into account the above deficiencies was highly desired by pharmaceutical companies for testing anti-cancer drug libraries. They were also favorable to the idea of using a complete "EMT kit" that would include all the necessary components for performing the assay. We thus aimed to design and produce a cell-based assay with a minimal tissue model for detection of EMT inhibitors in the form of a product to be sold as a kit. The minimal model of tissue comprised of two cells recapitulates tissue polarity and cell dispersion behavior of cells in the process of EMT (Chapter I and II).

The key steps for designing the 'EMT kit' were defined as below,

- Definition of the Benchmark- Classical scattering assay
- Final Readout- Inter-nuclear distance between cell doublets
- Contents of the 'EMT kit' - Protocol and assay to detect cell scattering in 96-well format and Image analysis software for calculating the readout

Figure 3.2

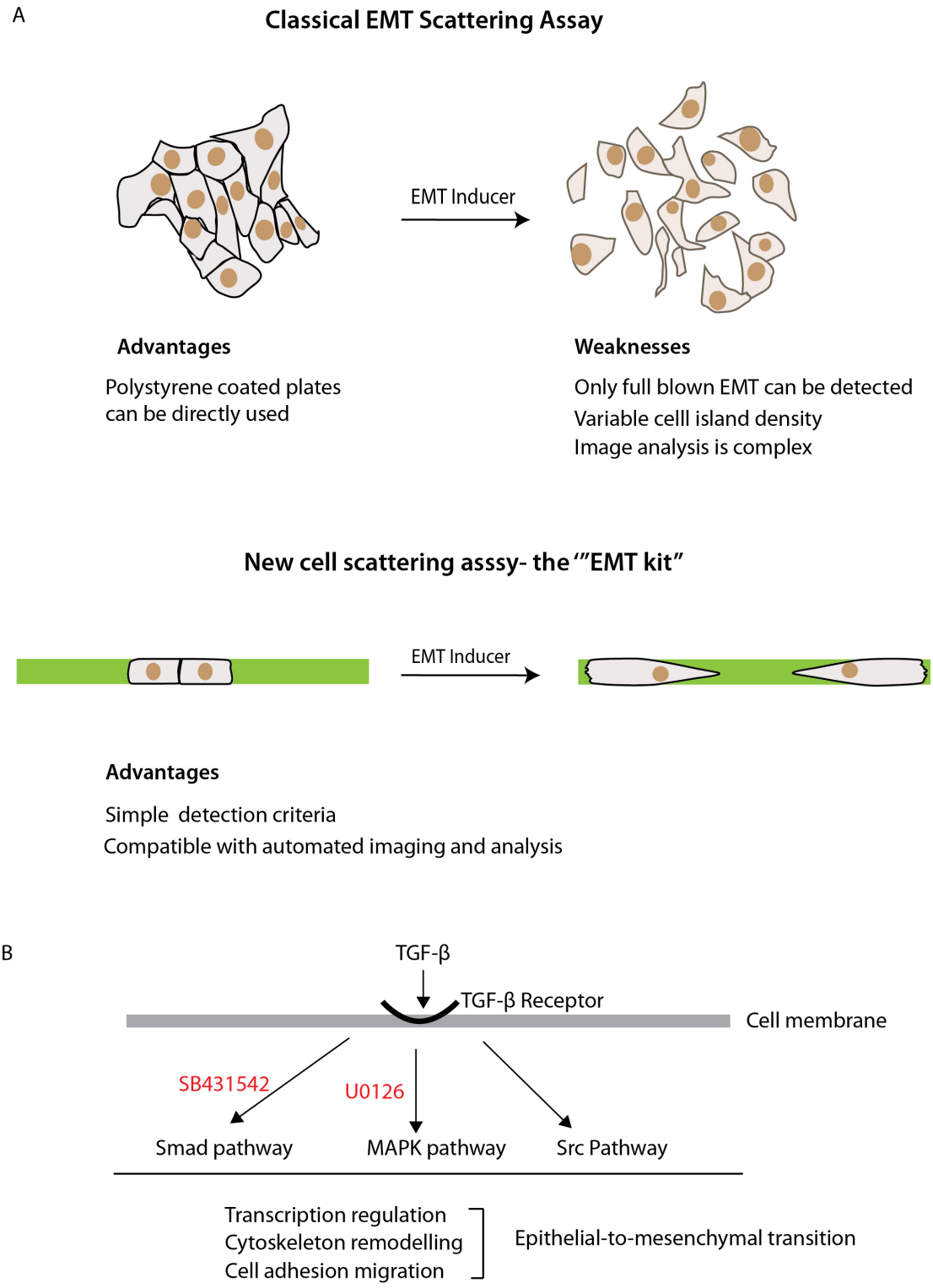
A
Classical EMT Scattering Assay
EMT Inducer
Advantages
Polystyrene coated plates
can be directly used
Weaknesses
Only full blown EMT can be detected
Variable celll island density
Image analysis is complex
New cell scattering asssy- the '"EMT kit"
EMT Inducer
Advantages
Simple detection criteria
Compatible with automated imaging and analysis
B
TGF-β
TGF-β Receptor
Cell membrane
SB431542
U0126
Smad pathway
MAPK pathway
Src Pathway
Transcription regulation
Cytoskeleton remodelling
Cell adhesion migration
Epithelial-to-mesenchymal transition

Figure 3.3

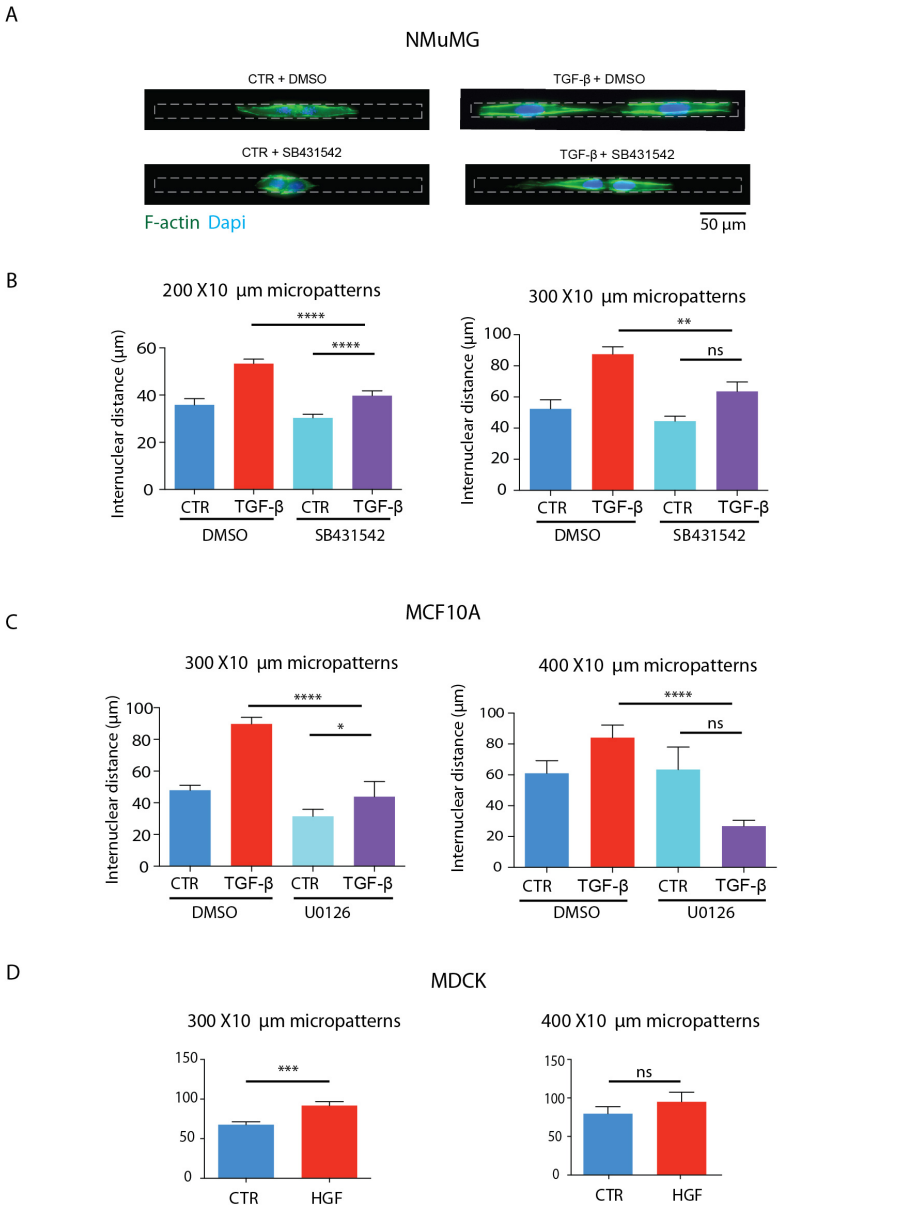

(A) Images of two NMuMG cells spread onto micropatterns (marked by white line). Cells are stained for actin(green) and nuclei(blue)
(B-D) Quanfication of internuclear distance between cell pair of NMuMG, MCF10A and MDCK cells spread onto micropatterns of different lengths, before and after EMT induction. NMuMG and MCF10A cells are treated with smad pathway inhibitor (SB431542) and MAPK pathway inhibtor respectively. CTR- Control. Error bars represent Standard Error of Mean

Figure 3.4

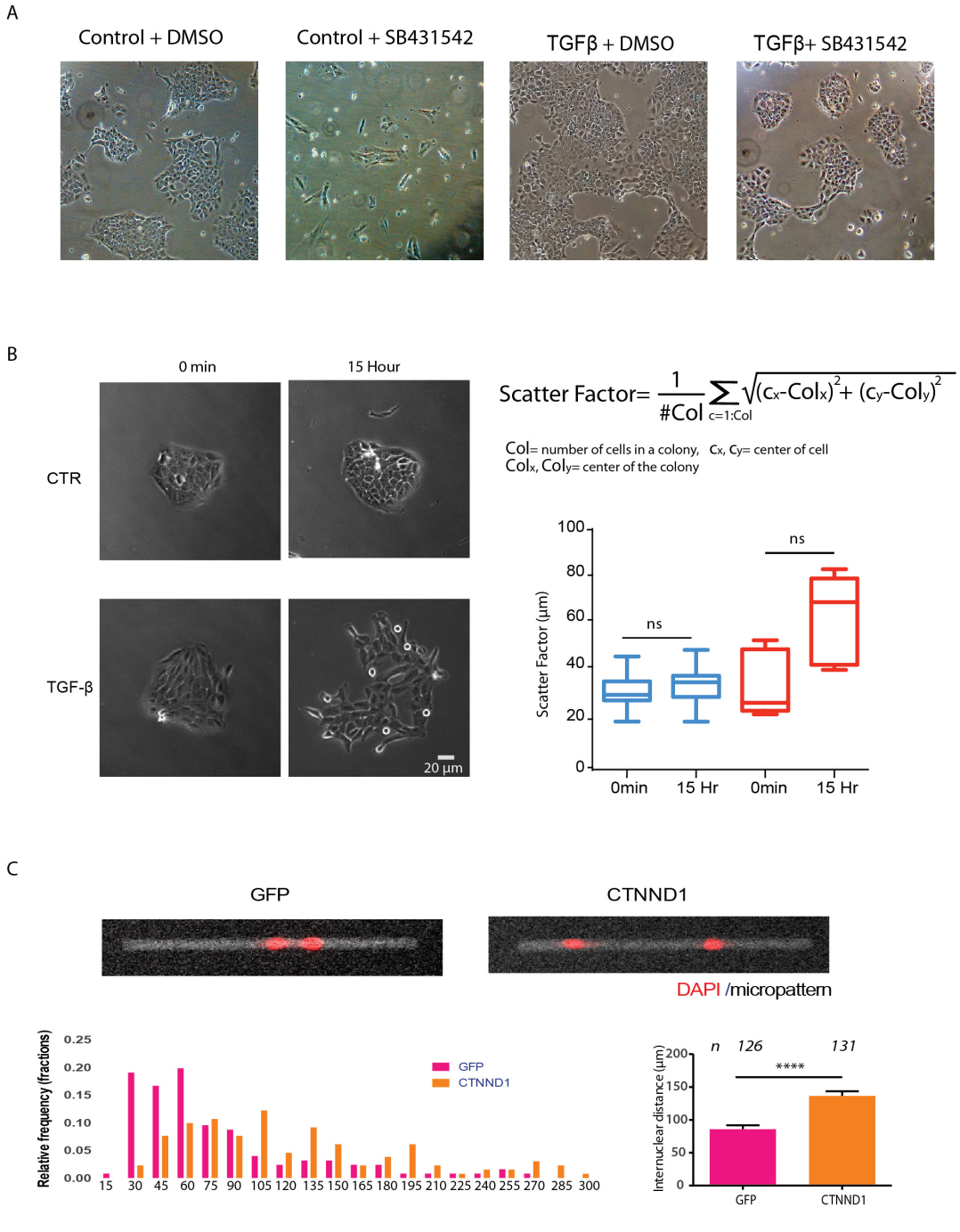

(A) Images of NMuMG cells treated with Smad-pathway inhibitor SB431542
(B) Classical scattering assay with MCF10A cells. On right, quantification of scattering index.
(C) Quantification of internuclear distance of MCF10A cells after knock down of Catenin (CTNND1)

Assessment of the assay readout

First, micropatterns of different lengths were fabricated on 20X20 mm glass coverslip using a photomask. Initially, we tested 3 different epithelial cell lines (MCF10A, NMuMG and MDCK) for their ability to scatter upon EMT induction in response to TGF-β and HGF. Cells were seeded onto these chips and 24 hours later cells were fixed and labeled for F-actin and nuclei. EMT induction clearly increased cell separation in all the three cell lines suggesting that the cell dispersion criteria as a readout was very versatile (Figure 3.3 A-D). To test whether the increased cell separation between the cell pairs was an EMT specific effect, we used inhibitors against different EMT pathways (Figure 3.2 B). Inhibition of Smad pathway by SB154342 in NMuMG cells clearly restored cell separation between TGF-β treated cells (Figure 3.3 A-B, Figure 3.4 A). Similarly inhibition of MAPK pathway by U0126 restored cell separation of MCF10A cells subjected to TGF-β stimulation of EMT. These results confirmed that EMT and inhibition of EMT could be successfully detected using cell-pairs spread onto a single micropattern. On the contrary, the classical scattering assay, which was performed by scoring dispersion of MCF10A colonies in response to TGF-β, did not reveal significant cell separation, mostly because of the variability in cell dispersion within different colonies (Figure 3.4 B). The new EMT assay was further validated in the absence of inducing EMT by using an siRNA against Catenin delta 1 (CTNND1), a protein important for cell-cell adhesion formation. Inhibition of CTNND1 in MCF10A cells caused an increase in cell-cell separation within cell doublets on micropatterns (Figure 3.4 C).

Development of the EMT assay

We chose 300X10 µm patterns for developing the final 'EMT kit' as with 200X10 µm micropatterns, EMT inhibitor action on TGF-β treated NMuMG cells did not reduce cell scattering compared to control samples treated with SB431542 (Figure 3.3 B). On 400X10 µm micropatterns, MDCK cells did not show a significant change in cell dispersion upon HGF treatment. Hence, we chose 300X10 µm patterns for the assay in 96 well plate format in order to accommodate all the cell lines with a single design. The design of the final 'EMT kit' in CYTOOplates is shown (Figure 3.5 A). Each well contains about 600 micropatterns of length 300X10 µm. The patterns are fluorescently labeled in order to be able to detect and exploit them during image analysis (Figure 3.5 B). The images are acquired at 10x magnification and stitched together to obtain an image of the whole well. On the left, the zoomed image shows cells that are spread on the micropatterns (red) and are labeled for actin (green) and DAPI (blue). Several micropatterns covered with only two cells can be seen (Figure 3.5 B).

Figure 3.5

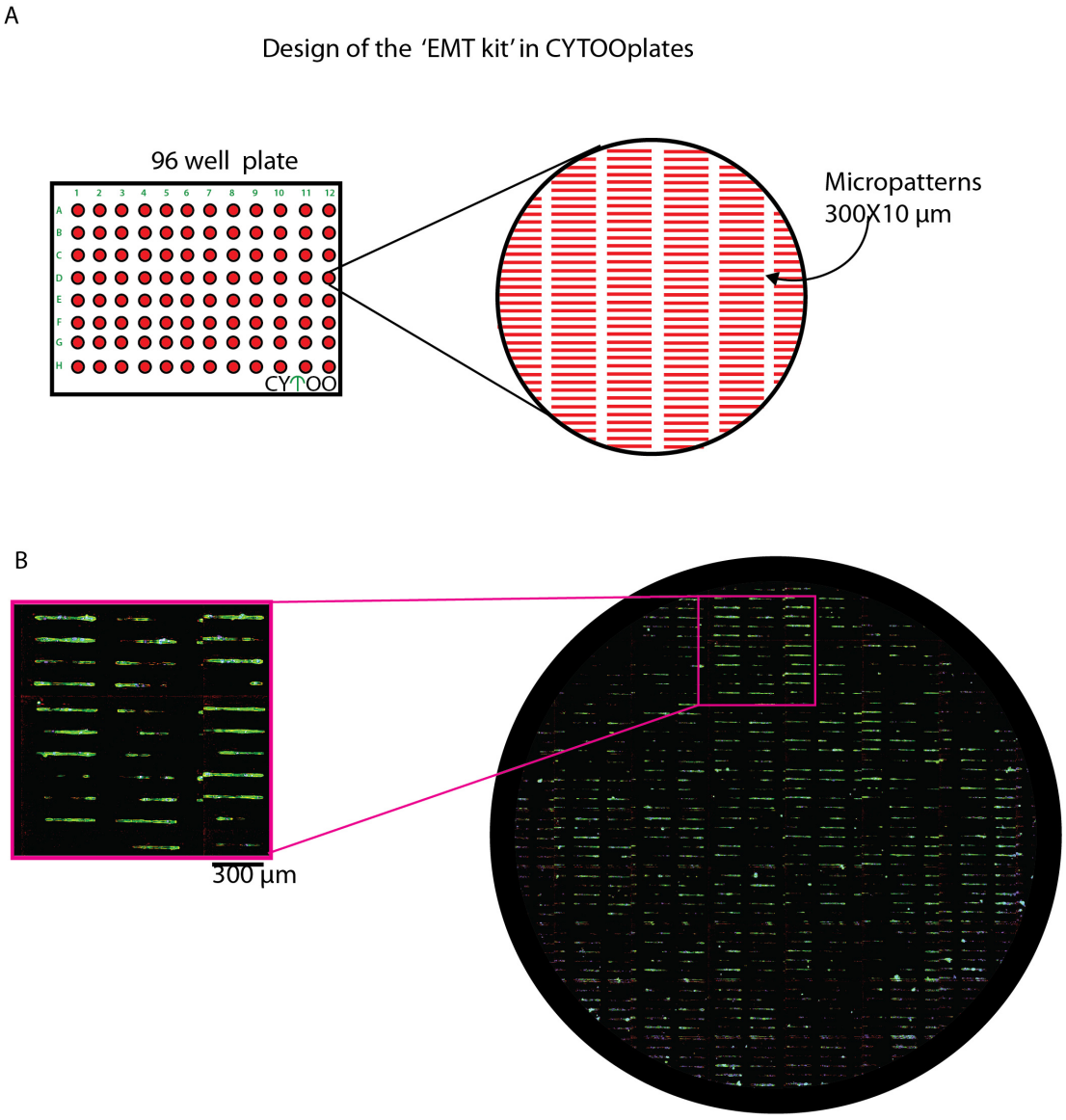

(A) Design of the final 'EMT kit' in 96 well format fabricated by CYTOO
(B) Image of single well in 96-well plate with MCF10A cells spread on micropatterns (red) stained for F-actin (Green) and nucleus (Blue) on right. Cropped and zoomed image on the left.

Figure 3.6

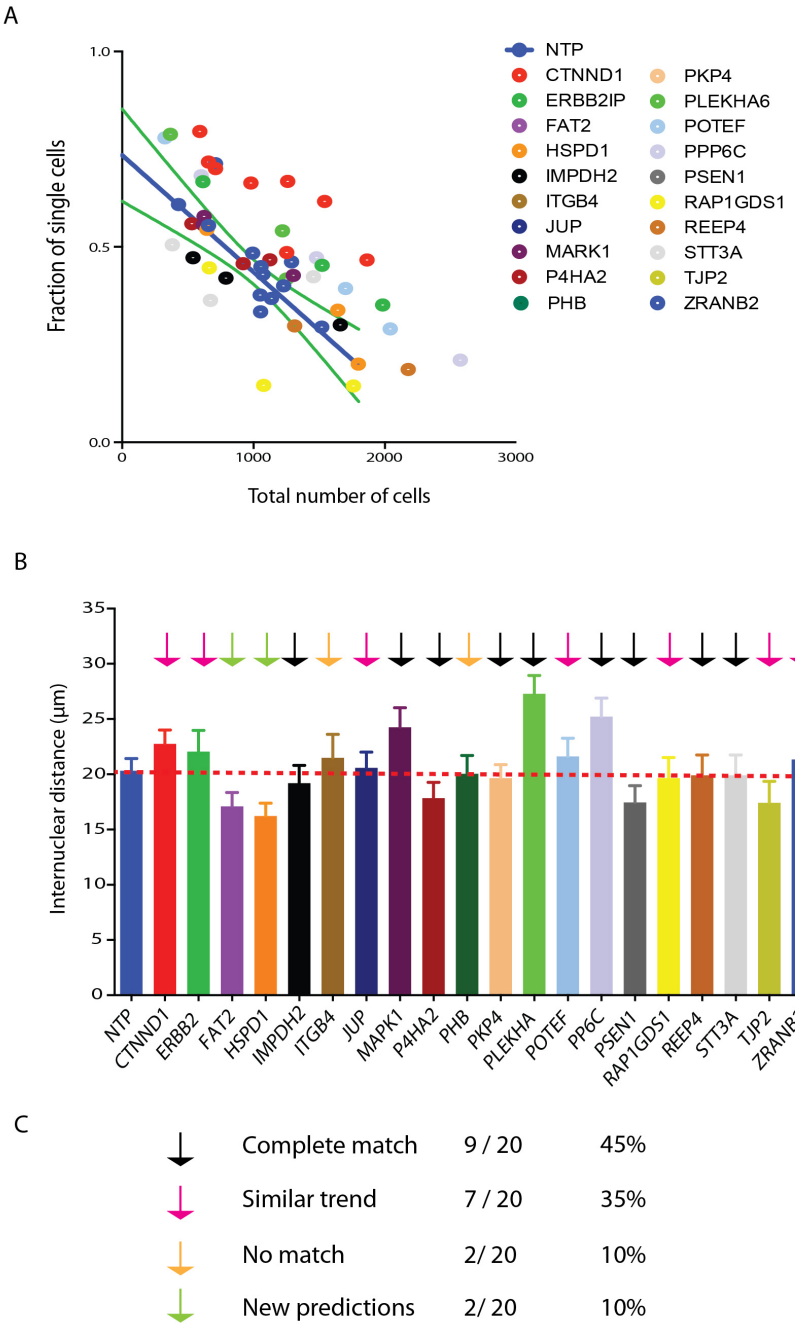

(A) Evaluation of siRNA cadidates for cell dispersion using classcial 'cell scattering assay'. NTP is control. Blue line on the graph indicates the reference and green dotted line is 5% regression around the reference.
(B) Evaluation of siRNA cadidates for cell sepearation using the 'EMT kit' Red line indicates NTP as reference
(C) Comparision of the results obtained by both assays using 20 candidate siRNAs. black arrows indicate number of siRNA hits which had similar effect on cell scattering in both the assays. Pink arrows indicate siRNA hits which did not show statistically significantdifferences but had similar effect on ability of cell separation. yellow arrow indicates siRNA with oppoiste effects in two assays. Green arrow indicates siRNA hits which were detected only by new 'EMT kit' and not by classical scatterin assay.

EMT assay validation by performing a small siRNA screen

To validate the final EMT kit and tools developed, we approached Lisa Gallegos from Joan Brugge's lab at Harvard medical school who performed a primary screen of 20 siRNA candidates against cell adhesion molecules. The screen was performed in CYTOOplates containing the 300X10µm micropattern and using siRNA treated MCF10A cells. In parallel, the effect of these siRNAs were tested using the 'classical scattering assay' (Figure 4.6 A). Knockdown of CTNND1 was used as a positive control for the siRNA screen. The dispersion of cells in response to candidate siRNAs was assessed using non-targeting siRNA pool (NTP) as a reference (Figure 4.6 B). Comparison of both the screens revealed that 45% (9/20) of the 20 siRNAs showed a similar capacity to affect cell-cell cohesion (eg. PKP4, IMPDH2). Thirty five percent (7/20) showed a similar trend of cell separation in both assays but the difference compared to the reference siRNAs were not statistically significant. Twenty percent (4/20) of the candidates did not correlate at all (Figure 4.6 C).

3.4 Comments

The new EMT assay is simple and versatile

Large scale screening of drug libraries requires a robust and simple cell based assay. We have developed the new EMT kit that includes an assay using micropattern geometries and a minimal cell model system. Use of a low number of cells during seeding avoids the variability generated because of various cell arrangements and different physiological behavior within group of cells typically observed in the conventional 'cell scattering assay'. We showed that the assay was sensitive enough to detect EMT behavior in three different cell epithelial cells lines and two different EMT inducers. The assay also allowed successful assessment of EMT inhibitor action. In addition, estimation of the internuclear distance, which is the final readout of the assay, is simple and universal. Furthermore, the EMT kit can also be adapted for screening siRNAs libraries.

High content screening with the new EMT assay

Most industrial-scale cellular screens prefer the use of fluorescence detection for high content screening. The new EMT kit in the format of 96-well plates, provides the possibility to use high-throughput anti-cancer drug or siRNA screening by observing phenotypic changes in the ability of cells to scatter. The assay readout requires only a single picture at the end of the assay with a low magnification objective (10x), which can possibly be further reduced down to 4x as the detection of fluorescently labeled nuclei is particularly robust. The EMT assay can be readily adapted to HCS bioimaging platforms, such "Cellomics" by Thermo-scientific or "Opera" from PerkinElmer. Low sample size (up to 100 cell-pairs) is sufficient to detect changes in internuclear distance between different treatments. This sample size is 6x less than the number of 300x10 µm micropatterns in a single well (about 600). Thus, data generation could be reduced to the size of a single 96-well, which ensures use of low amounts of library compounds. This feature of low sample size requirement may be further exploited in 384 well format allowing higher throughput. An siRNA screen performed using the EMT kit validated some of the main EMT candidates, thus there is a possibility of adapting this assay for screening large-scale siRNA libraries.

The assay works on a short-time scale

The assay window is 24 hours as it relies on formation of cell doublets by one round of cell division. In our previous study where we looked at the time course of EMT induction for polarity reversal (Figure 2, Burute et al,), we saw that polarity reversal could manifest starting from 4 hours after addition of EMT inducer. Hence, although conventional EMT treatments extend over days, which cannot be directly tested using this EMT assay, the assay allows detection of early changes in EMT induction. Thus the EMT assay can be used as an early sensitive marker of EMT and can be useful for academic investigation of early EMT changes. The major advantage of the short-time scale assay is that one assay can be completed within 24 hours and thus several rounds of screening can be performed per week while with the conventional assay, typically 3-5 days are required to complete one assay.

Shortcomings of the new EMT assay

The main disadvantage of the new EMT assay is that it requires custom designed plates with micropattern geometries. Currently to my knowledge, only CYTOO provides these custom designed plates, which can pose a limitation for pharmaceutical companies in terms of a lack of alternatives for purchasing and no competition for pricing. Secondly, the short assay window can detect only early changes of EMT inducers and EMT inhibitors. Also, the 5 days of EMT induction or the siRNA treatments, which require 48 hours for knockdown of proteins, cannot be directly performed in the CYTOOplates with this short-term assay. This requires an additional step of pre-treatment of cells in larger cultivation vessels. Similar pre-treatment step in a larger cultivation vessel will be required for anti-cancer compounds (EMT blockers or reversers) whose mode of action requires more than 24 hours. Unfortunately, this step is difficult to perform in a high throughput setting when working with hundreds of precious compounds available in minute quantities, and represents a blocking point that will limit adoption of the assay by industrials. Possibly, the assay can be marketed instead as a downstream secondary assay with the aim of confirming a handful of selected hits rather than primary identification of candidate compounds.

Future directions

The EMT assay has not been yet tested for its robustness which is determined by standard Z' factor to estimate variation of the parameter measured in about 50 replicates. Estimation of Z' is a crucial step before the assay can be adapted for HCS. In addition, the EMT assay has not yet validated using bioimaging platforms for HCS. It still requires optimization of image processing mainly for micropattern detection and nuclei detection. Although our preliminary screen with siRNA successfully validated some of the main EMT candidates, additional preliminary screening with 20-50 anti-cancer drugs will be required for final validation of the kit performance and determination of false positive and false negative identification rates. These 2 consequential steps will be essential before CYTOO can approach pharmaceutical companies to convince them to apply their library screens using the new 'EMT kit'.

To summarize, we successfully developed a proof-of-concept of the new 'EMT kit' using micropattern geometries and a two-cell model, which can be adapted for High Content Screening of anti-cancer drugs or siRNA libraries.

3.5 Short Q&A

Q. Can the "EMT kit" be used for assays other than EMT related cell scattering?

A. We developed the EMT kit with the aim to provide a robust assay for screening of anti-cancer drugs. However, the parameters for scoring cell dispersion used here are general. So the kit can be used for other types of non-EMT related cell scattering for example to study effect of cell-cell junction proteins, cytoskeleton elements, different ECM proteins on the ability of cells to separate from each other.

Q. Does width of line micropattern affect scattering ability of cells?

A. Cells show increasing scattering behavior on smaller widths of micropattern. We tested a range (5-30 μm) width of line micropatterns and on 10 μm cells showed 1D morphology and a higher rate of scattering. In addition, 1D mode of migration is similar to 3D mode of migration through confined tissue microenvironment (Doyle et al., 2009) thus we used 10 μm width for all cell lines. Notably, the cells involve different organelle positioning while migrating on different widths of substrate (Pouthas et al., 2008) so any further investigations to study the role of cell polarity in promoting cell scattering behavior would require a consideration of the different mode of cell migrations (collective invasion versus individual opportunistic cell motility) and thus mechanisms involved.

Q. Are the two cells on micropattern always the two daughter cells?

A. The answer is No. The cell seeding procedure was optimized to have one cell attached to a single micropattern although this does not guarantee that more than two cells would not attach to a single micropattern. Cell synchronization prior to seeding on micropatterns using a cell-cycle block or serum deprivation could be an option to rectify this problem. With cell cycle synchronized cells, even if more than one cell attaches to a single micropattern, after one round of cell division micropatterns containing only two cells would confer presence of daughter cells

3.6 References

Cavallo, F., De Giovanni, C., Nanni, P., Forni, G., and Lollini, P.L. (2011). 2011: The immune hallmarks of cancer. Cancer Immunol. Immunother. *60*, 319–326.

Chua, K.N., Sim, W.J., Racine, V., Lee, S.Y., Goh, B.C., and Thiery, J.P. (2012). A cell-based small molecule screening method for identifying inhibitors of epithelial-mesenchymal transition in carcinoma. PLoS One *7*.

Cichon, M., Nelson, C.M., and Radisky, D. (2015). Cancer Informatics. New York *14*, 1–13.

Degot, S., Auzan, M., Chapuis, V., Béghin, A., Chadeyras, A., Nelep, C., Calvo-Muñoz, M.L., Young, J., Chatelain, F., and Fuchs, A. (2010). Improved visualization and quantitative analysis of drug effects using micropatterned cells. J. Vis. Exp. 1–7.

Doyle, A.D., Wang, F.W., Matsumoto, K., and Yamada, K.M. (2009). One-dimensional topography underlies three-dimensional fi brillar cell migration. J. Cell Biol. *184*, 481–490.

Graham, N.A., Pope, M.D., Huang, B.K., and Asthagiri, A.R. (2008). Automated quantitative analysis of epithelial cell scatter. Cell Adh. Migr. *2*, 110–116.

Hay E.D. (1995) an overview of epithelio-mesenchymal transition. Acta Anat. 154(1):8-20.

Hoelder, S., Clarke, P.A., and Workman, P. (2012). Discovery of small molecule cancer drugs: Successes, challenges and opportunities. Mol. Oncol. *6*, 155–176.

Huang, R.Y.-J., Guilford, P., and Thiery, J.P. (2012). Early events in cell adhesion and polarity during epithelial-mesenchymal transition. J. Cell Sci. 4417–4422.

J. D'Souza, R.C., Knittle, A.M., Nagaraj, N., van Dinther, M., Choudhary, C., ten Dijke, P., Mann, M., and Sharma, K. (2014). Time-resolved dissection of early phosphoproteome and ensuing proteome changes in response to TGF- . Sci. Signal. *7*, rs5–rs5.

Kalluri, R., and Weinberg, R. a (2009). Review series The basics of epithelial-mesenchymal transition. J. Clin. Invest. *119*, 1420–1428.

Loerke, D., le Duc, Q., Blonk, I., Kerstens, a., Spanjaard, E., Machacek, M., Danuser, G., and de Rooij, J. (2012). Quantitative Imaging of Epithelial Cell Scattering Identifies Specific Inhibitors of Cell Motility and Cell-Cell Dissociation. Sci. Signal. *5*, rs5–rs5.

Nixon, P., and Act, N.C. (1973). War on Cancer 25. Adv. Cancer Res. *347*, 1377–1381.

Pouthas, F., Girard, P., Lecaudey, V., Ly, T.B.N., Gilmour, D., Boulin, C., Pepperkok, R., and Reynaud, E.G. (2008). In migrating cells, the Golgi complex and the position of the centrosome depend on geometrical constraints of the substratum. J. Cell Sci. *121*, 2406–2414.

Thiery, J.P. (2002). Epithelial–mesenchymal transitions in tumour progression. Nat. Rev. Cancer

2, 442–454.

Tsai, J.H., and Yang, J. (2013). Epithelial – mesenchymal plasticity in carcinoma metastasis. Genes Dev. *27*, 2192–2206.

Varelas, X., Samavarchi-Tehrani, P., Narimatsu, M., Weiss, A., Cockburn, K., Larsen, B.G., Rossant, J., and Wrana, J.L. (2010). The Crumbs Complex Couples Cell Density Sensing to Hippo-Dependent Control of the TGF-??-SMAD Pathway. Dev. Cell *19*, 831–844.

Zanella, F., Lorens, J.B., and Link, W. (2010). High content screening: Seeing is believing. Trends Biotechnol. *28*, 237–245.

4.0 General Discussion

In this thesis I explored the mechanisms of tissue remodeling which mainly involved microtubule-guided processes. Within the conceptual framework of three projects described in this thesis I mainly focused on intra-cellular changes that are responsible for modifying cell-cell connection which leads to cell dispersion of mesenchymal cells during metastatic cell-scattering from 3D orgonoid with centrosome abnormality (Chapter I), during EMT (Chapter II). Finally we developed an assay to detect cell scattering for drug screening purpose (Chapter III). It also appeared quite strikingly that centrosome MTOC activity and position is modulated during the EMT and cancer invasion. The three projects were begun by a common aim which was to understand different mechanisms guided by microtubules that affect centrosome position and generate different morphological phenotypes like mesenchymal cell, cell separation and cell invasion. As the study of centrosome positioning during EMT revealed an important evidence of polarity reversal, which may be manifested in other EMT processes during development, I would like to discuss possible mechanisms that could be involved in polarity reversal. We also found that the cell separation was controlled by different mechanisms during different morphological processes and moreover, centrosome directed microtubule network played a major role in controlling these distinct mechanisms. Thus I would like to discuss mechanisms that lead to cell scattering and plausible role of centrosome as molecular signaling center in addition to its MTOC function. As all the three projects involved extensive use of tissue models of two cells confined on micropattern geometries, I would like to discuss the relevance of minimal tissue models as important tool in cell biology.

4. 1 Mechanisms of polarity reversal

We found that centrosome position responds to different cortical cues provided by cell-cell and cell-Matrix adhesions (Figure 4.1A). When a cell is subjected to symmetric or asymmetric cell-ECM adhesions, the centrosome localizes to the geometric center of the cell. The establishment of NC axis polarization in this case is a result of off-centering of the nucleus with respect to the geometric center of the cell. Interestingly, we found that when cells were provided with asymmetric cell-cell adhesions using two-cell model confined on <H> micropattern, centrosome is off-centered preferentially toward the cell junction (Figure 4.1A). The modulation of the centrosome position during EMT suggested that the centrosome localization within cell is controlled by dynamic alteration of cell-adhesion landscape, which in turn changes the MT interaction with these adhesions. It is well established that cell-adhesion landscape of the tissue is highly modified during morphogenetic processes involving EMT and

Figure 4.1

A

Centrosome responds to asymmetric cues of cell-cell adhesion

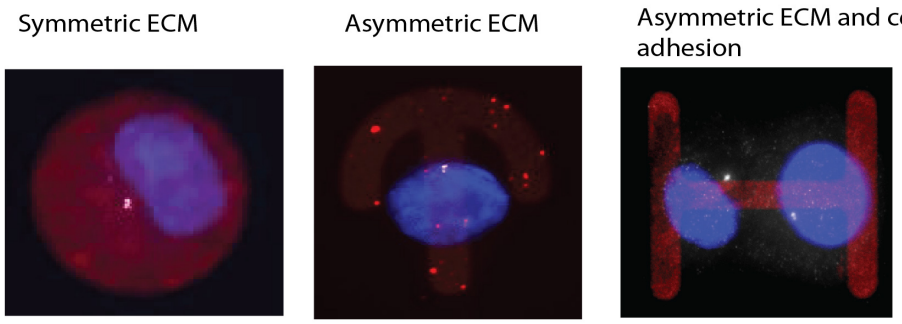

B

The central theme - modulation of centrosome position in response to cell-adhesion remodelling

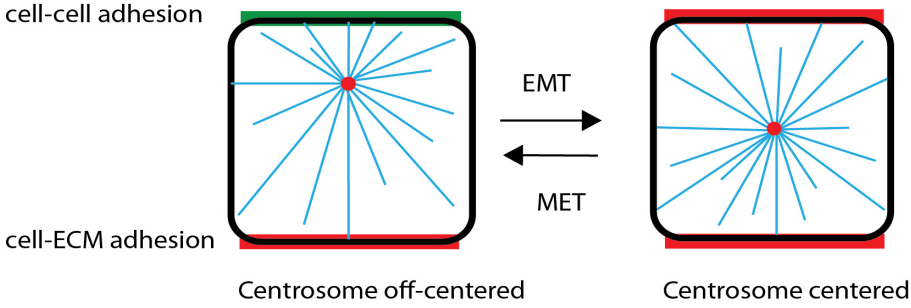

C Possible mechanism of polarity reversal initiated by nucleus-displacement during EMT

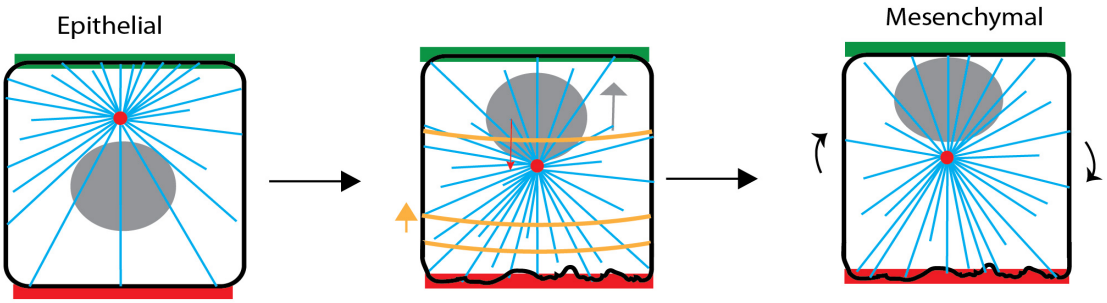

progression of cancer metastasis. We indeed found that alteration of cell-cell junction composition by reduction of Par3 was responsible for centrosome off-centering which is typically seen in the epithelial cells. We also noticed reduction of MT nucleation in EMT induced cells and numerical simulations provided insight into the new role of microtubule number at the centrosome which can provide the flexibility for centrosome movement in response to cortical cues (Burute et al. Figure 4). Here I would to discuss possible mechanisms for centrosome centering and off-centering that are mainly based on MT-guided processes.

Centrosome Positioning

In Chapter II we demonstrated that during EMT there is progressive loss of Par3 and centrosome off-centering is also progressively lost. This high correlation between between Par3 localization at the CCA and centrosome positioning close to the CCA suggests a causal link dependent on Par3. In the literature it is shown that Par3 is associated with Dynein which can capture, stabilize and pull on microtubules (Ligon et al., 2001; Schmoranzer et al., 2009). As Dynein is minus end directed motor and when it is anchored to the cell-cell junction Par3, it would pull MTs that have emanated from the centrosome causing centrosome movement towards cell-cell junction (Figure 4.2B1). In addition to this widely accepted mechanism, there are other mechanisms, which could be involved in centrosome-off centering in epithelial cells. Similar to epithelial cells, neurons as well have microtubules bundles, which are formed because of Microtubule associated proteins (MAPs) such as Tau protein. Presence of MAPs along the microtubules, which are associated at the CCA can increase the rate of stabilization and assembly of microtubule bundles that are growing toward the CCA (Figure 4.2 A&B3). Another tantalizing hypothesis for the selective MT stabilization close to CCA is, whether existing microtubules guide the growth of newly growing microtubules (Figure 4.2B2). An existing microtubule could provide a scaffold for a newly growing MT by facilitating its polymerization at the plus tip. The mechanism can be of structural or molecular nature meaning that existing MT can provide structural stability to protofilaments of growing MT, which will increase the instances of MT growing along another MT. Also the proteins attached to existing MT could facilitate the assembly and growth of the complex at the plus tip of the MT. For example Kinesin-based microtubule guidance for generation of different microtubule arrays in the Drosophila neurons has been observed and thus there is a possibility that similar mechanisms are involved in epithelial cells, which can control centrosome positioning (Doodhi et al., 2014).

On the other hand forces acting on MTs at the rest of the cortex could generate cumulative pushing force on the centrosome, which can push centrosome towards cell-cell junction (Figure 4.2B4). Using numerical simulations we already saw that in the absence of dynein generated pulling forces at the cell cortex only the pushing forces by MT growing ends can generate

Figure 4.2

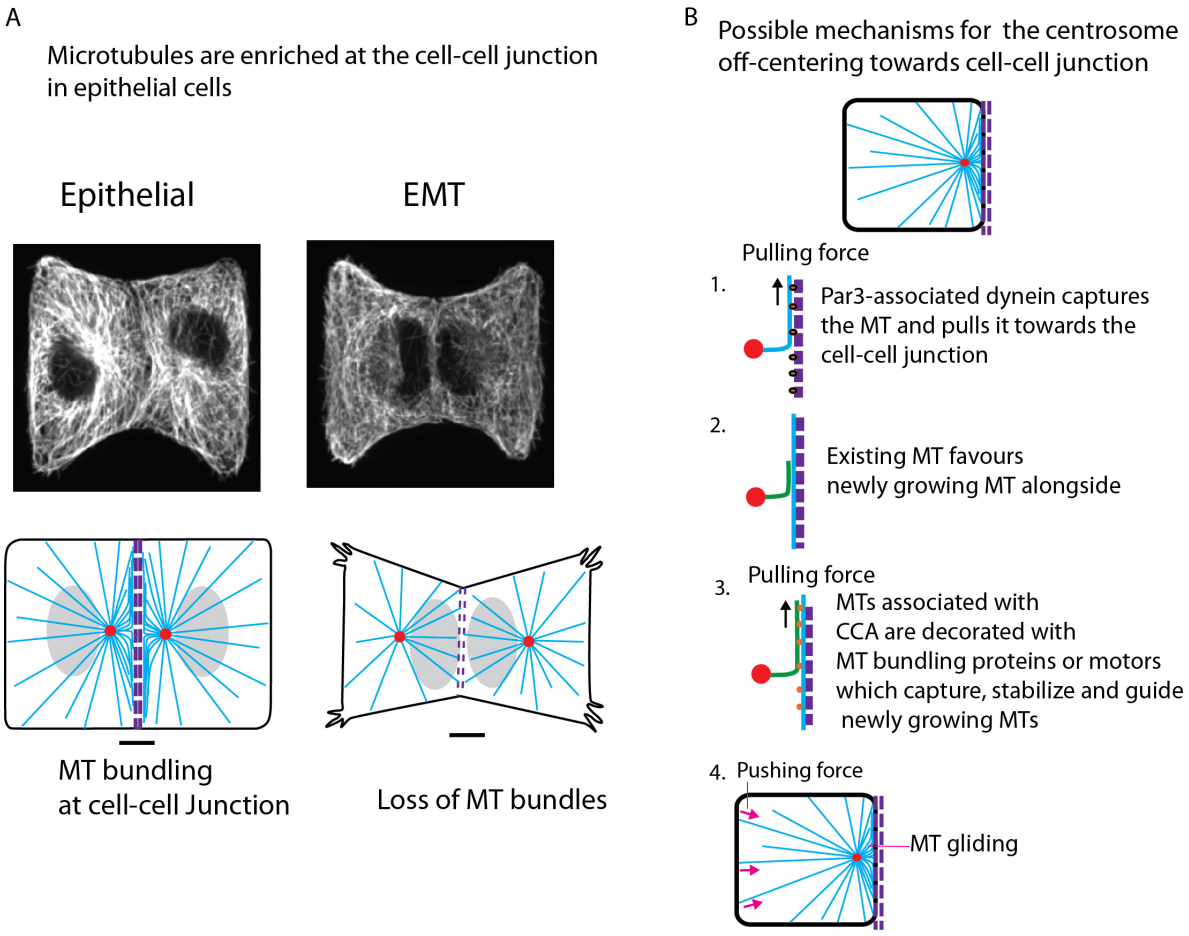
A
Microtubules are enriched at the cell-cell junction in epithelial cells
Epithelial
EMT
MT bundling at cell-cell Junction
Loss of MT bundles
B
Possible mechanisms for the centrosome off-centering towards cell-cell junction
Pulling force
1.
Par3-associated dynein captures the MT and pulls it towards the cell-cell junction
2.
Existing MT favours newly growing MT alongside
3.
Pulling force
MTs associated with CCA are decorated with MT bundling proteins or motors which capture, stabilize and guide newly growing MTs
4. Pushing force
MT gliding
C
Proposed mechanism of polarity reversal during Epithelial-to-mesenchymal transition
Epithelial Polarity
Apical
Basal
ECM layer
EMT
MET
Primitive Streak

MTOC off-centering forces (Burute et al. Figure 4). In addition, change of microtubule numbers emanating at the centrosome governs efficiency of centrosome centering suggesting that microtubule interaction with cortex is indeed important for controlling positioning of the centrosome and maintaining its position (Burute et al. Figure 4).

Nuclear Positioning

An important aspect of polarity reversal is that it involves repositioning of the centrosome and the nucleus. We did not see consistent trend for nucleus repositioning in different cells lines associated with the polarity reversal during EMT (Burute et al. Figure 2) and thus we did not investigate mechanisms that control nucleus position. However, nucleus is the largest organelle and its asymmetric localization is observed in several instances such as neuroepithelium, epithelial tissue of kidney and mammary gland (Dupin and Etienne-Manneville, 2011; Gundersen and Worman, 2013). We saw that nucleus-centrosome axis orientation is completely reversed with respect to the cell-cell adhesion during EMT (Figure 4.1C). It is a possibility that the addition of TGF-β, first elicits the cytoskeletal mechanisms to increase lamellopodium activity at the cell-ECM adhesions. The increased actin assembly at the focal adhesion can generate transverse arcs, which are known to engage at the nuclear envelope through LINC (Linker of Nucleoskeleton and cytoskeleton) complexes consisting of Lamins, SUN, KASH, Nesprin proteins that can change the nucleus position (Dupin and Etienne-Manneville, 2011). The resulting displacement of nucleus at the opposite side of CCA can in turn displace MTOC because of geometrical constraints (Figure 4.1C). The resulting change of nucleus-centrosome position generates reversed NC axis compared to the epithelial cells. This configuration is probably reinforced by lesser MTs growing on the side of the nucleus and increasing lamellopodial activity at the cell-ECM adhesions. TGF-β action results into reduction of E-cadherin and increase of focal adhesion proteins at the late stages of EMT induction, which may support reinforcement of this configuration finally culminating into the cell separation. Inhibiting the expression of KASH or SUN proteins can verify the definite role of nucleus position during the process of EMT. Intermediate filaments surround the nucleus and involved in the nucleus positioning through actin retrograde flow (Dupin et al., 2009). Vimentin, is an intermediate filament protein and a bona fide marker of EMT. However, mode of action of vimentin in driving EMT progression is still mostly elusive and it will be important to investigate whether it is involved in controlling nucleus positioning during EMT.

It is also important to note that centrosome can be linked to the nucleus and the nucleus movement can guide the MTOC position. Perturbation of nucleo-cytoskeletal connection by Lamin A knockout in mouse fibroblast reduced the polarization extent of the Nucleus-centrosome axis in the cells (Hale et al., 2011). In epithelial cells, we often observed centrosome localization farther from the nucleus (close to CCA) while in mesenchymal cells;

Figure 4.3

A

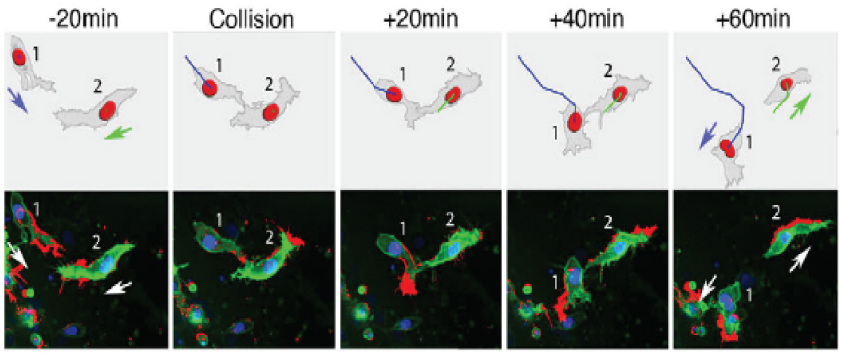

Scarpa, 2015

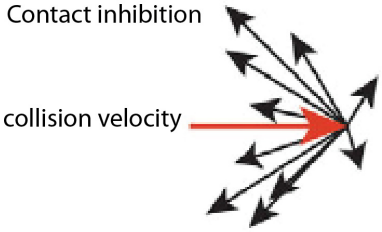

B

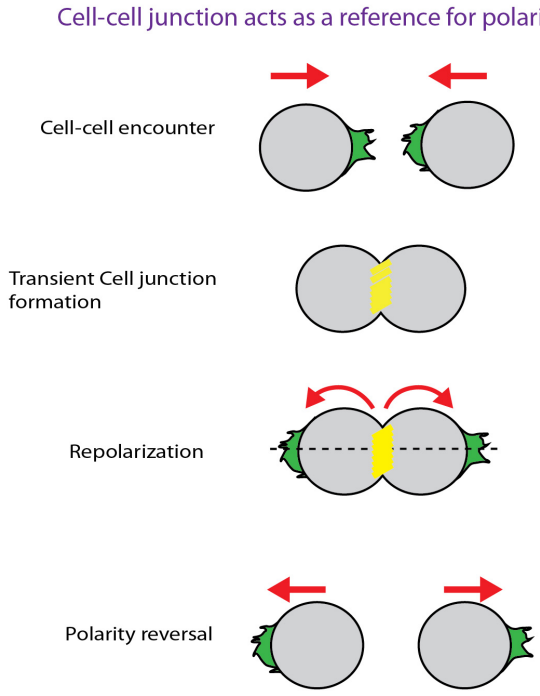

(A) Polarity reversal during contact inhibition of neural crest cells. (Below) velocity vectors of cells before and after collisions (B) Cell-cell junction proivdes cues for repolarization before cells seperate

nucleus-centrosome is probably strengthened in mesenchymal cells, which have migratory potential like fibroblast cells.

As we observed progressive grades of polarity reversal in temporal manner after TGF-β or HGF treatment to cells (Figure 2F Burute et al), we propose that the primitive streak formation at the early gastrulation stage in embryo also involves progressive polarity reversal of the cells in the epithelial layer. The spatial and temporal polarity reversal in this case would depend upon transformation of cells by growth factors (eg. Nodal, Wnt signaling) and different degree adhesions formed by the cells (Figure 4.2 C).

4.2 Different modes of Cell Scattering

Cell migration is highly studied in the context of development and cancer progression. Different modes of single cell migration are described as amoeboid movement or fibroblast-like movement depending upon the presence of mature focal adhesions and stress fibers within the cell, while collective cell migration serves purpose during morphogenesis, tissue regeneration and in pathological conditions (Friedl and Gilmour, 2009). These different modes of migration are described by the properties of extra-cellular matrix such as its density, dimension, stiffness, topography and cellular components including CCA, CMA and proteolysis mechanism, however the detailed description of how cell junctions are dissolved and whether cells separate because of weak junctions or simply by pulling on the matrix is still unresolved. The combination of all above factors including cell-ECM and cell-cell adhesion, orientation of internal cytoskeleton and differences in force generation by Rho/Rac machinery is responsible for cell separation. The study of cell scattering within different models in this thesis revealed at least two distinct mechanisms, which lead to cell dispersion.

By increasing cell-ECM adhesion forces

The tissue is maintained intact through the mechanical balance between CCA and CMA forces as depicted in (Figure 4.4 A). Activation of EMT pathway by TGF-β1 involves reduction of cell adhesion protein, E-cadherin. It was previously demonstrated by Liu and colleagues that force maintained at the cell-cell junction is directly to proportional to amount of E-cadherin at the cell junction so we had expected to observe a drop in cell-cell junction forces after EMT (Liu et al., 2010). To our surprise, EMT-induced cells with smaller cell-cell junction sustained comparable amount of force like their control counterparts (Burute et al., Figure 6). This cell-cell force is likely to be either sustained by N-cadherin, which is expressed and recruited at the CCA after EMT induction. On the other hand, higher CMA forces associated with increased

Figure 4.4

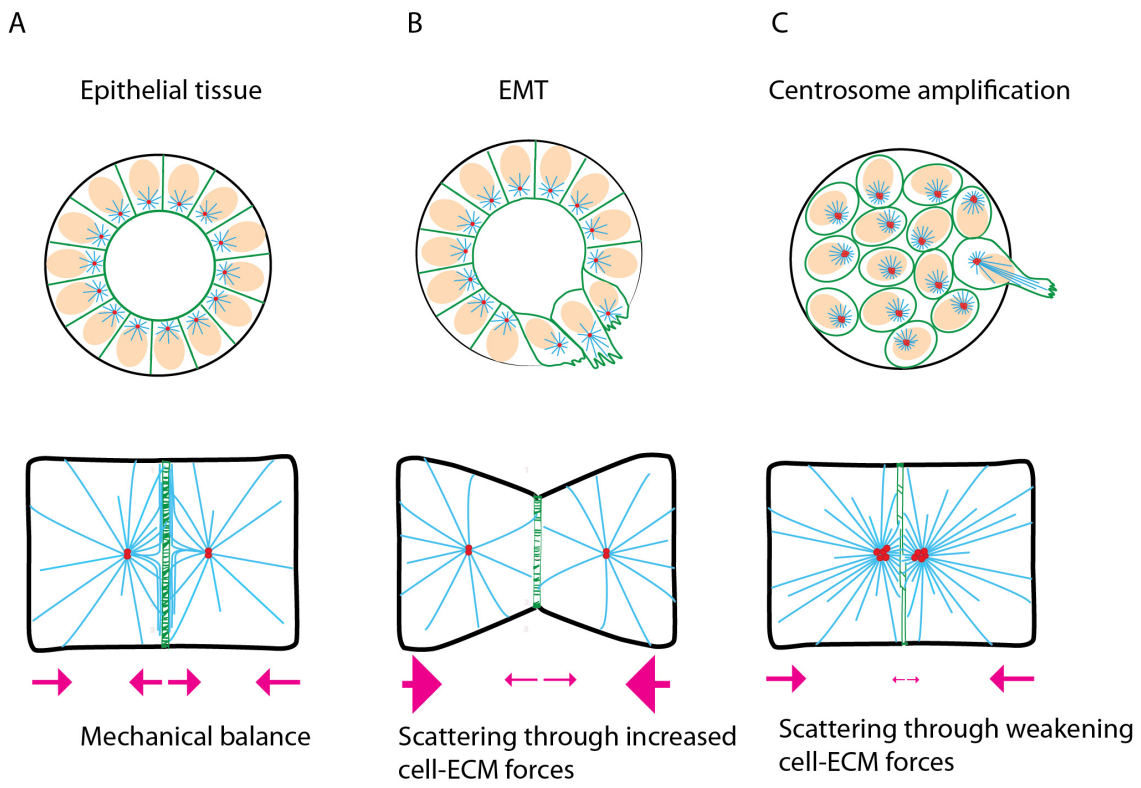

(A) Mechanically balanced tissue where tension at the cell-cell junction is balanced by forces at the cell-ECM junctions
(B) EMT induction involves increase of cell-ECM forces
(C) Centrosome amplification involves weakening of cell-cell junction and thus likely to reduce forces sustained at the cell-cell junction

focal adhesions promoted cell separation. Thus cell separation after EMT, which was coupled to polarity inversion of nucleus-centrosome axis was result of increased pulling on matrix by cells that most likely ripped apart the cell-cell junction (Figure 4.4 B)(Rooij et al., 2005). Thus EMT progression does not simply involve dissolution of CCA, but it seems that cells go through sequence of force balance modulation. R. Mayor and colleagues demonstrated similar example of polarity reversal coupled with force balance redistribution during contact inhibition of neural crest cells after EMT. The study showed that transient CCA formation by differentiated Neural crest cell generated polarized activation of Rac1 at the focal adhesion which triggered cell junction disassembly and cell scattering (Scarpa et al., 2015). The striking feature of contact inhibition of locomotion (CIL) is that when a cell encounters another cell, it collapses its protrusion, reorients protrusions and migrates in the opposite direction (180° opposite) with the least possibility of encountering the same cell again (Figure 4.3 A). Hence the cells exhibit polarity reversal for changing the direction of cell migration and the contact site between the cell acts as a reference to guide this directional cues (Figure 4.3 B). It is important to note that in the literature, cell separation and invasion during cancer progression is mostly described as cell-scattering process as an outcome of cell junction disruption. Although CCA dissolution occurs during EMT, it is not clear whether CCA dissolution is necessary for promoting cell separation during EMT (Rooij et al., 2005). Recent evidences have shown that stability of cell-cell junction is maintained by recycling of junction components (Baum and Georgiou, 2011). We think that change of the Golgi position coupled to the NC axis reorientation during EMT facilitates weakening of CCA prior to cell scattering by restricting the transport of CCA components to the cell junction. Our study and few other examples suggest that cells actively reorient their direction through coupling of internal and cortical polarity cues for directional mesenchymal migration that has likened to cancer metastasis (Moore et al., 2013). Further investigations of cell force modulation staring from early stages of EMT induction until the final cell separation will reveal that at what point in the course of EMT, cell-cell junctions are disrupted.

By weakening cell-cell adhesions

The second mode of cell scattering was observed in the centrosome-amplified cells by destabilization of cell-cell junction (Figure 4.4 C). The destabilization of CCA was result of Rac1 activation at the microtubule +tips. Centrosome amplified cells did not show classical EMT markers and thus retained high E-cadherin expression (Godinho, 2014, Figure S3 F). The cell scattering in the 3D organoid system showed that amplified centrosome was maintained behind the nucleus during migration away from the 3D organoid suggesting that the centrosome was at the back of the cell during initial migration. This mode of migration with centrosome at the back of cell has been observed in the immune cells and confined cells on

Figure 4.5

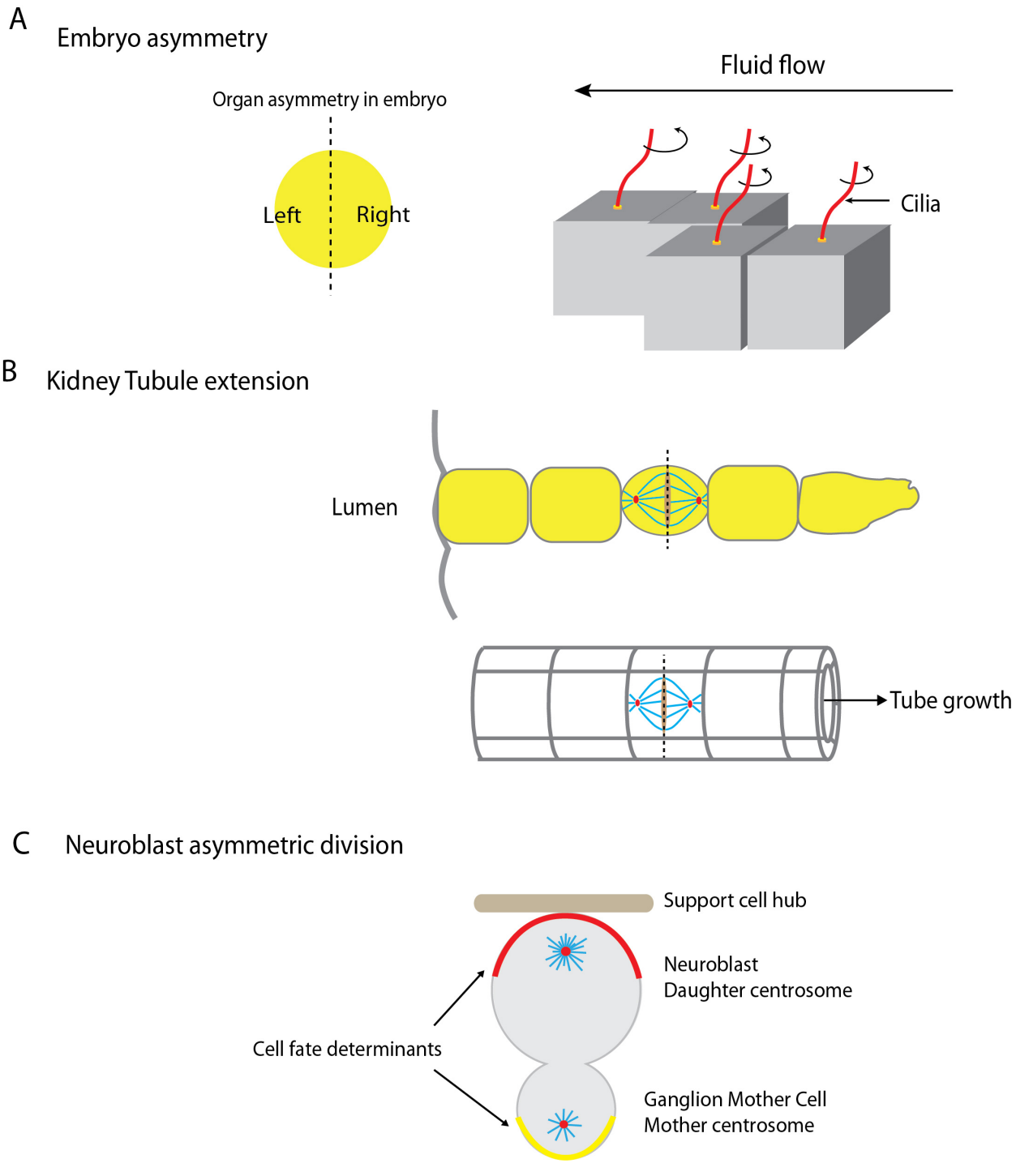
A
Embryo asymmetry
Organ asymmetry in embryo
Left
Right
Fluid flow
Cilia
B
Kidney Tubule extension
Lumen
Tube growth
C
Neuroblast asymmetric division
Support cell hub
Neuroblast
Daughter centrosome
Cell fate determinants
Ganglion Mother Cell
Mother centrosome

narrow ECM substrate (Luxton and Gundersen, 2011; Pouthas et al., 2008). Determination of force maintained at the CCA using cell-pair model on <H> micropattern will clearly reveal whether the cell-cell junction force in centrosome amplified cells is reduced as a result actin protrusion close to the CCA. Thorough investigation of mechanisms that are responsible for cell-separation is highly desired especially for the development of therapeutic targets against cancer metastasis. Currently cell migration is characterized by speed of migration, mode of cell migration, ECM remodeling, persistence etc for understanding cancer metastasis. However, cell dispersion occurs prior to cell migration during cancer metastasis and understanding origin of cell separation will be more important. Thus exploring mechanisms that initiate cell dispersion is really important to discover specific inhibitors that could block the cancer spread at the early stages.

4. 3 Centrosome in generating the asymmetry

In this thesis we revealed important functions of the centrosome during cell interphase however centrosome's crucial role as a mitotic spindle pole in dividing cell is essential for tissue maintenance as well for morphogenesis. Centrosome is inherently asymmetric; owing to its morphometric and functional differences of centrioles. Furthermore, mother and daughter centrosomes generated prior to the cell division also have different MTOC activity and mobility. I would like to discuss different instances where the cellular asymmetry is generated by the centrosome since these anisotropies are mainly operated by microtubules emanating from the centrosome. Under the scope of this thesis it is important to understand how centrosome couples and responds to cortical cues to establish anisotropic phenotype during different morphogenetic events.

Asymmetric organ positioning

The centrosome position has an important role in oriented planar cell division (OPCD) during axial elongation and determining organ shape. A transient ciliated epithelium during vertebrate development generates an asymmetric fluid flow across the midline of embryo that conveys positional information for organs locations. The left-right organ asymmetry depends on tilted motile cilia on the surface of epithelium and thus the role of centrosome as 'basal body' is critical for orienting the Left-Right (LR) body axis (Figure 4.5 A) (Amack, 2014). Further during development, the centrosome plays crucial role by orienting cell-division axis through interaction of microtubules with cell cortex and the plane of cell division controls underlying tissue architecture (Figure 4.5 B).

Local asymmetry in the cell

Cells can be categorized by their phenotype such as epithelial vs mesenchymal, migrating vs non-migrating, differentiated vs non-differentiated etc in the context of tissue morphogenesis. The proteomic and mRNA analysis approaches have revealed that there are plethora of proteins differently expressed and modified during EMT (J. D'Souza et al., 2014). However, the cellular level characterization does not take into account the local asymmetries within the cell, which can be central to cell polarization. In the context of EMT, we observed that the asymmetry of microtubule arrays in epithelial and mesenchymal cells could be result of selective stabilization of MTs close to CCA and/or recruitment of molecular motors to CCA. Similarly change of centrosome positioning and associated migration capacity of the cell could be direct result of local contractility of the cell generated by the Myosin IIA and IIB isoforms (Chapter II Figure 2.3). Thus it is necessary to take into account the architecture of the cell, which is generated by local anisotropies of cytoskeletal elements while investigating cell phenotype. The work of this thesis emphasizes on how cells sense the environmental cues to guide asymmetric organelle positioning inside the cell that defines internal axis of the cell. Use of light controlled activation and localization of molecules to different parts of the cell holds a great promise for studying cell architecture. (Chapter II Figure 2.5) By locally controlling microtubule dynamics, microtubule nucleation, its post-translational modification, MAP binding levels in cells constrained on defined geometries will be helpful to reveal how microtubules regulate centrosome position in response to environmental cues.

Asymmetric cell division

As described by Michel Bornens, the centrosome is 'back in the limelight' because of one of its newly revealed feature that is, generating mother-daughter cell asymmetry. Asymmetric cell division generates daughter cells of distinct identities by asymmetrically localizing proteins and RNAs, which act as the cell fate determinants to only one of the daughters. Asymmetric cell divisions of stem cells are important to generate differentiated cells, which can be tissue-specific progenitor cells or terminally differentiated cells. In Drosophila, neuroblasts generate self-renewing pool of neuroblasts, which retain new centrosome and differentiating ganglion mother cell (GMC), which gets the mother centriole with insignificant MTOC activity (Figure 4.5 C). This asymmetric cell division is tightly linked to the cortical polarity, mitotic spindle alignment and additionally to the Centrobin, protein that binds only to the daughter centriole to give its high MT nucleating ability (Januschke et al., 2013). The molecular dimorphism present at the mother-daughter centrioles imparts different fates to the daughter cells and reveals another crucial feature of intrinsic asymmetry of the centrosome. Even within the differentiated tissue like mammary gland, tissue specific-stem cells reside which have ability to repopulate the tissue. In the typical acini of the mammary gland, epithelial luminal cells

surround the central lumen while myoepithelial cells (also called as basal cells) are situated at the base of the luminal cells. A study by Prater MD and colleagues revealed that high proportion of basal cells have ability to give rise to a mammary repopulating unit (Prater et al., 2014). Subpopulation of the basally residing stem cells could be capable of asymmetrically divisions to give rise to luminal and basal cells. The asymmetric ECM cues provided by the basement membrane at only one side of the stem cell could involve mechanisms of asymmetric MTOC activity associated with cell fate determinants segregation like seen in the neuroblast division described above. Recent study has reported that during the lifetime of a human the number of stem cell divisions in a tissue is positively correlated with the occurrence of cancer (Tomasetti and Vogelstein, 2015). In tissues like skin, intestine and kidney, which undergo several rounds of tissue renewal, harbor tissue specific stem cells. Understanding role of centrosome is driving symmetric (stem cell renewal) and asymmetric division (differentiation) will be necessary to understand its role in controlling tissue maintenance and in induction of cancer phenotype.

EMT and stem cell-like traits

We observed that gain of mesenchymal properties after EMT induction were associated with the reduced MTOC activity in the cells. The mesenchymal state also represents a dedifferentiation state of the cell as it acquires ability to harbor a place in another tissue and re-differentiate. The EMT induction involves dramatic change of transcription profile of the cell and imparts dedifferentiated or stem cell-like property. An eminent report in the field by Robert Weinberg and colleagues showed that induction of EMT in human mammary gland cells result into acquisition of mesenchymal traits and in the expression of stem-cell markers (Mani et al., 2008). The stem cell-like traits are confirmed by molecular markers at the protein level (Twist, snail), cell-surface markers by FACS (CD44 and CD24) and in addition, ability of cells to form mammospheres in suspension cultures. Putting these results in the context of our studies, it is tempting to speculate whether acquisition of stem cell traits is associated with the low MTOC activity. This speculation certainly needs a critical scrutinization before it can be considered as a valid hypothesis, however, a brief phylogenetic overview of the presence of centrosome and regeneration capacity of an organism shows that progressive acquisition of centrosome is associated with loss of regeneration capacity. For example, Plants (A. thaliana), amoeba (D. discoideum), lower eukaryote like S. pombe do not possess centrosome and have ability to regenerate (Bettencourt-Dias, 2013). Interestingly, multicellularity within metazoans with highly differentiated and polarized organ formation is strongly associated with the presence of centrosome. Furthermore, lower metazoans like flatworms (planaria) and hydra do not posses centrosome and maintain ability to regenerate (Bornens & Azimzadeh 2007). If we extrapolate this observation to the regeneration capacity of the stem cells in higher metazoans,

it could be possible that the pluripotent stem cells present at the early developmental stages exhibit lower activity of MTOC, which might be necessary for regeneration capacity of the cells. Over the past years role of centrosome as molecular hub of signaling molecules has emerged (described in chapter I comments) and thus molecules residing at the centrosomal PCM might be involved in giving regeneration potential to the cytoplasm.

4.4 How relevant minimal models are?

As most of the work done towards completion of this thesis is affirmed by the use of the minimal models of tissue, I have been often encountered with the question of 'how relevant the study with minimal model is'? Although minimal models do have a charm of simplicity and the ability to reveal phenomena, which are otherwise hard to observe in the complex multi-cellular systems, the relevance of these phenomena is almost always in question. Biological systems undoubtedly have a very complex nature and it is obvious to wonder how far can we extrapolate the results obtained using in-vitro minimal models of biological systems. To discuss this question, I would like to think of the biological systems, whether it is a DNA replication, protein translation, a cell, tissue, organ or an organism in a form of a function composed of several biophysical laws. The biological processes can manifest themselves when provided by minimum essential components and the right boundary conditions (Vignaud et al., 2012). For example, a purified MTOC with its ability to nucleate microtubules possess the self-centering property which is attributed by microtubules growth and pushing forces on the walls of the chamber (Holy et al., 1997). The system provides understanding of the basic principle that gives centering ability to the centrosome, which is often witnessed in single and layers of cells. Although this minimal system does not confirm whether microtubule pushing by +tips is the sole process involved in centrosome centering, it still provides information about minimum requirement of components (Centrosome, tubulin, GTP) that govern properties of the process, which probably have evolutionary basis in lower form of organisms. Secondly, it does provide a method to test additional possibilities eg. Whether MT sliding and MT pulling by dynein are also involved in the centrosome centering. Vertebrate mammalian system evolved from simple primitive life forms and hence the properties revealed by use of minimal models provide clues about principal mechanisms that probably existed from the beginning of organelle biogenesis. Thus use of minimal models could be looked at as fundamental tools that reveal key aspect of biological system and this approach is similar to that of reverse engineering.

A revolutionary concept of 'Organs-on-chip' in the biotechnology field is taking the center stage for its use in the academic research as well by pharmaceutical companies with the advantage of avoiding animal models for drug screening. The set up of 'Organ-on-chip' consist

of microfluidic devices for culturing living cells to model physiological function of organs. The goal of fabricating such system is not to build whole living organs but rather to synthesize minimal functional unites that recapitulate tissue and organ-level functions (Bhatia and Ingber, 2014). In order to build such tissues, the understanding of basic blocks of functional units of tissues is mandatory. Using the two-cell model, which we adopted to describe complex EMT process revealed important mechanisms involved during morphogenesis. The knowledge of cell confinement, spatial distribution of CCA and CMA, ECM geometry cues will be essential to further build minimal mammary tissue which can generate a lumen, allow secretion of milk-proteins and can also allow investigation of abnormalities. Similar tissue models of kidney tubules, lung-capillary surface or blood-brain barrier can incorporate physical forces, fluid flow and permit analysis of organ-specific responses. A motivating theme is explained by Susanne Rafelski and Wallace Marshall in 'Building the cell: design principles of cellular architecture' and with the increasing understanding of multi-cellular organization revealed by use of minimal tissue system, I believe, we are on the way of 'Building the tissue'.

4.5 References

Amack, J.D. (2014). Salient features of the ciliated organ of asymmetry. Bioarchitecture *4*, 6–15.

Baum, B., and Georgiou, M. (2011). Dynamics of adherens junctions in epithelial establishment, maintenance, and remodeling. J. Cell Biol. *192*, 907–917.

Bettencourt-Dias, M. (2013). Q&A: Who needs a centrosome? BMC Biol. *11*, 28.

Bhatia, S.N., and Ingber, D.E. (2014). Microfluidic organs-on-chips. Nat. Biotechnol. *32*, 760–772.

Doodhi, H., Katrukha, E.A., Kapitein, L.C., and Akhmanova, A. (2014). Mechanical and geometrical constraints control kinesin-based microtubule guidance. Curr. Biol. *24*, 322–328.

Dupin, I., and Etienne-Manneville, S. (2011). Nuclear positioning: Mechanisms and functions. Int. J. Biochem. Cell Biol. *43*, 1698–1707.

Dupin, I., Camand, E., and Etienne-manneville, S. (2009). Classical cadherins control nucleus and centrosome position and cell polarity. *185*.

Friedl, P., and Gilmour, D. (2009). Collective cell migration in morphogenesis, regeneration and cancer. Nat. Rev. Mol. Cell Biol. *10*, 445–457.

Gundersen, G.G., and Worman, H.J. (2013). Nuclear positioning. Cell *152*, 1376–1389.

Hale, C.M., Chen, W.-C., Khatau, S.B., Daniels, B.R., Lee, J.S.H., and Wirtz, D. (2011). SMRT analysis of MTOC and nuclear positioning reveals the role of EB1 and LIC1 in single-cell polarization. J. Cell Sci.

Holy, T.E., Dogterom, M., Yurke, B., and Leibler, S. (1997). Assembly and positioning of microtubule asters in microfabricated chambers. Proc. Natl. Acad. Sci. U. S. A. *94*, 6228–6231.

J. D'Souza, R.C., Knittle, A.M., Nagaraj, N., van Dinther, M., Choudhary, C., ten Dijke, P., Mann, M., and Sharma, K. (2014). Time-resolved dissection of early phosphoproteome and ensuing proteome changes in response to TGF- . Sci. Signal. *7*, rs5–rs5.

Januschke, J., Reina, J., Llamazares, S., Bertran, T., Rossi, F., Roig, J., and Gonzalez, C. (2013). Centrobin controls mother-daughter centriole asymmetry in Drosophila neuroblasts. Nat. Cell Biol. *15*, 241–248.

Ligon, L.A., Karki, S., Tokito, M., and Holzbaur, E.L.F. (2001). Dynein binds to β -catenin and may tether microtubules at adherens junctions. *3*, 913–917.

Liu, Z., Tan, J.L., Cohen, D.M., Yang, M.T., Sniadecki, N.J., Ruiz, S.A., Nelson, C.M., and Chen, C.S. (2010). Mechanical tugging force regulates the size of cell-cell junctions. Proc. Natl. Acad. Sci. U. S. A. *107*, 9944–9949.

Luxton, G.W.G., and Gundersen, G.G. (2011). Orientation and function of the nuclear –

centrosomal axis during cell migration GW Gant Luxton and Gregg G Gundersen. Curr. Opin. Cell Biol. *23*, 579–588.

Mani, S.A., Guo, W., Liao, M.-J., Eaton, E.N., Ayyanan, A., Zhou, A.Y., Brooks, M., Reinhard, F., Zhang, C.C., Shipitsin, M., et al. (2008). The epithelial-mesenchymal transition generates cells with properties of stem cells. Cell *133*, 704–715.

Moore, R., Theveneau, E., Pozzi, S., Alexandre, P., Richardson, J., Merks, A., Parsons, M., Kashef, J., Linker, C., and Mayor, R. (2013). Par3 controls neural crest migration by promoting microtubule catastrophe during contact inhibition of locomotion. Development *140*, 4763–4775.

Pouthas, F., Girard, P., Lecaudey, V., Ly, T.B.N., Gilmour, D., Boulin, C., Pepperkok, R., and Reynaud, E.G. (2008). In migrating cells, the Golgi complex and the position of the centrosome depend on geometrical constraints of the substratum. J. Cell Sci. *121*, 2406–2414.

Prater, M.D., Petit, V., Alasdair Russell, I., Giraddi, R.R., Shehata, M., Menon, S., Schulte, R., Kalajzic, I., Rath, N., Olson, M.F., et al. (2014). Mammary stem cells have myoepithelial cell properties. Nat. Cell Biol. *16*, 942–950, 1–7.

Rooij, J. De, Kerstens, A., Danuser, G., Schwartz, M.A., and Waterman-storer, C.M. (2005). Integrin-dependent actomyosin contraction regulates epithelial cell scattering. October *171*, 153–164.

Scarpa, E., Szabó, A., Bibonne, A., Theveneau, E., Parsons, M., and Mayor, R. (2015). Cadherin Switch during EMT in Neural Crest Cells Leads to Contact Inhibition of Locomotion via Repolarization of Forces. Dev. Cell *34*, 421–434.

Schmoranzer, J., Fawcett, J.P., Segura, M., Tan, S., Vallee, R.B., Pawson, T., and Gundersen, G.G. (2009). Par3 and Dynein Associate to Regulate Local Microtubule Dynamics and Centrosome Orientation during Migration. Curr. Biol. *19*, 1065–1074.

Tang, N., and Marshall, W.F. (2012). Centrosome positioning in vertebrate development. J. Cell Sci. *125*, 4951–4961.

Tomasetti, C., and Vogelstein, B. (2015). Variation in cancer risk among tissues can be explained by the number of stem cell divisions. Science (80-.). *347*, 78–81.

Vignaud, T., Blanchoin, L., and Théry, M. (2012). Directed cytoskeleton self-organization. Trends Cell Biol. *22*, 671–681.

Cell Reports
Report

Cell Adhesion Geometry Regulates Non-Random DNA Segregation and Asymmetric Cell Fates in Mouse Skeletal Muscle Stem Cells

Siham Yennek,[1,2] Mithila Burute,[3,4,5] Manuel Théry,[3,5] and Shahragim Tajbakhsh[1,*]
[1]Institut Pasteur, Stem Cells & Development, Department of Developmental & Stem Cell Biology, CNRS URA 2578, 25 rue du Dr. Roux, Paris F-75015, France
[2]Sorbonne Universités, UPMC, University of Paris 06, IFD-ED 515, 4 Place Jussieu, Paris 75252, France
[3]Institut de Recherche en Technologie et Science pour le Vivant, UMR5168, CEA/UJF/INRA/CNRS, 17 rue des Martyrs, Grenoble 38054, France
[4]CYTOO SA, 7 Parvis Louis Néel, BP50, Grenoble 38040, France
[5]Hôpital Saint Louis, Institut Universitaire d'Hematologie, U1160, INSERM/AP-HP/Université Paris Diderot, 1 Avenue Claude Vellefaux, Paris 75010, France
*Correspondence: shahragim.tajbakhsh@pasteur.fr
http://dx.doi.org/10.1016/j.celrep.2014.04.016

SUMMARY

Cells of several metazoan species have been shown to non-randomly segregate their DNA such that older template DNA strands segregate to one daughter cell. The mechanisms that regulate this asymmetry remain undefined. Determinants of cell fate are polarized during mitosis and partitioned asymmetrically as the spindle pole orients during cell division. Chromatids align along the pole axis; therefore, it is unclear whether extrinsic cues that determine spindle pole position also promote non-random DNA segregation. To mimic the asymmetric divisions seen in the mouse skeletal stem cell niche, we used micropatterns coated with extracellular matrix in asymmetric and symmetric motifs. We show that the frequency of non-random DNA segregation and transcription factor asymmetry correlates with the shape of the motif and that these events can be uncoupled. Furthermore, regulation of DNA segregation by cell adhesion occurs within a defined time interval. Thus, cell adhesion cues have a major impact on determining both DNA segregation patterns and cell fates.

INTRODUCTION

Stem cells can exhibit distinct behaviors in different physiological contexts, such as organogenesis and regeneration. For example, some cells can divide asymmetrically by partitioning a variety of subcellular components, whereas others can divide symmetrically. These types of divisions can be governed by extrinsic stimuli that relay to intrinsic regulators to generate invariant, or randomized, cell divisions consecutively (Yennek and Tajbakhsh, 2013). Numerous intrinsic cell fate regulators have been identified in organisms ranging from flies to humans (Li, 2013; Neumüller and Knoblich, 2009). Of these, perhaps the most intriguing is the asymmetric segregation of old and new template DNA strands, referred to as non-random DNA segregation (or template DNA strand segregation, biased DNA segregation, or "immortal" DNA; Tajbakhsh and Gonzalez, 2009; Yennek and Tajbakhsh, 2013).

Semiconservative replication of DNA results in chromatids containing older template and nascent DNA strands. Label-retaining experiments with nucleotide analogs suggested that labeled DNA strands can persist in certain conditions after extensive cell divisions (Yennek and Tajbakhsh, 2013). These observations led to the hypothesis that chromatids containing older DNA strands segregate collectively to only one of the daughter cells in consecutive asymmetric divisions (Cairns, 1975); however, unequivocal evidence for long-term "immortality" of old DNA strands in vivo is lacking. Support for non-random DNA segregation comes from studies in several tissues, including skeletal muscle (Elabd et al., 2013; Falconer et al., 2010; Karpowicz et al., 2005; Potten et al., 2002; Quyn et al., 2010; Rocheteau et al., 2012; Shinin et al., 2006; Yadlapalli and Yamashita, 2013; Yennek and Tajbakhsh, 2013). Adult skeletal muscle stem cells are quiescent during homeostasis and express the upstream transcription factor Pax7 (Seale et al., 2000). After muscle injury, they enter the cell cycle and generate myoblasts that will divide and differentiate, while a subpopulation of myogenic cells that retain *Pax7* expression will self-renew. During muscle regeneration, DNA and other molecules are partitioned asymmetrically or symmetrically as myogenic cells undergo mitosis (Kuang et al., 2007; Le Grand et al., 2009; Liu et al., 2012; Rocheteau et al., 2012; Shinin et al., 2006; Troy et al., 2012). Non-random DNA segregation occurs in a subpopulation of muscle stem cells, and a correlation with the fates of the resulting daughter cells has been noted (Conboy et al., 2007; Rocheteau et al., 2012; Shinin et al., 2006; Yennek and Tajbakhsh, 2013). Studies examining the mechanisms that regulate this process have focused essentially on intrinsic regulators,

notably, epigenetic marks on the DNA molecules or associated proteins postreplication (Elabd et al., 2013; Evano and Tajbakhsh, 2013; Lansdorp, 2007; Lew et al., 2008; Tajbakhsh and Gonzalez, 2009). However, cell contact, cell density, and microenvironment have also been reported to play a role in non-random DNA segregation (Freida et al., 2013; Pine et al., 2010; Shinin et al., 2006). A network of extracellular matrix (ECM) that surrounds the cell is connected to intracellular cytoskeletal actin via transmembrane proteins. Previous studies using micropatterns coated with ECM showed that its spatial distribution plays a critical role in determining the orientation of the axis of division by controlling the localization of actin-associated cues at the membrane that can interact with spindle microtubules (Minc and Piel, 2012; Théry et al., 2007). Moreover, asymmetric distribution of adhesion cues was shown to induce asymmetric spindle orientation (Théry et al., 2007), suggesting that it could further impact division symmetry by regulating non-random DNA segregation and unequal cell fate. Here, we manipulated the shape of ECM-coated micropatterns and consequently the spatial distribution of cell adhesion, and examined the fate outcome of single mouse skeletal muscle stem cells during cell division.

RESULTS

Polarized Cell Architecture Correlates with Extrinsic Adhesion Asymmetry on Micropatterns

In a previous study (Rocheteau et al., 2012), we showed that a subpopulation of skeletal muscle stem cells isolated from *Tg:Pax7-nGFP* mice can perform non-random DNA segregation (Figure S1A). This phenotype was correlated in part with the distribution of the transcription factors Pax7 (stem/progenitor) and Myogenin (differentiated). In that study, the overall frequency of asymmetry in the total population was not determined.

To investigate cell division outcomes in a controlled microenvironment, we examined single skeletal muscle stem cell divisions on fibronectin/fibrinogen-Alexa Fluor 594-coated micropatterns as described previously for other cell types (Azioune et al., 2010; Théry et al., 2005, 2007), where the differential adhesion and shape of the micropatterns were asymmetric or symmetric in design. Muscle stem cells isolated by fluorescence-activated cell sorting (FACS) using *Tg:Pax7-nGFP* mice (Figure S1B), as well as their progeny cells, are smaller in size than most somatic cells (Figure 1A), with an average surface area in culture of about 250–300 μm^2. This value was determined in an initial series of experiments when micropatterns of various sizes and shapes were designed. The micropattern size was chosen so that all cells could spread on the entire micropattern adhesive area (Azioune et al., 2010). One symmetric and two asymmetric motifs were fabricated for these studies (Figures 1B and 1C). Stainings for F-actin and alpha-tubulin showed dramatic differences in the polarity of the cells seeded on micropatterns. Actin stress fibers were prominently polarized on asymmetric micropatterns but were relatively homogeneous on the symmetric motifs, although in both cases, stainings showed high levels of cortical actin localized at the cell membrane, likely due to the constraints imposed by the micropatterns compared with a nonpatterned surface. Tubulin staining was also strikingly polarized, and to a greater extent on asymmetric motifs (Figure 1B). The polarized nature of the cells on the micropattern motifs that were made for this study is in agreement with previous observations that adhesion cues can impact cell polarity (Freida et al., 2013; Théry et al., 2005), validating the use of micropattern designs for investigating the role of adhesion cues on asymmetric cell divisions in muscle stem cells.

Non-Random DNA Segregation in Muscle Stem Cells Is Promoted on Asymmetric Micropatterns

Incorporation of nucleotide analogs into either template or nascent DNA strands can be achieved by using different labeling regimes (Figure S1A). To investigate the influence of adhesion cues on asymmetric cell divisions, in a first series of experiments we used our previously defined pulse-chase protocol to label dividing myogenic cells in vivo with 5-ethynyl-2′-deoxyuridine (EdU) from 3 to 5 days postinjury (DPI). Following one cell division of chase in vivo, the total Pax7-nGFP$^+$ myogenic population was isolated by FACS and plated on the micropatterns to allow the second division. Using this labeling regime (inclusion protocol; Figures 2A and S1A), template DNA strands were EdU positive, whereas EdU-negative cells contained nascent DNA strands after the two cell divisions of chase (Figures 2A and S1A; Rocheteau et al., 2012; Yennek and Tajbakhsh, 2013). The vast majority of micropatterns contained a single cell following plating (data not shown; see Movies S1 and S2). After a second division during the chase period, DNA segregation and cell fate outcomes were assessed by immunostaining. In some cases, videomicroscopy was used in parallel to ensure that single cells were seeded and daughter cell pairs were obtained on the patterns (Movies S1 and S2). These videos showed the extensive motility of the myogenic cells on the micropattern motifs before and after mitosis. As a control, Pax7-nGFP$^+$ myogenic cells were seeded on fibronectin/fibrinogen-Alexa Fluor 594-coated slides to assess the frequency of asymmetric divisions on a nonpatterned surface.

Strikingly, on both types of asymmetric micropattern motifs, the majority of the cells performed non-random DNA segregation with a frequency of 60%–62% (n = 2 mice; Asym1, n = 163 daughter cell pairs; Asym2, n = 189 daughter cell pairs; Figures 2B and 2C), which is significantly greater than previous results obtained at 5 DPI (Rocheteau et al., 2012). Interestingly, the frequency of non-random DNA segregation on a symmetric pattern was also relatively high at 26% (n = 2 mice; n = 106 daughter cell pairs; Figures 2B and 2C). To verify this effect of cell adhesion on DNA segregation patterns and to rule out biases due to the labeling regime, we incorporated nucleotide analogs into nascent DNA strands instead (exclusion protocol; Figure 2D). We obtained similar results, in that about 71% of cells performed non-random DNA segregation on the asymmetric patterns (n = 9 mice; Asym1, n = 328 daughter cell pairs; Asym2, n = 304 daughter cell pairs) compared with about 29% for the symmetric micropattern (n = 9 mice; n = 330 daughter cell pairs; Figures 2E and 2F). As a control, the frequency of non-random DNA segregation on a nonpatterned surface coated with fibronectin/fibrinogen-Alexa Fluor 594 was noted to be 33% (n = 5 mice; n = 76 of 231 daughter cell pairs; Figure S1C), which was not significantly higher than the frequency on the symmetric

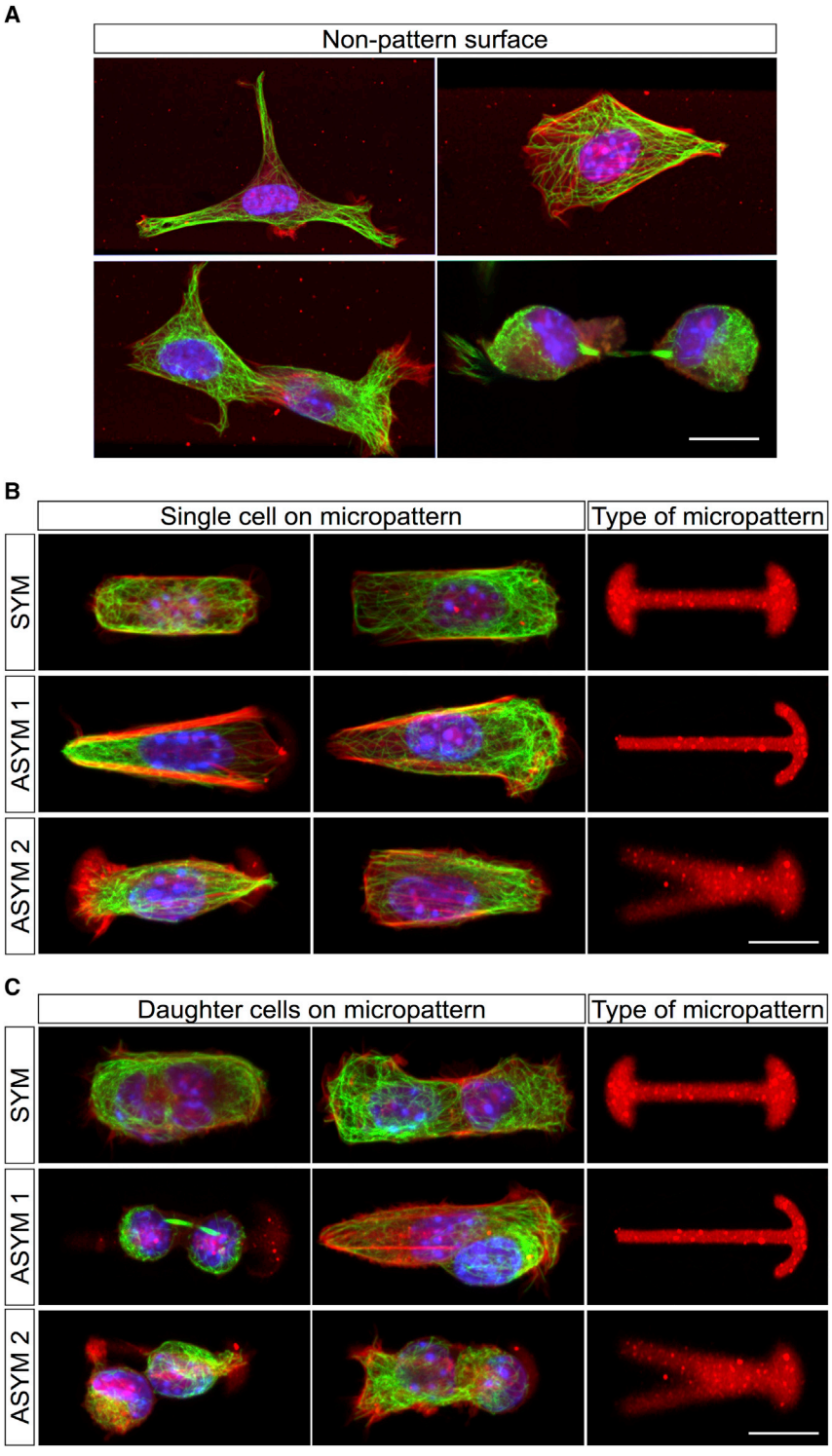

Figure 1. Muscle Stem Cells Are Polarized on Asymmetric Micropatterns

(A) Examples of muscle stem cells isolated by FACS from the TA muscle of *Tg:Pax7-nGFP* mice at 5 DPI, plated on slides coated with fibronectin/fibrinogen-Alexa Fluor 594, and then stained for actin (red) and tubulin (green).

(B) Examples of muscle stem cells isolated and treated as in (A), seeded on symmetric (top) and asymmetric (bottom two rows) micropattern motifs (two examples shown for each). Note the prominent actin stress fibers, particularly on asymmetric motifs, and in some cases the polarized distribution of tubulin on asymmetric motifs.

(C) Examples of muscle stem cells isolated and treated as in (A), seeded on symmetric (top) and asymmetric (bottom two rows) micropattern motifs (two examples shown for each). Cells were allowed to divide on the micropattern. Note that both daughter cells occupy the micropattern surface, and in some cases display polarized tubulin on the asymmetric motifs.

Scale bars: (A), 10 μm; (B and C), 20 μm.

micropattern ($p > 0.37$). In this experiment, we used cytochalasin D to block cell separation after mitosis to ensure the identification of daughter cell pairs, as this drug does not appear to overtly interfere with non-random DNA segregation when applied for a short interval (Conboy et al., 2007; Huh and Sherley, 2011; Karpowicz et al., 2005; S.Y. and S.T., unpublished data). As an additional control for cell division ex vivo, in some experiments we added a second nucleotide analog to the cells on micropatterns prior to cell division to ensure correct nucleotide uptake by both daughter cells during the experiment (Figure S1D). We performed the remaining experiments in this study using the exclusion protocol because it exposes cells for a shorter period to the nucleotide analogs.

Asymmetric Daughter Cell Fates in Muscle Stem Cells Are Promoted on Asymmetric Micropatterns

We next asked whether manipulating the cell adhesion topology would alter the outcome of the resulting daughter cell fates. We showed previously that old DNA strands segregated to the stem cell and that asymmetric cell fates, as assessed by the differential distribution of the transcription factors Pax7 and Myogenin after mitosis, were correlated in part with non-random DNA segregation (Rocheteau et al., 2012). The link between these distinct asymmetric readouts has not yet been established. To assess the effect of adhesion cues on these asymmetries, we analyzed DNA and transcription factor segregation patterns by staining for EdU, Pax7, and Myogenin. When we examined the total Pax7-nGFP$^+$ population on the symmetric motif, we found that the majority of the cells performed random DNA segregation (70%; n = 78 of

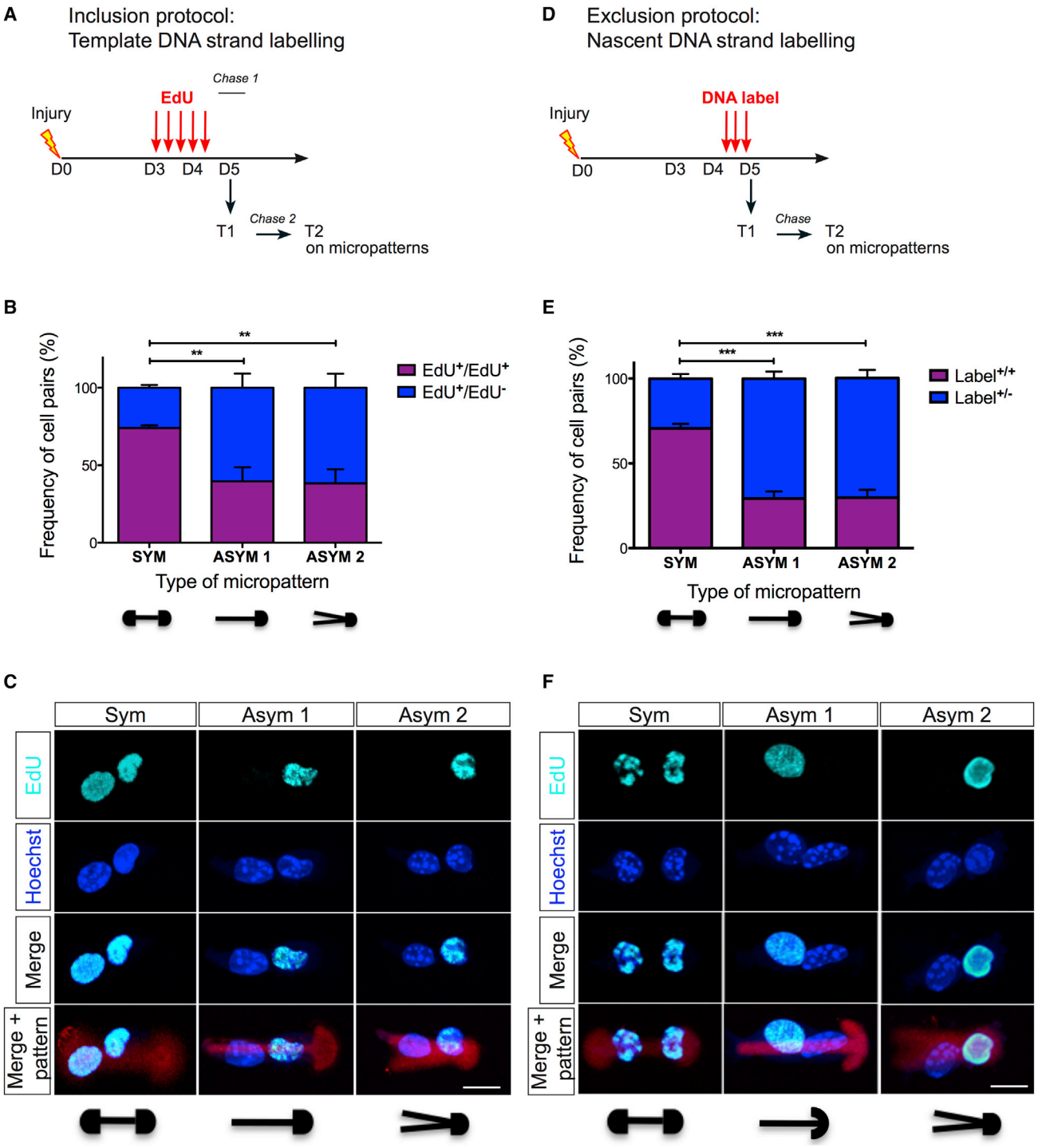

Figure 2. Extrinsic Cues Mediated by Cell Adhesion Regulate the Frequency of Non-Random DNA Segregation on Micropatterns

(A) Scheme illustrating labeling of old template DNA strands. To label older template DNA strands ("inclusion" protocol), label was added for several rounds of cell division to label both DNA strands. After two cell divisions, non-random DNA segregation patterns were assessed empirically.

(B) Histogram showing the frequencies of non-random DNA segregation on one symmetric and two asymmetric micropatterns. Pax7-nGFP$^+$ myogenic cells were isolated by FACS from TA muscle of *Tg:Pax7-nGFP* mice as indicated in (A) ($p < 0.007$). Error bars indicated as SEM.

(C) Click-iT detection of EdU in examples of daughter cell pairs indicated in (B) after two divisions during the chase period. The micropattern shapes are in red (scheme below).

(legend continued on next page)

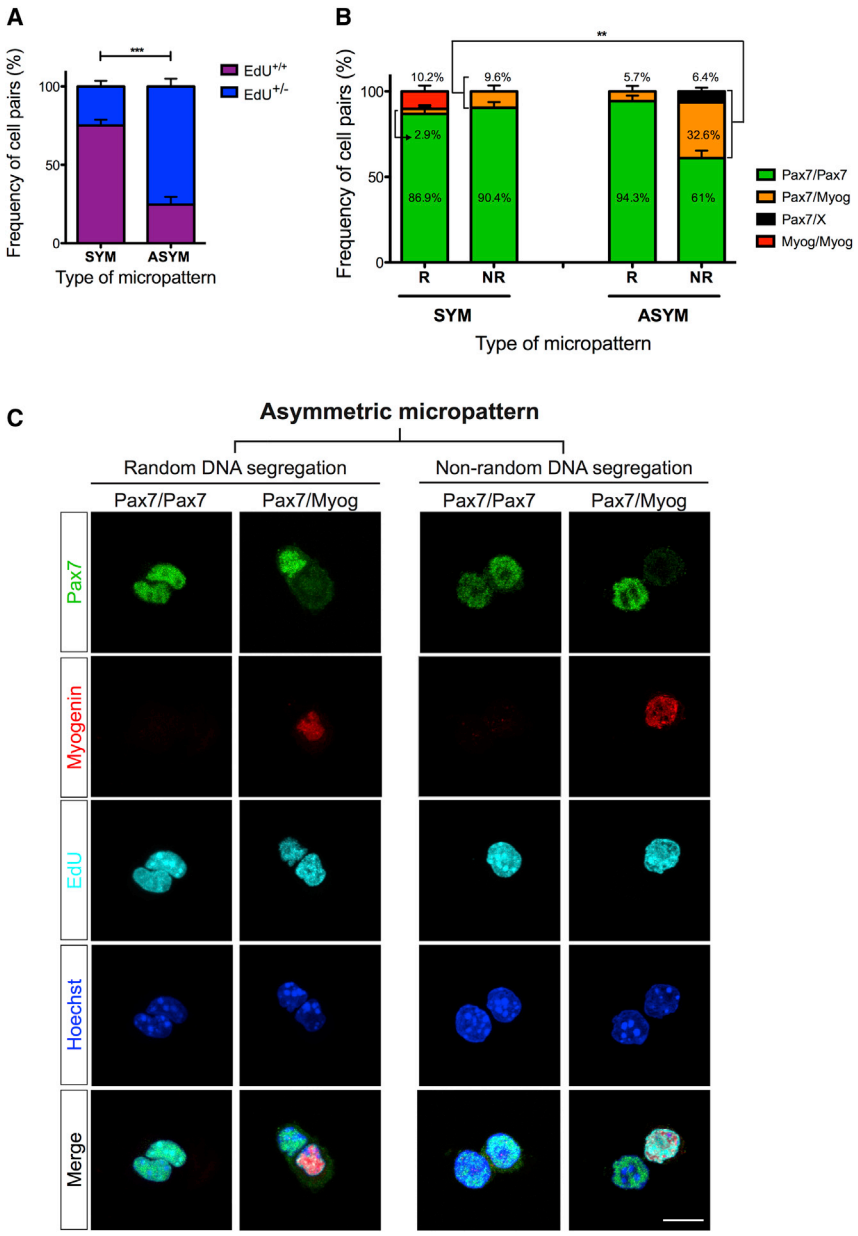

Figure 3. Cell Adhesion Topology Regulates Asymmetric Distribution of Transcription Factors and Correlates with Non-Random DNA Segregation

(A) Pax7-nGFP$^+$ myogenic cells were isolated by FACS from TA muscle of *Tg:Pax7-nGFP* mice as indicated in Figure 2D. Histogram shows the frequencies of DNA segregation patterns on symmetric and asymmetric micropatterns (n = 6 mice, obtained from those indicated in Figure 2E). Note that ASYM represents the average obtained from Asym1 and Asym2 motifs. Error bars indicated as SEM.

(B) Random and non-random DNA segregation patterns indicated in (A) were normalized in each category to 100%. Symmetric (Pax7/Pax7) and asymmetric (Pax7/Myogenin) transcription factor distributions were determined in cell pairs for each category on symmetric and asymmetric micropatterns. Note that Pax7/X cell pairs (X represents a Pax7-negative cell) were a minor fraction in which Pax7 stained only one daughter cell (data not shown). Error bars indicated as SEM.

(C) Examples of Click-iT chemical detection of EdU with anti-Pax7 and anti-Myogenin antibody immunostainings of daughter cell pairs indicated in (B) on the asymmetric micropattern. Examples of symmetric micropatterns are provided in Figure S2. Scale bar, 10 μm.

113 total cells, n = 6 mice; Figure 3A), and among these, the cell fates corresponded to 86.9% Pax7/Pax7, 2.9% Pax7/Myogenin, and 10.2% Myogenin/Myogenin. Further, 30% performed non-random DNA segregation (n = 35 of 113 total cells, n = 6 mice), with 90.4% Pax7/Pax7 and 9.6% Pax7/Myogenin where old DNA strands were retained in the Pax7$^+$ (EdU$^-$) cell (Figures 3A, 3B, and S2).

In contrast, the majority of the cells performed non-random DNA segregation on the asymmetric motifs (74%; n = 201 of 272 total cells, n = 6 mice; Asym1/Asym2 motifs combined), and among these, the cell fates corresponded to 61% Pax7/Pax7 and 32.6% Pax7/Myogenin or 6.4% Pax7/X (Figures 3A–3C). In the latter, a minor fraction of cells that were asymmetric for Pax7 but negative for Myogenin were noted, and these were scored as asymmetric fates. As with non-random DNA segregation on symmetric patterns, old DNA strands were retained in the Pax7$^+$ (EdU$^-$) cell. Random DNA segregation on asymmetric motifs corresponded to 26% of the total population (n = 71 of 272 total cells, n = 6 mice), with 94.3% Pax7/Pax7 and 5.7% Pax7/Myogenin (Figures 3A–3C and S2). Therefore, asymmetric cell fates were preferentially

(D) Scheme illustrating labeling of nascent DNA strands. To label nascent DNA strands ("exclusion" protocol), several pulses of nucleotide analog were administered for the equivalent of one cell division, resulting in labeled nascent strands in hemi-labeled DNA (Rocheteau et al., 2012). A second division during the chase is needed to distinguish labeled nascent DNA strands and unlabeled old template DNA strands in daughter cell pairs.

(E) Histogram showing the frequencies of non-random DNA segregation on one symmetric and two asymmetric micropattern motifs. Pax7-nGFP$^+$ myogenic cells were isolated from TA muscle of *Tg:Pax7-nGFP* mice as indicated in (D). Note that independent experiments were done with either EdU or BrdU from n = 9 mice ($p < 10^{-5}$). Data are represented as Label$^{+/+}$ or Label$^{+/-}$. Error bars indicated as SEM.

(F) Click-iT detection of EdU in examples of daughter cell pairs indicated in (E). The micropattern shapes are in red (schemes below).

Scale bars, 10 μm.

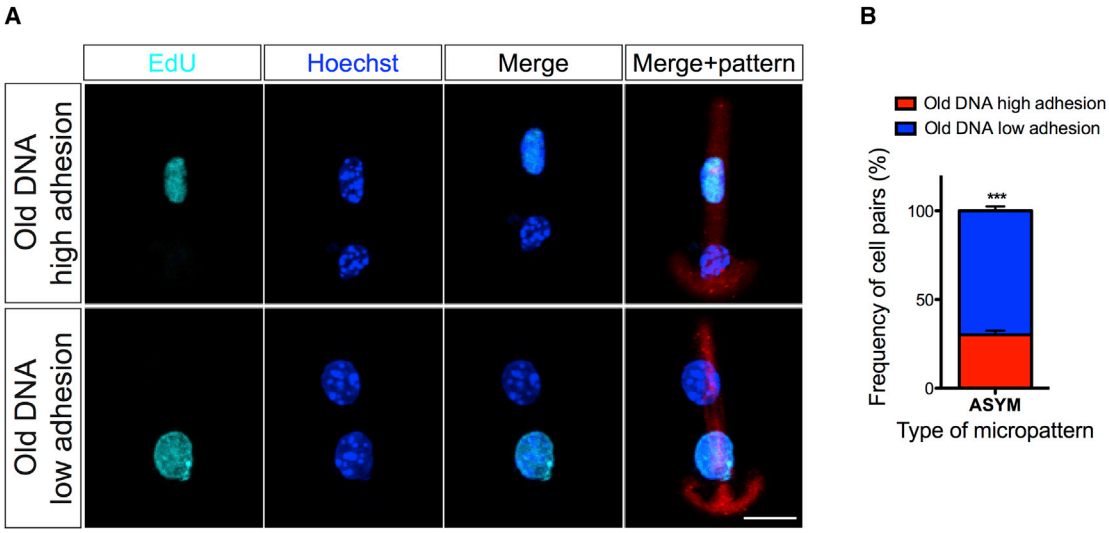

Figure 4. Old Template DNA Strands Are Associated with a Low-Adhesion Surface on Asymmetric Micropatterns

(A) Images of daughter cell pairs aligned along the asymmetric micropattern motif. Cells are labeled as indicated in Figure 2D.

(B) Histogram showing the frequencies of cells retaining old template DNA strands in association with high (curved side of micropattern) or low adhesion on asymmetric micropatterns. n = 168 cells, n = 3 mice; scale bar, 10 μm. Error bars indicated as SEM.

associated with non-random DNA segregation on both motifs, and cells that retained old DNA strands (EdU^-) were associated with Pax7 expression in Pax7/Pax7 and Pax7/Myogenin daughter cell pairs. In addition, 4-fold more asymmetric cell fates were associated with non-random DNA segregation on asymmetric motifs compared with symmetric motifs in this category (9.6% versus 39%). These observations also show that asymmetric cell fates tend to be associated with non-random DNA segregation; however, this correlation is not absolute, as these two events can be uncoupled.

Old Template DNA Strands Are Preferentially Associated with Low Adhesive Surface after Mitosis

The polarized microtubular network on asymmetric micropatterns, as well as the dominant effect of adhesion topology in determining asymmetric cell divisions outcomes, prompted us to assess whether old and new DNA strands show a bias relative to the extent of adhesion on the asymmetric micropattern motifs. To address this question, we examined EdU^+/EdU^- daughter cell pairs (see experimental protocol in Figure 2D) that were oriented along the long axis of the asymmetric micropattern motifs (Figure 4A). Interestingly, about 70% of cell pairs captured after mitosis had old template DNA strands (EdU^-) retained in the daughter cell that was located adjacent to the side with low adhesion (n = 51 of 168 total cell pairs, n = 3 mice; average of Asym1 and Asym2 motifs; $p < 0.0005$; Figure 4B).

Prospectively Isolated Cells Performing Non-Random DNA Segregation Resist Symmetric Micropattern Adhesion Cues

We showed previously that a subpopulation of muscle stem cells corresponding to the Pax7-nGFP^{Hi} fraction after isolation by FACS preferentially executed non-random DNA segregation (Rocheteau et al., 2012). Given the strong influence of extrinsic adhesion cues on determining the type of DNA segregation pattern, we asked whether manipulation of the spatial distribution of adhesion in micropatterns can override this decision in cells that are already engaged to perform non-random DNA segregation. Since relatively large numbers of cells are required for seeding on micropatterns, the top 20% of the total population corresponding to Pax7-nGFP^{Hi} cells was isolated by FACS (Figure 5A) and plated on nonpatterned fibronectin/fibrinogen Alexa Fluor 594-coated slides as a control. We noted that 68% of the cells performed non-random DNA segregation (Figures 5B and 5C; compared with 33% indicated above for the total population; Figure S1C), consistent with our previous findings that non-random DNA segregation is enriched in Pax7-nGFP^{Hi} muscle stem cells during regeneration.

When we examined the Pax7-nGFP^{Hi} population on the asymmetric motifs, we found that the majority of the cells performed non-random DNA segregation (75%; n = 146 of 194 total cells, n = 3 mice; Figures 5D and 5E; average of Asym1/Asym2 motifs), similar to the nonpatterned surface. Strikingly, when seeded on the symmetric motifs, the majority of the Pax7-nGFP^{Hi} cells continued to perform non-random DNA segregation (79%; n = 84 of 107 total cells, n = 3 mice; Figures 5D and 5E). Thus, prospectively isolated cells that perform non-random DNA segregation do not alter their mode of DNA distribution significantly when seeded on a symmetric micropattern.

DISCUSSION

Evidence for the asymmetric distribution of old and new DNA strands during cell division comes from studies in prokaryotes and eukaryotes (Yennek and Tajbakhsh, 2013). How this differential DNA strand identity can be registered during replication and then propagated to cells at the metaphase plate for selective distribution of chromatids containing old and new DNA strands is

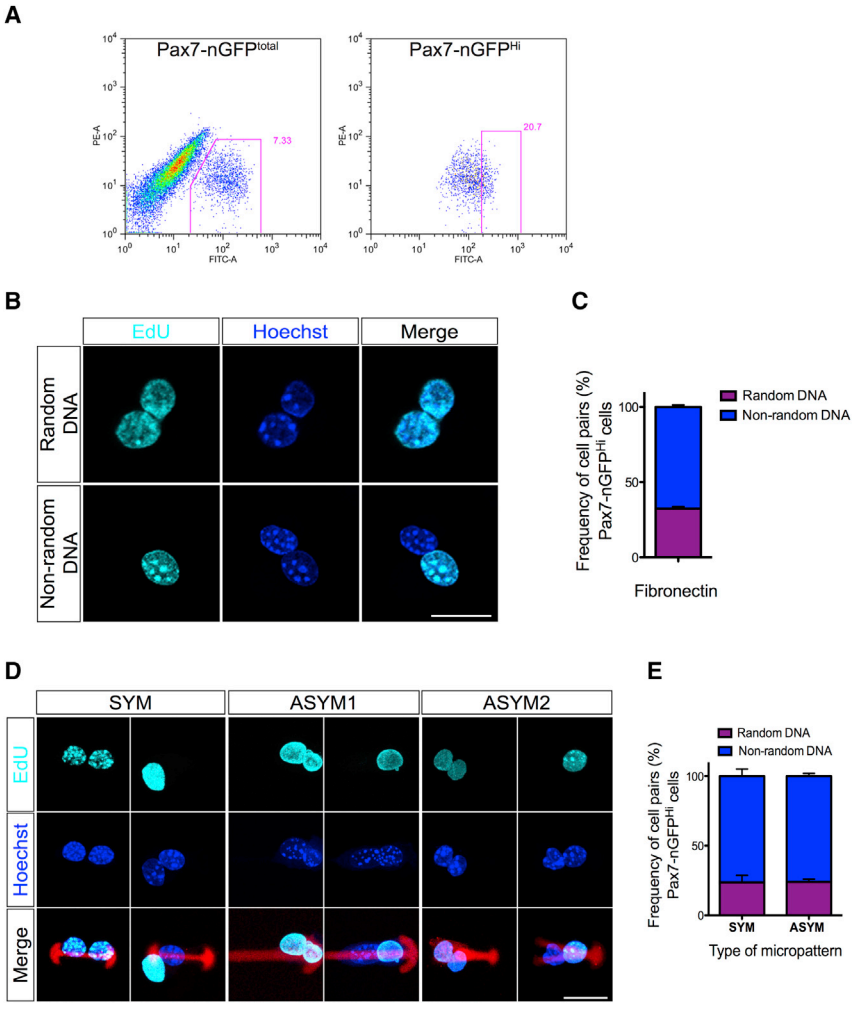

Figure 5. Prospectively Isolated Muscle Stem Cells Performing Non-Random DNA Segregation Resist Extrinsic Symmetry Adhesion Cues on Micropatterns

(A) FACS profiles of myogenic cells isolated from the TA muscle of *Tg:Pax7-nGFP* mice at 5 DPI. Total Pax7-nGFP and Pax7-nGFP^{Hi} (top 20%) cells are shown.

(B) Pax7-nGFP^{Hi} (top 20%) myogenic cells labeled with EdU (see Figure 2D) were isolated from TA muscles of *Tg:Pax7-nGFP* mice at 5 DPI and then plated on nonpatterned fibronectin/fibrinogen-Alexa Fluor 594-coated slides. Examples of random and non-random DNA segregation are shown. Cells were treated with 2 μM cytochalasin D for 2 hr to prevent cell separation.

(C) Histogram showing the frequencies of DNA segregation patterns as indicated in (B). Error bars indicated as SEM.

(D) Pax7-nGFP^{Hi} (top 20%) myogenic cells were isolated as indicated in (B) and seeded on symmetric and asymmetric micropatterns, and EdU staining was revealed by Click-iT chemistry. Micropatterns can be seen in red.

(E) Histogram showing the frequencies of DNA segregation patterns as indicated in (D). Note that ASYM represents the average obtained from Asym1 and Asym2 micropatterns (non-random DNA segregation: SYM, 84/107 cells; ASYM, 146/194 cells; n = 3 mice). Error bars indicated as SEM. Scale bar, 10 μm.

a major unresolved question. Although a clear mechanism to explain this phenomenon is still lacking for stem cells in vivo, studies have focused mainly on intrinsic factors that are largely epigenetic in nature (Elabd et al., 2013; Evano and Tajbakhsh, 2013; Lansdorp, 2007; Lew et al., 2008; Tajbakhsh and Gonzalez, 2009). A role for extrinsic cues in guiding template DNA segregation and cell fates has not been overtly explored. Here, we focused on extrinsic cell adhesion cues on micropatterned artificial niches. We report that by manipulating the spatial distribution of adhesion to the ECM, we could significantly alter the frequency of non-random DNA segregation and corresponding cell fates.

Various forms of mechanical stimuli, ECM, cell-cell contact, and signaling have been shown to play critical roles in the orientation of the plane of division to generate symmetric and asymmetric cell fates after mitosis (Chen et al., 2013; Engler et al., 2006; Freida et al., 2013). For the segregation of molecules associated with the membrane, cytoplasm, or nucleus, the axis of cell division, which is defined perpendicular to the spindle pole, is critical for asymmetric or symmetric outcomes. During mitosis, rotation of the spindle pole complex occurs before its final position is fixed, thereby determining the cell fate outcome (Li, 2013; Morin and Bellaïche, 2011). There is an additional level of complexity when DNA segregation patterns are considered. Old and new DNA strands are identified during DNA replication, and this information is thought to be retained in the condensed chromatin at metaphase prior to DNA segregation. As chromatids are aligned with the spindle pole apparatus, they will segregate to opposite poles along this axis. Therefore, extrinsic cues that can determine spindle pole orientation have been considered less likely (compared with intrinsic factors) to directly promote non-random DNA segregation (Lansdorp, 2007; Yennek and Tajbakhsh, 2013).

Several studies have shown that the behavior of individual or groups of cells and their differentiation on artificial surfaces can be modified on micropatterns (Blong et al., 2010; Freida et al., 2013; Gilbert et al., 2010; Li et al., 2011; Tang et al., 2010; Yu et al., 2013). For example, mesenchymal stem cells plated on microgrooves with regular patterns were reported to exhibit altered nuclear morphology, reduced levels of histone deacetylase activity, and increased histone acetylation (Li et al., 2011). Our finding that cell adhesion can regulate non-random DNA segregation patterns provides insights into the role of extrinsic cues in this process, and this finding is supported by a recent report that non-random DNA segregation in human bone marrow mesenchymal stem cells is regulated by cell adhesion differences on micropatterns (Freida et al., 2013). Interestingly, in that study, non-random DNA segregation patterns

involved some, but not all chromosomes as reported previously (Falconer et al., 2010; Yadlapalli and Yamashita, 2013), in contrast to muscle stem cells, where all chromatids are engaged in this process (Rocheteau et al., 2012). Furthermore, we obtained the highest frequencies reported for non-random DNA segregation in primary cells, and by manipulating cell adhesion were able to show that the majority of muscle stem cells are permissive for this type of asymmetric DNA segregation.

To understand the phenomenon of non-random DNA segregation, it is important to assess its relationship with the cell fates of the resulting daughter cells after cell division. We showed previously that asymmetric cell fates (stem, Pax7; differentiated, Myogenin) are associated with non-random DNA segregation in muscle stem cells on a population level (Rocheteau et al., 2012). Our present study of single cells dividing on micropatterns shows that both symmetric and asymmetric fates are associated with non-random DNA segregation. Interestingly, Pax7/Myogenin asymmetric fates were also found to be associated with random DNA segregation on micropatterns, and this frequency was higher on asymmetric micropatterns. Thus, cell adhesion cues play an important role in the regulation of both of these processes. Notably, non-random DNA segregation was not systematically correlated with the asymmetric distribution of Pax7 and Myogenin in resulting daughter cells. It is possible that we underestimated the overall frequency of asymmetric fates if the downregulation of Pax7 and concomitant upregulation of Myogenin take place well after mitosis has occurred. In this scenario, an intermediate asymmetric state would be scored as a symmetric Pax7/Pax7 event if the daughter cell pairs were captured immediately after mitosis. Our preliminary results suggest that this might be the case, since in Pax7/Pax7 daughter cell pairs, uneven Pax7 immunostainings were also observed in some cases, suggesting that one daughter cell might subsequently downregulate this marker. Nevertheless, our findings suggest that in some cases, DNA asymmetry and cell fate events can be uncoupled. We speculate that the frequency of non-random DNA segregation can be regulated by adhesion molecules located subjacent to the dividing stem cell in the niche in vivo. The coupling of this event with differential cell fates can occur, likely with the intervention of another event(s) that is as yet unidentified. In cases where non-random DNA segregation was associated with symmetric daughter cell fates, it is possible that the differential cells fates were not fixed; thus, subsequent rounds of asymmetric DNA distribution would need to be monitored. We note also that old template DNA strands were consistently inherited by the stem cell in Pax7/Myogenin daughter cell pairs independently of the labeling regime (labeling of old or new DNA with nucleotide analog) or the micropattern shape. Moreover, whether consecutive rounds of non-random DNA segregation occur without an intervening symmetric DNA distribution remains to be explored. Previous studies have reported that transcription factors can be distributed asymmetrically on isolated myofibers, as muscle stem cells divide planar and perpendicular to the myofiber and the basement membrane that ensheathes it (Cossu and Tajbakhsh, 2007; Kuang et al., 2007; Yennek and Tajbakhsh, 2013). Future studies with micropatterns can attempt to mimic this topology to explore the influence of different types of ECM on symmetric and asymmetric cell divisions.

Given that muscle stem cells are highly motile on micropatterns, continuously forming and releasing membrane contacts with the substrate in a dynamic manner (see Movies S1 and S2), we propose that the frequencies obtained for non-random DNA segregation and asymmetric cell fates were underestimated. In other words, a "symmetric" outcome can potentially arise on an asymmetric pattern depending on the probability of polarized contact with the substrate. Similarly, although symmetric patterns are designed to provide a homogeneous microenvironment, cells that release membrane contact on one side can experience temporary asymmetry with a certain probability, even on a symmetric micropattern. This can explain in part the finding that asymmetric outcomes were observed on symmetric micropatterns. Our findings lead us to propose that the adhesive geometry has a predominant effect on the fate of the dividing cells. With the caveat that extensive cell movements occur on the micropatterns, and in contrast to human bone marrow mesenchymal stem cells (Freida et al., 2013), the daughter cell that retained old template DNA strands was found to be preferentially associated with the low-adhesion side of the asymmetric micropattern motif following mitosis. We note, however, that extrinsic cues might be interpreted well before the initiation of mitosis. Future studies should focus on defining the timing of these events in relation to DNA segregation patterns and cell fates. It is also possible that other as yet undefined cues cooperate with cell adhesion to provide a second signaling event for guiding the type of cell division, as suggested above. Indeed, the nature of the substrate could potentially play a role, since fibronectin was suggested to modify Wnt signaling and increase symmetric cell division frequency (Bentzinger et al., 2013). A systematic evaluation of different ECM molecules, as well as the link among extrinsic cell adhesion cues, mother and daughter centrosomes, and kinetochore proteins (Evano and Tajbakhsh, 2013; Lansdorp, 2007; Lew et al., 2008; Tajbakhsh and Gonzalez, 2009) should be a major objective in future studies.

Finally, we report here that prospectively isolated muscle stem cells engaged in non-random DNA segregation resisted reversion to a random segregation pattern when seeded on symmetric micropatterns. Thus, our study shows that adhesion cues have a major impact on the type of DNA segregation pattern; however, this mechanism operates with a defined period corresponding to one cell cycle to regulate DNA segregation patterns. Beyond this window of opportunity, the non-random DNA segregation is irreversible. In summary, we provide evidence that the frequency of non-random DNA segregation and cell fates can be regulated by the spatial distribution of cell adhesion in skeletal muscle stem cells. The ability to control asymmetric and symmetric cell fates is of major interest for stem cell-based therapies in which a key objective is to maintain the stem cell state during amplification of the population ex vivo.

EXPERIMENTAL PROCEDURES

Micropatterns

After initial assessment of the size of activated myogenic cells was made, asymmetric (two types) and symmetric patterns were designed and manufactured on polystyrene-coated glass slides to allow spreading of single muscle stem cells or two daughter cells after cell division (Azioune et al., 2010). Due to the relatively small size of the myogenic cells, two asymmetric patterns

were designed, and they yielded similar results. Briefly, glass coverslips were spin coated at 3,000 rpm with a 1% solution of polystyrene in toluene. This polystyrene layer was further oxidized with an oxygen plasma treatment (Harrick Plasma) for 15 s at 30 W and incubated with poly-L-lysine polyethylene glycol (PLL-PEG; SuSoS) in 10 mM HEPES, pH 7.4, at room temperature (RT) for 30 min. PLL-PEG-coated slides were placed in contact with an optical mask containing transparent micropatterns (Toppan Photomask) using an in-house-made vacuum chamber and then exposed to deep UV light (Jelight). Micropatterned slides were subsequently incubated with a PBS solution containing 20 μg/ml fibronectin (Sigma) and 20 μg/ml Alexa Fluor 594-fibrinogen (Invitrogen) for 30 min and then rinsed three times in PBS. Coverslips were dried then rinsed in PBS before cell seeding.

Mice, Muscle Injury, and Injections of Thymidine Analogs

Animals were handled according to national and European community guidelines, and protocols were approved by an ethics committee. *Tg:Pax7-nGFP* mice were described previously (Sambasivan et al., 2009). Muscle injury was done as described previously (Gayraud-Morel et al., 2007). Briefly, mice were anesthetized with 0.5% Imalgene/2% Rompun. The Tibialis anterior (TA) muscle was injected with 10 μl of notexin (10 μM; Latoxan). 5-Bromo-2′-deoxyuridine (BrdU; #B5002; Sigma) and EdU (#E10187; Invitrogen) analogs were dissolved in 0.9% saline (GIBCO) and stored at 10 and 6 mg/ml, respectively. For the pulse-chase labeling after notexin injury, transgenic mice (6–10 weeks old) were injected intraperitoneally with 30 μg/g of EdU or 50 μg/g of BrdU. For the inclusion protocol, EdU was injected five times, 8 hr apart, from 3 DPI (Figure S1A). For the exclusion protocol, BrdU or EdU was injected three times, 2 hr apart, 14 hr prior to sacrifice (Figure S1A).

Muscle Stem Cell Isolation, Culture, and FACS

Dissections were done essentially as described previously (Gayraud-Morel et al., 2007). Injured TA muscles were removed from the bone in cold Dulbecco's modified Eagle's medium (DMEM; Invitrogen) containing 1% of penicillin-streptomycin (PS; Invitrogen), minced with scissors, and then digested with a mixture of 0.08% Collagenase D (Roche) and 0.2% Trypsin (Invitrogen) in DMEM/1% PS/DNase I (10 μg/ml; Roche) for five consecutive cycles of 30 min at 37°C. For each round, the supernatant was filtered through a 70 μm cell strainer and trypsin was blocked with 8% fetal calf serum (FCS; Invitrogen) on ice. Pooled supernatants from each digestion cycle were centrifuged twice at 1,600 rpm for 10 min at 4°C. Between centrifugations, pellets were resuspended in cold 2% FCS/1% PS/DMEM, washed with 1% PS/DMEM and filtered through a 40 μm cell strainer. Prior to FACS, the pellet was resuspended in 500 μl of cold 2% FCS/1% PS/DMEM and the cell suspension was filtered through a 40 μm cell strainer. Cells were sorted using a FACS Aria III (BD Biosciences) and collected in 1 ml of 2% FCS/1% PS/DMEM. Cells were displayed as phycoerythrin (PE, red) on the FACS profile. All analyses and quantitations were performed using FlowJo software. Satellite cells were cultured in 1:1 DMEM (Invitrogen)/MCDB (Sigma) containing 20% FCS, 2% Ultroser (Pall), and 1% PS. The medium was filtered through a 0.2 μm filter. Cells were cytospun on the chip at 40 *g* for 4 min, and 1 hr after plating, nonattached cells were washed with media. Cells were kept in an incubator (37°C, 5% CO_2, 3% O_2) for 12 hr.

Immunocytochemistry

For nuclear immunostainings, cells were fixed with 4% paraformaldehyde (PFA) in PBS 1× (GIBCO) and then washed three times with PBS 1×. Cells were permeabilized with 0.5% Triton X-100 5 min, washed once with PBS 1×, and blocked with 10% serum for 30 min. For the BrdU immunostaining, cells were unmasked with DNaseI (1,000 U/ml; Roche) for 30 min at 37°C prior to blocking. Cells were incubated with primary antibodies (Pax7, mouse monoclonal 1/30, DSHB; Myogenin, rabbit polyclonal, #sc-576, Santa Cruz, 1/200; anti-BrdU, BD, 1/100) for 3 hr at RT. Cells were washed with PBS 1× three times and incubated for 1 hr with Alexa-conjugated secondary antibodies (1/500; Life Technologies) and washed in PBS 1×. EdU staining was chemically revealed with the Click-iT kit (#C10640; Life Technologies). For cytoskeleton stainings, cells were fixed and permeabilized with 0.1% Triton X-100/0.5% glutaraldehyde in cytoskeleton buffer sucrose (CBS) for 10 min at RT and then washed three times with PBS 1×. Glutaraldehyde was reduced with 0.1 M glycine for 10 min at RT and then washed three times with PBS 1×. Cells were blocked in 3% BSA for 45 min at RT. Cells were incubated with anti-alpha-tubulin, rat monoclonal (#MCA77G, 1/1,000; Serotec) for 1 hr at RT. Cells were washed three times with PBS 1× and incubated with alexa 488-conjugated secondary antibody (1/500, Life Technologies) and phalloidin conjugated with rhodamine (1/1,000; Molecular Probes); stainings were protected from light. After three washes with PBS 1×, cells were incubated with Hoechst 33342 (1/1,000; stock 1 mg/ml). Chips were mounted with Slow Fade Gold reagent (#S3940; Life Technologies). Chips were analyzed with a Leica SPE confocal, Zeiss Observer Z1, and Zeiss LSM700. All antibodies were diluted in 0.1% BSA/0.1% Tween/PBS 1×. CBS contains 10 mM of 4-morpholineethanesulfonic acid (pH 6.1), 138 mM of potassium chloride, 3 mM of magnesium chloride, and 2 mM of ethylene glycol tetraacetic acid (Mitchison lab, Harvard Medical School; http://mitchison.med.harvard.edu/protocols.html).

Live Imaging

Cells isolated by FACS were plated on micropatterns as described above (Azioune et al., 2010). The plate was then incubated at 37°C, 5% CO_2, and 3% O_2 (Zeiss, Pecon). A Zeiss Observer.Z1 connected to an LCI PlnN 10×/0.8 W DICII objective and Hamamatsu Orca Flash 4 camera piloted with Zen (Zeiss) was used. Cells were filmed and images were taken every 8 min with bright-field and DICII filters (Zeiss). The raw data were transformed and presented as a video.

Statistics

Statistical analysis was performed with GraphPad Prism software using appropriate tests and a minimum of 95% confidence interval for significance (*$p < 0.05$, **$p < 0.001$, ***$p < 0.0001$). Graphs display the average values of all animals tested (SEM).

SUPPLEMENTAL INFORMATION

Supplemental Information includes two figures and two movies and can be found with this article online at http://dx.doi.org/10.1016/j.celrep.2014.04.016.

AUTHOR CONTRIBUTIONS

S.T., S.Y., and M.T. proposed the concept and designed the experiments. S.Y. performed the experiments. M.B. and M.T. designed and prepared the micropatterned chips. S.Y. and S.T. wrote the paper. All authors read and agreed with the manuscript.

ACKNOWLEDGMENTS

We thank Theo Cambier for the optical mask design and members of the lab for helpful discussions. S.T. acknowledges support from the Institut Pasteur, Agence Nationale de la Recherche (Laboratoire d'Excellence Revive, Investissement d'Avenir; ANR-10-LABX-73 and ANR-06-BLAN-0039), the Association pour la Recherche sur le Cancer, and the European Research Council (Advanced Research Grant 332893). S.Y. is funded by a PhD fellowship from La Ligue contre le Cancer. M.T. acknowledges support from the ERC (Starting Grant 310472) and the ISI program of BPIFrance.

Received: October 10, 2013
Revised: February 24, 2014
Accepted: April 9, 2014
Published: May 15, 2014

REFERENCES

Azioune, A., Carpi, N., Tseng, Q., Théry, M., and Piel, M. (2010). Protein micropatterns: a direct printing protocol using deep UVs. Methods Cell Biol. *97*, 133–146.

Bentzinger, C.F., Wang, Y.X., von Maltzahn, J., Soleimani, V.D., Yin, H., and Rudnicki, M.A. (2013). Fibronectin regulates Wnt7a signaling and satellite cell expansion. Cell Stem Cell *12*, 75–87.

Blong, C.C., Jeon, C.-J., Yeo, J.-Y., Ye, E.-A., Oh, J., Callahan, J.M., Law, W.D., Mallapragada, S.K., and Sakaguchi, D.S. (2010). Differentiation and behavior of human neural progenitors on micropatterned substrates and in the developing retina. J. Neurosci. Res. *88*, 1445–1456.

Cairns, J. (1975). Mutation selection and the natural history of cancer. Nature *255*, 197–200.

Chen, S., Lewallen, M., and Xie, T. (2013). Adhesion in the stem cell niche: biological roles and regulation. Development *140*, 255–265.

Conboy, M.J., Karasov, A.O., and Rando, T.A. (2007). High incidence of non-random template strand segregation and asymmetric fate determination in dividing stem cells and their progeny. PLoS Biol. *5*, e102.

Cossu, G., and Tajbakhsh, S. (2007). Oriented cell divisions and muscle satellite cell heterogeneity. Cell *129*, 859–861.

Elabd, C., Cousin, W., Chen, R.Y., Chooljian, M.S., Pham, J.T., Conboy, I.M., and Conboy, M.J. (2013). DNA methyltransferase-3-dependent nonrandom template segregation in differentiating embryonic stem cells. J. Cell Biol. *203*, 73–85.

Engler, A.J., Sen, S., Sweeney, H.L., and Discher, D.E. (2006). Matrix elasticity directs stem cell lineage specification. Cell *126*, 677–689.

Evano, B., and Tajbakhsh, S. (2013). Sorting DNA with asymmetry: a new player in gene regulation? Chromosome Res. *21*, 225–242.

Falconer, E., Chavez, E.A., Henderson, A., Poon, S.S., McKinney, S., Brown, L., Huntsman, D.G., and Lansdorp, P.M. (2010). Identification of sister chromatids by DNA template strand sequences. Nature *463*, 93–97.

Freida, D., Lecourt, S., Cras, A., Vanneaux, V., Letort, G., Gidrol, X., Guyon, L., Larghero, J., and Thery, M. (2013). Human bone marrow mesenchymal stem cells regulate biased DNA segregation in response to cell adhesion asymmetry. Cell Rep. *5*, 601–610.

Gayraud-Morel, B., Chrétien, F., Flamant, P., Gomès, D., Zammit, P.S., and Tajbakhsh, S. (2007). A role for the myogenic determination gene Myf5 in adult regenerative myogenesis. Dev. Biol. *312*, 13–28.

Gilbert, P.M., Havenstrite, K.L., Magnusson, K.E., Sacco, A., Leonardi, N.A., Kraft, P., Nguyen, N.K., Thrun, S., Lutolf, M.P., and Blau, H.M. (2010). Substrate elasticity regulates skeletal muscle stem cell self-renewal in culture. Science *329*, 1078–1081.

Huh, Y.H., and Sherley, J.L. (2011). Molecular cloaking of H2A.Z on mortal DNA chromosomes during nonrandom segregation. Stem Cells *29*, 1620–1627.

Karpowicz, P., Morshead, C., Kam, A., Jervis, E., Ramunas, J., Cheng, V., and van der Kooy, D. (2005). Support for the immortal strand hypothesis: neural stem cells partition DNA asymmetrically in vitro. J. Cell Biol. *170*, 721–732.

Kuang, S., Kuroda, K., Le Grand, F., and Rudnicki, M.A. (2007). Asymmetric self-renewal and commitment of satellite stem cells in muscle. Cell *129*, 999–1010.

Lansdorp, P.M. (2007). Immortal strands? Give me a break. Cell *129*, 1244–1247.

Le Grand, F., Jones, A.E., Seale, V., Scimè, A., and Rudnicki, M.A. (2009). Wnt7a activates the planar cell polarity pathway to drive the symmetric expansion of satellite stem cells. Cell Stem Cell *4*, 535–547.

Lew, D.J., Burke, D.J., and Dutta, A. (2008). The immortal strand hypothesis: how could it work? Cell *133*, 21–23.

Li, R. (2013). The art of choreographing asymmetric cell division. Dev. Cell *25*, 439–450.

Li, Y., Chu, J.S., Kurpinski, K., Li, X., Bautista, D.M., Yang, L., Sung, K.-L.P., and Li, S. (2011). Biophysical regulation of histone acetylation in mesenchymal stem cells. Biophys. J. *100*, 1902–1909.

Liu, W., Wen, Y., Bi, P., Lai, X., Liu, X.S., Liu, X., and Kuang, S. (2012). Hypoxia promotes satellite cell self-renewal and enhances the efficiency of myoblast transplantation. Development *139*, 2857–2865.

Minc, N., and Piel, M. (2012). Predicting division plane position and orientation. Trends Cell Biol. *22*, 193–200.

Morin, X., and Bellaïche, Y. (2011). Mitotic spindle orientation in asymmetric and symmetric cell divisions during animal development. Dev. Cell *21*, 102–119.

Neumüller, R.A., and Knoblich, J.A. (2009). Dividing cellular asymmetry: asymmetric cell division and its implications for stem cells and cancer. Genes Dev. *23*, 2675–2699.

Pine, S.R., Ryan, B.M., Varticovski, L., Robles, A.I., and Harris, C.C. (2010). Microenvironmental modulation of asymmetric cell division in human lung cancer cells. Proc. Natl. Acad. Sci. USA *107*, 2195–2200.

Potten, C.S., Owen, G., and Booth, D. (2002). Intestinal stem cells protect their genome by selective segregation of template DNA strands. J. Cell Sci. *115*, 2381–2388.

Quyn, A.J., Appleton, P.L., Carey, F.A., Steele, R.J., Barker, N., Clevers, H., Ridgway, R.A., Sansom, O.J., and Näthke, I.S. (2010). Spindle orientation bias in gut epithelial stem cell compartments is lost in precancerous tissue. Cell Stem Cell *6*, 175–181.

Rocheteau, P., Gayraud-Morel, B., Siegl-Cachedenier, I., Blasco, M.A., and Tajbakhsh, S. (2012). A subpopulation of adult skeletal muscle stem cells retains all template DNA strands after cell division. Cell *148*, 112–125.

Sambasivan, R., Gayraud-Morel, B., Dumas, G., Cimper, C., Paisant, S., Kelly, R.G., and Tajbakhsh, S. (2009). Distinct regulatory cascades govern extraocular and pharyngeal arch muscle progenitor cell fates. Dev. Cell *16*, 810–821.

Seale, P., Sabourin, L.A., Girgis-Gabardo, A., Mansouri, A., Gruss, P., and Rudnicki, M.A. (2000). Pax7 is required for the specification of myogenic satellite cells. Cell *102*, 777–786.

Shinin, V., Gayraud-Morel, B., Gomès, D., and Tajbakhsh, S. (2006). Asymmetric division and cosegregation of template DNA strands in adult muscle satellite cells. Nat. Cell Biol. *8*, 677–687.

Tajbakhsh, S., and Gonzalez, C. (2009). Biased segregation of DNA and centrosomes: moving together or drifting apart? Nat. Rev. Mol. Cell Biol. *10*, 804–810.

Tang, J., Peng, R., and Ding, J. (2010). The regulation of stem cell differentiation by cell-cell contact on micropatterned material surfaces. Biomaterials *31*, 2470–2476.

Théry, M., Racine, V., Pépin, A., Piel, M., Chen, Y., Sibarita, J.-B., and Bornens, M. (2005). The extracellular matrix guides the orientation of the cell division axis. Nat. Cell Biol. *7*, 947–953.

Théry, M., Jiménez-Dalmaroni, A., Racine, V., Bornens, M., and Jülicher, F. (2007). Experimental and theoretical study of mitotic spindle orientation. Nature *447*, 493–496.

Troy, A., Cadwallader, A.B., Fedorov, Y., Tyner, K., Tanaka, K.K., and Olwin, B.B. (2012). Coordination of satellite cell activation and self-renewal by Par-complex-dependent asymmetric activation of p38α/β MAPK. Cell Stem Cell *11*, 541–553.

Yadlapalli, S., and Yamashita, Y.M. (2013). Chromosome-specific nonrandom sister chromatid segregation during stem-cell division. Nature *498*, 251–254.

Yennek, S., and Tajbakhsh, S. (2013). DNA asymmetry and cell fate regulation in stem cells. Semin. Cell Dev. Biol. *24*, 627–642.

Yu, T., Chua, C.K., Tay, C.Y., Wen, F., Yu, H., Chan, J.K.Y., Chong, M.S.K., Leong, D.T., and Tan, L.P. (2013). A generic micropatterning platform to direct human mesenchymal stem cells from different origins towards myogenic differentiation. Macromol. Biosci. *13*, 799–807.

Figure 5. 1 -Annex

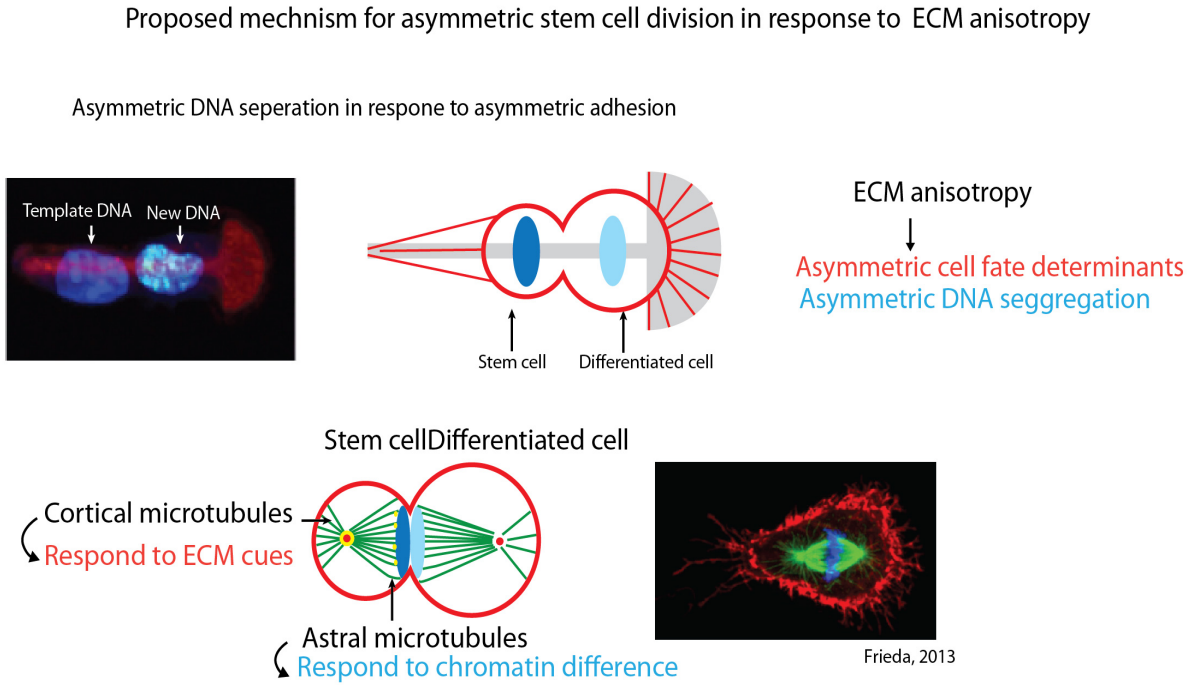

(A) Organ asymmetry is generated because of cilia beating and resulting fluid flow (B) Cell divisions are oriented during tubulogensis by spindle pole positioning (C) MTOC acitivty is responsible for asymmetric neuroblast division (D) Possible role of MTOC activity of centrosome which can be involved in chromatin seggregation

Description

The asymmetric cues for the cell division are often provided by stem cell niche made up of the surrounding ECM and neighboring cells. The anisotropic micropattern geometries could recapitulate asymmetric cell division of the human bone marrow and mouse skeletal muscle stem cell pools (Freida et al., 2013; Yennek et al., 2014). Surprisingly, segregation of the template and the new DNA in the daughter cells was non-random on the asymmetric micropattern wherein newly synthesized DNA was on the side of high ECM adhesion and template DNA was retained on the side of low ECM adhesion (Figure 5.3 D). The resulting DNA segregation was coupled to the respective cell fate markers such as Pax7 (stem cell) and Myogenin (progenitor). The extrinsic ECM cues direct cell division axis orientation through cytoskeletal structures like actin rich retraction fibres and by microtubule interaction with cortical cues during symmetric cell division. It is most likely that the anisotropic arrangement of these structural elements in response to the cell adhesion cues drive asymmetric DNA segregation of these stem cells. The process could involve epigenetic factors associated with DNA modification coupled with old and new chromatin alignment with the spindle pole apparatus that can segregate old and new DNA to the opposite poles.

Annex-2: Candidate siRNAs used for validation of the 'EMT kit'

	Gene	Name of the Genes
1	NTP	Non Targeting pool of SiRNA
2	ERBB2	Receptor tyrosine kinase
3	FAT2	FAT atypical cadherin 2
4	CTNND1	Catenin, delta1
5	HSPD1	Heat shock protein 1
6	JUP	Junction plakoglobin
7	IMPDH2	Inosine 5'-monophosphate dehydrogenase 2
8	ITGB4	Integrin beta 4
9	MAPK1	Mitogen activated protein kinase
10	P4HA2	Prolyl 4-dydroxylase, alpha polypeptide II, Collagen synthesis
11	PHB	Prohibitin, evolutionarily conserved, role in cellular senescence and tumor suppression
12	PKP4	Plakophilin 4, may be part of desmosomal plaque
13	PSEN1	Presenilin 1, clevage of Notch receptor
14	PLEKHA6	Pleckstrin homology domain containing
15	POTEF	POT Ankyrin domain family, adapter protein
16	PPP6C	Protein Phosphotase 6
17	RAP1GDS1	RAP1, GTP-GDP dissociation stimulator
18	REEP4	Receptor accessory protein 4
19	STT3A	Subunit of oligosaccharyl trasnferase complex
20	TJP2	tight Junction protein 2